Independent Parallel Capillary Array Separations for Rapid Second Dimension Sampling in On-Line Two-Dimensional Capillary Electrophoresis of Complex Biological Samples

John D. Chin

A Thesis
in the Department of
Chemistry and Biochemistry

Presented in Partial Fulfillment of the Requirements
for the Degree of Doctor of Philosophy (Chemistry) at
Concordia University
Montreal, Quebec, Canada

May 2020

© John Chin, 2020

CONCORDIA UNIVERSITY
SCHOOL OF GRADUATE STUDIES

This is to certify that the thesis prepared

By: John Diefenbaker Chin

Entitled: Independent Parallel Capillary Array Separations for Rapid Second Dimension Sampling in

On-Line Two-Dimensional Capillary Electrophoresis of Complex Biological Samples

and submitted in partial fulfillment of the requirements for the degree of

Doctor Of Philosophy   Chemistry

complies with the regulations of the University and meets the accepted standards with respect to originality and quality.

Signed by the final examining committee:

Dr. Uri Shalev   Chair

Dr. Karen Waldron   External Examiner

Dr. William Zerges   External to Program

Dr. Yves Gelinas   Examiner

Dr. Pat Forgione   Examiner

Dr. Cameron D. Skinner   Thesis Supervisor (s)

Approved by   Dr. Yves Gelinas

Chair of Department or Graduate Program Director

July 17, 2020

Date of Defence

Pascale Sicotte   Dean, Faculty of Arts and Sciences

ABSTRACT

Independent Parallel Capillary Array Separations for
Rapid Second Dimension Sampling in
On-Line Two-Dimensional Capillary Electrophoresis of
Complex Biological Samples

John D. Chin, Ph.D. Chemistry
Concordia University, 2020

Biological samples remain challenging in proteomic separations due to their complexity and large concentration dynamic range. Improvements to separation power are needed to interrogate proteomes more deeply and facilitate the advancement of biomarker discovery for personalized medicine.

Current online multidimensional separations require compromise; long analysis times if the second dimension (^{2}D) must be regenerated between injections, or reduced separation efficiency if the ^{2}D is operated rapidly. Using an array of capillaries as the ^{2}D, operated in parallel, allows fast sampling of the first dimension (^{1}D). This relaxes the constraints on the ^{2}D separation, allowing it to operate at optimal separation conditions that would otherwise be sacrificed for speed. This configuration allows total separation times to approximately equal to the ^{1}D separation time.

We have developed a novel interface that enables continuous sampling of a ^{1}D separation by a ^{2}D capillary array for rapid, high peak capacity two-dimensional (2D) separations, based upon automated precision positioning of capillaries. Within a laminar flow regime, a capillary electrophoresis (CE) ^{1}D separation was coupled to an array of eight independent CE ^{2}D separations. The instrument terminus provides laser-induced fluorescence detection via a sheath flow cuvette.

Effluent transfer efficiency, from the ^{1}D to the ^{2}D, and detection was optimized using visible and fluorescent dye tracers. To that end, this dissertation will discuss characterization of interface and detector parameters, including: inter-capillary transverse alignment accuracy, injection distance,

injection time, hydrodynamic flow rate, density considerations, inter- and intra-capillary differences, signal crosstalk and laser intensity.

Separation performance will further be demonstrated using model protein and serum digestates. Each dimension of the 2D instrument will be operated as a one-dimensional (1D) instrument to compare against an optimized commercial 1D CE instrument. These results will be used to evaluate the quality of the separations operated in on-line 2D capillary electrophoresis-to-capillary array electrophoresis (CE×CAE) mode. A novel application of the CE×CAE design will be discussed in the spirit of resolving the long-standing challenge of migration time reproducibility in CE separations.

Acknowledgements

I would like to first thank my research advisor, Dr. Cameron D. Skinner, for the opportunity to work in his lab, the guidance that helped me to complete this dissertation. I would also like to thank my committee members Prof. Yves Gelinas and Dr. Pat Forgione for their support throughout my graduate training.

I am grateful for the colleagues I have had the chance to share the Skinner lab experience with (Michel Boisvert, Maria Kaltcheva, Alex Lawandi, Brigitte Desharnais, David Boivin).

Much thanks to the machine and electronics shops, and other staff in the department who were willing to offer their time, advice and help.

I luckily gained friendships throughout the department that are too numerous to list here, but please know I appreciated our conversations through the thick and thin of it.

Finally, I wish to thank Laura. Without her enduring encouragement, this thesis may never have reached its end.

Table of Contents

List of Figures

List of Tables

List of Equations

List of Abbreviations

<β>: undersampling factor

1-DE: one-dimensional polyacrylamide gel electrophoresis

1D: one-dimensional

^{1}D: first dimension

n_c: peak capacity

^1n_c: first dimension peak capacity

^2n_c: second dimension peak capacity

$^1n'_c$: corrected first dimension peak capacity

2-DE: two-dimensional polyacrylamide gel electrophoresis

2D: two-dimensional

2D-LC: two-dimensional liquid chromatography

^{2}D: second dimension

$n_{c,2D}$: two-dimensional peak capacity

3D: three-dimensional

^{3}D: third dimension

AD: amperometric detection

AMF: amniotic fluid

BGE: Background electrolyte

BSA: bovine serum albumin

C^{4}D: contactless capacitively coupled conductivity detector

CAD: computer-aided design

CAE: capillary array electrophoresis

CCD: charge-coupled device

CE: capillary electrophoresis

CE×CAE: two-dimensional capillary electrophoresis to capillary array electrophoresis

CE×CE: comprehensive two-dimensional capillary electrophoresis

CZE: capillary zone electrophoresis

COW: correlation optimized warping

ddH$_2$O: deionized distilled water

DNA: deoxyribonucleic acid

ECD: electrochemical detection

EOF: electroosmotic flow

$f_{coverage}$: fractional coverage

FL-SO$_3^{-3}$: fluorescein-5-(and-6)-sulfonic acid

GA: genetic algorithm

HETP: height equivalent of a theoretical plate

HILIC: hydrophilic interaction chromatography

HP 3D-CE: Agilent HP 3D-CE capillary electrophoresis system

HSA: human serum albumin

HV: high voltage

i.d.: internal diameter

IVF: in vitro fertilization

LC-CE: linear or heart-cut on-line two-dimensional liquid chromatography

LC-LC: on-line two-dimensional liquid chromatography

LC×LC: comprehensive two-dimensional liquid chromatography

LIF: laser induced fluorescence

MDS: multidimensional separation

mLC×LC: multiple heart-cutting two-dimensional liquid chromatography

MS: mass spectrometry

MudPIT: multidimensional protein identification technology

n: peak capacity

$n_{c,2d}$: two-dimensional peak capacity

n_{rate}: peak capacity generate rate

$N_{sampling}$: number of times the ^{1}D is sampled

N_{sep}: number of parallel separations

NGS: next generation sequencing

NOTLC: narrow open tubular liquid chromatography

o.d.: outer diameter

PAGE: polyacrylamide gel electrophoresis

PDA: photo diode array

RNA: ribonucleic acid

RSD: relative standard deviation

SDS: sodium dodecylsulfate

sLC×LC: selective comprehensive two-dimensional liquid chromatography

t_A: migration time of the earliest migrating analyte

t_{cycle}: cycle time for as set of sequential capillary array injections

$t_{sampling}$: ^{1}D effluent sampling time

t_m: migration time

t_{window}: length of separation window

t_Z: migration time of the latest migrating analyte

UV: ultraviolet

Vis: visible

Chapter 1 **Introduction**

Part A: Introduction to Separation of Biological Samples

1.1 Biomarkers, The Elusive Frontier

Life, a precarious and complex balance of coordinated, self-replicating chemicals has been a mystery since Antiquity and, to a large degree, remains so despite millennia of scientific and technological advancements. In a bid to wrest control over mortality, the Ancients sought out indicators that could be used in medical diagnosis, so-called biomarkers in current parlance. Historical attempts at using biomarkers were poorly predictive as they were limited to observation of the patient, at best, and spiritual mysticism. Systematic use of diagnostic protocols, as endorsed by Hippocrates (ca. 300 B.C.), called for careful examination of a patient's bodily fluids and outward appearances using the mind and all of the human senses.[1] This led to his relations of urine abnormalities—such as bubbles on its surface, or inclusion of blood, pus or certain sediments—to diseases or chronic illnesses.

Current prognostic tools can interrogate these biochemical soups at with greater detail and depth than ever before. However, even the simplest of life still poses a huge hurdle. For example, yeast, a key model organism in the field of cell biology and the development of functional genomics and systems biology, has a paltry ca. 5300 functional genes[2,3] (genome). Its genome produces a complement of proteins (proteome) and small molecule metabolites (metabolome) of an estimated 21 400 biomolecules[2,4] implicated in over 28 000 metabolic and signaling pathways[4]. The challenge to understanding Life, especially when it goes "off the rails", is to have the capacity to measure the complement of biomolecules produced by the organism.

Although the human senses are still relevant in measuring externally observable biomarkers (pulse, breathing abnormalities, blood pressure) the set of human biomolecules, analogous to that of yeast, provides a vast mosaic of potential targets for chemical analysis. Being highly regulated in all Life, these biomolecules can act as powerful diagnostic and prognostic indicators of health states if their identities, functions and biological concentrations could be harnessed. The National Institutes of Health (NIH) broadly defines a biological marker (biomarker) as any "characteristic that is

objectively measured and evaluated as an indicator of normal biological processes, pathogenic processes or pharmacological responses to therapeutic intervention"[5]. However, the number of yeast biomolecules is dwarfed by the number of human biomolecules, estimated to be 132 084 (proteome: 20 230[6], metabolome: 114 100[7]) as well as the analytical complexity found in human biological samples. Making use of these biomolecules as specific proxy indicators of physiology is of great interest, but fully analyzing samples of such complexity is currently out of reach.

Separations are a fundamental technology for the analysis of complex biological samples. Many instrumental variants exist in the realm of separation science, but they all aim to fractionate analytes of interest by exploiting subtle chemical differences between these biomolecules such as acidity, chirality, density, electrostatic charge, hydrodynamic size, hydrophobicity, polarity, volatility and specific morphological features. Adequately separated biomolecules in a sample can be identified and quantified to comprise biomolecular profiles and correlated with the health of the organism. The complexity arising from the full complement of biomolecules from any one organism is too challenging for most systems to come close to adequately separating. This thesis will demonstrate the coupling of two separations to dramatically improve the achievable separation capacity with the goal of applying it to biological samples.

1.1 Proteomics

Early protein investigations were limited to techniques such as precipitation, protein crystallography and ultra-centrifugation-based methods. These methods provided minimal specificity for proteins of interest and limited analyte information, were resource intensive and could only analyze one or a handful of proteins at a time.[8]

A turning point came in the 1970s with the introduction of two technologies. First was 2D-PAGE[9] (Section 1.4), where proteins undergo two spatial separations, sequentially and perpendicularly, in a thin gel matrix; first by isoelectric focusing, second by SDS-PAGE. 2D-PAGE provided exquisite resolving power and high-component discrimination for complex biological samples. However, the technique requires long separation times which are further extended by the decoupled analysis steps of staining and visualization. This workflow is limited by the exclusion of proteins at the upper end of the range in hydrophobicity, size and pH as well as low abundance proteins.[10] It also requires multiple manual steps where contamination could be introduced.

Concurrently, the first successes in preparation of monoclonal antibodies (mAb) were being discovered.[11] Prior to this point, inoculation of a host animal with an antigen of interest would faithfully initiate the production of polyclonal antibodies; where the structure of each clone and its antigen epitope binding site could vary which lead to poor specificity. The discovery that antibody generating cell lines could be isolated and further hybridized with cancer cells to produce mAbs enabled the preparation of monoclonal cell lines. These reproducibly produce mAbs with highly specific recognition of antigen epitopes, which paved the way for the proliferation of immunoassays in today's clinical laboratories. One example is immunometric sandwich assay, where a primary mAb is immobilized on the surface of a vessel to which an analyte (antigen) of interest can bind. A secondary mAb, with an attached fluorophore, is next used to bind to a different region on the captured analyte. This system of analyte capture and fluorescent tagging enables rapid and highly sensitive detection of analytes in complex samples with high specificity. A commonality among immunoassays is that they are amenable to rapid workflows and are well suited to high throughput testing of large batches of samples. However, despite being able to produce monoclonal cell lines, cross-reactivity with unintended antigen targets remains an inherent possibility with any antibody-based assay. Furthermore, the number of different molecules that a multiplexed immunoassay can detect is limited, precluding comprehensive analyses of complex samples.

Mass spectroscopic (MS) based techniques have come to dominate the bioanalytical laboratory, bringing benefits of automation and ever-increasing instrument performance.[12] During the early 1990's, analysis of proteomic samples by MS was initially very cumbersome as it required isolation of target proteins by gel electrophoresis, digestion of excised gel segments and introduction to the MS by soft ionization techniques which were limited at the time.[13] High resolving power separations were required prior to sample introduction to the MS instruments available at the time which were limited to low resolution and scanning speeds. However even at this early stage, MS based proteomics promised intrinsic analyte specificity if accurate mass techniques were available as such mass spectra could be used to infer specific peptide and protein sequences.

In the 1990's, MS based proteome analysis emerged due to advancements in instrument sensitivity, speed and ionization characteristics, which began to be suitable for detecting proteins and peptides

from low concentration samples. These early instruments, the framework for current MS based proteomics, were only made possible by two key innovations. The first, innovation was the ability to pre-fractionate the sample using linear liquid-phase separations, such as liquid chromatography (LC). LC separates a sample plug as it travels through a column as a function the differential partitioning of analytes between a mobile phase and a stationary phase, resulting in a dramatic reduction in the complexity of the emitted effluent and elution in a consistent matrix. The other innovation was the development of soft ionization techniques for proteins, in particular electrospray ionization (ESI) introduced in 1989.[14] ESI enables intact proteins in solution to be liberated as gas-phase protein cations. The combination of these two technologies fortuitously allowed LC effluent to be continuously introduced to the MS at a rate that greatly reduced the likelihood of overwhelming the MS with the number of contained analytes. However, high-resolution separations require low flow rates leading to long separation times, which restricts the throughput of these experiments.

The complexity of sample components also hinders the quality of proteomic separations. To overcome the challenging sample complexity and limits of instrumental mass sensitivity, two general approaches emerged in proteomic workflows—bottom-up and top-down.

Bottom-up workflows begin with proteolytic digestion using an enzyme with a known cleavage specificity, with trypsin being most popular.[15] Trypsin produced peptides averaging 500 to 3000 Da which simplifies the separation conditions required and narrows the mass range to be detected, making them suitable for early MS instruments.[16] Thus, bottom-up strategies have had the longest time to advance technologically.

In typical workflows, sample is introduced to a triple quadrupole MS to undergo ionization, followed by isolation of precursor ions by the first quadrupole (Q_1), fragmentation of the precursor ions in the second quadrupole (q_2), and pass through the third quadrupole (Q_3) which scans through the ions that are counted by the electron multiplier.

However, the number of peptides increases with each proteolytic cleavage during the digestion step, resulting in samples with a vastly increased number of analyte molecules that easily overwhelm the MS. Thus, experimental strategies were developed to manage and limit the regions of signal the MS detects to accommodate instrumental limits.

Sample digestion has the effect of decreasing the sample mass spectral complexity. Unique proteins that undergo cleavage result in many short peptides with identical sequences, producing a mixture that falls within a relatively narrow mass range (500 – 3000 Da for trypsin)[16] and MS ions that span a narrow number of isotopic variants (3 – 4) and narrow range of charge states (2 – 3)[17]. These characteristics are well suited to the scanning speed and range of mass spectrometers. Smaller peptides also benefit from less problematic adsorption to separation media than proteins. However, they are still challenging samples to separate due to their poor retention on RPLC columns resulting in the co-elution of many peptides with the dead volume where MS detection is unfavourable.

Three main MS strategies are most prevalent, data dependent acquisition (DDA), multiple reaction monitoring (MRM) and data independent acquisition (DIA). Each of these modes differs in how it selects ions that will be detected or discarded as they pass through the two mass selectors in the MS. Each mode allows the operator to optimize for sensitivity, reproducibility and the breadth of peptides to be identified during a run.

DDA has had the most impact on untargeted (discovery) proteomics, where the number of unique peptide identifications is paramount. Each chromatographic sampling window is further segmented into a set of MS scans. Each set is comprised of an initial precursor scan (MS1) followed by a series of product ion scans that each result in a mass spectrum. The precursor scan acts to survey the entire mass-to-charge (*m/z*) range (typically 400 – 1600 *m/z*).[18] The instrument algorithmically selects a subset of precursor *m/z* regions that will be fragmented during the subsequent set of product ion scans.[19] Precursor selection rules are preset before an experiment and are based on relative abundance of peptides detected during the precursor scan. This effectively limits the amount of sample to what the mass analyzer can handle. The mass spectra are analyzed by searching peptide databases for matching peptide sequences.[20] Since DDA continually scans the entire precursor mass range, it has the greatest chance of detecting the largest number of peptides in a single experiment.

In MRM, or targeted proteomics, the expected proteins of interest are predicted along with their parent ion, precursor ions, product ions and their elution time in the chromatographic window. Only *m/z* ranges that correspond to unique nonoverlapping product ion peaks are selected for detection by the MS throughout the run and measured repeatedly.[21] The result is that a small

number of product ion peaks are measured with high specificity and quantitative precision. This has seated MRM as the gold standard for bottom-up protein quantitation.[16,22]

DIA, combining aspects of both DDA and MRM, was introduced more recently as it was enabled by dramatic improvements in the speed and resolution of MS instruments over the past decade. In both DDA and MRM, precursor ions are isolated within a narrow mass window (0.5 – 1.0 Da) and fragmented to minimize interference from coeluting species with similar *m/z*. In contrast, DIA uses large (10 – 20 *m/z*) precursor mass windows with all contained precursor ions undergoing fragmentation and detection.[23] This precursor mass window is used to evenly divide the entire experimental mass range. For each chromatographic sampling window, the MS sequentially analyzes each precursor mass window, and detects the resulting product ions. This generates a repeating set of product ion spectra at each interval that the preceding separation is sampled. Since the entire m/z range is scanned it covers the entire available *m/z* space, similar to DDA. The repeating sets of windowed measurements allows DIA to collect reproducible spectra that are suitable for quantitation, similar to MRM.

DDA is the gold standard method for biomarker discovery owing to its ability to identify the largest number of fragments among the bottom-up methods, thereby providing the richest peptide sequence data, and having the most mature spectral libraries and data analysis workflows. MRM provides the greatest reproducibility and highly confident protein quantitation and precision owing to the repeated targeted measurement and tailored technological advancements.[22,24,25] DIA combines an untargeted approach that is similar to DDA, with the repeatability in detection of analytes entering the MS, as is offered by MRM—making it suitable for both discovery and quantitation experiments. However, these bottom-up strategies make fundamental trade-offs to achieve the key merits in each case.

The automated precursor selection in DDA introduces an inherent randomness which makes quantitation difficult. The selection bias, inherent with fragmentation of precursors based on ion abundance, can cause peptides with low physiological abundance to remain undetected. On-line precursor filtering algorithms are optimized for highest mass coverage and prioritize precursors by signal intensity. This results in each precursor being sampled only once and low abundance proteins being neglected.[26]

To achieve the targeted scanning of product ion *m/z* ranges in MRM, a high initial resource cost is necessary to predict and generate optimized peptide assays prior to any data acquisition.[21] Prior to performing a proteomic MRM experiment, target proteins must be identified from preceding experiments, scientific literature or prior knowledge. From these proteins, optimal representative peptides must be selected, and their sets of transitions predicted. These transitions sets must be validated, and the MRM assay parameters optimized, before the assays can be used for detection and quantification of target proteins. Additionally, the repeated measurement of the restricted set of selected fragment ions that enables the sensitivity advantage in MRM also limits it to identifying 10's to 100's of target peptides. Precursor ion scans are also omitted to maximize the fragment ion signal.[21] Thus, it is unsuitable for broad interrogation of complex samples.

In DIA, scanning through the full isolation window range requires 2 – 4 s of MS analysis time for each chromatographic sampling window, precluding fast separations.[27] For comprehensive MS analysis, 30 s average peak widths would be needed to maintain peak shape information. Compared to MRM, DIA has yet to achieve the same sensitivity by a factor of 3 – 10.[28–30] Compared to DDA, DIA produces highly convoluted data due to the larger *m/z* isolation windows (15 – 25 *m/z*) and resulting overlapping species in product ion scans. Data deconvolution requires generation of mass spectral libraries in advance of each experiment, which can be performed experimentally or in silico. Well established workflows for generation of these spectral libraries and the subsequent data deconvolution do not yet exist with advancements only recently being introduced.[31,32]

A challenge that is common to all bottom up methods is the loss of proteoform information. Proteoforms are the family of final protein expression products that arise from the same gene.[33] The wide variability arises from allelic differences between individuals, alternative splicing of RNA transcripts and a wide variety of post-translational modifications (PTMs) where protein structure is modified after ribosomal synthesis (e.g. phosphorylation, glycosylation, acetylation). The result of these processes is that up to 100 proteoforms can be produced by a single gene.[34] The proteolytic digestion step makes bottom-up methods best suited to measuring gross expression of a particular gene. It is likely that only a subset of proteoforms are physiologically relevant to disease states, making retention of proteoform abundance information valuable in proteomic assays.

Top-down proteomics, unlike bottom-up approaches, introduces intact proteins to the MS. Early top-down experiments required considerable work to isolate individual proteins prior to MS detection to avoid spectral overlap with other sample components. Continual rapid improvements over the past two decades have recently allowed MS instruments to accept top-down proteomics samples directly from liquid-phase separations. Detection of intact proteins is desirable as it eliminates the need to perform enzymatic digestion. Protein identification does not rely on inferential pattern matching of peptide sequences from large scale databases. Instead, the final product of protein expression can be determined directly. Thus, quantitation is more direct and PTM information can be retained within a given family of proteoforms. Since single PTM shifts can activate/deactivate a proteoform, this information is useful in biomarker discovery.

Although instruments have reached the milestone of enabling experiments that utilize intact protein samples to be analyzed, biological samples remain challenging due to the complexity of these samples, their dynamic range in concentration and wide range of molecular masses.

Top-down workflows keep proteins intact with their higher order structure and proteoform heterogeneity. This heterogeneity is further complicated by the increased isotopic and charge state variation (4 – 20 isotopes and > 5 charge states)[17] This is estimated to increase the number of detectable peaks by two orders of magnitude over bottom-up proteomics samples. Even the recent instruments are limited to 1 Hz sampling rates when scanning over a 300-4000 m/z mass range.[17] Since typically accepted signal resolutions require 10 data points across a peak, the coupled chromatographic separations are necessarily lengthened.

Samples of intact proteins are instrumentally challenging due to their wide concentration dynamic range and the variability in molecular weight of sample components. The difference between low and high abundance proteins at physiologically relevant concentrations range from 5 pg/mL for select cytokines to 50 mg/mL for albumin, which exceeds the linear response of most detectors.[12] The molecular masses also vary widely from small 1 kDa peptides such as angiotnensin[35] to over 150 kDa for the immunoglobulins[36]. This challenges the separation that precedes the MS, resulting in many coeluting peaks and overlapped spectral components in the mass spectra. The majority of spectrometers in use are unsuitable to handle the dynamic range in concentration, the species variability in molecular weight and the number of unique species.[8]

One strategy to alleviate this ongoing problem of biological sample complexity, as demonstrated in this thesis, is in improving the separation scheme that precedes detection. LC is well established in proteomic workflows due to its long history which has garnered familiarity by the community.[37] However, LC separations are greatly underpowered compared to the challenges required for biological samples, with upper limits in the range of 1000 chromatographic peaks achievable by typical monophasic separation columns.[38] CE boasts higher separation power, owing to its electrophoretic separation mechanisms as used in 2D-PAGE (Section 1.4), that significantly reduce extracolumn band broadening.[39] CE separations can also be operated quickly and can avoid the column regeneration times required for gradient LC separations. Though CE popularity lags that of LC, the qualities of separation power and fast operation make it a suitable candidate for gains in both bottom-up[40] and top-down[41] proteomics separations that provide complementary information to LC due to the electrophoretically mediated separation mechanisms involved.

Of note, metabolomics is a related field of research and a growing application of CE separations.[42–44] Metabolite sample components are small molecules and are comprised of a significant proportion of polar and charged analytes, making them ideal for high-resolution CE separations. However, there is a dearth of natively fluorescent metabolites and no suitable, universal, labelling reagents for these analytes/samples. Since the CE detection system used in this work relies on fluorescence detection, and requires analytes to be fluorescently labelled, metabolites were incompatible with this separation system. Thus, this thesis focuses on application towards proteomics samples.

1.2 Biomarker Discovery

The goal of clinical biomarker use is to provide reliable determination of the existence or cause of a medical event to make informed choices for care. Biomarkers can be used as diagnostic, prognostic or predictive tools to achieve care that is optimal for each patient.[45] As a diagnostic tool, biomarkers can determine the presence or absence of a health condition. Prognostic biomarkers provide information about the likelihood of progression of a disease or medical condition in a patient. Predictive biomarkers are used to classify individuals as being likely to have favourable or unfavorable outcomes if exposed to a treatment or environmental factors. Used in ways such as these, biomarkers can be substitutes for determining a medical state, referred to as surrogates. Surrogate biomarkers provide an alternate target (e.g. gene polymorphisms, nucleic

acids, proteins) for detection of a symptom or allow prediction of the clinical outcome resulting from a medical condition or treatment. A clinical endpoint, as used in clinical drug trials, is a measurable direct change in a patient's health, function or quality of life resulting from the intervention used in a study. Biomarkers may act as surrogate endpoints for clinical endpoints only if they are an integral mechanistic component of the causal pathway for the medical condition of interest.[46] Surrogate endpoints are attractive because they have the potential to be detected earlier and detected more easily than the symptoms of the clinical outcome. This provides actionable information before symptoms from the clinical endpoint develop, allowing more rapid decisions to be made. As a general example of surrogate use, a cancer tumor patient could be diagnosed using a surrogate endpoint and receive treatment in advance of detection by imaging techniques, when the number of cancer cells is already high. The same patient could be screened ahead of a pharmaceutical intervention for possible allergic reactions. Subsequent monitoring could be used to determine whether the drug is having the desired effect, prior to observable morphological changes to the tumor, and affect an earlier shift to an alternate therapeutic. Thus, by informing tailored decisions in patient care, there is the opportunity for reduced harm and reduction of costly healthcare resources. However, before use as a surrogate, biomarkers must be validated.

Validation of surrogate endpoints, from a regulatory standpoint, is a challenging task that the vast majority of discovered biomarkers reported in the literature do not meet. The FDA-NIH Biomarker Working Group defines validation as "a process to establish that the performance of a test, tools, or instrument is acceptable for its intended purpose"[45]. Two key afreas required in this process are analytical validation and clinical validation.[47] Analytical validation establishes the performance characteristics required for the technical method (sample preparation, instrument parameters) and instrument figures of merit (reproducibility, accuracy, sensitivity) used, without regard for the biomarker's clinical utility. Clinical validation establishes that the biomarker can be acceptably identified, measured or predicted within a specific context of use. Complete validation generally requires that the mechanism, relating a biomarker to the medical condition of interest, be understood and a large body of data be generated to demonstrate this relationship.

A major pitfall in the discovery of surrogates is the spurious acceptance of biomarkers that do not act as true surrogate endpoints for clinical outcomes. It is possible for a biomarker and medical condition to be perfectly correlated but fail to be a valid surrogate.[48] Previous studies have

produced biomarkers demonstrating high correlation to disease but were unable to meaningfully improve clinical outcomes.[49,50] When applying treatments that modified these false surrogates, so that they mimicked the surrogate's behaviour in healthy patients, they failed to affect a commensurate improvement in actual clinical outcomes. As an example, blood HDL cholesterol levels have been long established as inversely correlated to the development of coronary artery disease and cause increased mortality rates.[51,52] This spurred the introduction of drug therapies that increased HDL cholesterol levels in at-risk patients.[53] However, subsequent clinical trials demonstrated that affecting patient HDL cholesterol levels had no effect on cardiovascular events, or resulted in an increase in morbidity and mortality.[54–58] Thus, a true surrogate must precisely predict the future clinical outcome given the current clinical state, and any treatment affecting the surrogate must precisely predict the effect of the treatment on the clinical outcome.[50]

Unfortunately, the conflation of biomarker correlation with the mechanism or causation of clinical outcomes is not uncommon.[49] A major challenge arises from the difficulty in figuring out the biochemical pathway required for a disease.[46] A disease that results in a clinical outcome frequently does not have a unitary path that determines disease progression. Nor must the detectable markers manifested by a disease only relate to the clinical outcome. They may be part of a clinically unrelated, but perfectly correlated pathway.[48] Only biomarkers that lie on the path that is causal for the disease outcome will be effective for clinical use. This is further complicated by multifactor nature of many diseases, requiring that a network of biomarkers be considered simultaneously to be reliable.[59] A single valid biomarker for a disease may miss additional causal pathways that are equally effective at promoting disease progression. Due to numerous biomarker discoveries failing to result in effective surrogates, regulatory bodies and clinical labs are rightly conservative with the approval of new surrogate biomarkers.

The biomarker discovery landscape has changed dramatically since their heyday over 4 decades ago. The most productive time in proteomic biomarker discovery, over the period of 1977-1993, saw on average 5.8 new biomarker tests for serum and plasma samples being introduced per year.[60] This discovery rate sharply declined after this period and has remained close to 1.5 new biomarkers per year, though and continuing to fall at a gradual pace.[61] It's worth noting that immunoassays account for a majority of the early discoveries in approved biomarkers, while having expected equal competition during the same period from high-resolution 2D-PAGE technologies.[8]

11

However, neither of these two methodological pipelines were able to continue the pace of biomarker discovery following the golden years.[61] The slowed pace of biomarker adoption likely points to complexity of the remaining biomarkers yet to be discovered.[62] Likely, the number of single gene expression diseases and those with dramatic phenotypic symptoms have already been discovered. Identifying the remaining biomarkers tests will be challenging as many are likely to be multifactor network biomarkers.[59,63,64]

Approaches to biomarker discovery falls into two general camps, hypothesis-driven and hypothesis-free.[65] This golden period was also dominated by hypothesis-driven approaches to biomarker discovery, where clear candidate biomarkers were identified during the study of disease processes. Later advancement in technologies enabled the complementary approach of -omics-based hypothesis-free discovery. This data-driven approach has no clear targets identified in advance. Rather, large analytical data sets are mined using computational methods and statistical modelling to identify patterns that correlate to clinical variables—thus identifying candidate biomarkers. In both cases, the selected putative biomarkers are winnowed to a manageable set that is subjected to further targeted investigation. These investigations will determination whether causal linkages exist to support their application as surrogate biomarkers.

Technologies for hypothesis-free discovery, especially high-resolution MS based workflows (Section 1.1), has seen continual and rapid advancement since the 90s.[17] Despite this, they have not delivered on the promise of a return to higher rates of biomarkers being discovered despite continual increases to research funding.[61,66] The lack of practical utility is made apparent by the voluminous publication rates of studies that declare high sensitivity and high specificity results that do not translate to clinical use.[66,67] The majority of studies do not perform adequate validation of initial findings made from the set of experimental samples.[12] However, clinical utility requires that a predictive calibration model for a biomarker must continue to make accurate predictions when generalized to new samples from the population.[68,69] Historically, hypothesis-free discovery studies use small sample sizes while trying to detect as many features as possible in each sample data set. This leads to studies with low statistical power.[66,70]

The proliferation of statistically underpowered biomarker discovery studies has contributed to a longstanding roadblock in the introduction of new clinical biomarker tests (discussed in Section 1.3.3). A key factor contributing to the roadblock to the approval and acceptance of newly

discovered biomarkers arises from insufficient numbers of samples used in discovery experiments. However, the causes for low sample sizes is not singular but arises from an array of interconnected constraints that are political and regulatory in nature as much as they are technological and physical. For the remainder of this section, I will describe how these constraints have contributed to the problem of sample size and point to the area that this thesis will tackle.

1.3 The Case for High-Throughput Separations

It has been suggested that the landscape governing the introduction of new biomarkers is trapped in a cycle that undervalues diagnostic tests and disincentivizes investments into more productive pipelines.[71] These factors include: low remuneration fees provided for clinical testing, low investment rates for R&D, high costs, inconsistent and ununified regulatory standards governing experimental design and validation criteria, a publication system that promotes positive results and a predominant low evidence for analytical and clinical validity. This has fostered a lack of trust in discovered biomarkers and discourages translation of candidate biomarkers to clinical tests, which perpetuates this cycle. The biomarker discovery pipelines that are currently employed broadly follow a multi-staged progression beginning with a discovery phase followed by a verification phase and a clinical validation phase.[63]

1.3.1 The Discovery Phase and the Challenge of Complex Samples

Generally, the goal of the discovery phase is to identify as many analytes as possible using unbiased exploratory studies to identify protein expression patterns that show promise for classifying control (negative observation) versus treatment (positive observation) samples. Small sets of data (10's) are typically used since comprehensive analysis is time and resource intensive. In these experiments, the analysis is optimized to identify the greatest possible number analytes in the samples, at the cost of low sample sizes. From these initial studies, assays are developed and validated for use on a subset of promising candidate biomarkers. During the verification phase, targeted analysis is performed on candidate biomarkers using larger data sets that include greater population diversity, using upwards of 100's of samples. Statistical models are developed which guide a further winnowing of the candidate biomarkers. In the final clinical validation stage, a select few candidate biomarkers that showed the most promise have their assays optimized and are used on a large sample. Clinical trials require high-throughput analyses of large sets of samples

(1000's), typically employing immunoassays. As a candidate biomarker advances through each stage of the pipeline, resource costs increase dramatically commensurate with the increasing sample size. Concurrently the number of candidate biomarkers follow an inverse path, starting with 1000's of possible protein analytes during discovery and ending with the testing of less than 10 during clinical trials.[12,63] Thus, there is a great burden on the early discovery stages to generate high quality data to maximize the likelihood that candidates selected for further investigation lead to successful biomarkers.

A significant impediment to the discovery phase is that biological samples are challenging to analyze comprehensively, particularly in the case of serum. Serum has the potential to be the ideal sample because it can, in principle, provide information about every part of the body while being relatively non-invasive to obtain.[72] However, this virtue is also a persistent problem due to its inherent complexity. The number of unique proteoforms in serum has been estimated at 0.6-6 million.[34] The concentration of proteins in serum spans over 10 orders of magnitude. Albumin marks the upper end of the abundance range (50 mg/mL)—it alone makes up half of the total mass of serum proteins—and long-range messengers, such as hormones and cytokines (5 pg/mL), mark the low end. This concentration dynamic range in serum can be broken up into three broad classes. High abundance proteins originating from constantly replenished secretions with a functional role in serum, medium abundance proteins made up of leakage products from damaged tissues or following cell death and low abundance proteins encompassing extracellular effectors. For perspective, the high abundance proteins span five decades in the g/L to mg/L range, the medium abundance proteins span the three decades of the μg/L range and the long-range extracellular effectors span two decades in the ng/L range.[72]

While the majority of discovered biomarkers exist in the high abundance class, the lower abundance proteins are expected to be the most promising for future biomarker discoveries.[12] However, these proteins are difficult to determine and quantitate because they are easily masked by the high-abundance proteins.[73] Together, the dynamic range and number of species makes dire any attempts to comprehensively analyze all components within proteomic samples. Leading current chromatographic methods woefully lack the resolving power required to isolate all serum components[74,75] and the concentration range restricts MS detection to a few hundred of the most abundant species[12]. Immunodepletion of high abundance proteins is commonly used to enrich

those of lower abundance, but this suffers from unintended protein depletion due to non-specific interactions or binding to depleted carrier proteins such as albumin.[76,77] Additionally, removal of major plasma proteins can also lead to the obfuscation of their important contributory biomarker effects.[78]

Thus, strategies for analyzing whole samples are needed. However, these strategies involve extensive fractionation and are inherently low-throughput. This constraint further encourages small sample sizes that have dramatic negative effects on the data quality produced at the top of the pyramid structured pipelines. The insidious effect of low sample size in biomarker discovery studies, as outlined above, is the proliferation of statistically underpowered studies. Small sample sizes result in statistical models with overestimated prediction accuracy but underestimated variance.[69,79,80] Thus, there is a need for sample sizes in the initial stages of biomarker discovery must to approach those of the later stages where 100s or 1000s of samples are analyzed.

1.3.2 Calibration Models and the Challenge of Small Sample Sizes

A predictive classification model is a calibration model, similar to a simple regression, where model calibration data (protein expression) is correlated to known outcomes (phenotypic classification). The generated model acts as a function that can accept a new set of data and predict the phenotype or outcome of the new sample. Performance assessment using statistical tests is the critical step of estimating the generalizability of a predictive model, that is, its ability to correctly classify new samples from the population. Two general types of tests used to assess model performance are external validation and cross-validation.[81] The gold standard is external validation, where an independent sample cohort is used to test the performance of the model's predictive ability. Since this external test set is excluded from any data used for developing the model, it can act as a proxy for new samples from the population and be used to estimate the prediction error. However, collection of sufficient numbers of sample to form both training and test sets that capture representative demographics of the whole population is resource intensive and rarely used in discovery studies.[68]

Cross-validation strategically resamples a single calibration data to create independent training and test sets by using a stepwise partitioning of the data during development. In cross-validation, the complete calibration data is first broken up into several equal segments, called folds. Each fold

is, in turn, segregated from the rest of the calibration data. During each turn, every sample not in the current fold is used to train a new model. The segregated fold is then used as a test set to estimate the prediction error of the model generated in that turn. The prediction errors from all turns are aggregated to arrive at an averaged prediction error which provides an estimate of the model's generalizability to the population. The initial number of samples contained in each fold is typically arbitrary and is optimized during model development. Cross-validation is widely used in performance assessment in proteomics studies as it relies on few assumptions and can be used on a single originating data set.

When cross-validation is used with small sample sizes, the predictive models can result in large uncertainties that are often underestimated, generating biased results and being limited to detecting large effect sizes.[68,82] A leave-one-out strategy is often employed with small sample sizes to maximize the number of samples used for training by using folds containing one sample. However, this can introduce higher variance. Alternately, when large folds are used it decreases the number of samples used for training which can lead to bias in the model.[69]

1.3.3 The Importance of Statistical Power and Sample Size

Poor generalization often occurs due to a lack of statistical power; which is the probability of correctly classifying the true positive results when they are observed, and not falsely declaring them as negatives. Low statistical power results in the chance of discovering a true effect to be low, the effects that are observed having a lowered probability of reflecting a true effect and the true effects that are observed being more likely to have exaggerated estimated effect sizes.[79,80] Proteomics is more sensitive to sample sizes than standard statistical approaches leaving important effects to remain undetected.[69] Unlike standard statistical calibrations, in proteomics data the number of predictive variables that have any chance of demonstrating an effect is often < 10 %, leaving 90% to be negative outcomes. Conventionally, during development of a model, false positive and false negative rates are set at 0.05 and 0.2, respectively. Since the expected ratio of true positive to negative observations is 10:90, these error rates will result in 2 positives being reported as false negatives and 4.5 negatives being reported as false positives. Thus, despite 8 out of 10 positive results being correctly obtained, less than two thirds (0.64) of the observed positives will be correctly classified.[80] Increasing sample size is the best way to reduce variance and bias in study results which enables greater data reliability and makes small effects easier to detect.

Variance decreases at a rate of $1/\sqrt{n}$, while bias decreases due to larger sample sizes better representing population variability. Both effects improve the chances that putative biomarkers will surface and that confirmation studies will succeed.[83]

Robust identification of candidate biomarkers demands larger sample sizes and validation cohorts, but this is not born out by the publication record.[12,61,79] The actual number of samples depends on the goals for a given study and the minimum target effect size. Online calculators exist to determine sample size based on the statistical parameters above.[84] While minimum sample sizes of 50 have been suggested to reach minimum levels of acceptable statistical power[70], it is likely that 1500 or more is the target that is necessary for not only statistical power but clinical acceptance[61]. Simple calculations such as Lehr's "Rule of 16" can be applied to determine a rough estimate of the sample size required per group as described by $n_{group} = 16 \times (\sigma^2 / \delta^2)$; where n_{group} is the sample size, σ^2 is the standard deviation and δ is the difference between the mean values of the two groups being compared.[84]

Due to technological practicalities of today, the pyramid pipeline reserves large sample sizes for late stage clinical trials. However, by starting with a discovery phase that uses low sample size poisons the rest of the pipeline that follows. Pyramidal pipelines waste resources when they follow up on putative markers that have low chances of success from the start. To meet the challenge of discovering the biomarkers expected to be in the low abundance regions of the serum proteome, improved data quality is imperative at the early stages of development. To facilitate this, a rectangular pipeline has been proposed.[12] Here, sample sizes in the discovery and verification phases would be replaced with those found in current clinical validation phase (100s – 1000s) and the number of proteins analyzed in the discovery phase would be maintained through to clinical validation.

However, analyzing thousands of samples this comprehensively at every stage of a rectangular pipeline will require much higher throughput than current instrumentation provides. Despite continuing rapid rates of improvements to MS technologies, they cannot singularly enable this type of pipeline. Furthermore, separations technologies have not kept in lockstep with the same rates of improvement. Thus, separations technology—the crux of this thesis—is an important area where contributions can make a large impact. Next, I will cover the separations techniques that are

common in proteomics research and evaluate their suitability for improving throughput and data quality moving forward.

1.4 The Proteomic Separations: 2D-PAGE

The decades long workhorse for separation of complex biological samples has been two-dimensional polyacrylamide gel electrophoresis (2D-PAGE).[72] This electrokinetically driven technique induces molecules to migrate within a buffer-filled polymeric network due to the interaction of charged molecules in the presence of an electric field applied across the polymer gel. During a 2D-PAGE separation (Figure 1) each species is subject to two separation mechanisms; the first based on isoelectric focusing (IEF), and the second based on molecular mass (if denaturing SDS is present). IEF is performed in a segment of gel that contains an immobilized pH gradient. Each protein migrates until its isoelectric point (pI) matches the surrounding pH, where its net charge is effectively zero. The molecular size separation occurs due to sieving by the pores that form in the cross-linked gel media used. The pores slow the migration of proteins through the gel, with migration rate being proportional to the molecule's charge and inversely proportional to its hydrodynamic size (which is often approximated to their molecular weight). These two sequential separations result in a gel slab with a series of spots observed across its area, each representing one or more proteins that have been separated from their neighbours.[85]
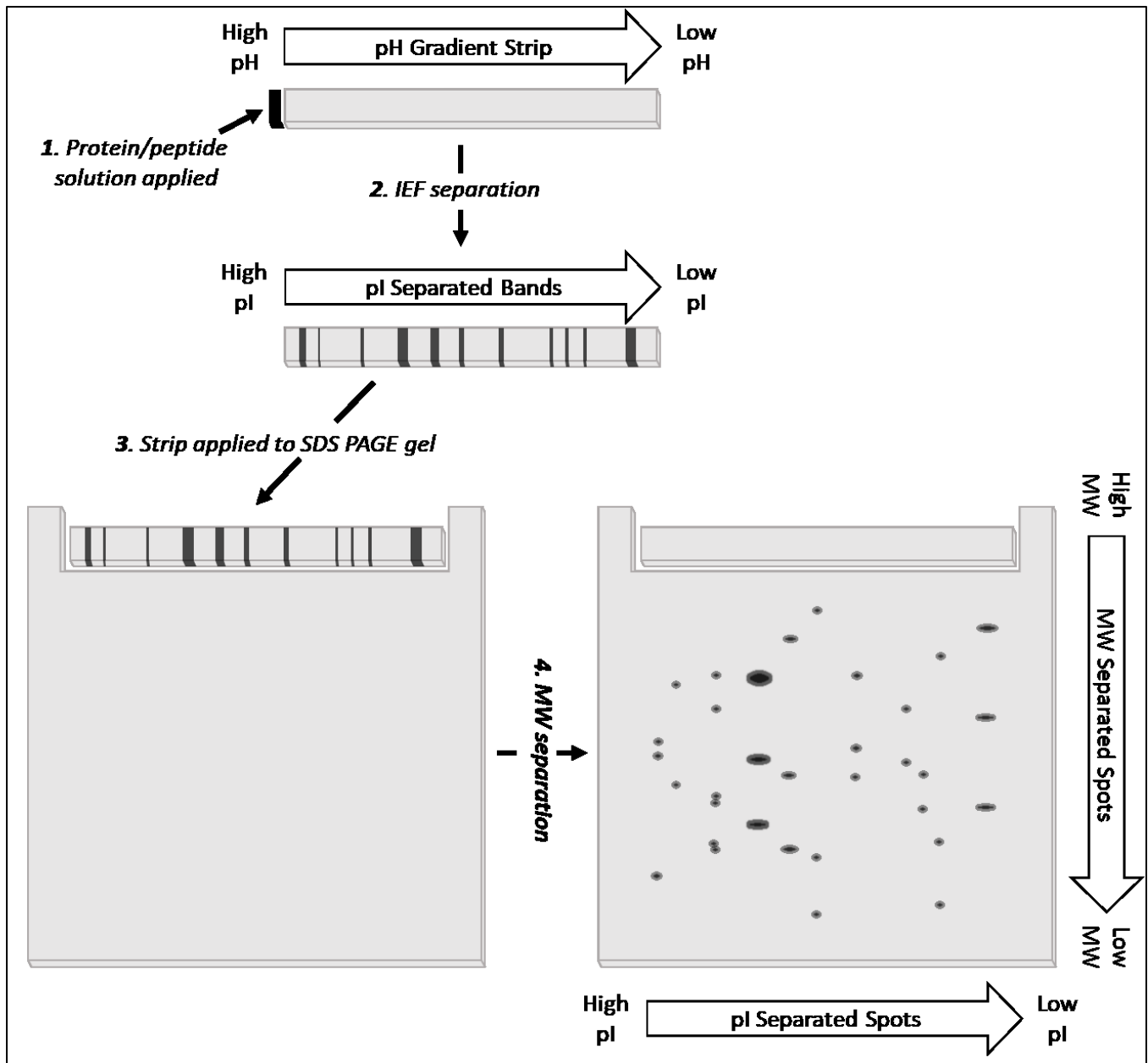
Figure 1 2D-PAGE separation. Sample is applied to one end of the pH gradient gel strip (1). A voltage applied across the gel separates the compounds into bands according to their pI (2). The strip gel is applied to a SDS PAGE gel (3) where a voltage applied in the perpendicular direction separates each band into spots according to their MW (4).

Separations by 2D-PAGE begin with introduction of the sample onto a narrow strip of gel, which has been impregnated with a pH gradient along its length by fixing carrier ampholytes. An electric field is applied along the length of the gel, and proteins migrate to the position with the pH that matches it pI. This gel strip is then equilibrated with buffer to be used in the next phase of separation, which includes sodium dodecyl sulfate (SDS). SDS associates with proteins in a ratio of about one SDS molecule per two amino acid residues. This imparts a net negative charge to all

protein analytes such that they all, to a first approximation, have the same charge-to-mass ratio. The gel strip is then laid across the leading edge of a square gel slab. An electric field is applied to the gel assembly in the direction perpendicular to the IEF separation, such that the second separation migrates in the direction of unused separation space towards the anodic end of the slab. Visualization of the separated spots is typically done by applying a dye that preferentially binds proteins and the excess can be washed away from the gel matrix. Each of these spots contains one or more proteins which can be removed by excising a spot from the gel where it can be subjected it to further manipulations or analyses such as enzymatic digestion and/or mass spectrometry. In order to perform quantitative analysis of the components of a complex biological sample, considerable prefractionation is required to overcome the large number of species and high dynamic range issue. The strength of 2D-PAGE is that the combination of two orthogonal separation mechanisms can achieve very high separation power that results in spot capacities exceeding 10 000 spots.[86] By enabling the separation of many serum components from one another, lower abundance proteins have a much better chance of being isolated from high abundance proteins which otherwise act as immutable interferences. Changes in affected protein expression is visually intuitive, observed as changes in size and intensity of spots within the separation space. Individual spots resulting from the extensive fractionation makes it so that excised spots are simplified enough to undergo analysis using methods whose dynamic range would be exceeded by the original sample. These high spot capacities have been enabled by a variety of advances over time, with particularly large gains made by the introduction of immobilized pH gradient (IPG) gels used in the ^{1}D IEF separation. Manufacture of these IPG gel strips could be performed with more precise control of the contained pH gradient.[87] This allowed much sharper bands to develop during the ^{1}D IEF separation, which was previously the bottleneck in the two separation dimensions. 2D-PAGE separations remain relatively low effort to perform and low in cost.

However, 2D-PAGE separations are accompanied by a variety of limitations. Inalienable ones include the exclusion of hydrophobic membrane protein analysis due to their insolubility in the IEF buffers.[10] Separation at the extreme ends of pI and MW ranges are difficult as they will exit the ends of the gel during the IEF step or be too large to enter the MW sieving media.[88] Other challenges include limited dynamic range for detection of proteins, due to the sensitivity of most dyes used for visualization of the spots.[85] Even if one chooses to use high sensitivity silver staining

it is laborious, procedurally complicated and poorly quantitative. Very low abundance proteins can be missed even with the currently available dyes.[10] Reproducibility in spot position is low due to batch-to-batch variation in the separation media and/or protein loss at various steps of the workflow.[85] Although stability of the IEF step has improved with the introduction of IPG gels, batch variation remains.[89] Run-to-run spot precision has improved with automation of various procedural steps and internal standardization via Difference Gel Electrophoresis along with the availability of software packages to warp and normalize the data.[89] However, skilled operators are required for a number of the complex methodologies used in the procedure. One challenge is that IPG strips that encompass a wide pH range typically do not achieve adequate separation in the ^{1}D to achieve high total spot capacities. To achieve high spot capacities, multiple 2D separations must be performed, each with a different IPG strip that contains a narrow segment of the total pH range to be covered.[90] Alternatively, long IPG strips (24 cm) and large scale 2D gels (20 cm × 25 cm) can be used but are difficult to handle and are prone to tearing.[88] Even with automation of several manipulations, throughput is inherently low requiring a week for comprehensive analysis that begins with biological sample preparation to complete spot data analysis.[88] Despite these limitations, 2D-PAGE remains a key tool in the biomarker discovery pipeline.

Alternatively, liquid-phase separations offer a number of advantages when separating biological mixtures. A common strategy is to fractionate the original sample in order to decrease complexity is frequently performed using high-performance liquid chromatography (HPLC) or capillary electrophoresis (CE).[91]

1.5 A Brief Introduction to High Performance Liquid Chromatography

High performance liquid chromatography (HPLC) has become the workhorse for the bioanalytical chemist. Numerous advantages make HPLC an attractive separation platform, such as ease of automation, a wide selection of separation mechanisms and on-line coupling to a variety of detector systems, including mass spectrometry. The liquid-phase separation eases sample preparation, allowing samples to remain in their native environments.

Separations occur linearly in a stainless-steel cylindrical column packed with a solid microparticle or polymer stationary phase material and filled with a mobile phase fluid. Dissolved sample is introduced as a discrete plug at the column inlet and additional mobile phase is pumped through

the column, propelling the sample components toward the outlet. The separation mechanism in HPLC is a function of the differences between the partition coefficients of each analyte, which is basically the instantaneous equilibrium constant of the analyte as it moves between the stationary and mobile phases. Analytes with greater affinity for the stationary phase move through the column slower than those with less affinity, enabling separation even between similar compounds. Tubing easily connects the column outlet end to a detector system, where the flowing analyte exits, and can be ideally observed as Gaussian peaks during their transit through the detection zone.

Although other modes of HPLC have a place in biological separations, reversed-phase HPLC (RPLC) remains a very common first choice. Thus, a brief review of RPLC will be provided to sufficiently quantify the improvements made in this thesis. For a more detailed introduction, a review by Unger *et al.*[92] provides a comprehensive perspective on the key role of HPLC on bioseparations in the life sciences. Typical operating conditions involve using acidic buffered mobile phases in order to protonate peptide and protein samples for uniform interaction with the hydrophobic hydrocarbon stationary phase functionality (C4 – C18). Separation efficiencies in RPLC are largely dependent on using small packed particle sizes covered in a mono-layer of stationary phase. These can achieve theoretical plate numbers, a measure of how narrow a chromatographic peak is, that are upwards of 10 000. This contributes to a maximum, theoretical, 153 peak capacity that can be achieved during a high quality separation with a target separation time of one-hour.[93] Peak capacity in a linear separation is analogous to the number of differentiated spots that can be observed in a 2D-PAGE gel. Here, peak capacity describes the number of peaks that can, hypothetically, fit in a chromatogram within the window of time that species elute from the separation column. This equates to peak generation rate of ~ 2 – 3 peaks/min. Selectivity and resolution manipulation via solvent type and gradient structure is another flexible benefit of RPLC. Current column technologies, such as wide-pore core-shell particles and polymeric stationary phases, have ameliorated many of the problems with proteins having tailing peaks.[94,95]

1.5.1 MudPIT

An important HPLC technique that has had wide application to bottom-up proteomics is multidimensional protein identification technology (MudPIT) pioneered by the Yates laboratory in 2001.[96,97] This technique employs a single biphasic microcapillary column, wherein the first segment of the column is filled with an ion exchange chromatographic (IEC) stationary phase,

22

commonly strong cation exchange (SCX), followed by a longer segment filled with RPLC stationary phase. The IEC segment retains the sample plug which undergoes an iterating stepped salt gradient elution program. First a salt pulse is introduced to selectively elute portions of the sample from the IEC portion of the column onto the adjacent RP portion. Following each salt pulse, a RPLC gradient elution program is used to separate the sub-sampled plug which is directly injected into the MS as it elutes from the column. This cycle of salt pulse and RPLC separation is repeated with increasing salt concentrations until a salt gradient range (1 % – 100 %) is traversed.

MudPIT enables LC separations that compete with to 2D-PAGE in terms of resolving power. This is due to the IEC and RP separations being highly orthogonal to each other, analogous to the IEF and PAGE separations in 2D-PAGE. However, MudPIT also introduces the additional benefits of being amenable to direct interfacing with MS and fully automated analysis. It has become a widely applied separation mode for deeply probing proteomic samples.[98–100]

MudPIT separations have some drawbacks. The IEC step can be challenging when separating peptides that carry a +2 or +3 charge, which are common under typical separation conditions. These peptides elute in a narrow window of the salt gradient, reducing the distribution of analytes within the separation space.[101–104] Due to the serial nature of the biphasic columns, all solvents introduced to the system must pass through both stationary phases. Thus, solvent compatibility restricts the separation modes that can be paired in MudPIT columns. Additionally, the salt pulses used to elute peptides from the IEC segment of the serial biphasic columns cause problematic contamination of the ion optics in MS instruments.[105]

1.6 Capillary Electrophoresis Concepts

Capillary electrophoresis (CE) has also had much success in its application to biological separations. Owing to similar separation principles as gel electrophoresis, it can achieve high separation efficiencies and peak capacities, while using instrumentation that is relatively simple to design. Reagent and sample volumes are advantageously small being in the mL and μL ranges, respectively. Unique design characteristics in CE allow for much higher electric fields to be applied to the separation medium, which decreases separation time dramatically compared to 2D-PAGE.

As this thesis chiefly investigates instrument design and characterization, and not CE method development, the following section will focus on theory required to evaluate the advancements made to multidimensional CE separations in the work presented. For a more thorough accounting, the interested reader can find a comprehensive introductory review of CE theory in the *CRC Handbook of Capillary and Microchip Electrophoresis and Associated Microtechniques*[106] in addition to several chapters covering many aspects within the CE field. A good review specific to CE separations of biomolecules by can be found in Krylov *et al.*[107]

In the simplest form of CE, capillary zone electrophoresis (CZE), an instrument is comprised of a narrow fused-silica column with the inlet and outlet ends each in a separate vial (Figure 2). Each vial and the capillary lumen are filled with a background electrolyte. One electrode from a high-voltage power supply is also placed in each vial in order to apply a high electric field across the capillary; with the cathode typically in the outlet vial and the anode at the inlet. Sample can be introduced at the capillary inlet by placing it in a sealed sample vial and applying a gentle pressure at the inlet, gentle vacuum at the outlet or by momentarily applying a potential across the capillary. Upon introduction of a sample plug (1 – 20 nL) at the inlet of the capillary, an electric field applied across the capillary drives the analytes towards the outlet as they separate, where detection can be performed using a variety of methods.
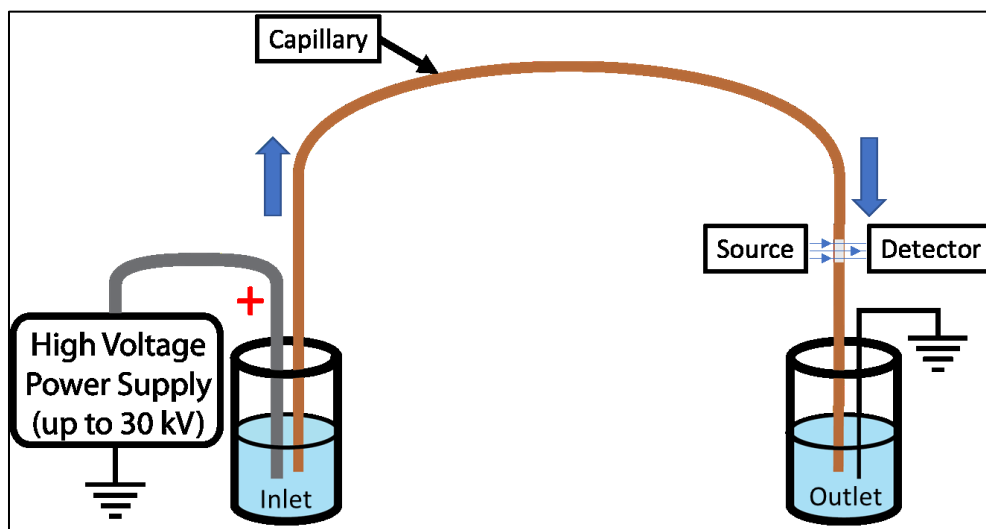
Figure 2 Depiction of a basic capillary electrophoresis instrument. Immersed in the inlet and outlet buffer vials are the two ends of a buffer filled separation capillary along with the anodic and cathodic electrodes of a high voltage power supply. Blue arrows indicate direction of migration through the capillary. The power supply is used to apply a voltage potential across the capillary. For on-capillary detection a window is made near the outlet by removing the protective polyimide coating to create an optical path for the detector system. Sample introduction can be performed by replacement of the inlet vial with a sample vial and performing an electrokinetic injection by applying a potential or enclosing the vial and applying pressure to perform a hydrodynamic injection.

High-purity fused silica capillaries are used as separation columns. Common capillary dimensions include internal diameters from 10 – 100 μm, outer diameters of 165 – 365 μm, and lengths of 5 – 100 cm. These dimensions ensure a large surface-to-volume ratio of the inner capillary lumen, which allows for more efficient cooling than in gel electrophoresis. This minimizes the Joule heating effects that limit gel electrophoresis to the typical 15 – 40 V/cm and allow electric fields as large as 500 – 1000 V/cm, which speeds analyses from hours to minutes.[106] CE capillaries are manufactured with a polyimide coating (~10 – 20 μm) to protect the quartz outer surface from damage, allowing the capillaries to be quite flexible and withstand sharp bending with radii as small as 2 – 4 cm. This also offers flexibility in physical design of CE instrumentation.

The mechanism driving a CE separation relies on two key features, electrophoretic mobility of the analytes and electroosmotic flow (EOF). Unlike SDS-PAGE separations, where all peptides and proteins are imparted a negative charge by the bound SDS molecules, analytes can be negative, positive or neutral as mediated by their isoelectric points and the pH of the background electrolyte chosen.

Electrophoretic mobility, μ, of a charged particle, such as a peptide, describes the velocity, v, it will adopt when subjected to an electric field. This velocity can be represented by

$$v = \mu_{app} \frac{V}{L} \qquad (1)$$

This terminal velocity is proportional to the applied voltage, V, and inversely proportional to the distance between electrodes, L (*i.e.* the electric field). Thus, the magnitude of the applied voltage can be used to speed or slow separations. Electrophoretic velocity is dependent on the apparent mobility of the ion, μ_{app}, which can be described as

$$\mu_{app} = \frac{q}{6\pi\eta r} \qquad (2)$$

The mobility of an ion is proportional to the magnitude and sign of its charge, q, and inversely proportional to the viscosity, η, of the surrounding buffer as well as the hydrodynamic radius, r, of the ion. Under an applied field, mobilities are proportional to charge and inversely proportional to hydrodynamic size. The charge also indicates whether the analyte will migrate towards the

25

anode or cathode. Thus far, only cationic species would be detected. Neutral species would remain immobile at the injection site, while anionic species would migrate from the capillary into the inlet vial. A bulk flow can be applied to cause a net migration towards the detector for all species. This bulk flow is generated in CZE by way of an electroosmotic flow (EOF).

Generation of the EOF occurs due to the bulk background electrolyte (BGE) in the capillary interacting with the applied voltage potential, with particularly interesting behaviour at the capillary wall (Figure 3). At the molecular level, the capillary wall is an expanse of repeating silanol functional groups (Si–OH), whose pKa of 4 – 6 is slightly acidic.[106] When the pH of the BGE is higher than this pKa range protons are abstracted, leaving a uniform layer of negative charges along the wall (Figure 3). To counter this excess charge, cations in the BGE pair with the wall charges and are tightly held in a static Stern layer. Next to the Stern layer, a diffuse layer of cations gathers, creating a so-called electrical double layer. As the distance from the wall increases into the bulk solution, the cations form a concentration gradient which decreases exponentially towards the bulk solution. The diffuse layer is mobile and migrates toward the electrode of opposite charge (here, the cathode) under an electric field in a uniform surface that follows along the capillary wall. This layer has extensive hydrogen bonding with the water molecules in the surrounding solution transferring momentum to the solution which generates a bulk flow throughout the capillary. This EOF can be mediated in the capillary by adjusting the pH and ionic strength of the BGE. The EOF increases with increasing pH and decreasing ionic strength.
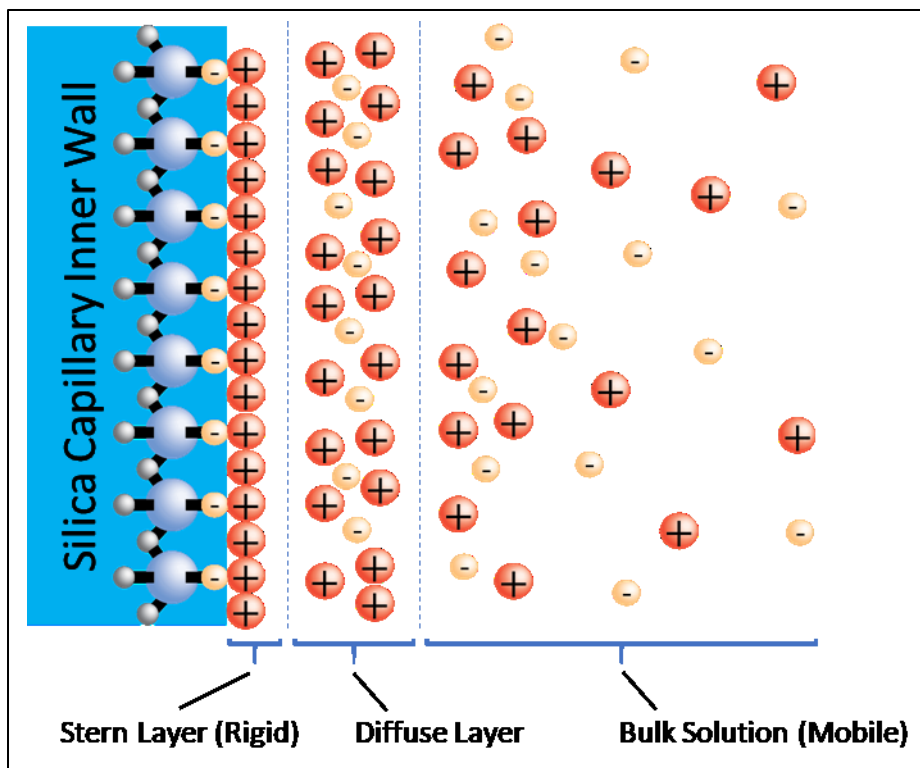
Figure 3 Diagram of the ion distribution at the capillary wall. An electrical double layer forms surface to maintain charge balance, made up of a rigid Stern layer and diffuse layer. The diffuse layer primarily contains cations, which are mobile and will migrate towards the cathode when subject to an electrical potential. Waters of hydration surrounding the migrating diffuse layer ions hydrogen bond with the bulk solution causing electroosmotic flow.

Separation efficiencies in CE can be very high as compared to HPLC, with theoretical plate numbers that are typically an order of magnitude better (10^6 vs 10^5 plates per meter).[108,109] HPLC is affected by a number of critical band broadening factors: sorption kinetics, multi-path flow effects and the laminar flow profile found in the pressure driven hydrodynamic flow. Finite sorption kinetics result mass transfer delays that increase band broadening. Packed LC columns also have a multitude of flow paths between the particles which increase band broadening. Due to frictional forces at the interface between the mobile phase and the particle's surface, the mobile phase velocity profile is parabolic, or laminar, across the network of channels in-between the packing. This laminar flow further broadens the analyte bands.

Since CE does not rely on a stationary phase, and is carried-out in an open tube, longitudinal sorption kinetics, multi-path flow effects are largely absent. The EOF produces a flat, plug-like flow profile originating at the capillary wall results in a uniform flow throughout the capillary and

avoids broadening that would be introduced with laminar flow. Instead, diffusion and sample volume (plug length) are the main factors determining peak bandwidth.

For small molecules, longitudinal diffusion is, in most instances, the limiting factor during a separation. However, for large molecules, and in many instances for small molecules, sample introduction is the factor that results in the greatest degree of band broadening in CE and thus must be precisely controlled. Narrow sample band injections can be performed hydrodynamically by placing a sample vial at the capillary inlet and pressurizing the inlet or applying vacuum at the outlet, as in commercial systems, or simply raising the inlet vial by several centimeters for a short time in home-built systems. Electrokinetic injections can also be performed by simply applying a potential across the electrodes. This does create a bias in the analyte concentrations in the sample plug, due to the electrophoretic flow differences between charged analytes. Thus, it is important to be aware that late migrating components will produce a lower signal than if hydrodynamic injections are used with CZE separation. A number of methods can be used to further ameliorate this effect by focusing the sample plug into a narrower band after injection, known as sample stacking, which have been reviewed in the literature.[110,111]

1.7 Peak Capacity, Peak Generation Rate: Theory and Importance.

The practical goal in separation of simple samples is typically to separate all components during a separation window of reasonable duration. With biological samples, whose complexity exceed the separation power of current instrumentation, it is convenient to focus on figures of merit that can be used to develop and compare instrumentation. Peak capacity, a key figure of merit in multidimensional separations (MDS), can be predicted using mathematical models describing chromatographic separations based on separation conditions (stationary phase, mobile phase, temperature, etc.). For CE empirical measurements of peak capacity, rather than mathematical expressions, are commonly used.[112] This method of estimation utilizes measured peak width statistics and will be employed in this thesis. The following is an introduction to the basic theory covering how peak capacity can be inferred from peak widths. This theory assumes all peaks are Gaussian and have uniform baseline width. While a small degree of peak distortion is typically considered acceptable, any significant peak asymmetries should be investigated. Improvements can be made through the use of existing theoretical and semi-empirical models that can perform better peak fitting or optimization of instrumental sources of peak distortion.[113]

The peak capacity (n) of any 1D separation, such as LC, GC and CE, can be approximated as the number of peaks that can fit into the separation time with a resolution of $R = 1$. When $R = 1$, the mean of each peak is separated by four standard deviations (σ) from either of its nearest neighbours. This results in each peak having minimal overlap (2.3 %) with any adjacent peak. These idealized Gaussian peaks each have 95.4 % that is not overlapped and are considered equivalent to the baseline width of the peak (W). The peak capacity is a measure of the number of peaks, with width W, that can, in principle, fit within a separation time that spans $t_n - t_0$.

$$n = 1 + \frac{t_n - t_0}{W} \tag{3}$$

Applying this equation, using typical CE conditions with 93 000 theoretical plates (N), arising from peak widths of 1.08 s, and a separation window of 83 s produces an ideal peak capacity of 77. In practice, non-ideal peak shape at the baseline is common and causes this number to decrease. The more reliable method of estimating W is to use non-linear regression methods and the easily measured width of a peak at half of its maximum height ($w_{1/2}$), the so called full-width half maximum. Using the standard conventions of measuring theoretical plate numbers

$$N = 5.54 \times \left(\frac{t}{w_{1/2}}\right)^2 \tag{4}$$

and,

$$N = 16 \times \left(\frac{t}{W}\right)^2 \tag{5}$$

leads to

$$W = 1.699 \, w_{1/2} = 4\sigma \tag{6}$$

In practice, high-resolution peak capacities for 1D separations by HPLC and CE can approach 10^2 peaks. However, it remains one, or more, orders of magnitude below that of 2D-PAGE spot capacities[72,114] and MudPIT 2D peak capacities[105,115]. The explanation for the huge difference in peak capacities will be explained in the Part B of this chapter. To put it simply here, the high peak capacities of these 2D separations have a significant cost to their applicability when the processing times are considered. Linear separation methods typically require under one hour, whereas the 2D-PAGE and MudPIT separations easily exceed 10 hours of separation time which severely limits throughput.[114,115]

In addition to total peak capacity, peak generation rate is also an important metric to evaluate separations. A linear separation that produces 100 peaks in an hour has a peak generation rate of 1.67 peaks/min. This is significantly less time the 32 hours a 10 000-spot 2D-PAGE gel requires but achieves 5.21 spots/min.[86] Even time optimization MudPIT analyses require 14.8 hours to achieve 4488 protein identifications, equivalent to 5.05 proteins/min.[115] An important note is that MudPIT studies are not directly comparable as they are typically reported in protein identification numbers rather than peak capacities, and much of the analyte resolving power can be attributed to the MS rather than the preceding IEC × RPLC separation. Thus, the peak capacity from the separation alone is expected to be considerably lower than the number of protein identifications found in MudPIT studies.

Thus, there is still an additional benefit to the two-dimensional separation, but the long processing times exceed the typical desired target of one to two-hour separations per sample that is required for reasonable throughput. Throughput is particularly important as it often dictates the number of samples and/or replicates that can be incorporated into an experimental design and may limit statistically significant sample sizes.

1.8 Outline of the Problem and Solution

The problem currently facing 1D separations is that the upper limits of peak capacity are already in sight and remain a far cry from what is needed for high proteome coverage. Conversely, 2D separations are inherently low throughput, limiting its use to small exploratory studies. The holy grail of MDS science is a hybrid technique that uses two 1D linear separations to virtualize a 2D gel separation, allowing such a system to maintain the high-throughput of linear separations while gaining the high peak capacity of 2D-PAGE. MudPIT succeeds in much of this, achieving peak

capacities comparable to 2D-PAGE with the addition of fully automated operation. However, MudPIT analysis times remain lengthy, much of its resolving power is reliant on the MS detector and the MS is susceptible to contamination from the salt gradients used in the IEC elution steps.

The challenges in designing and building a 2D system that combines high peak capacity *with* high speed lie in coupling disparate instruments such that the benefits of the underlying 1D separations are not degraded, while the data density benefits of 2D separations are gained.

1.8.1 **The Path Towards 2D Separations**

The approach that will be demonstrated in this work is to interface a 1D separation with a multitude of 1D second dimension separations, effectively operating in parallel to gain a multiplex advantage. The chief problems are (1) efficient separation-to-separation interfacing at the microscale, (2) operating the parallel second dimension separations concurrently and without interruption (3) detecting analytes emerging from the parallel separations and (4) deconvoluting the data into practical 2D representations. The remainder of the introduction will focus on these elements.

Part B: Two-Dimensional Liquid-Phase Separations: Considerations & Caveats

1.9 Two-Dimensional Separations for Proteomics: Challenges Remaining with Current Interface Designs

The goal of MDS, using linear separations, is to separate analyte bands that are unresolvable using 1D methods alone. Consider, as an example, a mixture of eight compounds that cannot be resolved by two given separation conditions, as depicted by the separations in Boxes A and B in Figure 4. Neither the first dimension (^{1}D) nor second dimension (^{2}D) separations can, alone, provide adequate separation power to resolve all of the component peaks. But, due to the different displacement of the bands between the ^{1}D and ^{2}D separations, their combined MDS produces a 2D plot (box C) that is resolved successfully. An important feature of 2D separations that result from two 1D separations, is that the data output is an ordered set of separation profiles (chromatograms, electropherograms). The number of separation profiles that are generated equals the number of times the ^{1}D effluent is sampled by the ^{2}D. These separation profiles must be rearranged to produce the familiar visual contour representation (box C) that mimics the output of a 2D-PAGE separation.[116]
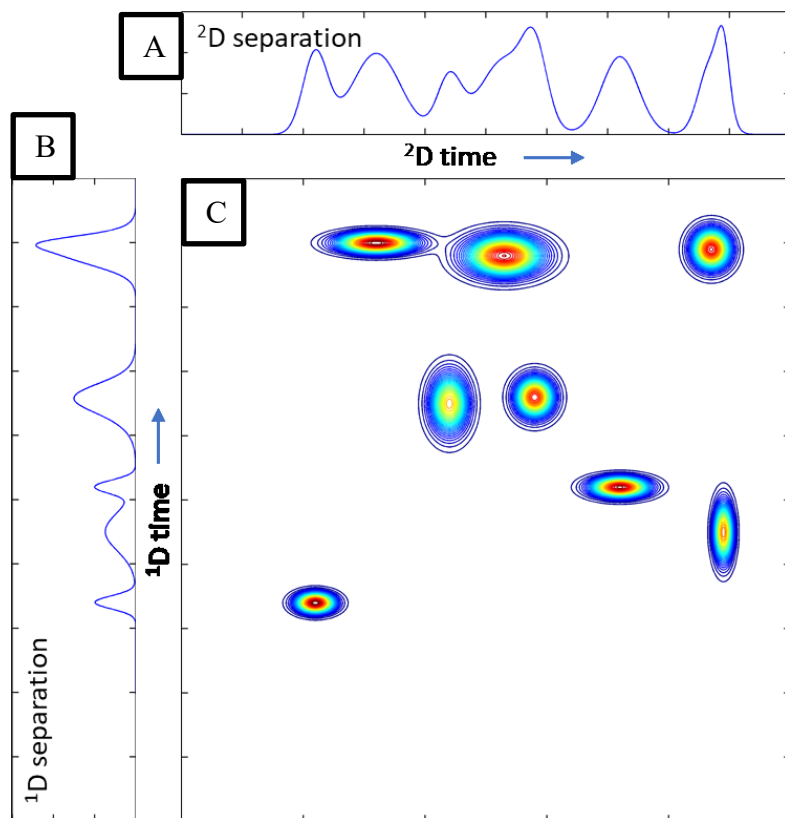
Figure 4 Depiction of two 1D separations (A, B) with overlapping peaks that are combined to produce a higher efficiency 2D separation (C) displayed as a 2D heat map. Overlapped peaks in the ^{1}D separation are well separated upon 2D separation.

Giddings formalized the concept of MDS in 1984, promising much greater peak capacity when a sample is subjected to two orthogonal (mechanistically unrelated) methods.[117] This resulted in an expression of the total peak capacity of a two-dimensional separation, ^2n_c, being the product of the individual peak capacities in the first, ^1n_c, and second dimension separations, ^2n_c. Thus, an ideal 2D separation would have a peak capacity described by

$$n_{c,2D} = {}^1n_c \times {}^2n_c \tag{7}$$

The consequence of this effect is easily seen when high-resolution 2D-PAGE separations are performed. By pairing a separation based on isoelectric point with one based on molecular weight which are orthogonal properties, exquisite peak capacity can be attained.

MDS, utilizing paired linear separations, is a little more complicated than the 2D-PAGE example above. The complication is in transferring fractions of the effluent from the first-dimension

separation (^{1}D) to a second-dimension (^{2}D) separation. These ^{1}D and ^{2}D separations are akin to the combined IEF and gel electrophoresis (MW) separations in 2D-PAGE. The first linear separation migrates analytes through a column (HPLC or CE) with the exiting effluent being sampled by a ^{2}D separation. For liquid-phase separations, analytes can be detected as they are transferred between the ^{1}D and ^{2}D by integrating a non-destructive detector (e.g. UV, fluorescence) in-line with the flow path. Linear MDS introduces one or more ^{1}D fractions to a secondary linear separation that acts as a new sample to be subjected to a second separation. Thus, linear MDS require a high degree of coordination and ultimately subjects a given sample to two disjointed separations in a serial fashion. Their resultant data output consists of a set of traces, such as a chromatogram, with one for each of the injections performed on the ^{2}D separation. This data format requires deconvolution to produce an interpretable 2D map that would be comparable to 2D-PAGE.

Linear MDS can be performed in either offline or online modes. In offline mode, a fraction collector deposits fractions from a ^{1}D HPLC or CE separation into a multi-well plate. These fractions are then separated serially. This can be performed on the same instrument after modifying the separation mode. This method is time consuming and the required sample handling can introduce loss of resolution, contamination, sample degradation and evaporation. Thus, research efforts have focused on the development of online methods that allow automated handling and immediate processing of the ^{1}D effluent.

Physical design restrictions have limited the variety of online interdimensional interfaces that have been demonstrated in the literature encompassing MDS instrumentation. Ideally, all fractions of the ^{1}D separation are introduced to the ^{2}D separation, which is referred to as a comprehensive 2D separation. However, the ^{1}D effluent output often exceeds the rate which the ^{2}D can accept sample. One way to deal with the mismatched rates is for the ^{1}D separation to be halted in between injections or run at sub-optimally low flow rates. This allows enough time for each ^{2}D separation to complete prior to the following injection. This leads to long separation times and can add significant extracolumn band broadening due to long diffusion times in the ^{1}D column. Another strategy is to only perform the ^{2}D injections at pre-selected points in the ^{1}D separation where the elution times of "important" peaks have been recorded from previous test separations, which is termed heart-cutting. Comprehensive MDS is preferred since all sample components are retained

from initial introduction of sample on the ^{1}D to final output from the ^{2}D but can be impractically long if many ^{2}D injections are required. In some cases, separation goals can make heart-cutting an attractive technique. Examples of both will be covered in the following sections.

An important criterion for successful MDS is having an adequate sampling rate. Earlier work by Murphy *et al.* suggests that a ^{1}D peak can lose over ~25 % of its resolution if it is sampled less than three or four times across its width by the ^{2}D.[118] This Murphy, Schure and Foley (M-S-F) criterion has been the basis for further development in MDS peak capacity estimations. To avoid undersampling a ^{1}D effluent peak, as described by M-S-F, samples should be in-phase (spaced symmetrically across the peak). Thus, in the case of three samples taken across a peak, one sample should be centered on the peak and the other two should capture the tails on either side of the center. When samples are out-of-phase (non-symmetrically spaced), the peak apex can be missed in the captured ^{2}D samples. This can lead to peak skewness and aliased peak heights which results in unreliable peak integration and overly complicated data interpretation. An additional challenge includes instances where the ^{2}D sample volume is large relative to the ^{1}D peak volume. This causes mixing of the effluent inside the sample loop used in 2D-HPLC instrumentation and results in peak shape information loss for that interval. These factors result in losses of ^{1}D peak capacity when undersampling occurs. Continued development of this work by Davis *et al.* demonstrated that an first dimension broadening factor could be expressed mathematically.[119]

$$< \beta > = \sqrt{1 + 3.35 \times \left(\frac{t_{cycle}}{^1w} \right)^2} \qquad (8)$$

Here, the broadening factor, $<\beta>$, is modified by the sampling time, $t_{sampling}$, and width, ^1w, of a ^{1}D peak exiting the ^{1}D separation column. And the corrected peak capacity, $^1n'_{c}$, as mediated by undersampling of ^{1}D peaks is related by

$$^1n'_c = \frac{^1n_c}{<\beta>} \qquad (9)$$

The amount of ^{1}D peak capacity conserved can be represented as a function of the number of times the ^{2}D captures fractions across an 4σ peak eluting from the ^{1}D, as shown in Figure 5. Using the undersampling broadening factor, the estimated loss from sampling a peak three times is nearly 15%. To retain 99% of the ^{1}D peak capacity, 13 samples must be collected across any peaks transferred between dimensions. Undersampling must also be avoided to maintain accuracy and precision in quantitation of peaks resulting from 2D separations.[120] In essence, the problem is that the separation speeds of the first and second dimension separations are too similar to be successfully coupled without significant compromises that degrade the separation. The typical compromise that is made to meet sampling requirements is to slow down the ^{1}D separation and/or speed up the ^{2}D separation. Typically, the ^{1}D separation time is "stretched" to the hours scale, where analyte diffusion becomes a significant source of band broadening and the ^{2}D separation is operated very rapidly under compromised separation conditions. While functional, these compromises cause a loss of ^{2}D peak capacity.
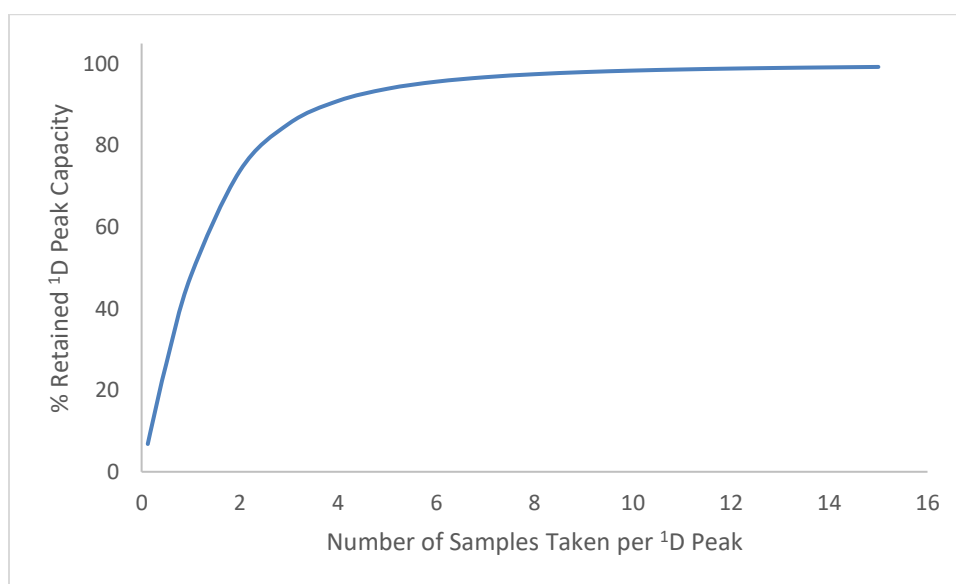
Figure 5 Plot of the fractional peak capacity retained from the ^{1}D as a function of the number of times each ^{1}D peak is sampled by the ^{2}D.

1.10 Peak Capacity and Separation Mechanism Orthogonality

Another aspect of MDS that must be carefully considered is orthogonality between dimensions. This is a measure of the difference between the separation mechanisms that underlie each dimension of the separation. Higher orthogonality allows for greater distance between neighbouring peaks and greater opportunity for baseline resolution. An ideal 2D separation has

peaks that are not clustered, but instead are spread across the entire 2D separation space (in a perfect world uniformly, but at best randomly). For effective coverage over the 2D separation space, the chemical characteristics that each individual separation exploits should be as different as possible. In 2D-PAGE, this is used to great effect as the isoelectric point and M.W. of proteins tend to be uncorrelated.

In linear separations, the mechanism of separation often has some similarity, giving rise to 2D separations with some degree of correlation between dimensions. This results in 2D data maps with a dearth of peaks in some areas while others have clusters or patterns of closely spaced peaks. The effect of this unused separation space on the 2D peak capacity has been described as the fractional coverage, $f_{coverage}$. Combining the above factors, Stoll *et al.* defined a conditional[121] (or effective) peak capacity, $n^*_{c,2D}$, for a given 2D separation

$$n^*_{c,2D} = \frac{^1n_c}{<\beta>} \times \, ^2n_c \times f_{coverage} \qquad (10)$$

This form of the peak capacity accounts for the complex effects of both the separation system and the sample characteristics on the observed orthogonality. Metrics have been developed to quantify this orthogonality and is a continuing area of research interest.[122–125]

For any development of MDS techniques and methods, best practices should include careful consideration of ^{1}D sampling rates and orthogonality of separation modes. Each can significantly benefit or harm the resultant peak capacity and separation quality.

These concerns are relevant for both off-line and on-line MDS. While off-line methods are more flexible, in terms of separation mode selection and sampling, the long analysis times and requirement for sample handling makes this unappealing for high-throughput analyses. On-line methods have the potential for rapid automated analysis but utilize specialized interfaces that couple the ^{1}D and ^{2}D separations and, as discussed above, face significant sampling and operating compromises. The work shown in this thesis will demonstrate that there is an unexplored opportunity for on-line MDS; and it will be the focus of the material presented.

1.11 2D HPLC

Early on, it was recognized that designing effective online MDS interfaces would be a major challenge in coupling two linear liquid-phase separations. The seminal 2D-LC instrumentation was demonstrated by Erni and Frei in 1978, introducing the multi-port loop type valve system that remains the basis for current 2D-LC instrumentation.[126] Due to constraints in automation and computer data processing available at the time, only seven contiguous fractions were made across a single broad peak in a five hour long separation window. Fully-automated 2D-LC instrumentation would be introduced over a decade later by Bushey and Jorgenson[127], and began the rapid growth that leads to our current state of the art 2D-LC separations. 2D-LC separations can be performed in a heart-cutting or comprehensive fashion. Each has advantages and disadvantages which are described below.

Heart-cutting refers to the method of partially sampling the effluent of a ^{1}D separation for subsequent separation in a ^{2}D. One or more discrete segments (typical: < 10) from the ^{1}D separation are collected for further separation. The segments are captured at long time intervals so that the ^{2}D separation time is not constrained by the ^{1}D separation speed. This leads to less stringent design requirements for mechanical operation, automation and separation optimization. Since a limited number of discrete segments of the ^{1}D separation are captured, effluent emission times must be targeted to capture the intended peak. The peak of interest could be captured in its entirety or, using a smaller or shifted sampling window, a segment of it could be used captured for downstream ^{2}D separation. A drawback of heart-cutting is the necessity of have prior knowledge of the entire ^{1}D chromatogram in order to capture the elution time of peaks of interest and to correctly accommodate the width of each peak. Thus, except for highly repeated sample analyses, a ^{1}D test separation must be performed for each sample prior to 2D-LC separation resulting in longer processing times. Another drawback occurs when an entire peak is captured as a single fraction, as is common when quantitatively sampling a ^{1}D peak. Since to the ^{1}D peak being captured in a single volume, all peak shape information is lost. This combination of features make heart-cutting unsuitable for use on complex proteomic samples.

In comprehensive 2D-LC (LC×LC) separations all of the ^{1}D effluent is sampled, thereby providing much greater potential for information density. This comes at the expense of the compromises required to interface two LC systems. The ^{1}D separation length can be extended by reducing the

^{1}D flow rate, or operating the ^{1}D in a stop-and-go[128] fashion to allow the ^{2}D time to complete a separation between injections. These strategies can lead to hours long analysis times and causes diffusion to become a significant source of band broadening. Alternatively, the ^{2}D can be operated at high speed to match the ^{1}D effluent flow rate. Previous groups have gone to great lengths to operate the ^{2}D separation with run times as short as 20 s.[129] There is still the inescapable trade-off of compromised ^2n_c peak capacity, and thus the total peak capacity of the system.[130–133]

An obvious alternative to using a single fast ^{2}D is to use two parallel ^{2}D separations to effectively relax the sampling/separation speed problem.[133–136] However, a significant challenge of this "numbering-up" strategy is the not-insignificant expense of increasing the number of HPLC systems. Additionally, mismatches between systems (*e.g.* dwell volumes) and retention characteristics of the columns complicates data alignment.

Another modification has been the integration of multiple parallel ^{2}D sample loops into the mechanical valve interface, which allow capture of multiple ^{1}D segments. This has been used in two configurations. One is multiple heart-cutting (mLC-LC)[137–139], which involved the capture of multiple ^{1}D peaks. In essence, the interface acts as an autosampler by capturing and holding a limited number of peaks for later injection. The ^{2}D can then complete separations while further ^{1}D peaks are captured and stored concurrently.

Using a similar valve system, selective comprehensive (sLC×LC) separations utilize the storage loops in another sampling scheme. Instead of each sample loop capturing an entire peak, very short sampling times (3 s cycle times) can be used to capture multiple discrete segments of a single ^{1}D peak.[140] This easily overcomes the undersampling problem, as typical ^{1}D peaks are on the order of 30 s.[121] However, both mLC-LC and sLC×LC remain methods that sample only a small fraction of the total ^{1}D effluent for further separation by the ^{2}D.

Both strategies seek to decouple the sampling time from the ^{2}D separation time, but in two different ways. mLC-LC allows for targeted analysis of multiple peaks of interest across an entire ^{1}D chromatogram, whereas sLC×LC attempts to extract highly detailed information over a short span of ^{1}D effluent. Ideally such an interface would be able to accommodate an entire ^{1}D separation. But typical LC×LC separations often require the ^{2}D to handle greater than 100 samples.[141] There has yet to be introduced a valve interface with that level of multiplexing.

1.12 2D Separations Using CE in the Second Dimension

Soon after demonstrating their LC×LC interface[127], Jorgenson and co-workers soon adapted a similar interface for 2D LC×CE separations[127]. The ^{2}D capillary, inserted into one of the valve ports, could be enveloped in BGE flow during runtime. Simultaneously, the sample loop could be filled with ^{1}D effluent. To make an injection, the valve introduced the sample loop into the BGE path, and an electrokinetic injection was performed while the sample volume moved past the capillary inlet. The valve acted as the ground terminal in the high-voltage circuit driving the CE separation. The ability to simply apply a voltage potential across the capillary while a flowing stream enveloped the inlet was an important innovation, as it abstracts the high pressure of the chromatographic system from the low-pressure CE system which obviates the need to add a precise low-pressure injector. The sample loop used had a 10 μL volume; much larger than the typical nanoliter volume CE injection, which leads to significant quantity of the sampled peak going to waste and increased demands on the ^{2}D detection apparatus sensitivity.[142,143] However, this is necessary to maintain high plate numbers and high resolution in the CE dimension. As with all serial 2D separation interfaces, the separation time was long, typically greater than 4 h. CE separations have a few inherent advantages that are appealing for MDS; namely, no need to regenerate the stationary phase between runs and multiple separations can be carried-out concurrently within the same capillary. This allowed the system to sample the ^{1}D in one-minute intervals. The authors recognized that the system they built produced long analysis times and introduced significant ^{1}D undersampling, but these were due to limitations in the slew times for the mechanical valve and the data acquisition tools that were available.

Valve based interfaces have been used for CE×CE as was demonstrated by Zhang et al., where capillary isoelectric focusing (cIEF) was coupled to a ^{2}D capillary electrochromatography (CEC) separation.[144] This interface had a smaller dead volume (25 nL) compared to Bushey's[145] interface. The authors recognized that this remained much larger than a typical injection. Careful selection of ^{1}D (cIEF) and ^{2}D (CEC) separation modes was used to overcome this. Control of the aqueous cIEF separation allowed the focused sample to be positioned at the inlet of the ^{2}D CEC separation column, which elutes under similar principles as liquid chromatography. This design is thus only appropriate to couple a specific sequential pair of separation mechanisms.

Though other interfaces have been introduced for MDS that include CE as one mode of separation[146,147], the most widely applied is the flow-gating interface.[148] The general design uses a mechanical support to align two capillaries end-on-end, such that the outlet of a donor capillary is facing the inlet of a receiver capillary with a small gap between them (~40 – 100 μm).[149,150] This support can be made by custom fabrication, or constructed using a simple cross with appropriate fittings and sleeves. A channel, that is perpendicular to the capillary axis, is made to surround these capillary tips. The channel is filled with BGE, which envelops the capillary tips. Injections are performed by allowing effluent to migrate from the ^{1}D outlet and fill the space between the two capillaries. An electric field applied across the ^{2}D capillary draws sample (and later BGE) into the inlet electrokinetically. If the sample volume is sufficiently small, it can be transferred entirely to the receiver capillary.[151] Otherwise, the transverse flow path can be used to flush the capillary inlet to prevent peak distortion due to inefficient sample introduction.

The first flow-gated designs were introduced by the Jorgenson lab, where microbore HPLC was coupled to CE.[152] Their latest design used a polycarbonate interface, which allowed observation of the flow behaviour in the interface during use. Due to the continuous nature of the ^{1}D HPLC effluent, the transverse wash flow was used to draw effluent to waste between injections onto the ^{2}D. Injections were performed by stopping the wash flow momentarily, allowing the gap between the capillary tips to fill with effluent and be drawn into the receiver capillary. Thus, key optimization parameters included ^{1}D effluent flow rate, the distance between ^{1}D outlet and ^{2}D inlet, the transverse wash flow rate and the length of time used to clear effluent from the channel after an injection was completed. A key benefit of flow-gated interfacing is that it can sample a small heart-cut from a peak, which can ameliorate some of the undersampling problem. Since the peak is sampled midstream, remixing of a peak cannot occur as it does in 2D-LC when injecting from a sample loop that has stored a ^{1}D peak.

Dovichi's group introduced the first flow-gated interface for CE×CE, focusing on proteomics separations.[151,153] Because of the matched separation mode and volumes in each dimension, the ^{1}D effluent could be sampled entirely, with no requirement for drawing it to waste. This work also employed highly sensitive fluorescence detection using a sheath flow cuvette, previously developed by the same group. Over the course of their work, multiple interface designs were prototyped, as there was continued recognition of challenges of aligning capillaries in the interface

and the ease of use when replacing capillaries. The general schema of the apparatus had the interacting capillaries laid end to end in a plane on a platform. Alignment was performed using a microscope, allowing for simple lateral alignment, but very challenging depth alignment. A recent design used a micro-dicing saw to produce a deep nick in the side of a short capillary that acted as a guide for two separation capillaries inserted on either side of the nick.[154] The nick was then centered in a transverse wash channel, similar to the traditional flow-gated interface. While this greatly facilitates the construction and alignment of the capillaries in the interface, there is still the fundamental problem of sequential analysis of any ^{2}D injections.

Parallel CE separation technologies are well-developed, but only in specific applications. Highly multiplexed CE DNA sequencers have been commercially available since the 1990s, with instruments containing as many as 384 capillaries.[155] But, designs using parallel CE in MDS are sparse. Work from this lab previously demonstrated a two capillary ^{2}D coupled to a ^{1}D gel-filtration chromatography (GFC) separation using a cast polydimethyl siloxane (PDMS) interface.[156] The capillaries accepted electrokinetic injections from the ^{1}D effluent stream using a novel modification of the flow-gated interface. Effluent from the ^{1}D was delivered to two channels that also contained a flowing BGE stream, such that the streams coexisted side-by-side in a non-mixing laminar flow. The ^{2}D separation capillaries were inserted into each channel orthogonal to the flowing stream. These capillaries could be switched between two positions in the parallel streams using servo motors; (1) where the inlet was surrounded by the GFC effluent, and (2) where the inlet was surrounded by the fresh flowing BGE. This way an electrokinetic injection could be performed with the capillary inlet bathed in GFC effluent. By simply moving the capillary inlet into the fresh BGE flow any residual surrounding effluent quickly became entrained in this wash flow, allowing for highly efficient injections onto the ^{2}D. Unlike typical flow-gated interfaces where the channel is sequentially filled and cleared of sample, the moving capillary design allows the ^{2}D to be parallelized. The PDMS sheath flow cuvette used for detection allowed for highly sensitive LIF detection.[157] This design was not easily scalable to higher numbers of capillaries, due to the PDMS casting requirements and footprint of the servo motor assemblies used.

Another unique CE×CE interface was used to couple a capillary isoelectric focusing (cIEF) ^{1}D separation with a capillary gel electrophoresis (cGE) ^{2}D separation as Yang et al. demonstrated.[146] A hybrid microfluidic platform was used, where a dynamic microfluidic cIEF ^{1}D channel could be

connected to eight parallel cGE ^{2}D capillaries. Three glass wafers were laid down on a platform and abutted against each other on their longest side. The two outer wafers were held stationary while the center wafer could slide between the outer two by an attached micrometer. The glass wafers were etched with various channel patterns. The outer two wafers had channels that allowed connection of eight capillaries each, which then terminated on their inside face and contacted the center wafer. They also had adjacent short U-shaped channels with each opening terminating against the center wafer. The center wafer contained a modified serpentine channel, where the path of each crest and trough extending past the outer faces of the wafer such that they were cut off. This left behind a series of eight angled channels that each spanned the width of the wafer, and their openings terminated at the faces of the outer wafers. By sliding the center wafer between two configurations, the center channels were first mated with the U-shaped channels of the outer wafers to create a continuous serpentine channel where cIEF was performed. Upon completion of the ^{1}D separation the center wafer was slid to the second configuration, which mated each of the center channels to a pair of capillaries on the opposing outer wafers, allowing the subsequent ^{2}D cGE separation to occur. The main drawbacks of this interface centered around the mating of channels in the two configurations. Sealing the device was a major challenge, resulting in BGE leakage forming salt bridges leading to frequent arcing, which limited the separation voltages. Besides creating a significant high-voltage hazard for anyone operating the instrument, this resulted in lowered resolution and lengthened separation time. The channel alignment precision was also critical to transfer efficiency and required the operator to determine the correct positioning for each movement. The authors were actively pursuing efforts to automate the instrumentation at the time of publication, but no work has been published on an updated interface. Although eight separations are operated in parallel, there were only eight samples taken from the ^{1}D, resulting in dramatic undersampling of the ^{1}D.

Novel systems utilizing ^{2}D micro free flow electrophoresis (μFFE) separations coupled to ^{1}D nano-HPLC and CE separations were introduced by the Bowser lab.[158,159] In principle μFFE is a planar electrophoretic separation that occurs in a channel of flowing carrier buffer. Separation occurs in an enclosed wide shallow channel with hydrodynamically pumped buffer flowing through it. Sample is introduced at the upstream end of the channel and is subjected to a perpendicular electric field as it flows downstream. The electric field causes charged solutes to separate across the width of the channel based on their charge-to-hydrodynamic size ratio. The

simultaneous hydrodynamic flow carries the analytes to the downstream end of the channel and out to waste. Detection typically occurs optically at end of the channel before it enters the waste channels. Since sample is simply introduced continuously into the μFFE stream, it obviates any need for mechanical automation or timing schemes to interface the ^{1}D and ^{2}D. This has the effect of eliminating the undersampling problem at the time of sample introduction onto the ^{2}D. However, interfaces for downstream detection or sample processing is currently limited. LIF is the predominant detection method, with few examples in the literature for interfacing with other detector detectors that do not require labelling of sample components.[160]

1.13 The Challenge Ahead

How can MDS be operated while avoiding complex analysis procedures or compromises in the separation or detection conditions? Unlike the discrete ^{1}D effluent sampling techniques that have been demonstrated in 2D-LC or 2D-CE, the continuous nature of 2D-PAGE allows the separation achieved in the ^{1}D IEF to be entirely preserved as the separation transitions to the ^{2}D SDS-PAGE. A benchmark goal when designing linear 2D separations is to emulate the ability of 2D-PAGE to maintain the separation quality in the ^{1}D while coupling to a ^{2}D separation that only contributes beneficially to the overall peak capacity.

Consider a reasonable, if idealized, example of a 60-minute ^{1}D separation that produces 100 uniformly distributed Gaussian peaks, each 36 seconds wide. If the goal is to preserve 99 % of the ^{1}D peak capacity, then each peak needs to be sampled 13 times. This implies that the ^{1}D effluent is being sampled every 2.8 s—the so-called sampling time ($t_{sampling}$). If a single serially-operated ^{2}D separation is employed, it means that it must accept a new sample every 2.8 s which places extreme demands on the ^{2}D separation time. However, if multiple ^{2}D separations can operate in parallel then the ^{2}D separation time is relaxed as a function of the number of separations operating in parallel (N_{array}). The time between any two injections onto a single separation channel would be a cycle time (t_{cycle}), equivalent to $t_{cycle} = t_{sampling} \times N_{array}$, since the rest of the parallel separations would sequentially sample the ^{1}D effluent before the original separation received a second injection. This simple geometric progression of t_{cycle} with each added ^{2}D separation results in dramatically increases to the available ^{2}D separation time even with a modest number of parallel ^{2}D separations. Thus, t_{cycle} can be rapidly scaled to values that accommodate a wide range of separation times and peak widths for a variety of ^{1}D separation mechanisms in LC and CE. By

offering this sort of flexibility in the ^{2}D separation time, the ^{2}D separation modes available would not be limited to ones that operate at extremely fast speeds and avoid the compromised separation conditions they entail.

Consider a scenario using the separation and sampling conditions above and the ^{1}D separation is coupled to parallel ^{2}D separations whose lengths are not precisely known. One possibility is that each ^{2}D separation can only be used only once. Keeping the above $t_{sampling}$ implies that the number of sampling intervals, $N_{sampling}$, would be *60 min / 2.8 s per cycle = 1285 cycles*. Thus, this scenario would require 1285 parallel ^{2}D separation channels. The obvious advantage here is that all the ^{2}D separation times could be of any length as they are all independent. Unfortunately, operating this many ^{2}D separations in parallel would be a truly difficult feat!

One of the key benefits of 2D-PAGE separations is that the high resolution IEF separation is retained when sampled by the ^{2}D. Since the SDS-PAGE gel is a continuous matrix across its width, the resolution of any bands from the IEF strip that enter the ^{2}D is only limited by the size of the interstitial spaces within the cross-linked media. This practically preserves all of the ^{1}D resolution while undergoing the ^{2}D separation.

The above scenario provides a way to practically reproduce the spatial ^{2}D separation achieved in 2D-PAGE using a column format. One could imagine 1285 ^{2}D separation columns lying tightly in a row, forming a wall with the top edge made up of column inlets and the bottom edge the column outlets. Sample would separate from the inlet edge of the wall to the outlet edge, effectively mimicking the entrance and exit edges of the ^{2}D dimension of a 2D-PAGE gel but occurring in the lumens of linear separation channels. The ^{1}D IEF separation in 2D-PAGE is less conceptually similar, as it is the effluent emitted over the course of the separation window. In IEF, analytes across the entire length of the IEF gel simultaneously migrate into the SDS-PAGE gel that is in contact with the ^{1}D gel strip. Thus, the analytes in the ^{1}D are separated in space across the length of the gel. In the linear separation, the ^{1}D separation window is created in the time domain, where each segment becomes available as new effluent is emitted from the separation channel. This time separation window is transferred to the ^{2}D separations by passing ^{1}D effluent sequentially into the inlets of the wall of separation columns.

Another possibility is to allow each ^{2}D separation channel to be reused after any given sample injection has completed its separation, where all the analytes have exited as ^{2}D effluent. In this case, the number of ^{2}D separations required is dependent on the length of the ^{2}D separation and the number of $t_{sampling}$ intervals that fit within it. For example, if the longest ^{2}D separation window is 2-minutes, then the number of ^{2}D separation channels operating in parallel is equivalent to

$$no.\,of\ ^2\text{D}\ separation\ channels = \frac{length\ of\ separation\ window}{t_{sampling}} \tag{11}$$

Thus, the number of ^{2}D separation channels required to continually sample the ^{1}D is reduced to 43. While still a considerable number it is conceivable to build and operate. An apparatus that could perform this virtualization, of an infinite number of linear separations, would mimic the continuous nature of an SDS-PAGE separation matrix while limiting the resources required to operate the ^{2}D. Efforts to date have not succeeded in the design of a system that allows for fast, discrete ^{1}D effluent sampling rates without demanding compromised separation conditions in the ^{2}D to accommodate the ^{1}D separation window. Current designs also suffer from being difficult to scale up to higher numbers of ^{2}D separation channels.

As has been shown in existing high capillary-count DNA sequencers, parallelization scalability is relatively simple and inexpensive with electrokinetic separations (CE, CEC *etc.*). Thus, it is particularly well suited to incorporation into a highly multiplexed ^{2}D design. Additionally, CE separations can be performed in very short times while maintaining high efficiencies, and they can be performed without requisite regeneration steps in between separations.

The flow-gated designs covered above make use of predictable laminar flow regimes that are greatly utilized in the field of microfluidic system designs. In the work by both the Jorgenson and Skinner groups, laminar flow was used to effectively wash capillary tips to produce high quality injections onto the ^{2}D—a key attribute in successful interfaces. The requirement in this work is to design an interface where the outlet of a ^{1}D separation couples with the inlets of a ^{2}D capillary array in a continuous stream of fresh BGE, as depicted in Figure 6. An injection can be initiated by positioning the ^{1}D outlet in the stream of BGE coincident with the inlet of a ^{2}D capillary and stopped by simply moving the ^{1}D outlet away. Repositioning of the ^{1}D outlet to be coupled with a

subsequent [2]D capillary allows the next injection to be made. In such a design, when such sequential injections exhaust the number of available [2]D separations it can simply return to the position of the first capillary and allow continuous reuse of the [2]D array.
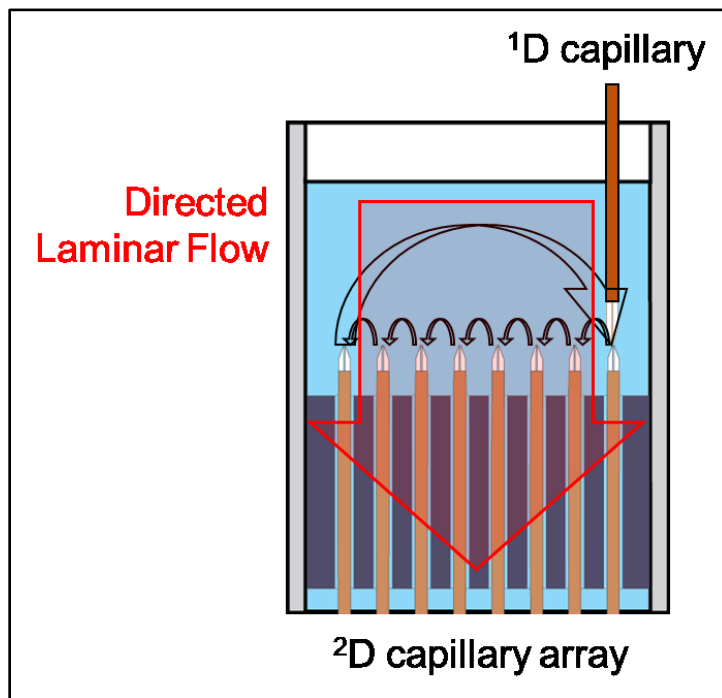
Figure 6 Depiction of a multidimensional CE × CAE laminar-flow interface. Injections onto the [2]D capillary array is achieved by momentarily positioning the end of the [1]D donor capillary in above a [2]D receiver capillary. Continuous reuse of the [2]D capillary array is simplified due to the shared laminar flow conduit. Once the last [2]D capillary has received an injection, the [1]D capillary returns to the position of the first [2]D capillary in the array to restart the sequence.

The work presented in this dissertation will cover the design, construction and characterization of a motor controlled, precision interface to couple a [1]D CE separation coupled to an eight-capillary array of [2]D CE separations. 2D separations have specific requirements above those of single dimension separations and successfully interfacing two CE separation modes for MDS is even more constrained. The following section will introduce pertinent aspects of experimental design for 2D-CE separations.

1.14 Microfluidic Considerations for Interface Design

Interfacing between dimensions is always the key challenge in hyphenating separation systems. Development of the interface, presented in this work, focused on performing injections using a moving laminar flow interface where precision motor movements could efficiently start and stop an injection. Whereas the underlying electrokinetically driven separations avoid band broadening,

any superposition of hydrodynamic flows caused by the interface can severely degrade separation performance. Completely eliminating hydrodynamic flow in microscale systems is unrealistic. Instead, realistic designs are achieved by careful selection of compromises that provide optimal system performance. Since the instrument presented herein is a hybrid system, employing both electrophoretic and hydrodynamic flows, a brief introduction to relevant fluid mechanics follows.

1.14.1 **Fluid Mechanical Considerations**

Laminar flow can be characterized as highly predictable flow where streamlines follow smooth continuous paths. This contrasts with turbulent flow, which is characterized by chaotic streamlines that are temporally dynamic and unpredictable.[161] A notable consequence of laminar flow is the parabolic flow profile of the fluid stream. Laminar flow in an enclosed tube can be envisioned as a series of concentric layers of fluid sliding past each other, where the center fluid moves the fastest and the fluid slows down at each successive layer that is closer to the tube surface (Figure 7). Despite the drawback in that this causes any stationary cross-section of fluid to distort as it conforms to a parabolic shape as it travels along the axis of flow, it does so with negligible mixing with the surrounding fluid along any other axis. A laminar flow regime is beneficial in analytical separations because it allows one to reliably predict the path a particle will take from any starting point within the flow field. This enables a stream of analyte to become entrained when introduced anywhere in the flow field of a miscible bulk fluid stream. (Figure 7) The boundary between the incoming stream and bulk fluid is maintained, limited only by the diffusion across their concentration gradients.
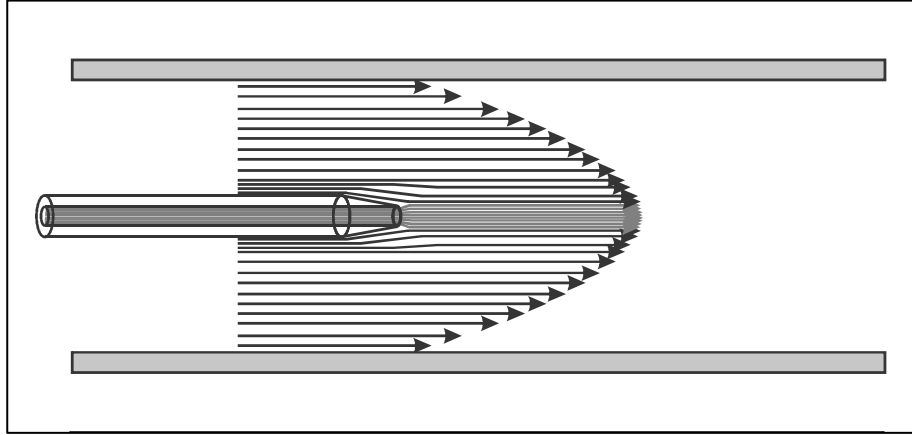
Figure 7 Diagram of the parabolic velocity profile in a laminar flow regime contained within an enclosed conduit. A capillary emitting effluent is depicted in the center of the bulk stream. The arrows indicate velocity vectors with the velocity lowest at the conduit walls and highest at the center.

Laminar flow regimes are common in small scale systems due to the favourable conditions of small conduit dimensions and low velocities. The existence of a laminar flow regime can be estimated by calculating the Reynolds Number (Re) which compares the ratio of inertial to viscous forces in a flowing system. The Reynolds number is proportional with density (ρ), velocity (V) and hydraulic diameter (D) and inversely proportional to the kinematic viscosity (µ) of the fluid.

$$Re = \frac{\rho V D}{\mu} \tag{12}$$

Critical Re values have been established to predict the flow regime in a hydrodynamic system; with general agreement that laminar flow prevails at Reynolds numbers below approximately 2300 for enclosed circular conduits. Reynolds numbers in non-circular conduits can be estimated by calculating an equivalent hydraulic diameter, D_h, based on the cross-sectional area, A_c, and the wetted perimeter, p, of the conduit.

$$D_h = \frac{4A_c}{p} \tag{13}$$

Laminar flow is not established instantaneously when fluid enters a conduit or channel. For the entering flow to become fully developed laminar flow, and gain its useful properties, it must

traverse a transitional region. If the conduit is facing a large body of liquid, then the fluid enters the conduit opening uniformly across its face. The incoming fluid is subject to a shear force exerted by the conduit walls. This is due to the so called no-slip condition, whereby the fluid in direct contact with a solid has zero velocity as it attempts to reach momentum and energy equilibrium with the contact surface.[162] This causes a drag on the fluid that extends radially toward the center of the conduit. Conservation of mass dictates that fluid at the center of the conduit undergoes a velocity increase to accommodate the slower moving fluid at the walls. This radial velocity gradient is what causes the parabolic velocity profile. Formation of this velocity profile occurs along an entrance length, L_E, that can be predicted with a known the Reynolds Number and the hydraulic diameter of the conduit. This quantity is useful for estimating ideal placement of objects or analytically relevant sample streams within an existing bulk flow.

$$L_{E,laminar} \cong 0.06 ReD$$

(14)

Stationary objects in the path of a laminar flow field modify the path lines of the radial velocity gradient. The surface of a stationary object acts as an additional surface at which the no-slip condition is observed. Thus, fluid velocity slows at the surface of the object and approaches the velocity of the bulk flow field. When the object is a capillary that is placed within the flow field and coaxial to it, as in Figure 7, the path lines do not deviate significantly. The flow field must expand downstream of the capillary end to fill the volume that was taken up by the capillary upstream. Turbulent flow can be a concern at the sharp boundaries at the end of a square-cut capillary. However, these concerns can be ameliorated, or eliminated, by using appropriate conduit dimensions and fluid velocities. It is also beneficial to taper the end of a capillary so the fluid path changes more gradually and the cross-sectional area at its end is near that of its inner lumen.

1.15 Washing Capillary Tips in a Laminar Stream

An early prototype was used to investigate whether bringing the ends of two CE capillaries into close contact, while both were in coaxial alignment, could facilitate transfer of sample from one capillary to the other. Modeled after previous work from this lab[156], the interface used a crossflow design with two intersecting channels cast inside it a PDMS block (Figure 8). From overhead, the [1]D capillary inserted in the top channel of the cross remained stationary with its outlet placed

~300 μm into the large channel. The ^{2}D capillary, at the bottom channel of the cross, was attached to a servo motor that could place the inlet in two positions: ~300 μm past the opening of its channel (Figure 8i) or insert it deeper so its inlet was in close proximity to the ^{1}D capillary outlet (Figure 8ii). The left and right channels used 1/8" PTFE tubing to provide flow of fresh BGE (left side) to waste (right side). A constant laminar crossflow was generated (from left to right) by applying pressure to a compressible supply reservoir. An LIF detector was constructed at the outlet of the ^{2}D capillary.
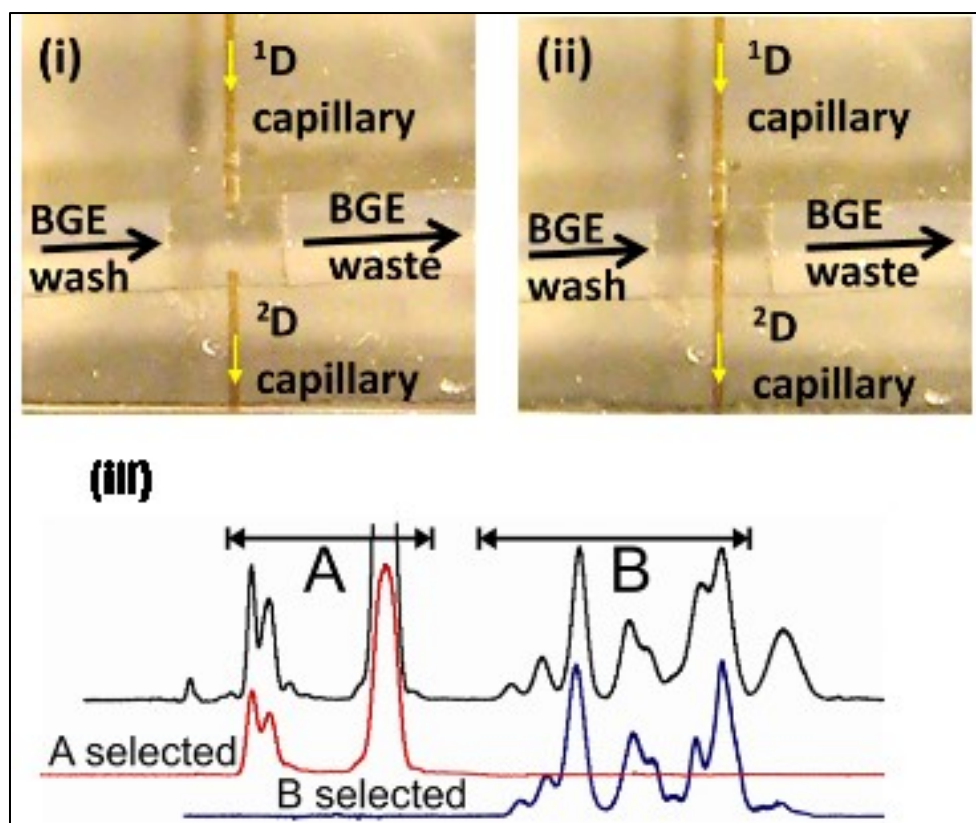
Figure 8 PDMS transverse wash-flow interface for CE×CE separations. Overhead images show the capillaries in the decoupled position (i) and in the coupled position (ii), by using a servo motor move the ^{2}D capillary between two positions. Yellow arrows indicate the direction of the separation in each capillary. Laminar buffer stream flows from left to right. The three electropherograms (iii) were generated by separation of fluorescently labelled serum with the capillaries in three configurations. The two capillaries were coupled throughout the separation (top trace), the capillaries began coupled and were decoupled near the midpoint of the separation (middle trace) and the capillaries began decoupled and wre coupled near the midpoint of the separation (bottom trace).

The ^{1}D and ^{2}D capillaries were successfully decoupled when the ^{2}D capillary was at the starting positing near its channel opening (Figure 8i) and coupled by placing the two capillary ends within approximately 30 – 60 μm of each other (Figure 8ii). As a separation in the ^{1}D capillary exited as effluent, placing the ^{2}D in the coupled position allowed efficient sample transfer. While in the decoupled position only BGE entered the ^{2}D capillary. The laminar BGE wash flow shown in the

large horizontal channel was expected to have a flow field similar to that shown in Figure 7, with a difference in that the capillaries were inserted perpendicular to the laminar flow rather than coaxial to it. The BGE velocity remained constant throughout each separation.

The constant laminar flow of BGE did not have a deleterious effect on the transfer efficiency. This was verified by performing three identical injections of fluorescently labelled human serum on the ^{1}D capillary. First, the capillaries were held in the coupled position to act as a single long capillary (Figure 8iii, top trace) to observe an unmodified parent separation profile. In two other separations, the capillaries were placed in the coupled position only during specified windows during the early half ^{1}D separation (Figure 8iii, middle trace) or the late half of the ^{1}D separation (Figure 8iii, bottom trace). These two separations that were momentarily coupled to the ^{1}D separation reproduced the separation profile in those subsections, while only baseline signal was observed during the rest of the separation. No tailing was observed to suggest there was significant carry over of sample after the capillaries were decoupled, demonstrating that the laminar flowing BGE efficiently washed the capillary tips to ensure clean injections.

Importantly, this demonstrated that capillary tips needed to be in very close proximity to each other for sample to be transferred when bathed in a constant laminar flowing stream, unlike classical transverse flow gating designs[149] where the coupling region is flushed each time sample was transferred from the ^{1}D to the ^{2}D. This experiment showed that the distance needed for effective capillary coupling was on the order of 100 μm, which was recognized as a challenging constraint with further consequences. The ultimate design would require precise mechanical systems for coupling, optical alignment with high magnification and, if using multiple capillaries, they would need to be well aligned with respect to each other and all be subjected to a uniform flow field to avoid biased sample transfer when coupled.

1.15.1 Multi-Capillary Laser-Induced Fluorescence Detection

Capillary electrophoresis systems demanding the highest sensitivity continue to be well served by laser-induced fluorescence (LIF) as the method of detection.[163–165] Well-designed CE instrumentation has been demonstrated to be capable of yoctomole range (10^{-24} mol) detection limits[166] and, when combined with nanolitre peak volumes, can achieve single molecule detection[167]. Given the dramatic sample fractionation promised by MDS—thousands of individual peaks from pL – nL scale sample plugs—it was an obvious aim to leverage the benefits afforded

by LIF detection. Incorporating LIF in a multi-capillary CE instrument comes with necessary challenges in detector cell fabrication and setup. The single capillary detector flow cells, known in the literature, are typically produced as relatively expensive custom preparations from quartz cell manufacturers. Scaling to higher numbers of parallel separations typically requires that each additional capillary brings along its own set of excitation and collection optics, along with assembly and calibration for each.

Thus, it was desirable to investigate an in-house design that could be prototyped using cost effective materials while also avoiding the need to outsource manufacturing steps to an expert commercial firm[168]. Laser-induced fluorescence has a number of distinct advantages in the context of this research lab. Chief among them was that there were many years of collective experience in working with PDMS to prepare low-cost polymer-based flow-cell detector systems. For this work, it was important adapt the detector design to address specific constraints required for the MDS interface with features not found in previous CE-LIF designs.

The benefit of the sheath flow cuvette arises from the entrainment of the effluent from a separation capillary outlet by a surrounding higher velocity (~10 ×) laminar flow, which produces an effect of hydrodynamic focusing.[169] Hydrodynamic focusing takes advantage of conservation of mass as the lower velocity effluent stream enters the higher velocity sheath flow. The effluent stream is rapidly accelerated upon exiting the capillary, where it narrows as it is quickly carried away from the point of introduction. Thus, the effluent diameter is inversely related to the velocity of sheath flow past the capillary outlet. This focused (*i.e.* funneled) cylindrical fluid volume can be efficiently excited by an orthogonal laser beam.

The exquisite sensitivity that is realized with efficient sheath flow cuvettes arises from a few unique attributes. The laminar flow that narrows the effluent stream also concentrates the sample within the detection volume. This also ensures the sample is directed away from the cuvette walls, which provides three benefits. Chiefly, this eliminates the scatter that normally arises when the laser reaches the BGE and silica wall surface interface, as encountered with on-capillary detection, due to the refractive index difference between the two materials. This lowered background allows higher excitation laser power to be applied which confers greater measurement sensitivity. Positioning the sample stream in the high velocity portion of the flow field also prevents increased residence time near the low velocity region hear the wall surface which can contribute to peak

tailing. Chemical interaction with the cuvette is also prevented, which can poison the optical surface. In aggregate, this arrangement eliminates a majority of the background noise sources, leaving luminescence and Raman scatter of the surrounding buffer being the main contributors to baseline noise and therefore the detection limits.[170]

1.16 Developing Two-Dimensional Separations

Since performing 2D separations online is an aim of this thesis, there will not be opportunity for manual manipulation of the sample during the separation. Methods development requires unified planning at every step so that the conditions used throughout the workflow are compatible and benefit the final separation. The stages that must be considered include the steps prior to the separation and the instrument path that the sample will travel through during a separation. Steps prior to the separation include sample selection and sample preparation, while separation steps include sample introduction, ^{1}D separation, effluent transfer from between dimensions, ^{2}D separation, transfer of ^{2}D effluent to the detector cell and signal transduction. Optimization of the method must consider sample characteristics, physical parameters, separation media and detection parameters. Sample selection should be guided towards those that demonstrate the efficiency of sample transfer between dimensions and the extent to which each dimension synergistically contributes to gains or losses in separation power. Sample preparation should, at a minimum, ensure the sample is soluble and stable in the sample matrix prior to separation. Sample matrices should not interfere with the downstream stability of analytes, nor alter their chemical nature that the selected separation mechanisms will act upon, nor cause any fouling of the instrument path. Physical parameters such as selection of capillary dimensions will dictate the voltage and current limits for optimal separation as well as affect detection limits and separation time. BGE selection affects many aspects of a CE separation, such as separation power and speed, and is important to consider for compatible BGE pairs to be compatible during coupling between dimensions. Optimized detection parameters are critical for CE since typical capillary inner diameters dictate tight tolerances for detection zones. Considerate planning when selecting these parameters will provide a good starting point for achieving 2D separations that will be informative to the investigator.

1.16.1 **Sample Selection and Preparation**

The goal of this work was to design instrumentation suitable for separating highly complex proteomics samples. These biological macromolecules have highly differentiated characteristics that can be exploited for separation selectivity. Though the key physical parameters driving electrokinetic mobility separations is charge and hydrodynamic radius, real-world separations are governed by additional factors.

Amino acid moieties within a protein can carry functional groups that can be charged, and an estimated pI can be easily calculated from the amino acid sequence. However, tertiary structure will dictate which functional groups are solvent facing, which alters the pI away from the predicted value. The tertiary structure also modifies apparent hydrodynamic radius of the molecule. Thus, whether the proteins are in a native or denatured state will affect the separation. Part of this tertiary structure is governed by hydrophobic domains which can lead to deleterious wall interactions, but have also been exploited as a separation target in CE.[171]

Pre-column digestion of protein samples is a common practice in bottom-up proteomics.[18] Analysis of proteolytic fragments is beneficial for protein identification due to greater ionization efficiency and fragmentation in mass spectrometric analysis. Peptides resulting from proteolytic digestion also benefit from smaller hydrodynamic radii, which increases electrophoretic mobility, and results in better separation efficiency than with intact proteins. The suppression of tertiary structure also minimizes wall adsorption characteristics, further improving separation quality. A variety of proteolytic enzymes are available from suppliers, with trypsin remaining the predominant choice.[15,172]

1.16.2 **Capillary Selection**

To ensure the ^{1}D effluent is sampled adequately, it is advantageous to have a ^{1}D that is operating slowly relative to the ^{2}D separation. Capillary dimensions dictate the limits of applied voltage and consequently the separation time. Thus, longer capillaries are suitable for the ^{1}D and shorter ones for the ^{2}D. Joule heating can be significantly mitigated by using smaller o.d. capillaries especially when air cooling is used. Analyte mass in the sample plug decreases in 2D×CE separations as ^{1}D peaks are split into multiple samples in the ^{2}D. This can make ^{2}D detection sensitivity challenging due to the short path lengths afforded by CE capillaries. Larger i.d. capillaries can allow for increased sample loading and mitigate some sensitivity challenges. However, this must be

balanced against the increased current and Joule heating that are concomitant with larger diameter capillaries.

1.16.3 **Background Electrolyte Selection**

Background electrolyte (BGE) is the primary variable for adjusting CE separations making careful selection of BGE greatly important. A key function of the BGE is to act as a buffer to establish and stabilize the pH within the capillary. This, in turn, determines the EOF within the during the separation as well as the net charge of the analytes in the sample. Combined with the viscosity, this dictates the migration velocity of all sample components. A good buffer should be of low conductivity in order to minimize Joule heating effects that cannot be mitigated with cooling. The buffers must also be transparent to the detector system, and not cause undue background signal that could mask analyte detection.

Separations in 2D add additional constraints when selecting pairings for the BGE used in each dimension. First, the EOF in the ^{1}D should be lower than the EOF in the ^{2}D to not diminish the benefit of the sampling speed gained by the multiplexed ^{2}D. Second, each buffer must provide adequate separation and, most importantly, the selectivities must be orthogonal in each dimension so each dimension can contribute to the overall separation. Third, the BGEs must be compatible with the other.

This third point deserves clarification. Since sample introduction is electrokinetic between dimensions, the ^{2}D must have adequate ionic strength to ensure enough buffering capacity to overcome any ^{1}D shift and ideally allow for focusing of each ^{2}D injection. The BGE constituents must also be miscible between dimensions and allow all sample components to remain dissolved as they transition between dimensions. Improper selection of buffer additives can themselves precipitate as in the case of pairing ionic buffers of opposite charge. Additionally, the ^{1}D effluent must be a suitable sample solvent for the ^{2}D and not degrade the ^{2}D separations. The sample must also remain soluble in the BGE throughout the separation.

1.16.4 **Detection**

Fluorescence remains the most sensitive detection mode available for capillary electrophoresis.[163–165] This high sensitivity and low limits of detection are achieved despite the nanolitre detection volumes typical in CE. Native fluorescence can be used with proteins due to the natural abundance

of tryptophan, tyrosine and phenylalanine residues, but reliance on autofluorescence introduces signal bias as each amino acid varies in quantum efficiency and natural abundance. Tryptophan would be the best candidate, being the amino acid with the greatest fluorescence and highest sensitivity but is rare in proteomic samples. Native fluorescence also depends on excitation and emission wavelengths in the UV region, where there is greater autofluorescence of contaminants in the sample solvents and run buffer.[163,173,174] Instead, it is advantageous for all sample components to be detected reliably without a dependence on natural abundance. The use of organic dyes conjugated to proteomic analytes allows for detection via easily constructed LIF in the visible wavelengths. However, it is of note that the commonly used 488 nm excitation line from the Argon ion laser suffers from interference from the water Raman scattering lines at 585 and 530 nm.[169] Similar Raman scattering lines occur with visible wavelength solid state lasers. Raman scattering and autofluorescence of the buffers used can contribute significantly to the background and ultimately dictates the detection limit.[163]

1.16.4.1 Fluorescent Labelling

A range of derivatizing agents are readily available for fluorescent labelling of biomolecules, with excitation and emission wavelengths in the visible region that are well paired with many common laser sources. Some commercially available reagents include the Alexa Fluor, ATTO and Chromeo dye families, which include dyes across many wavelenths.[175–177] These small organic molecules attach to target analytes through either covalent or non-covalent bonding, using a variety of attachment chemistries.

Attachment to primary amines is particularly convenient for proteomic samples, as labelling can occur at the n-terminus as well as the common lysine amino acid residues. This ensures all sample components can be visualized by the detector. The ATTO dyes (Invitrogen, Carlsbad, USA) are non-fluorescent natively. Upon reacting with a primary amine, it bridges two aromatic rings forming a fluorescent derivatized product. Fluorogenic molecules are particularly useful in bioanalysis as they produce low background signals (from unreacted dye) and therefore avoid the need for clean-up steps to remove unreacted reagent.

The lack of specificity in labelling can become problematic, as conjugation with the dye converts the positively charged lysine to a neutral or negative fluorescent site; and alters the isoelectric point of the biomolecule. This can lead to 2^n-1 different labelling products given *n* labelling sites if

labelling is partial. This can result in broad, poorly resolved peaks and overly complicated electropherograms. Fortunately, sub-micellar concentrations of an anionic surfactant, such as sodium dodecyl sulfate (SDS), have been shown to mask the heterogeneity introduced by incomplete labelling[178,179] and restore sharp well-resolved analyte peaks.

1.16.4.2 Dye Tracers: Fluorescent and Non-Fluorescent

Successful development of a new laminar flow interface requires an understanding of the fluid mechanics occurring during operation. Dye tracers are commonly used for visualizing flow processes in fluid systems in a range of applications from histological and cell analysis to instrumental microfluidic flows. A wide range of commercially available fluorescent and non-fluorescent dyes exist. The important characteristics for a dye to be useful for MDS system characterization include solubility throughout the system, small size to produce sharp peaks, lack of interaction with all surfaces and an electrophoretic mobility that allows detection in a reasonable time. Dyes that work at visible wavelengths are advantageous for simplifying setup and troubleshooting.

A key parameter to control in CE experiments is EOF. Thus, monitoring it is important during method development. Internal standards are often used to measure EOF in CE systems. However, commonly used markers (e.g., thiourea, DMSO) require UV absorption and are unsuitable for use with fluorescence detection. Organic fluorescent dyes, like those used to derivatize proteomic samples, can serve the same purpose. Ideal EOF markers have no electrophoretic mobility but, such dyes are usually insoluble in aqueous buffers. Ideally, two highly-charged, small-molecule dyes should be used to frame the separation window. Work has been done showing that fluorescent derivatization of multiply charged small peptides can be used for this purpose.[180] However, this is cumbersome to perform and was considered not critical to demonstrating the instrument design described in this dissertation.

Fluorescein is an inexpensive fluorophore with excellent quantum efficiency and soluble in aqueous buffers at concentrations that produce intense fluorescence signals. It is important to note that fluorescein emission is pH sensitive, requiring a basic environment to maximize the fluorescence signal. Newer dye conjugates (e.g., BODIPY, Alexa Fluor) improve on the drawback of pH sensitivity as well as stability. However, within its range of use, fluorescein is a highly effective fluorescence marker and is used extensively. The two acidic moieties on fluorescein each

imparts a negative charge at basic pH, causing it to migrate against the EOF. Fluorescein still migrates in the direction of the EOF which is typically much larger than the electrophoretic mobility of fluorescein allowing. However, the mobility of fluorescein causes it to lie generally near the center separation window and often overlap analyte peaks. Fluorescein sulfonic acid, with an additional negative charge, migrates at the end of the separation window and is unlikely to overlap with analyte peaks. This acts as a suitable late migration time marker for CE separations.

1.17 Data Processing for 2D Linear Separations

The primary goal of this work is to demonstrate high-speed, high-resolution separations for the purpose of accommodating the large sample sizes required for biomarker discovery studies. The modelling algorithms used to analyze such sample cohorts are sensitive to aberrations in the data they receive. Translation of the raw detector signal into analyzable data sets requires a series of steps that, if performed incorrectly, can result in unreliable results.[181–183] Thus, the quality of the data generated from 2D separations is as important as the quality of the separation itself. This section will describe the steps involved in processing data from a linear MDS instrument, using 2D-PAGE gels as a model, and lay out the challenges and techniques that were used in this work.

Analyzing separations originating from 2D-PAGE and linear MDS separations is conceptually very similar but procedurally and technically very different. In both workflows, the goal is to identify differences in the separations between different samples or between samples and a reference. With 2D-PAGE, comparison between two samples can be performed by simply laying one stained gel atop another and visually inspecting the differences between spots on each gel. To ensure the same spots are compared between gels, internal standards can be included in each separation, providing key alignment points on each gel.

For an MDS instrument utilizing a single ^{2}D linear separation, the raw output is a continuous stream of digital intensity values resulting from the effluent flowing past the ^{2}D detector. This is represented as a single column of data, with each row containing the intensity for one detector sampling interval. To create a representation comparable to 2D-PAGE, the data stream must be split into logical separation windows—one for each ^{2}D separation profile—and reorganized. The set of ordered separation profiles is transformed into a matrix, where each column is occupied by an independent ^{2}D separation window with the rows containing their time dependent signal intensities. Contained within a rectangular matrix, the data represents a rasterized image of the 2D

separation and can be viewed as a contour plot (or heat map) similar to a 2D-PAGE gel (Figure 4).[184]

A problem is that the 2D separation data matrix can contain artifacts due to unwanted variations in the data. Variations regularly occur due to multiple factors that can be random or systematic, such as environmental fluctuations in temperature, electromagnetic interference and stochastic effects in the separation. These effects can be reduced by controlling these causal parameters but are nearly impossible to fully remove or require solutions that would be too costly to implement. Thus, an important step required in 2D separations is in pre-processing the raw data such that corrections can be applied numerically. These steps can include signal intensity scaling, reduction of random noise and the removal of shifts in the baseline or peak migration times.[185] However, these pre-processing steps can sabotage data quality when methods are indiscriminately applied, especially if numerous methods are applied in combination.[182] This can lead to unwanted alterations in the data, overfitting the trained model and spurious interpretation of results from chemometric analysis.

Correction of migration time shifts is particularly important for 2D separations because they can cause misalignments of ^{1}D peaks that span multiple ^{2}D separations. These misalignments can cause a single peak to appear as two peaks or cause a given analyte to occupy different positions in the 2D separation space between samples making them incomparable. Correlation optimized warping (COW) is a popular method to align data is based on the correlation between a sample signal and a target (or reference) signal which acts as an alignment template (Figure 9).[186]
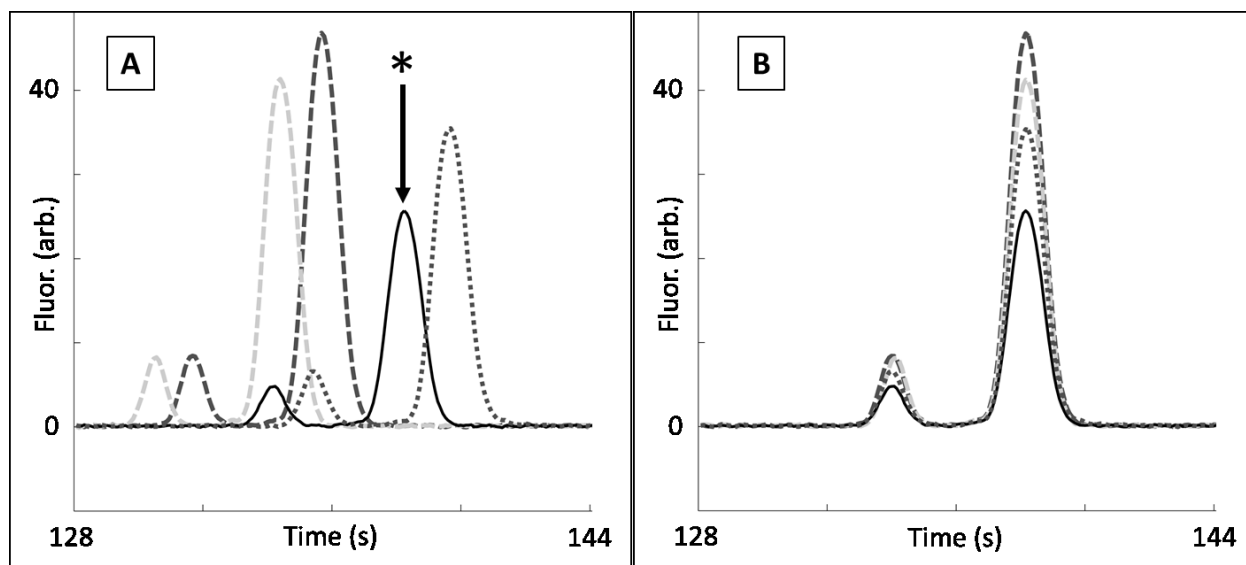
Figure 9 Example of time alignment to a target separation profile. Four poorly aligned separation profiles in are overlaid on the same plot (A). The solid-lined profile was chosen as the target (reference) profile (*). Alignment of the other three separation profiles to the target was automated using a correlation optimized warping algorithm, which resulted in good agreement of the peak locations between each of the separations (B).

Briefly, the steps performed in COW begin with the segmentation of both the sample and target separation windows equivalently into an arbitrary number of sections. Each sample section is iteratively stretched and compressed (warped) with each iteration being compared to the target section. A Pearson's correlation coefficient is calculated for each pairwise iteration. For that segment, the iteration with the highest correlation to the target is retained for inclusion in the final modified separation profile. The sample separation profile is then rebuilt by replacing each of its original segments with the warping iteration having the highest correlation to its complementary target segment. Optimization of the alignment is achieved by varying the number of data points to include in each segment (segment size) and the number of data points to stretch and compress each segment by (slack parameter).

Particular to the work presented herein, alignment difficulty is increased because eight different capillaries are used in the ^{2}D each with their own separation behaviour. The challenge will be in handling eight data streams that must be interleaved, correctly segmented into separation windows and aligned within a matrix. The alignment algorithm presented in this dissertation will feature a modified COW algorithm.

1.18 Contribution to Original Knowledge

This section will give an overview of the work comprised in this dissertation, with a focus on the novel aspects that contribute to original knowledge within the field.

In Chapter 2, an overview of the CE×CAE instrumental apparatus is accompanied by details on the design, construction and operation of each integral component and supporting instrumentation. A focus is placed on the multidimensional interface and the ^{2}D capillary array detector. A high-throughput capillary sharpening device was constructed to supply the ^{2}D with fresh capillaries and is described. Since the data generated in the ^{2}D is non-conventional, the procedures for chemometric pre-processing and data analysis is discussed. This chapter also covers the experimental parameters, materials and reagents used.

Chapter 3 examines the operation and performance of the ^{2}D capillary array when used as an array of 1D separations, independent of any ^{1}D separation. Experiments characterizing key operating parameters for optimizing sample transfer processes are discussed, such as capillary alignment, flow dynamics in the interface, BGE compatibility, etc. Although multi-capillary sheath flow detector cells have been described in the literature, construction using PDMS is a novel contribution and its characterization is discussed. The cumulative benefit of the aggregate optimizations is demonstrated in the results of a small protein digestate separated on the capillary array in an automated parallel fashion.

Chapter 4 covers the integrated MDS instrument used in an online 2D separation mode. Here, sample injections are performed at the ^{1}D inlet so that the ^{2}D capillary array captures the time-resolved effluent of a ^{1}D separation. The potential sampling rate benefit provided by using a multiplexed ^{2}D is demonstrated by rapidly sampling the effluent across a ^{1}D peak and reconstructing it with high sampling resolution. Estimates of 2D performance are derived from peak statistics gathered from 1D separations performed on the ^{1}D and ^{2}D independently. These estimates are compared to similar separations performed on a commercial CE instrument. The remainder of Chapter 4 is dedicated to evaluating the 2D separation of a model biological sample—the proteolytic digestate of human serum. This is used to assess the separation power of the online instrument and its broader suitability for biological samples. Attention is given to determine the quality of the generated raw data and the level of complexity required to deconvolute the raw data and perform analyses.

Chapter 5 shows the novel flexibility of the instrument design by introducing a modification whereby a second parallel ^{1}D capillary is installed alongside the primary separation capillary. An application of this modification is described, where it is used to introduce a migration time marker to the ^{2}D without interrupting normal operation. Its implications for improving data deconvolution and processing are discussed.

Chapter 6 provides a summary and outlook for this work.

Chapter 2 Instrumental Design, Materials and Methods

2.1 Instrument Overview

Fundamentally, the instrument developed for this thesis is comprised of a single ^{1}D capillary electrophoresis instrument, coupled to an array of capillaries in the ^{2}D arranged in parallel. By momentarily placing each ^{2}D capillary inlet downstream from the ^{1}D outlet, a discrete injection can be made onto the array in sequence. For this mechanism of hyphenation to be achieved, a new laminar flow interface had to be developed to allow precision automated computer manipulation of capillaries while bathed in a continuous flowing buffer stream. In addition to a multiplexed capillary electrophoresis coupling interface, a multi-capillary sheath flow cuvette for fluorescence detection had to be designed.

The underlying CE separation occurs at microfluidic scales (capillary lumen: $10 - 100$ μm) which makes interfacial and electrokinetic phenomena much more significant, enabling phenomena such as EOF. However, the supporting instrumentation was constructed using macroscale devices (motorized stages, supply and waste pathways, ^{1}D instrument, high-voltage electrodes) with masses and spring forces many orders of magnitude larger than that of CE capillaries. The requirement of using macroscale equipment to perform delicate manipulations at microfluidic scales presented unique challenges requiring novel solutions. This chapter will focus largely on the design of two key components of the MDS system: the inter-dimensional interface and the sheath flow cuvette; as well as describe their integration into the instrument as a whole.

Before the details of the designs are presented, an overview of the instrument is provided here to help the reader place all components into context. The ^{1}D consisted of a commercial CE instrument that was modified to allow the separation capillary to exit the chassis and terminate in the ^{1}D to ^{2}D interface, which a was assembled on an adjacent optical breadboard. The interface was held at ground potential. The ^{1}D high-voltage power supply of the commercial CE instrument was used to drive the ^{1}D separation. The inlets to the ^{2}D capillary array were mounted in the interface, and the outlets were placed in the multi-capillary sheath flow cuvette. To perform injections the entire interface was placed on a stepper-motor controlled translation stage with two axes of motion in the horizontal plane. An argon-ion laser mounted to the optical breadboard illuminated the region below the row of ^{2}D capillary outlets. A CCD camera and fluorescence filter allowed fluorescence

imaging of the ^{2}D capillary effluent. A second, high-current, high-voltage power supply was used to drive the ^{2}D separation. This power supply used the interface as its ground and applied the high voltage to the sheath flow cuvette. For operator protection, a polycarbonate sliding door with an interlock to terminate power across the ^{2}D was installed. The interface, 2D capillary array, 2nd HV power supply and detection camera are shown schematically (Figure 10, Figure 11).
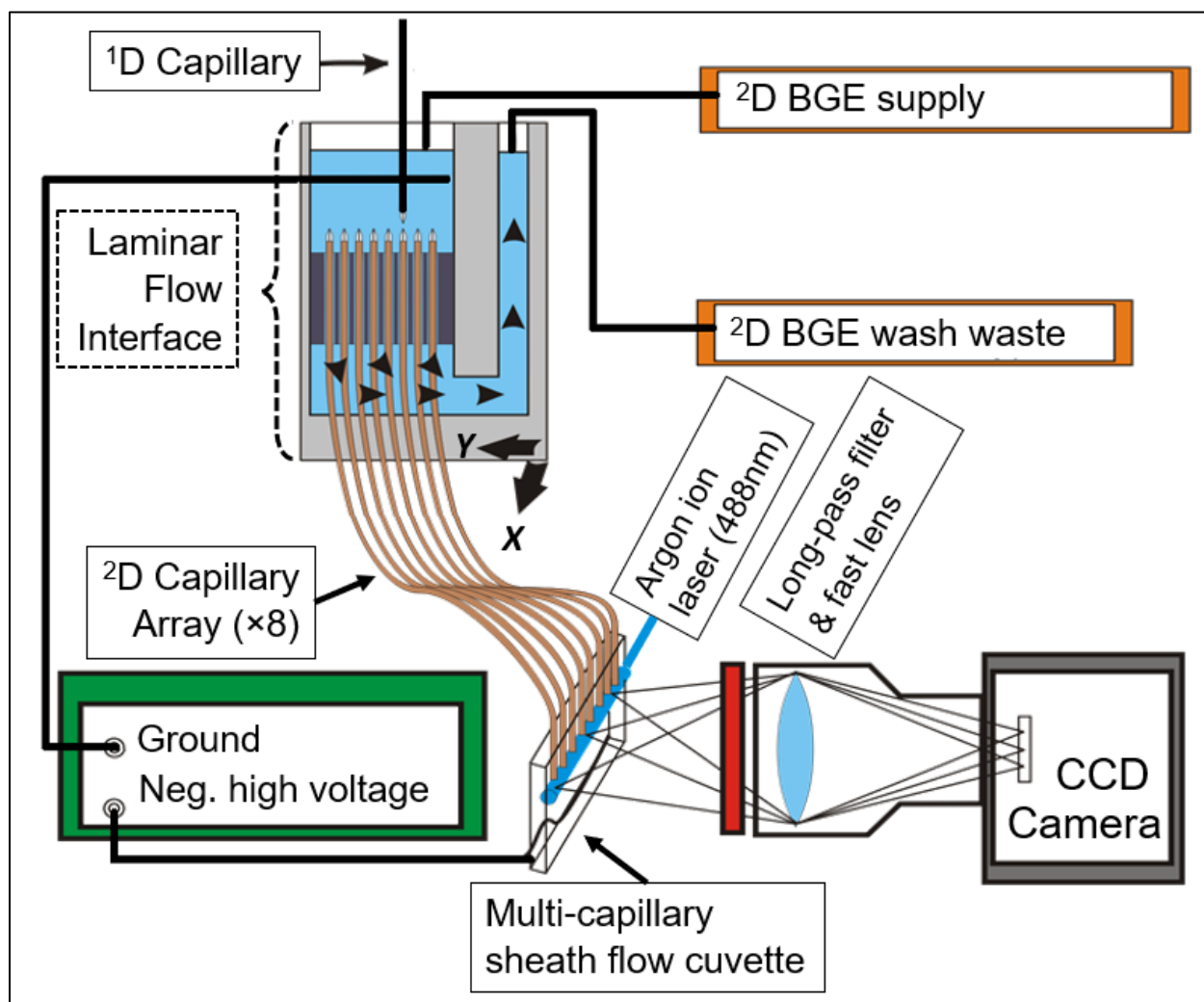
Figure 10 Schematic of the two-dimensional CE×CAE apparatus. Effluent from the ^{1}D capillary enters the laminar flow interface from above. The interface (8.89 cm × 6.35 cm × 1.27 cm, W×H×D) , mounted to a motor driven X-Y translation stage, positioned ^{2}D capillaries under the ^{1}D effluent to transfer sample for further ^{2}D separation. Detection of fluorescently labelled proteins/peptides is performed in the multi-capillary sheath flow cuvette (25.4 mm × 63.5 mm × 8.89 mm, W×H×D), where sample is excited via a common 488 nm Ar-ion laser beam, emission filtered through a long-pass filter and collected using a CCD camera. A constant flow of fresh BGE through the interface and out to waste provides the laminar flow required for efficient sample transfer. Driving the electrokinetically mediated capillary array separation is a single high-voltage power supply whose ground is shared with the ^{1}D sepration insrument (not depicted).
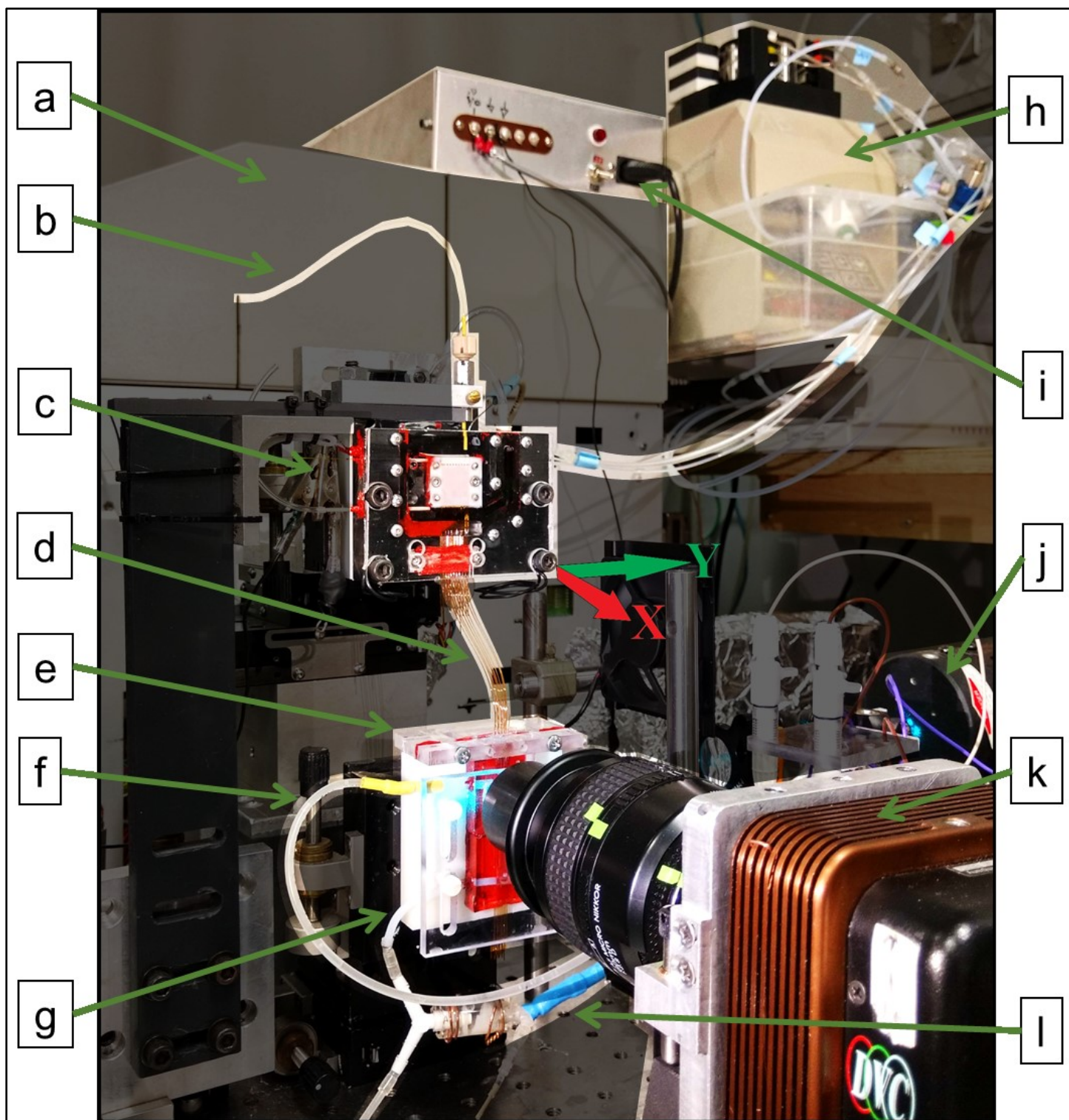
Figure 11 Photo of the two-dimensional CE×CAE instrument. Non-critical components are partially masked for clarity. (a) modified HP 3D CE instrument, (b) ^{1}D capillary, (c) capillary array interface, (d) ^{2}D capillary array, (e) multi-capillary sheath flow cuvette, (f) sheath flow cuvette supply line, (g) sheath flow cuvette waste line, (h) peristaltic pump for interface BGE supply and waste, (i) high-voltage relay, (j) argon-ion laser, (k) CCD camera with c-mount lens, (l) ^{2}D high-voltage lead. The X-Y coordinate arrows show the two degrees of freedom in motion. Not shown are (1) the two computers used to operate the various programs required to operate the instrument and (2) the ^{2}D high-voltage power supply (underneath the optical breadboard).

2.1.1 Note on Electronic Noise Minimization

The overall circuit design utilized a star ground to minimize electromagnetic interference which is especially common when digital and analog signals are mixed together in an instrument. A star ground is simply a single point to which every reference ground electrode, contained within any component of an instrument, is attached. The star ground was prepared by placing the bundle of reference ground wires under a metal washer and compressing them with a screw that was inserted into the optical breadboard upon which the instrument was built. Within the wire bundle was a master ground wire that was directly attached to earth ground via a nearby electrical outlet.

2.1.2 First Dimension Apparatus

The first dimension was operated using a modified Hewlett Packard HP 3D-CE (Agilent Technologies, Santa Clara, CA, USA). The outlet (right side) of the capillary cartridge and instrument lid were modified by drilling (1.6 mm dia.) holes, approximately 40 mm above the bottom-right edge of the cartridge and 40 mm above the bottom-right edge of the lid. The capillary inlet was installed as normal, with the outlet threaded through both holes (Figure 11, b) and extended to an adjacent optical table (Newport Corporation, Irvine, CA, USA). An insulated wire was attached to the HP 3D-CE, grounded, outlet electrode, threaded through a second hole in the right side of the chassis and attached to a 10 kΩ resistor and terminated at an electrode in the interface. The voltage drop across the resistor was used for ^{1}D current monitoring. Control of the HP 3D-CE instrument was performed using the included ChemStation software on a Windows XP computer. Instrument ground was connected to the star ground.

A Kilovac H-24 high-voltage relay (TE Connectivity Ltd, Berwyn, IL, USA) was placed in series with the CE instrument HV power supply and the capillary inlet electrode. This was assembled in an aluminum chassis with a power supply and amplifier circuit to energize the relay solenoid. Switching control was performed using a data acquisition (DAQ) module under in-house written software control. The instrument chassis, relay box cover and ground circuit were connected to the star ground.

2.1.2.1 Holder for ^{1}D Capillary Outlet

The ^{1}D capillary outlet was suspended above the ^{2}D capillaries in the MDS interface using an arm mounted to a micrometer equipped manual 3-axis translation stage on the optical table. The micrometer was used to initially set the position of the ^{1}D capillary outlet, which was used as the

reference zero-point along each axis for the rest of the system. The [1]D outlet was fixed firmly in this position during a given single separation.
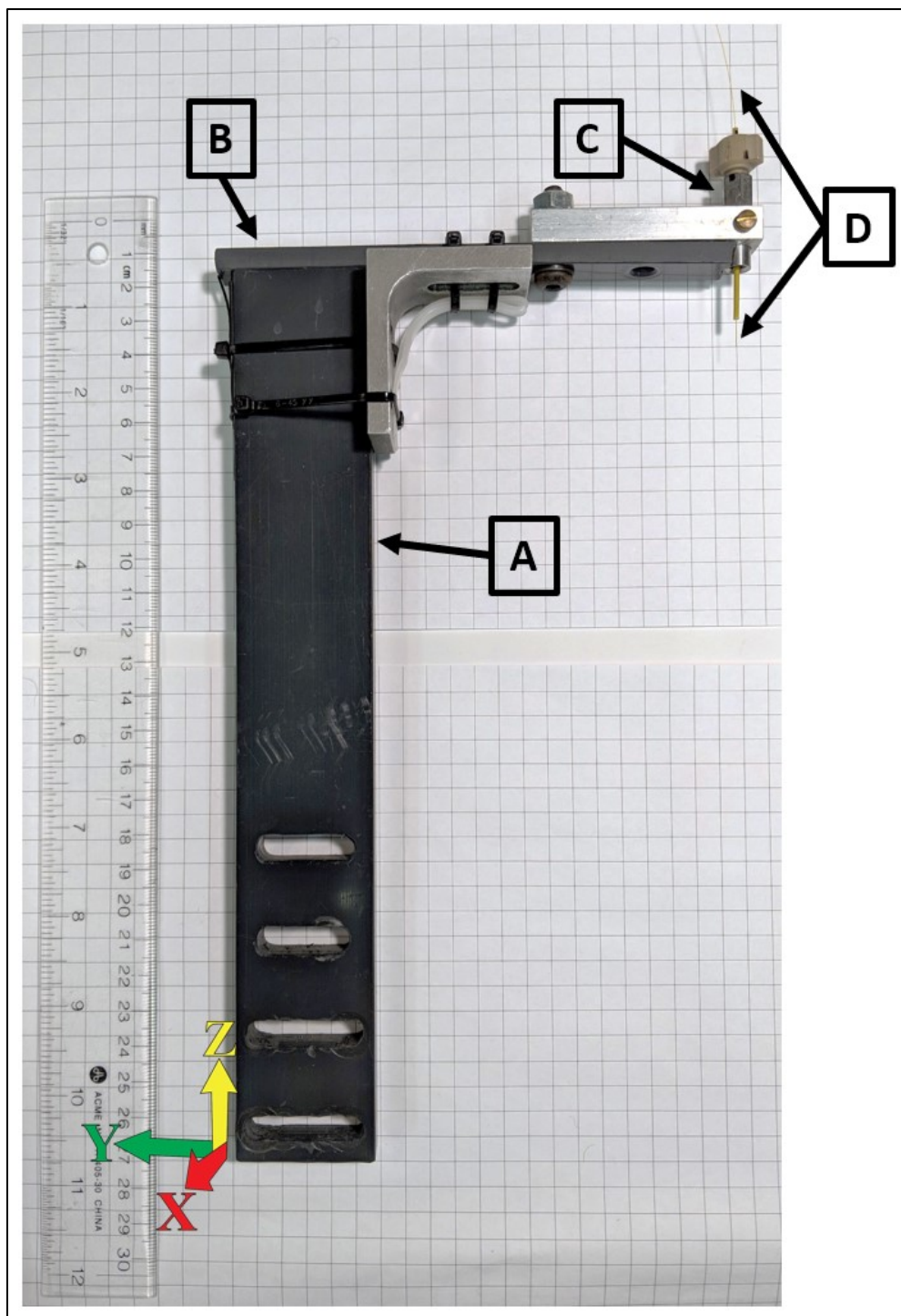
Figure 12 Support arm for [1]D capillary. The main PVC post (A) stands vertically on the optical table while mounted at its base to a 3-D translation stage. The PVC crossbar (B) had an aluminum riser fastened to the distal end, where a modified HPLC union (C) was installed in a vertical hole. Nested within the union was a finger tight fitting, a 1/16" o.d. PEEK tube and the [1]D separation capillary (D). The overlaid 3-D coordinate system depicts the freedom of motion provided when mounted to the 3-D translation stage.

As shown in Figure 12 the PVC arm was made from three main parts. Part A was a 1.5" × 10" × ⅜" (W×H×D) rectangular PVC post with four horizontal slots at its base used to mount it to a 3-axis translation stage. Part B, a 5" × ⅜" × ½" (W×H×D) crossbar, was screwed into the top of the column, such that its bottom face could be placed above the MDS interface. An aluminum brace was fastened to the distal end of the crossbar to increase stiffness. Part C consisted of a stainless-steel union designed for 1/16" tubing that was machined so its exterior was cylindrical over the bottom half of its length. The union was installed in a vertical hole in the crossbar. The union ensheathed a threaded PEEK finger-tight fitting, which ensheathed a straightened 3 cm length of 1/16" o.d. PEEK tube which finally ensheathed the ^{1}D capillary. The ^{1}D capillary (Part D), threaded through the PEEK tubing, extended downward to place its outlet in the liquid at the inlet of the interface. The ^{1}D capillary was fixed in place by tightening the finger-tight fitting. Fine adjustment of the capillary tip position was performed using the micrometers of the 3-axis translation stage at the capillary holder base.

The PEEK tubing used had either a 0.25 mm or 0.40 mm i.d. for use with 180 μm or 365 μm o.d. capillaries, respectively. Additionally, a 1.6" long Teflon FEP dual-lumen sleeve (Part # F-235, Upchurch, now IDEX Health & Science LLC, Oak Harbor, WA, USA) was used in some experiments to direct two ^{1}D capillaries to the interface. In these experiments, the second capillary was attached to a syringe mounted in a Harvard Apparatus Model 33 twin syringe pump (Instech Laboratories, Inc., Plymouth Meeting, PA, USA).

2.1.3 Support Apparatus for the Multidimensional Interface

2.1.3.1 Interface BGE Supply and Waste

Early versions of the BGE supply for the interface were assembled using a modified domestic pressure cooker. A gas fitting was mounted to the pressure cooker lid, to supply regulated air (1 – 2 bar) from the building air supply lines. Two bulkhead fittings were mounted on the side to seal/pass 1/16" or 1/8" o.d. tubing. Two collapsible 1 L low density polyethylene sample containers (I-CHEM Cubitainer #314-1000, ThermoFisher Scientific, Burlington, ON, Canada) were placed inside connected to the two bulkhead fittings using 1/8" o.d. PTFE tubing inserted into their caps via additional bulkhead fittings. These sample containers were used to hold BGE or water. PEEK tubing with various i.d. and lengths was used as flow restrictors and bridged the outer bulkhead fittings to downstream tubing. Flow rates were calibrated gravimetrically when needed. Vacuum

aspiration was used to draw off waste from the interface outlet via a tube connected to a nearby sink faucet.

Later, a Gilson Minipuls 3 Model 312 multichannel peristaltic pump (Gilson Inc., WI, USA) was used to supply fresh BGE to the interface as well as draw off waste, each using one channel. The supply (inlet) tubing was chosen to have a larger diameter than the waste (outlet) tubing. This caused the peristaltic pump to supply the interface inlet with BGE at a faster rate than it was removed at the outlet to waste. To avoid BGE overflow from the interface, excess BGE was drawn off by vacuum aspiration via a narrow tube placed at the interface inlet at the desired meniscus height. Since the interface inlet had a constant oversupply of BGE, the flow rate through the interface was set by the outlet tubing connected to the peristaltic pump.

In both configurations, a Series 1100 G1322A in-line vacuum degasser (HP, now Agilent, Santa Clara, CA, USA) was used to ensure bubble free BGE and water were delivered to the interface. In the first configuration, the BGE tubing path began at the pressure chamber, then the vacuum degasser and terminated at the interface. In the second configuration, the BGE started at the reservoirs, entered the vacuum degasser, the peristaltic pump and terminated at the interface.

2.1.3.2 Optical Apparatus

Fluorescence imaging of the interface was enabled by fiber optic guided laser illumination and a CCD camera. This allowed the fluorescence imaging of flow patterns within the interface as well as the detection of fluorescence signal from the [1]D capillary effluent. An Osram PLTB450 450 nm (nominal) diode laser with 1.4 W maximum output (DTR Laser Shop, Creve Coeur, MO, USA) was installed in a TCLDM9 laser diode mount and operated using a ICT 4005 controller; purchased from Thorlabs (Newton, NJ, US). The diode was kept at a nominal 10 °C by a Peltier cooling device that was controlled by the laser controller. The light was focused, using an aspheric lens (C240TMEA, 8.0 mm focal length, 0.5 NA), onto the end of a fiber optic. The 400 μm o.d., 4 m length fiber optic (Polymicro Technologies, Phoenix, AZ, USA) was prepared with ends that were square cut and polished (600 grit silicone carbide followed by 0.5 μm chromium oxide sandpaper from Lee Valley Tools, Ottawa, ON, Canada). The far end of the fiber was inserted into the interface and immersed with the cone of light aimed at the closest [2]D capillary inlet with the capillary tip near the center of the cone.

A colour CCD camera (GRAS-14S5C-C, Point Grey, BC, Canada) with a Navitar Zoom 7000 (#58-240, Edmund Optics, Barrington, NJ, USA) lens and a longpass filter (515EFLP EM XF18.19 502 9711) was used for image capture. Data was transferred via a Firewire 800 PCI card and the camera was controlled using the Point Grey FlyCap2 image capture software. This camera was used for alignment of capillaries within the interface as well as signal capture of ^{1}D effluent. For electropherogram data, the video was imported into Matlab (The MathWorks Inc., Natick, MA, USA) and pixel intensities were summed over a region of interest to create the signal column vector.

2.1.4 Second Dimension Apparatus

2.1.4.1 High Voltage Power Supply

Power was supplied to the ^{2}D capillary array using a Bertan 210-30R high-voltage power supply (Spellman, Valhalla, NY, USA). Both control and monitoring were performed remotely via connection to a DAQ module under software control, with wiring routed through a locally constructed breakout box before it reached the DAQ module. The wiring also included an interlock switch on the control circuit that was engaged when the safety door was closed fully and secured by a magnet to hold the door against the switch. The HV circuitry ground was connected to the star ground.

2.1.5 Support Apparatus for the Sheath Flow Cuvette

2.1.5.1 Optical Arrangement and Signal Collection

A 488-nm single line argon-ion laser (JDS Uniphase, Milpitas, CA, USA) was used throughout experiments for ^{2}D sheath flow cuvette excitation at minimum idle power (4 mW) except where otherwise noted. An achromatic lens (MG 01LA028, 80 mm focal length) was used to focus the laser so the waist of the beam was centered on the 2D array and passed about 10 – 30 μm below the capillary outlets.

A LabView controlled 12-bit monochrome CCD camera (DVC-1312M, DVC Company, Austin, TX, USA; now ThorLabs, Newton, NJ, USA) was used to image the sheath flow cuvette through a c-mount Nikon macro lens (Micro-Nikkor 105 mm f/2.8D, Mississauga, ON, Canada) and a long-pass filter (515EFLP EM XF18.19 502 9711). An IMAQ PCI-1422 (National Instruments, Vaudreuil-Dorion, QC, Canada) was used for fast image retrieval from the CCD camera while

under in-house prepared LabView (National Instruments, Vaudreuil-Dorion, QC, Canada) control software. The camera was fixed to a gimballed mount that allowed fine adjustment to ensure the camera assembly was parallel to the window of the sheath flow cuvette and perpendicular to the laser path. Fluorescence emission was collected at 12 frames-per-second (fps) across the ≈400 μm vertical distance below the ^{2}D capillary outlets. This utilized a region-of-interest (ROI) comprising 1000 × 60 (W×H) pixels, maximizing the number of horizontal pixels used on the CCD sensor, which was subdivided horizontally into eight 125 × 60 (W×H) pixel regions; one for each capillary. The pixel intensities in each subsection were summed to produce columns vectors in a matrix, with each column representing concatenated separation windows for their respective capillaries. Two additional columns in the data matrix were used to store timestamps for each data sample and to log dropped frames in the data file.

2.1.5.2 BGE delivery to the sheath flow cuvette

Gravity flow was used to provide BGE flow that ensheathed the ^{2}D capillary outlets within the detector cell. Two Corning 175cm² polypropylene angled neck cell culture flasks (Product # 431080, Corning, NY, USA) were modified by drilling 1/16" diameter holes through the cap and threading a 1/16" o.d. tube whose end was immersed below the meniscus of the BGE (or waste). Each culture flask was placed on a small support jack to offset their heights which produced the hydrodynamic head enabling siphon flow through the BGE path. Both small jack assemblies were placed on a large support jack to set the aggregate hydrodynamic pressure of the two reservoirs. This midpoint pressure was placed at the same height as the meniscus of the multidimensional interface, to minimize siphoning through the ^{2}D capillaries. Most tubing connections used for the BGE supply and waste path used 1/8" PTFE tubing to minimize resistance to flow. Where 1/16" tubing was required, the 1/8" tubing was adapted by nesting multiple sizes of flexible Tygon tubing such that they would couple the disparate PTFE tubing sizes. Two 6 cm lengths of 1/8" o.d. PTFE tube were inserted into 1/8" holes moulded into the sheath flow cuvette, one at the top to supply BGE and one at the bottom for waste.

2.1.6 **Additional Instrument Control and Monitoring**

2.1.6.1 Data Acquisition Module

Multiple peripheral components were controlled and monitored using a 14-bit USB-30 data acquisition module (DAQ) (EagleDAQ, Cape Town, South Africa). These included the ^{1}D

high-voltage relay, the ^{2}D high-voltage power supply and each of the digital and analog signals from the DAQ module. Since high voltages and significant currents were being used, and switched, each line in these DAQ circuits was connected to ground through a transient-voltage-suppression (TVS) diode for electrical isolation and protection in the event of excessive voltages (typically 12 V breakdown). Shielded wiring was used throughout except for grounding wires that led back to the star ground.

In order to programmatically switch the ^{1}D high-voltage relay, one of the digital TTL outputs on the DAQ module was used to send a low or high signal to the breakout box containing the high-voltage relay. This relay unit used the 5V digital signal to drive a low voltage relay which in turn delivered 23.3 V to the relay coil to actuate the high-voltage relay. The high-voltage relay was inserted in the HV circuit between the HP 3D-CE high-voltage power supply and the inlet vial electrode.

The output of the ^{2}D high-voltage power supply was set using an analog output (0 – 5 V) of the DAQ module to control 0 – 30 kV output. An interlock switch, in series with the analog control wire, allowed the control voltage to reach the high-voltage power supply only when a polycarbonate door was closed to prevent physical access to the high voltage sections of the optical table. When closed, the switch also enabled a flashing LED to be powered to alert the user to the presence of high voltages. When the switch was opened, a pull-down resistor ensured the HV power supply input was brought to zero.

Voltage and current, from the ^{2}D high-voltage power supply, were recorded using two of the analog inputs on the DAQ module using bipolar differential mode sampling at 2 kHz and storing averaged data at 10 samples/s. The LabView control software also contained a failsafe to terminate upon abnormally high current loads being detected (~300 μA).

2.1.7 Reagents and Materials

Except where noted, all stock solutions were prepared from analytical grade reagents or better. Sodium tetraborate decahydrate, sodium acetate, Nile Blue A, Coomassie brilliant blue G, fluorescein free acid, sodium hydroxide (reagent grade), bovine serum albumin (BSA) and β-casein were purchased from Sigma-Aldrich. Other reagents used included: formic acid, sodium dodecyl sulfate (Schwarz/Mann Biotech), glacial acetic acid (Fisher Scientific), ammonium

formate (Fluka), sodium formate (reagent grade, Fisher Scientific) and fluorescein 5-and-6 sulfonic acid (Invitrogen). Human serum experiments were performed using I.D.-ZONE Normal Protein Electrophoresis Control, REF 667600, LOT M604191 (Beckman Coulter, Fullerton, CA, USA).

2.1.7.1 Reagent Preparation and Labelling

All buffers and samples were prepared using distilled, deionized and filtered water from a Barnstead EASYpure II D7401 system (ThermoFisher Scientific, Burlington, ON, Canada) that was further filtered through 0.45 μm cellulose membrane filters or PTFE syringe filters. Sample stock solutions were filtered through PTFE syringe filters, nylon syringeless filters, or MW cut-off filters before aliquoting and storage. Molecular weight cut-off filters and cellulose membrane filters from Millipore Canada Ltd. (Etobicoke, ON, Canada) included 0.5mL Amicon Ultra Ultracel 3K and 10K centrifugal filters, 0.5mL Biomax 30K Ultrafree centrifugal filters and HAWG04705 cellulose membrane filters. Acrodisc CR 0.45 μm PTFE syringe filters were from Pall Canada Ltd. (St. Laurent, QC, Canada). Mini-UniPrep 0.2 μm nylon syringeless filters were from Whatman Inc. (Florham Park, NJ, USA).

Sodium acetate (20 mM, pH 5.75) and sodium formate (20 mM, pH 2.75) buffers for ^{1}D peptide separations were prepared by dissolving the appropriate quantities of their respective sodium salts and acid in 50 mL volumetric flasks to produce 1M stock solutions. These were filtered and transferred to 50 mL centrifuge tubes for storage. BGE, for daily use, was prepared by mixing the appropriate volumes of acid and conjugate base to produce the desired pH in a fresh 50 mL centrifuge tube, followed by dilution with water to the desired working concentration which was determined gravimetrically.

Sodium tetraborate buffer for ^{2}D peptide separations was prepared by dissolving the appropriate quantities of buffer salts to produce 20 mM borate, 5 mM SDS in a 2 L beaker to approximately 2/3 of the final volume in water. The pH was adjusted by dropwise addition of a 1 M NaOH or 1 M HCl until a pH of 9.2 was reached. The solution was transferred to a 2 L volumetric flask where the dilution was completed and subsequently filtered.

Fluorescent labelling of protein and peptides was carried out using the fluorogenic derivatizing agent 3-(2-Furoyl)quinoline-2-carboxaldehyde (FQ) obtained from Life Technologies (Eugene,

OR, USA). Because this reagent is moisture sensitive, it was prepared and then stored lyophilized. The stock powder was dissolved in ethanol to a concentration of 10 mM and transferred to 200 μL polypropylene PCR vials at the appropriate volumes for 50 nmol, 100 nmol and 200 nmol quantities. These aliquots were lyophilized and stored at -80 °C.

Fluorescent labeling with FQ was used as per manufacturer protocols with the following modifications. Dried FQ was resuspended using 5 μL of ethanol and buffered using pH 9.2 borate at 25 mM. Adequate buffered protein solution was added to achieve an FQ-to-protein molar ratio of 25:1. Upon mixing, the vial was placed in a 65 °C water bath for 15 minutes, followed by immediate dilution to the desired concentration with cold water and placement on ice until used.

Protein stock solutions were prepared by dissolving lyophilized protein in water, passing it through a non-syringe filter, dilution to the desired concentration and aliquoting in 10 μL portions which were stored at -80 °C. The human serum was obtained from the manufacturer as a 60 g/L (total protein) solution, which was aliquoted in 10 μL portions and stored at -80 °C. Frozen aliquots of protein and serum solutions were thawed in an ice bath immediately before use.

2.1.7.2 Capillary preparation

For the [1]D, approximately 73 cm of 100 μm i.d. × 180 μm o.d. fused silica capillary was cleaved from a stock spool. The capillary ends were squared off, as needed, using 1500 grit silicon carbide (SiC) sandpaper. New capillaries were rinsed with 100 mM NaOH for 30 minutes prior to use. All capillaries were purchased from Polymicro Technologies (Phoenix, AZ, USA).

Capillaries for the [2]D were prepared using 50 μm i.d. × 363 μm o.d. fused silica capillary cut to 145.0 ± 0.5 mm. Due to their larger o.d., these capillaries were shaped (Figure 13) to improve flow characteristics at the lumen openings. This is particularly important for detection since eddies can form at sharp interfaces causing laminar flow to be lost. This can introduce significant mixing which broadens peak shape of the analytes in the exiting effluent. Thus, the outlet ends of the capillaries were sanded sequentially using 400, 600 and 1500 grit SiC sandpapers, followed by polishing with 0.5 μm Cr_2O_3 abrasive sheet. Shaping was performed manually or mechanically. Manual shaping was performed by drawing the capillary across the sandpaper using a pull stroke, while simultaneously rotating it about the capillary axis to ensure systematic material removal. Typically, the inlet ends were tapered to shallow cones with a length of $\approx 100 - 150$ μm, whereas

the outlet ends were tapered to about $\approx$1.0 – 1.1 mm (Figure 13). All capillaries in a set were prepared such that the range of lengths was within 0.5 mm. Lastly, the first $\approx$2 mm of polyimide at the inlet was burned off with a heated wire in order to have an unobstructed view of sample entering the capillary during injection.
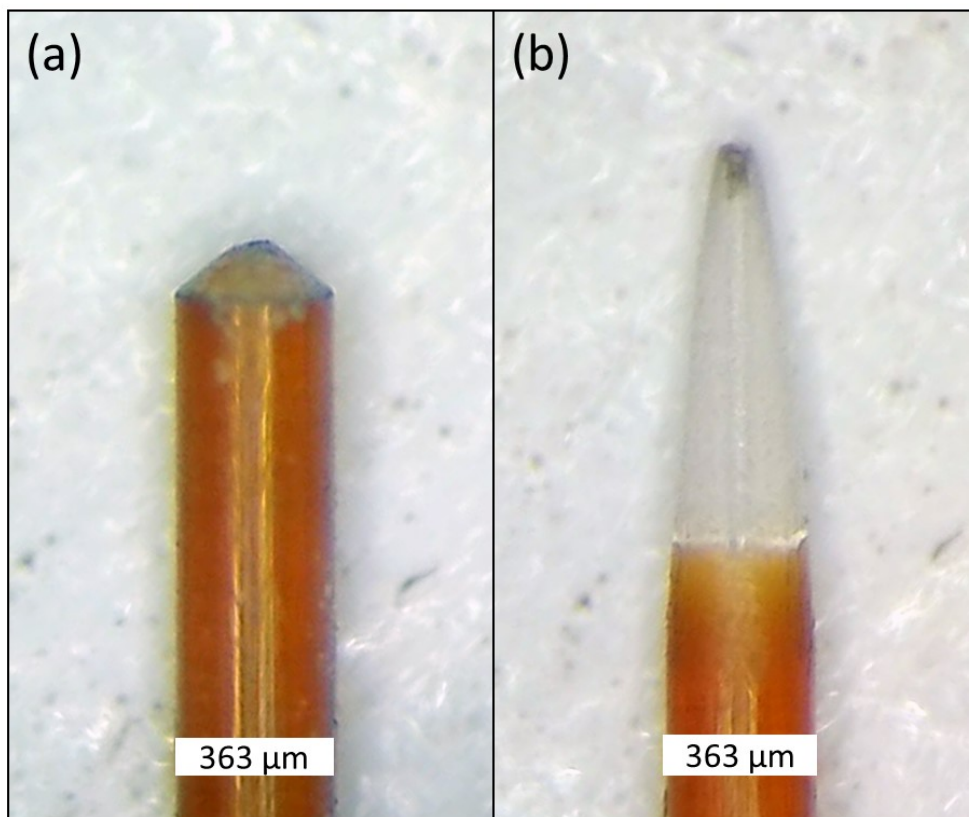
Figure 13 Images of tip shapes produced during fabrication of ^{2}D capillaries. The inlet ends (a) were tapered over a length of 100 – 150 µm. The outlet ends (b) were tapered over a length of 1.0 – 1.1 mm. Stock fused silica capillary dimensions: 50 µm i.d., 363 µm o.d..

Mechanically assisted shaping was performed using sandpaper discs, approximately 12 cm diameter mounted on an aluminium disc attached to a DC motor. An aluminum block with a hole drilled through it was suspended above the sandpaper at an angle to act as a bushing for a capillary holder prepared from a straight length of 1/16" HPLC tubing (Figure 14).
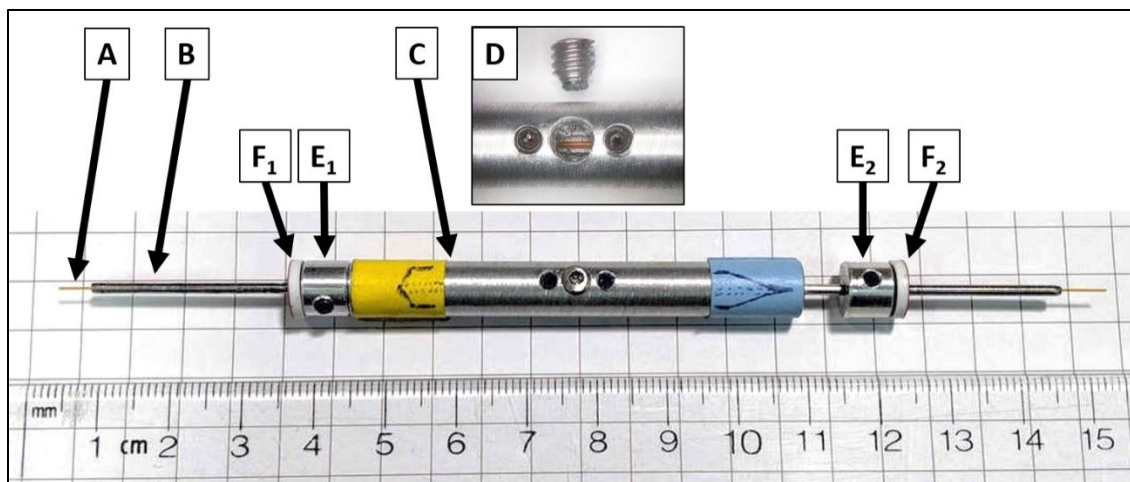
Figure 14 Image of the capillary holder used during motorized capillary tip fabrication. The capillary was (A) threaded through an HPLC tube (B) with a notch removed at its center, which was reinforced by an aluminum sleeve (C). The capillary was held in place using a nylon tipped set screw (D). Two aluminum sleeves (E_1, E_2), placed on either side of the reinforcing sleeve, acted as stops when used with a sanding guide (not shown). PTFE lined septa were placed at the ends to reduce friction when in contact with the guide.

The capillary holder had a 3 mm notch removed near its center, exposing the inner lumen. Three 1/16" i.d. × 5/16" o.d. aluminum sleeves were prepared by the university machine shop, with set screws to hold each in place after sliding them over the capillary holder; one 6 cm sleeve and two 6 mm sleeves. The 6 cm sleeve (Figure 14 C) was placed over center of HPLC tubing (Figure 14 B) to reinforce the notch. A tapped hole in this outer sleeve was aligned with the notch. This allowed a nylon tipped set screw to be tightened against the inserted capillary to prevent it from moving during fabrication (Figure 14 D). The 1 cm sleeves (Figure 14 E_1, E_2) were placed near the ends of the holder to act as stops when the capillary holder was inserted into a bushing block (Figure 15). PTFE lined septa (Figure 14 F_1, F_2), from HPLC vial screw caps with centered 1/16" holes, were placed adjacent to each of the 6 mm stops to reduce friction when pressed against the bushing block.
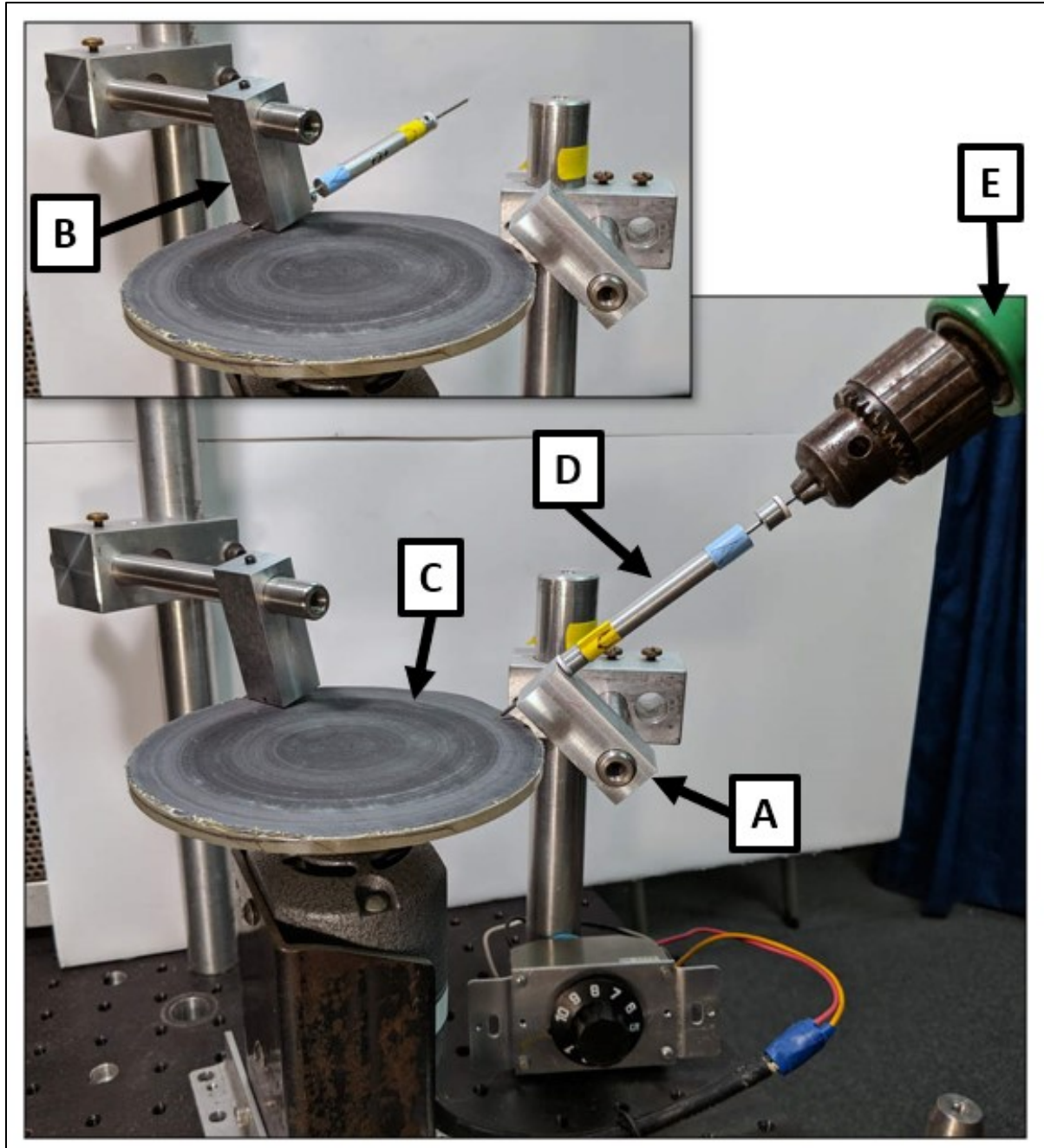
Figure 15 Images of the apparatus used for capillary tip fabrication. Two aluminum blocks with 1/16" holes drilled through them (A, B) were suspended near the motorized sanding disc (C). The capillary holder (D) was rotated using a hand drill (E). The aluminum blocks acted as guides for setting the capillary contact angle and length as it interacted with the sanding surface, as well as acting as a bushing while the capillary holder was rotated in the drill chuck.

Each stop on the capillary holder was paired with a bushing block. These stop/bushing block pairs determined the angle that the capillary was in contact with a nearby spinning sandpaper disc (Figure 15 C). The capillary holder was also rotated at low speed by mounting it in the jaws of a

hand drill (Figure 15 E). Using one bushing block for each capillary end, the rotating capillary was sanded against the spinning sandpaper disc until the end of the capillary no longer made contact.

Due to the large amount of sanding required to achieve reproducible ^{2}D capillary lengths, particulate routinely created blockages or contamination of the capillary lumen. To prevent these issues, the capillary was filled with 100 mM NaOH prior to fabrication and flushed with the same solution after each sanding step.

2.1.7.3 Optical Detector Cell Material

The ^{2}D sheath flow cuvette detector cell was primarily fabricated using polydimethyl siloxane (PDMS), a two-component polymer (Sylgard 184, Dow Corning, Montreal, PQ, Canada). PDMS is commonly used to cast microfluidic components due to its advantageous properties of being optically clear at visible wavelengths and faithfully conforming to moulds with micron-sized features. In addition to the sheath flow cuvette, sections of the MDS interface was also cast using PDMS. PDMS was prepared as per manufacturers instructions with one modification. A 1:10 w/w ratio of crosslinker-to-monomer was used in lieu of a 1:10 v/v ratio. Other supports used in the casting mould included standard 3" × 1" glass microscope slides and Trilene Big Game 12 lb test weight green fishing line (Berkley, Columbia, USA) with a 0.034 mm nominal diameter was used to cast individual capillary channels within the sheath flow cuvette. Schematics and specific details are given in Section 2.3.1.

2.2 Multidimensional Separations Interface Design and Fabrication

The key challenge in making reproducible injections between capillaries relies on two key factors: aligning the ^{1}D lumen outlet with the ^{2}D lumen inlet and washing the ^{2}D capillary immediately prior to, and after, the injection with the surrounding BGE. With capillary lumen dimensions on the order of tens of microns the instrumentation must provide precise, reproducible and quick alignment of the capillaries in three dimensions. The MDS interface must also provide effective wash flows to insure transfer from one dimension to the other and rapid clearing of sample from the ^{2}D capillary tip. These criteria dictate that movement must be rapid (100's of μm/s) while resolution and reproducibility must be on the tens of microns.

Much of the design of the MDS interface parts was first modeled in SolidWorks 2015 (Dassault Systems SOLIDWORKS Corp., Waltham, MA, USA), a 3D computer-aided design (CAD) and

computer-aided engineering program. These designs were manufactured using milling as a subtractive manufacturing technique in-house by machine shop staff using a mixture of manual processes and numerically controlled (CNC) equipment.

2.2.1 Capillary Array Holder 'Chip'

Since, as described above, the [1]D capillary was fixed and hanging downwards. The [2]D capillary array inlets were pointing upwards, held in position using an in-house built 'chip' device made from three sheets of plastic; a 1/8" white acetal sheet for the rear, a 1/16" clear acrylic sheet for the front window and a 0.25 mm white Hytrel film in the middle. The capillaries were sandwiched between the middle Hytrel sheet and the rear acetal sheet (Figure 16).
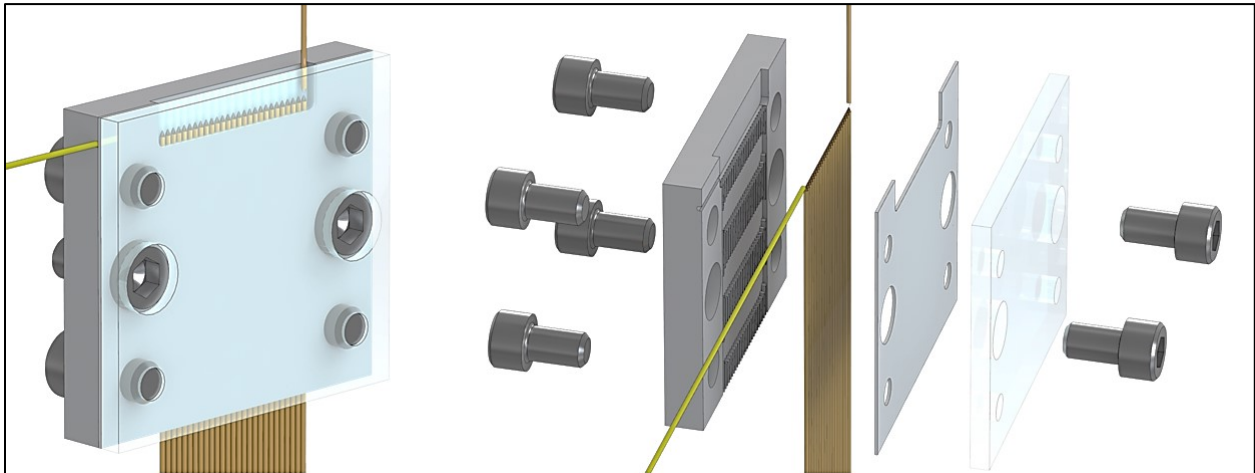
Figure 16 Isometric view and exploded view of the 27-channel CE×CAE interface chip assembly, comprised of three layers. In this work, eight channels held separation capillaries while the remaining channels held plugged dummy capillaries. The rear acetal plastic sheet was machined with channels to hold each capillary in place, along with a cut out at the top to allow the [1]D capillary entering the chip from above to have clearance to move behind the [2]D capillaries. A middle sheet of Hytrel plastic with a matching cut out provided clearance in front of the [2]D capillaries. The front acrylic plastic sheet acted as an enclosing wall and fluorescence emission window. The assembly was held together using screws on the corners entering from the rear. The middle screws entering from the front were used to mount the chip in a larger manifold. A fiber optic entering from the left acted as a light guide for a nearby laser excitation source.

Features were machined on the inside face of the rear 25 mm × 22 mm × 9.525 mm (W×H×D) acetal sheet by the machine shop staff at Concordia University (Montreal, Canada). At the top edge a center aligned shelf was cut with dimensions of 11 mm × 2 mm × 0.615 mm (W×H×D) using a 1 mm diameter square end mill (Harvey Tool, Rowley, MA, USA) (Figure 17 a). Three horizontal cuts were made across the vertical centerline using a 1/8" square end mill, producing shallow slotted holes with the dimensions 13.175 mm × 3.174 mm × 0.365 mm (W×H×D) (Figure 17 b). These were vertically spaced 6 mm apart between horizontal centers. The first cut was centered

6.25 mm from the top edge of the chip. An earlier prototype omitted these three slots, which were later deemed a requirement for uniform flow across the capillary array.
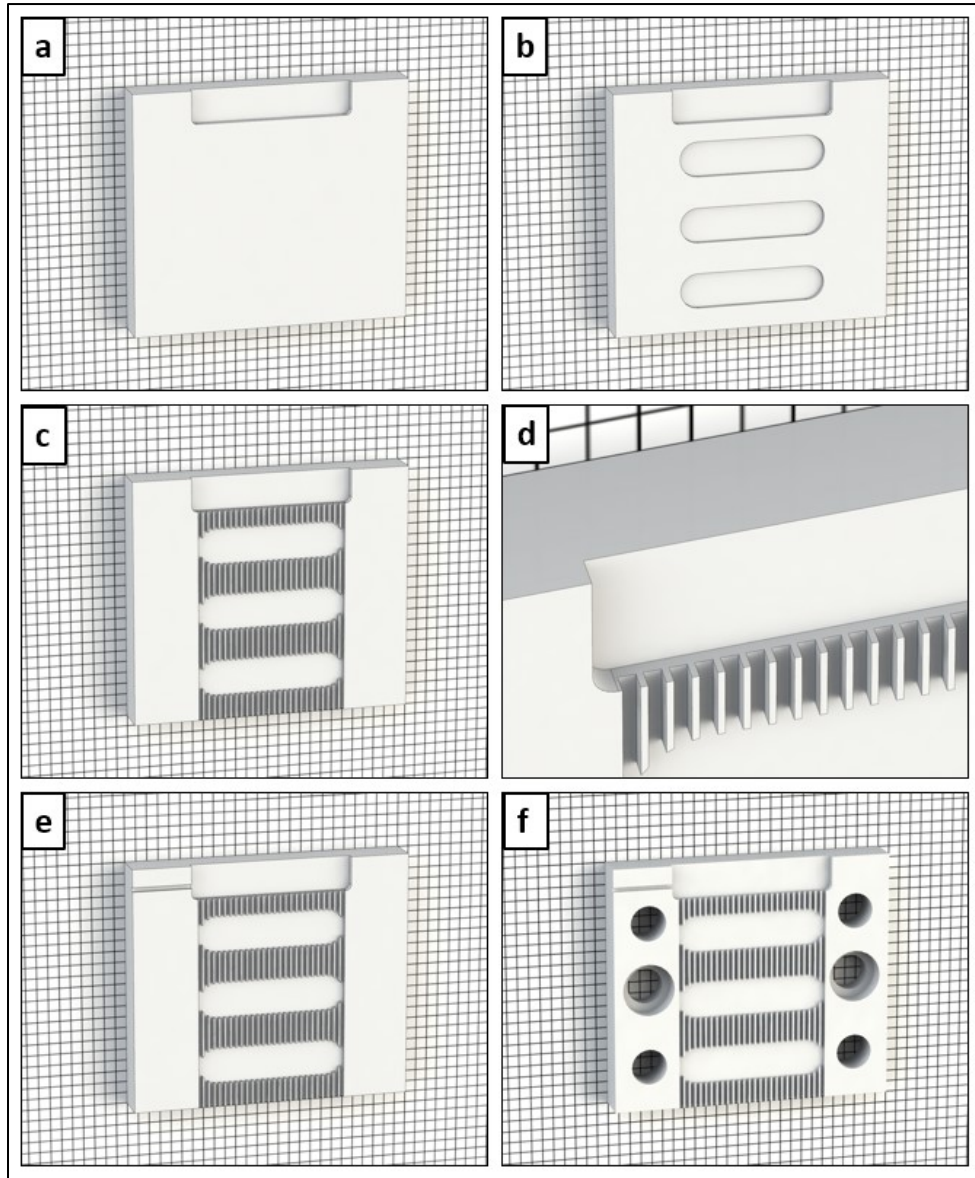
Figure 17 Depiction of the fabrication steps for the MDS interface chip rear layer, from the starting material of a 25 mm × 22 mm × 9.525 mm (W×H×D) acetal sheet. Features were cut into the base using a micrometer equipped manual milling machine. A 615 μm depression was placed at the top to act as the chip inlet (a). Three horizontal depressions (b) were placed so they overlapped the 27 capillary channel paths (c). The triplet depressions and capillary channels and were milled to a depth of 365 μm. A 400 μm deep channel connected the outer left wall to the interior left wall of the inlet depression. Screw holes were milled into the chip, with the vertically centered two countersunk to accommodate the heads of screws entering from the front face.

A set of 27 vertical channels were cut centered about the vertical centerline at a depth of 0.365 mm using a 0.014" square end mill with the channel centers 0.5 mm apart (Figure 17 c). These channels acted as pockets to hold each ^{2}D capillary and maintain their position relative to the width and

depth of the chip. The 0.25 mm depth difference between the channels and the shelf at the top ensured the ^{1}D capillary would have clearance to move away from the ^{2}D capillaries (Figure 17 d). A 0.365 mm deep rounded channel was cut from the left edge of the shelf and extended to the outer left wall for later insertion of a fiber optic (Figure 17 e). Three vertically aligned holes were drilled into the face following each of the left and right edges (Figure 17 f) for securing to the front window and to a larger manifold.

The front acrylic window 25 mm × 22 mm × 1.5875 mm (W×H×D) had concentric holes drilled, by the machine shop staff at Concordia University (Montreal, Canada), to match the positions of those in the acetal rear sheet with modifications to the holes. The four corner holes were tapped to allow 4-40 socket cap screws to enter from the chip rear and hold the capillaries within (Figure 18 a). The two center holes were counterbored from the front of the acrylic chip (Figure 18 b), to allow socket head screws to sit flush with the front of the chip as it was secured to the manifold (Figure 16). To allow the ^{1}D capillary clearance towards the acrylic front window, a film of 0.25 mm white Hytrel plastic was cut to match the chip size with sections removed to mirror the shelf and screw holes on the rear acetal sheet. This was placed between the two chip halves during assembly to act as a gasket and provide additional clearance for the ^{1}D capillary. The predicted entrance length is 0.59_8 mm, allowing about 1.4 mm of variability for optimizing capillary tip height (Figure 19).
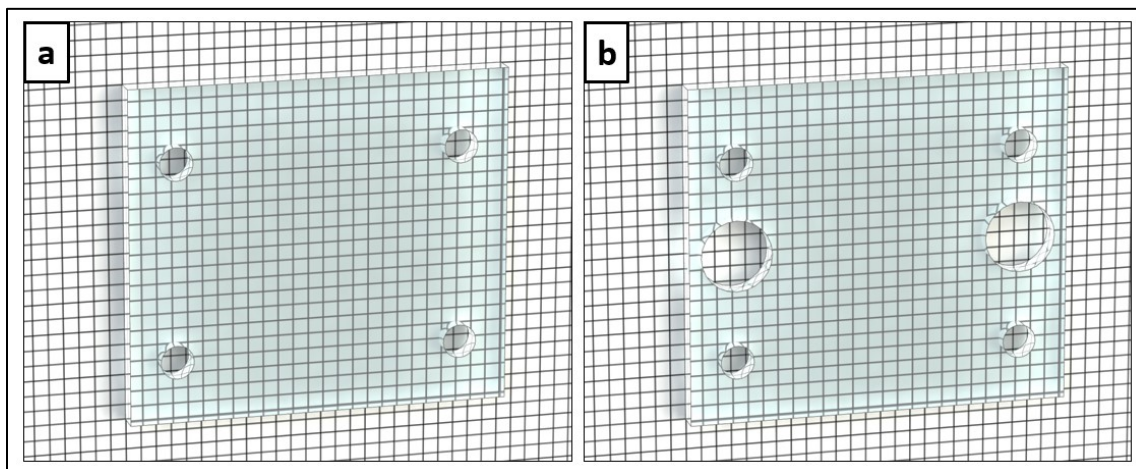
Figure 18 Depiction of MDS interface chip front window. A 25 mm × 22 mm × 1.5875 mm (W×H×D) acrylic sheet was drilled with 4-40 tapped holes at the corners (a) and holes to fit 4-40 screw heads at the vertical center.
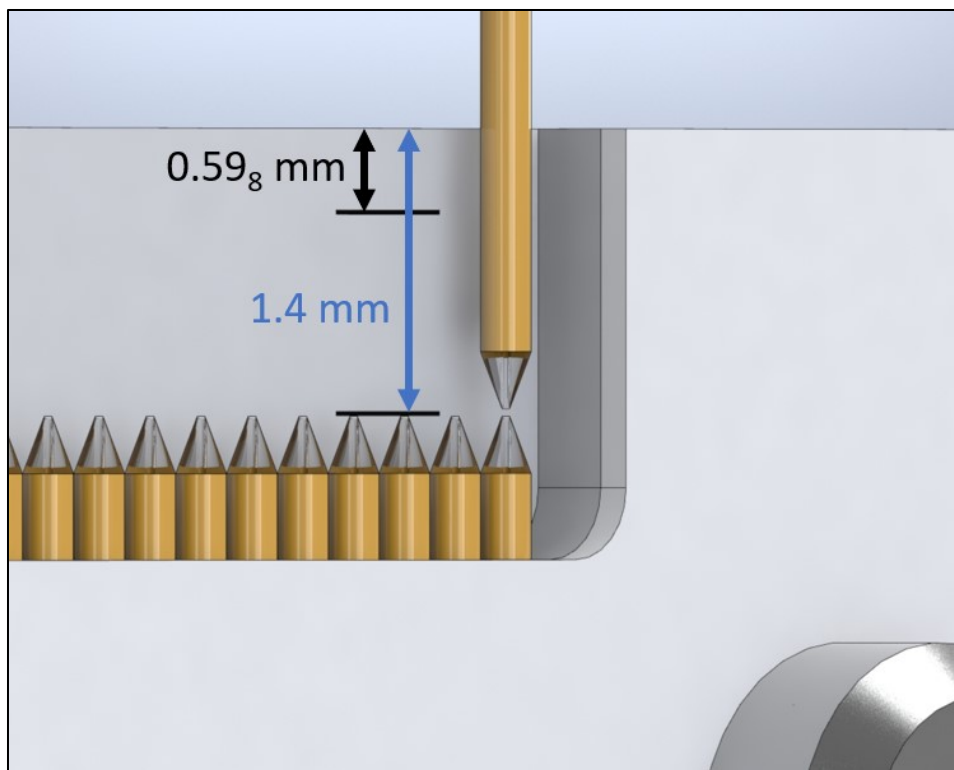
Figure 19 Depiction of the expected usable laminar flow region. The calculated entrance length was 0.59_8 mm for a BGE velocity of 3.3 mm/s. The ^{2}D capillary inlets were further from the chip entrance (1.4 mm) to accommodate higher velocities or lower viscosity BGE compositions.

A previous version of the chip used clear yellow polyetherimide sheet for its advantageous chemical resistance properties against organic solvents used in HPLC and CE. Unacceptably high autofluorescence, when illuminated by the fiber optic at 460 nm and 480 nm, precluded its use in further prototypes.[187] Acrylic can be attacked by many organic solvents, requiring careful selection of ^{2}D BGE and adequate bulk flow if ^{1}D BGE contains a high concentration of incompatible solvents.

2.2.2 **Multidimensional Separations Interface Manifold**

A manifold was designed to house the MDS interface chip and to direct buffer flow through the chip from the top to the bottom while providing a seal for the capillary array. A black acetal plastic resin sheet was cut to 8.89 cm × 6.35 cm × 1.27 cm (W×H×D) and features were machined using a QuickCircuit 5000 CNC micro-milling machine (T-Tech Inc., Norcross, GA, USA). Acetal is a convenient plastic due to its ease of machining and good chemical resistance (both pH and organic solvents), making it suitable for CE and allowing the flexibility of future incorporation of HPLC as the ^{1}D.
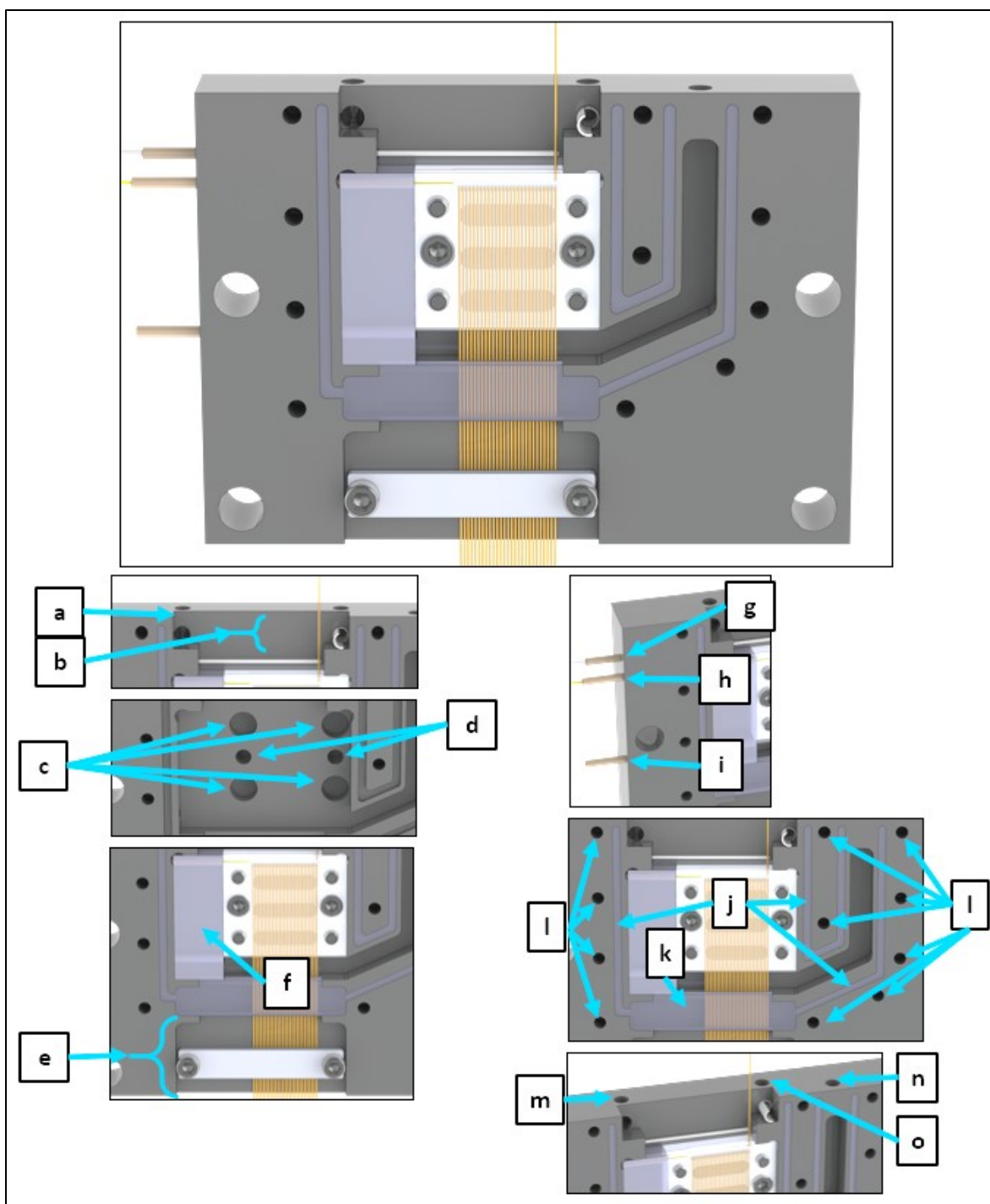
Figure 20 Schematic of the partially assembled MDS manifold with MDS interface chip installed. The acrylic front window and fastening screws were omitted for clarity. The BGE inlet opening at the top face (a) extended downward for 6.35 mm (b). The path narrowed for a 6.35 mm segment where the cathodic electrode was contained, followed by a widening to the section with holes used to mount the MDS interface chip (c, d). The ^{2}D capillaries exited the manifold over a depression cut to be in contact with the capillaries and held in place with PDMS sheet held secured with an aluminum bar (e). A PDMS block was cured in place to fill a void to the left of the MDS interface chip (f). Three holes drilled from the left face of the manifold were used as entry points for the cathodic electrode (g), fiber optic (h) and flushing port (i). A channel was milled around the inner and outer perimeter of the U-shaped flow path (j), which had a larger section to seal around the ^{2}D capillaries as they exited the manifold (k). Screw holes were placed around the inner and outer perimeter to secure the front acrylic wall (l). Three holes were drilled on the top face for the BGE supply (m), waste (n) and BGE overflow (o).

Features were milled into one 3.5" × 2.5" face of the acetal sheet to form a flow path for buffer as shown in Figure 20. A large rectangular entrance was located at the top of the sheet and offset to the left-hand side (Figure 20 a). This inlet directed buffer downwards through the mounted chip, to a channel underneath, then to the right and upward forming an asymmetric U-shaped channel which narrowed towards the outlet and terminated ¼" from the top of the manifold (Figure 20 b). These features were cut at a 4.76 mm depth to match the chip assembly thickness. Additional holes were drilled deeper into the sheet to form pockets for the four corner screw caps on the MDS chip (Figure 20 c). Two tapped holes were concentric with the two counterbored holes in the chip to secure it against the manifold (Figure 20 d).

A shelf was cut into the bottom of the manifold to allow the capillary array space to exit the manifold (Figure 20 e). Two tapped holes in the shelf front flanked the capillary array and were used to fasten an aluminum hold-down bracket to secure the capillaries. A PDMS sheet was placed between the capillaries and bracket to prevent the capillaries from being crushed. The manifold was designed to work with a 35 mm wide chip (to accommodate up to 51 capillaries). When used with the 27-capillary chip described above, a PDMS block (Figure 20 f) was cast to fill the void that would be taken up by a larger chip. Mounting holes for ¼"-20 screws were drilled on the left and right sides of the manifold to sister it to a polypropylene sheet with the same outer dimensions as the manifold. This acted as an insulating and mounting block, which was mounted to an L-bracket and mounted onto the top of the motorized X-Y translation stage.

Three 1/16" holes were drilled into the left side of the manifold (Figure 20 g, h, i) for insertion of 1/16" o.d. PEEK tubing that terminated at the nearest inside wall of the manifold. The lumen of the uppermost opening was made in line with the top of the chip assembly as a path for the platinum grounding electrode. The middle opening acted as a sleeve to hold the fiber optic entering the chip assembly with its lumen made concentric with the channel previously cut in the MDS chip. The lowest opening was placed just below the bottom edge of the PDMS spacer and chip assembly to be used to flush the manifold for cleaning and bubble removal.

A pair of nested U-shaped channels (Figure 20 j) was cut into the manifold face using a 1 mm square end mill in order to form in-place gaskets; one surrounding the perimeter of the liquid flow path and one bounding its interior. These gaskets were used to seal an acrylic plastic optical window against the face of the manifold. The outer U-channel was intersected near the capillary

array exit by a deeper pocket 35 mm × 6.35 mm × 4.76 mm (W×H×D) (Figure 20 k) to allow incorporation of a large PDMS plug to seal against the capillary array. The ends of both gasket channels terminated before the top edge of the manifold so the PDMS solution would be contained during curing. Tapped screw holes (Figure 20 l) surrounding the outer perimeter of the gasket channel and inset in the center of the U-shaped channel were concentric with holes in the optical window that was secured with 4-40 screws.

Three 1/8" holes (Figure 21 a, b, c) were drilled at the top of the manifold to serve as buffer supply (a), drain (b) and excess (c). The m and n holes were drilled to allow connection to the U-shaped channel. The rightmost hole (c) was drilled to meet with the U-shaped channel exit. This hole was tapped and fitted with a threaded 1/8" hose barb adapter. Primary buffer flow is represented by the green arrows in Figure 21. Fresh buffer was drawn through the online degasser by the peristaltic pump and subsequently delivered through the leftmost hole (a) to fill the MDS interface. At the outlet (c), Tygon tubing connected the hose barb to the peristaltic pump to draw off waste buffer. The internal diameters of the peristaltic pump tubing used for supply (1.00 mm i.d.) and drain (0.76 mm i.d.) were chosen to ensure oversupply of buffer and allow the drain to set the flow rate through the chip. The secondary waste hole (c) was used to draw off excess buffer via a curved stainless-steel tube, made from a modified 20-gauge blunt syringe needle that was connected to a faucet vacuum aspirator. Thus, meniscus height at the MDS interface entrance was set by this vacuum line. This is depicted by the yellow arrows overflowing the barrier and exiting the top of the manifold.
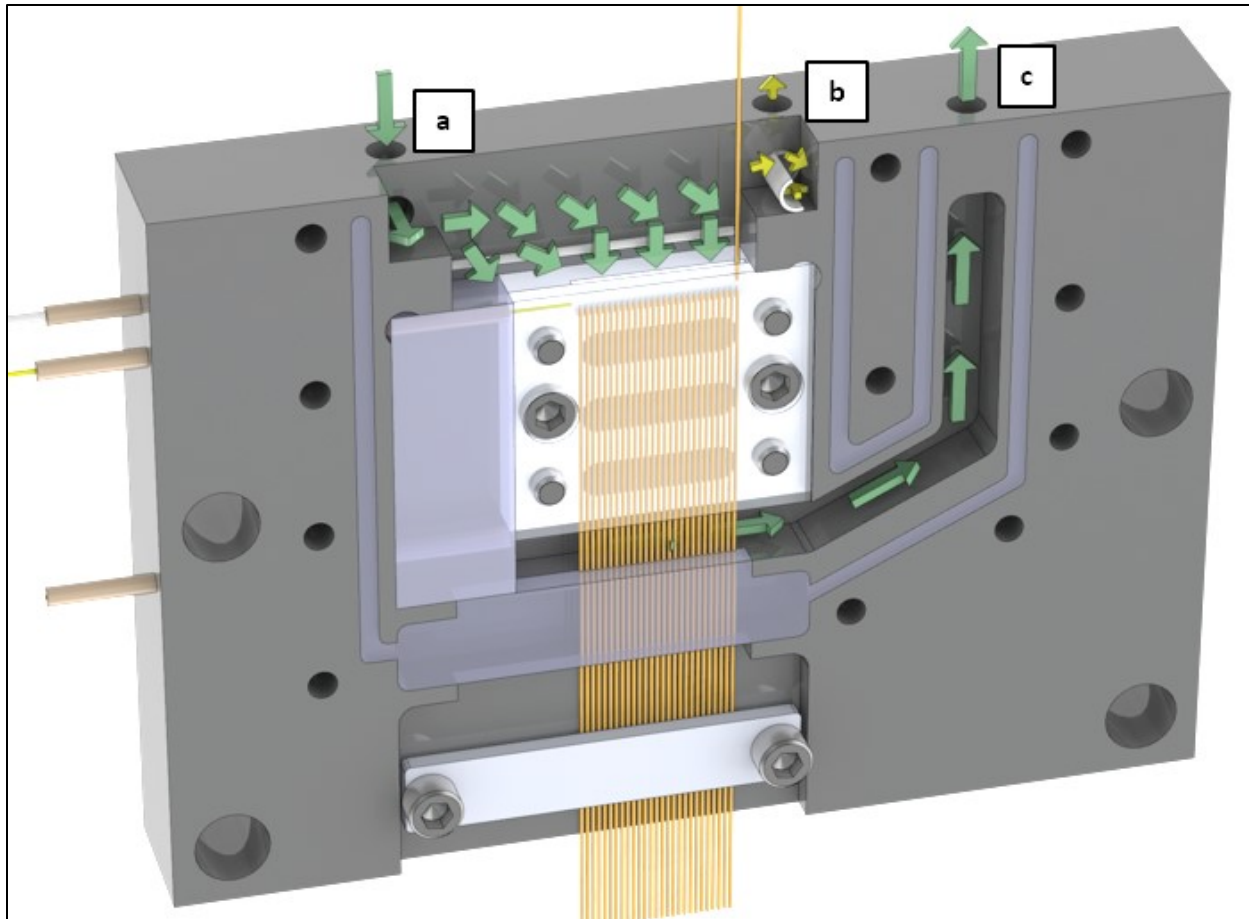
Figure 21 Depiction of directed buffer flows through the MDS manifold. Green arrows represent the majority of volumetric flow. Yellow arrows represent minor flow. BGE was supply into the entry port (a) and out from the waste port (c) was driven by a peristaltic pump. The supply flow rate was higher than the waste flow rate, creating a constant oversupply of BGE. A 25-guage tube was positioned in the center of the overflow opening (b) and connected to a vacuum supply to draw off excess BGE. To minimize perturbations caused by the intermittent vacuuming of BGE, a fabricated 1/8" PTFE tube was placed at the opening of the oversupply conduit. This also set the meniscus height, as the BGE had to flow over it to reach the conduit.

To permit the acrylic front window to seal the manifold face, an in-place gasket was prepared using the steps shown in Figure 22. Hytrel film (0.25 mm) was cut into strips and used as spacers between the body and the window during gasket preparation. These strips were arranged and temporarily glued (High-Temp Red RTV Silicone Gasket Maker Permatex, Hartford, CT, USA) to the manifold face. This confined the liquid PDMS to the desired areas until cured as well as set the distance the gasket exceeded the manifold surface (Figure 22 a). The manifold was then placed with its face directed upwards, the inner cavity was filled with a slight excess of PDMS and a glass or acrylic cover plate was placed on top. A ≈1 kg weight was placed over the cover plate to ensure air did not re-enter the cavity. This assembly was placed in a 60 °C oven and allowed to cure overnight. After curing (Figure 22 b), excess PDMS, polymer strips and RTV was cut away with

a scalpel and removed until only the gasket, now slightly proud of the surface, remained (Figure 22 c). Any voids due to leaked PDMS were corrected by applying a thin layer of RTV silicone sealant, which was air-cured while a weighted sheet of PTFE was pressed against the manifold face. These corrections are visible as the red segments of the clear PDMS gasket. During use, the manifold was sealed with a ¼" acrylic plate that was held tightly using 4-40 cap head screws surrounding the flow path (Figure 22 d).
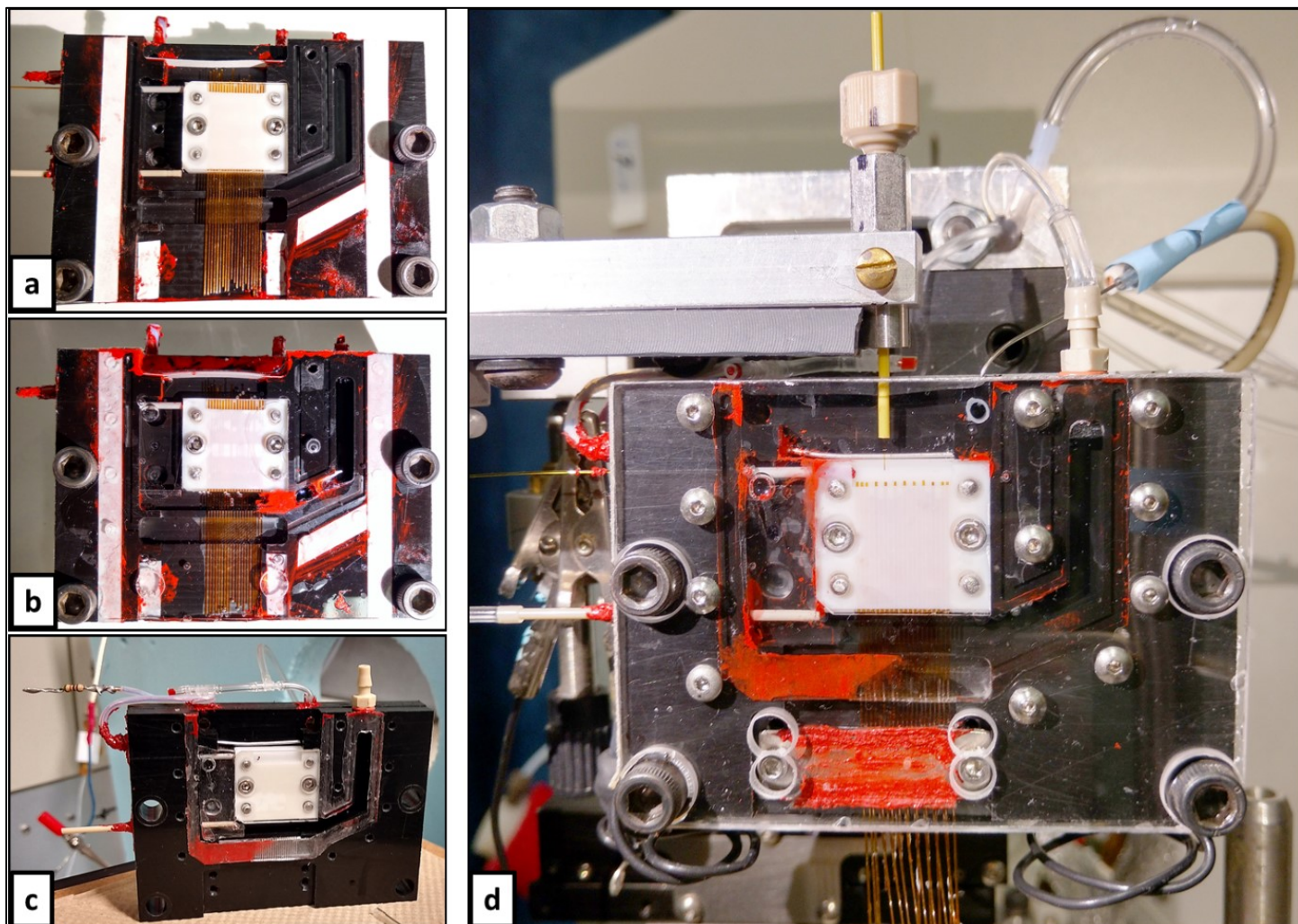
Figure 22 Stepwise preparation of the cover gasket for the MDS interface manifold. Strips of white plastic film (thickness 0.25 mm) were fixed to the front face to act as risers as well as on the top and bottom openings to act as walls to enclose the liquid PDMS during curing (a). After curing against the acrylic window, the window was removed to expose cured PDMS in all voids of the manifold (b). Excess PDMS was removed using a scalpel and poorly sealing sections were added to with red silicone (c). The front wall of the manifold sealed against the gasket using by the force of the cap head screws near the perimeter of the gasket (d).

2.2.3 **Precision Positioning of Capillaries Inside the MDS Interface**

In this prototype instrument, a 2D translation stage was used to perform the capillary positioning necessary to carry-out injections onto the capillary array.

2.2.3.1 Motorized Linear Translation Stages

In order to programmatically manipulate the MDS interface in the plane of the optical table (the X,Y plane), a Newport model 423 (3" × 3") linear translation stage (X-axis) was mounted on top of a model 433 (3" × 4") linear translation stage (Y-axis) (Newport Corp., Irvine, CA, USA), providing a nominal 1" and 1.8" linear travel, respectively. Each translation stage was outfitted with a Portescap 35DBM10B2U-K stepper motor driven captive linear actuator (West Chester, PA, USA). The captive actuators allowed these motors to translate their rotational force into reproducible linear motion. Stepper motor actuators are ideally suited to applications where open loop control—without positional feedback—is considered acceptable. Within their operating range, these motors provide 25.4 μm (nominal) of linear motion per step.

Each linear actuator was controlled using model 1063_0 Stepper Bipolar 1-Motor drivers (Phidgets Inc., Calgary, AB, Canada) under in-house written LabView control software. These drivers included digital inputs for feedback during operation from limit switches.

In order to set the initial zero point for each stage, a Honeywell HOA2005 side-mount Optoschmitt sensor (Honeywell, Morris Plains, NJ, USA) was used. These U-shaped sensors house an infrared (IR) emitting LED and photodiode in each of the arms of the 'U' and facing towards each other. Upon interruption of the IR beam, the sensor is triggered. This sensor was mounted to the upper half of the linear translation stage. An accompanying aluminum flag mounted to the bottom, which would pass into the 'U' of the sensor so it could act as a limit switch during motor calibration.

The two stepper motor drivers were each under independent control by the LabView control software via USB 2.0 interface. As a host-initiated bus protocol, USB 2.0 requires the multipurpose computer processor and operating system to negotiate all data transfers. This results in introduction of random latency during control software requests for motor movements. This, along with the inherent latency in the USB 2.0 bus, precluded synchronous motion between the motors/axes. Thus, a motion pattern was chosen to only use a single axis of motion during an injection event. (Figure 23)
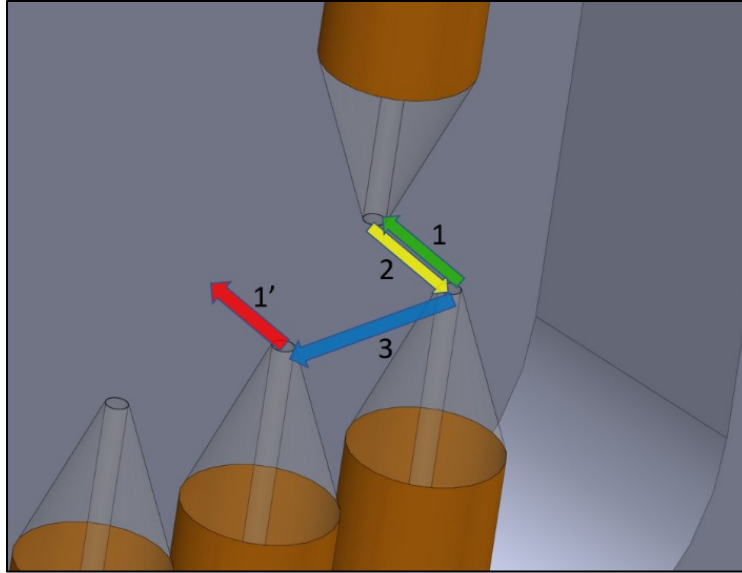
Figure 23 Depiction of the motion pattern used by the MDS interface perform electrokinetic sample transfer between dimensions. Prior to injection, the rightmost ^{2}D receiver capillary waits in a position offset 355.6 μm in front of the ^{1}D capillary, along the X-axis. To start the injection, the MDS interface moves 355.6 μm towards the rear along the X-axis (1) until the receiver is under the ^{1}D capillary effluent, where it waits for the prescribed injection time. Then it moves forward 355.6 μm along the X-axis to stop the injection (2). The MDS interface then moves to the right (~630 μm) until the second ^{2}D capillary is aligned with the ^{1}D along the Y-axis (3), where the next injection can be made (1').

The motion pattern used for sequential injections is depicted in Figure 23. Injections were made from the right-most capillary towards the left. Prior to an injection, the MDS interface was placed such that the receiver capillary (^{2}D separation) was positioned 14 full steps (355.6 μm, nominal) in front of the ^{1}D effluent from the donor capillary (X-axis). The camera was fixed in position and focused on the plane containing the donor capillary so that the injections could be observed. Upon beginning an injection sequence, the MDS interface was positioned such that the receiver capillary was directly downstream from (below) the donor capillary for the specified injection time (step 1), and then returned to the starting position (step 2). It was then moved towards the left to be aligned to the next capillary along the Y-axis (step 3) but offset 355 μm along the X-axis. Here, it would wait for the remainder of the cycle time until the appropriate injection time for the following capillary (step 1'). This repeated action was used across the eight-capillary array. Upon completion of the eighth injection, the MDS interface was moved so that the distance between the donor capillary and the capillary array was ≈ 400 μm and the MDS interface was "transited" to the initial position in preparation for a new round of injections beginning with the first receiver capillary.

2.3 Multi-capillary Sheath Flow Cuvette Detector

The detector cell was constructed using PDMS since it can be simply cast against positive and negative templating features in a mold. With easily modified molds, this enables rapid prototyping as compared to more complicated micromachining and/or annealing of glass as used in conventional glass and plastic cuvettes.

The sheath flow cuvette (Figure 24) held the ^{2}D capillary outlets in a line along the Y-axis of the optical breadboard, and at the same height (Z-axis) to allow the effluent for all capillaries to be simultaneously coincident with a single incoming excitation laser beam (Figure 24 i). The probe volume for each capillary was imaged by an orthogonally located CCD camera. (Figure 11 k). Optically clear surfaces for the laser excitation window and the emission window were produced by templating each surface against sections of new glass microscope slides. The cuvette directed BGE to flow over the ^{2}D capillary outlets in a laminar flowing stream (Figure 24 †; depicted by the arrows in the inset drawing). This stream entrained the effluent exiting each ^{2}D capillary, causing the effluent stream to narrow and reduce the probe volume. To produce the stream, a gravity fed siphoning system was used. This was connected via the inlet (Figure 24 b) and outlet (Figure 24 c) tubes of the cuvette, which were attached to the BGE supply and waste containers, respectively. Completion of the HV circuit required to drive the CE separation was enabled by a HV electrode placed inside a bubble trap attached to the waste tubing (Figure 24 d), which was attached to a HV cable (Figure 24 j) that was supplied by a nearby HV power supply (not shown). This overview covers the sheath flow cuvette design, with the salient details to understand the operation of the detector within the context of the overall MDS instrument.
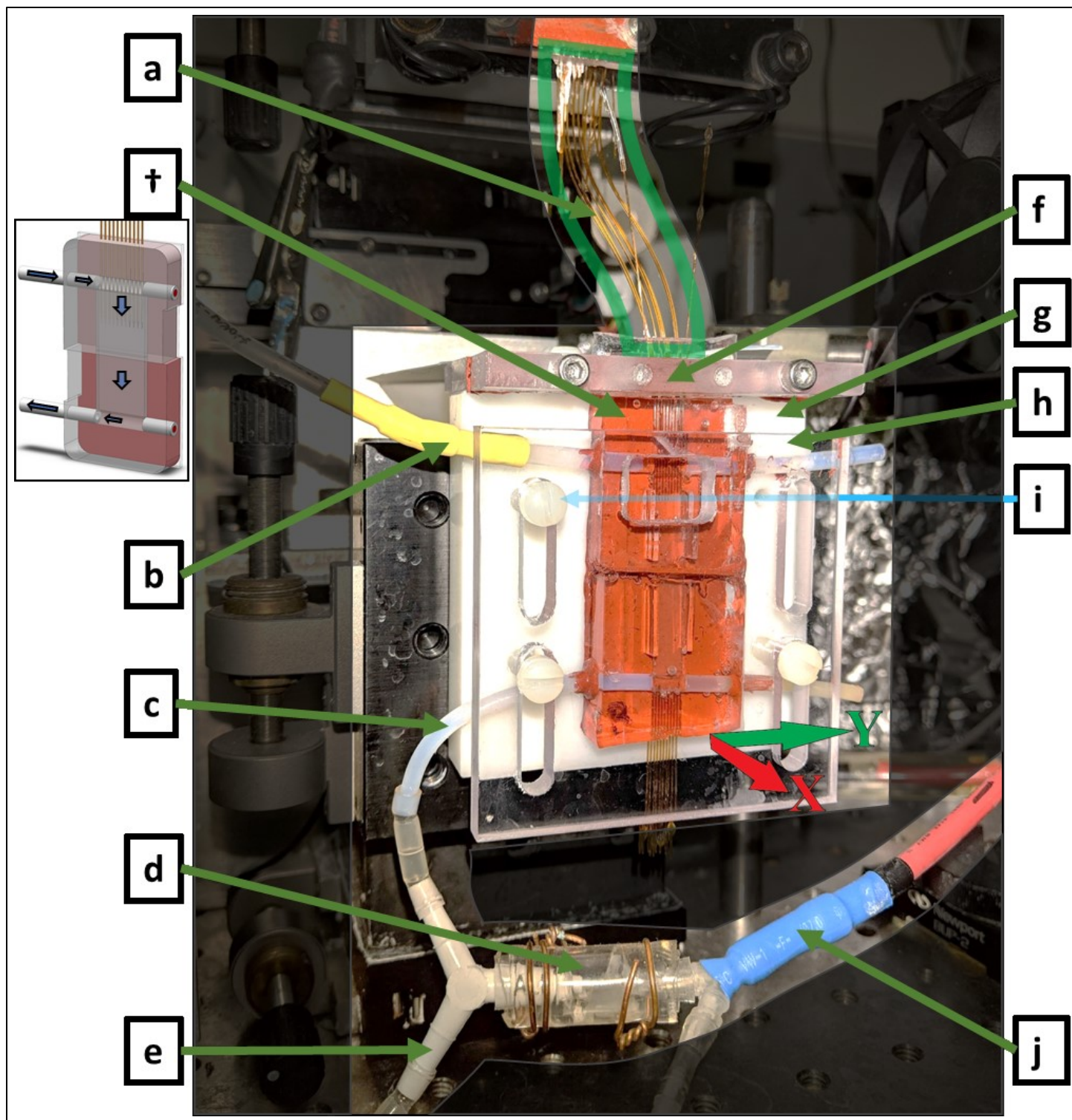
Figure 24 Partially masked image of the ^{2}D multicapillary detector, including an inset CAD drawing of the sheath flow cuvette with arrows to indicate BGE flow path (†). An array of ^{2}D capillaries (a) with an S-curve leading from the MDS interface to the sheath flow cuvette. Tubing for the BGE supply (b). Waste flow (c) was split using a Y-connector to couple it to both a bubble trap (d) and the bulk waste (e). The bubble trap contained the high-voltage electrode (j). A polycarbonate plastic bar held the the ^{2}D capillaries tightly (f) and locked to the polyethylene mounting block (g) which was attached to a micrometer driven 2D linear translation stage. A polycarbonate sheet pressed against the sheath flow cuvette using three nylon screws (h). The laser path is indicated by the blue arrow (i), which passes through a window cast into the PDMS and below the capillary outlets.

The following sections provide a description of the preparation of the PDMS sheath flow cuvette. This description includes a detailed, step-by-step procedure, and is aimed at a reader who intends to build a similar cuvette.

2.3.1 Sheath Flow Cuvette Detailed Description and Assembly

The final cuvette design, seen in Figure 24 and in greater detail in the next few figures, was a clear rectangular block 25.4 mm × 63.5 mm × 8.89 mm (W×H×D) cast from PDMS (Figure 24 a). The interior of the block contained a vertical rectangular channel of 38.1 mm × 6.5 mm × 0.865 mm (W×H×D). The capillaries enter this channel from the top face and were inserted deep enough such that the capillary outlets were positioned along the centerline and were spaced ≈0.635 mm apart. Two 3.175 mm access holes extended from the left-hand wall to meet with the rectangular channel; one at the top and one at the bottom (Figure 24 b, c). The top served as the buffer supply inlet, and the lower the waste and connection to the high voltage electrode. Approximately 35 mm of 1/8" o.d. PTFE tubing was inserted into the inlet and waste ports to act as unions for connecting Tygon tubing. The outlet tube was attached to a Y-connector with one arm leading to the waste reservoir (Figure 24 e), while the other was attached to the high-voltage electrode of the Bertan 210-30R power supply contained within a bubble trap (Figure 24 d). A polycarbonate support bar was screwed in to clamp capillaries and prevent them from moving in or out of the cuvette (Figure 24 f). A 63.5 mm × 76.2 mm × 12.7 mm (W×H×D) polypropylene sheet (Figure 24 g) was mounted to a 2D translation stage via an L-bracket. To hold the sheath flow cuvette in place, a front 63.5 mm × 76.2 mm × 2.7 mm (W×H×D) clear polycarbonate sheet (Figure 24 h) was screwed into the rear polypropylene sheet using three nylon screws. A 14 mm × 10 mm (W×H) opening was cut into the polycarbonate sheet, starting 5 mm from the top edge, to allow a clearer view of the capillaries and effluent. The excitation laser beam entered the cuvette from the right-hand side of the photograph (Figure 24 h) placed just below the ^{2}D capillary outlets.

Plastic plates were used to support the sheath flow cuvette mechanically and to electrically isolate it from nearby metal components. The 2D translation stage provided linear travel along the X-axis (into the image plane) and Z-axis (vertical dimension).

2.3.2 **Sheath Flow Cuvette Fabrication**

The cuvette was fabricated by casting PDMS in a mould built around a microscope slide as the primary base. Capillary channels were made by wrapping nylon fishing line around the microscope slide, once per capillary. Uniform spacing was achieved by threading the fishing line through the grooves of set screws glued to the slide (see Figure 25 a, b, c). The template for the central channel was prepared by suspending two rectangular sheets of plastic on either side of the fishing line (Figure 25 d) and placing glass walls in contact with the edges of the plastic sheets (Figure 25 e). The interior of these four walls served as the rectangular channel. A PTFE tube (1/16" or 1/8"), with a slot cut along its axis, was placed over the ends of the plastic sheets nearest the set screws to act as negative templates for buffer and waste openings. A thin aluminum sheet was inserted transverse to the channel (Figure 25 h-1, h-2), bisecting the sheath flow cuvette. The entire assembly was placed in an aluminium mould, filled with uncured PDMS and enclosed with plate glass on each side. After curing, it was removed from the mould, split into two halves (Figure 25 i) and underwent removal of the glass slide, fishing line, plastic strips and PTFE tubing. The two halves were glued back together using RTV silicone (red coloured material in Figure 25 j). A thin sheet of PDMS was also attached to the back side of the cuvette to seal gaps at the rear facing sides of the glass walls. Unused openings from the PTFE tubing were plugged using capillaries and PTFE tubing, respectively, with their lumens blocked with silicone. A schematic image, with the flow paths, is shown in Figure 25 k. A more detailed description of the fabrication steps can be found in the appendix.
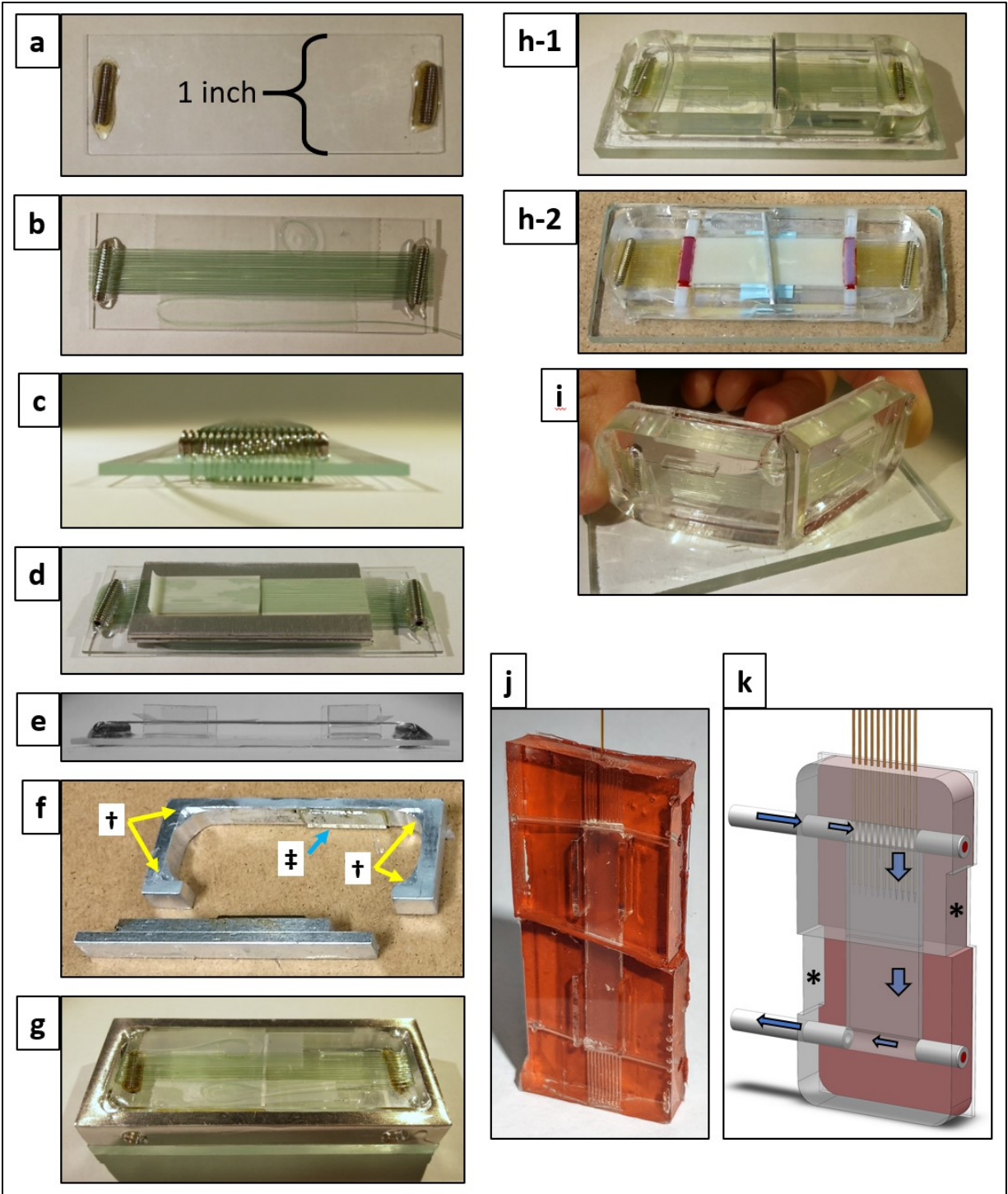
Figure 25 Fabrication steps for the PDMS-based sheath flow cuvette. 4-40 set screws were epoxied to a standard microscope slide (a). Fishing line was wound around to the slide (b) and through the threads of the set screws to achieve uniform spacing (c). Plastic sheets PDMS bonded to front and rear fishing lines while held by aluminum spacers (d). Glass walls PDMS bonded perpendicular to the parent microscope slide and in contact with the edges of the fishing line (e). Two variants of the aluminum outer mould (f, g), each with recesses at the filleted corners (f †) to hold the glass slide below the aluminum face (g) and epoxy bonded glass sheets (f ‡) for moulding the excitation windows. Cured PDMS after removal of the aluminum frame with 1/16" (h-1) and 1/8" (h-2) tubing used for the BGE supply and waste openings. The two halves of the cuvette were split along the aluminum spacer (i) and attached using red silicone (j). A rendered image (k) demonstrates the flow path through the device and the two available excitation windows (k *).

95

2.3.2.1 Removal of sacrificial templating and final assembly

Upon curing, the two sheets of plate glass were removed, followed by the cured PDMS cell assembly. The cell was cut perpendicular to the fishing line, just inside of each cemented set screw and the central PDMS sheath flow cell lifted away. The ends of the PDMS device were cut approximately "square" to ensure removal of any fishing line that had any curvature resulting from proximity to the set screws. The sheath flow cell was split in half by bending where the aluminum spacer was placed (Figure 25 i) and using a scalpel to cut through the connecting fishing line. Forceps were used to remove all PTFE tubes, the severed fishing line segments and the plastic sheets. To clear the free flow path, a 16-gauge syringe needle tip was bent at the last ≈0.6 mm and used to mechanically clear out any free PDMS left behind after removing the template materials. All clean-up operations were performed with the aid of a microscope. Great care must be exercised when removing these PDMS "stragglers" to avoid damaging the PDMS, while also ensuring removal of any PDMS that had cured to the interior glass walls of the excitation windows. Remaining stubborn, small, PDMS fragments were removed by repeatedly syringe flushing the cuvette using high concentration dish soap dissolved in warm water.

The two cuvette halves then had their central channel rejoined by applying Permatex RTV Silicone gasket maker (Permatex Inc., Solon, USA) to the faces where the aluminum sheet had bisected them. To align each lumen to the other, the cuvette halves were placed face down on a PTFE tape coated microscope slide and brought together under a microscope. This assembly cured overnight at room temperature. A pre-cured sheet of PDMS (≈1 mm thick) was cut to fit the cuvette rear side of the cuvette and adhered to the back using gasket maker to seal the narrow openings along the inset glass windows.

This process produced a symmetric sheath flow cell that could be used from either end by simply plugging the unused openings with silicone filled PTFE tubing (right-hand openings) and epoxy filled dummy capillaries (bottom openings). The work presented here used a 10-capillary sheath flow cuvette, where the two outermost capillary array positions were filled with dummy capillaries. These were used to provide control over velocity gradients through the cuvette that could be observed as non-symmetrical flow through the sheath flow channel. Those capillaries could also be raised or lowered to alter flow restriction through the cell and allow some control of the sheath stream.

The sheath flow cuvette was mounted on the two-axis translation stage by sandwiching it between the two sheets of plastic as described above.

2.4 Microscale Separations: Data Storage and Alignment

A primary aim of this work was to perform high-speed, high-resolution separations which would result in the high-throughput generation of datasets with many samples. However, for samples to be comparable their separations data must be linear—meaning analytes appearing within each sample varies only by their concentration, and thus signal intensity. This linearity assumption is broken if the peaks don't align between samples. No physical separation can be perfectly reproducible because of peak shifting. This effect is amplified when eight independent capillaries are used in the ^{2}D, each having its own imperfections, usage history and separation behaviour. This leads to a high probability that the raw data from one 2D separation will not be superimposable with another.

In this work, a 1D correlation optimized warping (COW) algorithm[188] was used, with modification, to correct migration time shifts between the ^{2}D separations. When performing a classical COW time alignment on two electropherograms, one is chosen to be the reference and the other is the sample. Each electropherogram is split into several short time segments (segment length/segment number parameter) as chosen by the user. The segment pairs for each electropherogram are then compared sequentially. During comparison, the sample segment undergoes an iterative series of modifications where it is warped by stretching and compressing it in the time dimension (slack parameter) and it is shifted towards earlier and later times (sideways movement parameter). Comparison between segment pairs is performed by computing correlation coefficients for each iterated warping and shifting combination. The combination of parameters with the highest ranked correlation coefficient is then chosen to be saved for that segment and appended to a new modified sample electropherogram. This is repeated for each subsequent segment until the entire electropherogram is parsed.

COW can be applied in a pairwise fashion to adjacent separations in a 2D separation. Initially, the first injection onto the ^{2}D would act as the reference while the second injection acts as the sample. Next, the second injection would act as the reference while the third injection acts as the sample. This paired window continues along the entire 2D separation space until all ^{2}D separations have been aligned.

An in-house modified alignment method was considered necessary due to the novel 8-capillary data generated, with the primary modification to the COW algorithm being the omission of the electropherogram segmentation step to lower the number of computational steps required. Instrumentally, care was taken to ensure the capillaries were similar, such as making their lengths identical to within 0.5 mm and cutting all capillaries from a single continuous length of starting capillary. However, without between-run rejuvenation of the silanol surfaces, significant inter-capillary variations between separations were expected and ultimately observed. As a result, it was found that large slack sizes were required for acceptable alignment. Large slack sizes dramatically increased computational requirements and resulted in long processing times to align each ^{2}D electropherogram. To reduce the number of warping steps performed the partitioning of the ^{2}D separation windows was omitted. Instead, the segment size was set equal to the entire ^{2}D separation window. Thus, only one segment needed to undergo a set of warping and shifting combinations. This avoided subjecting each ^{2}D electropherogram to a number of warping and shifting sets equal to the number of segments.

Application of the COW algorithm in this work needed to accommodate varying ^{2}D separations that resulted from the constantly changing ^{1}D effluent they received over time. A 2D separation generated a 2D matrix, with each column containing one ^{2}D separation window (m_2), with the number of columns equaling the number of ^{2}D separations (M). The 1D COW algorithm was originally conceived to align a set of replicate separation profiles to a single reference separation, which did not apply here. Rather than use any one separation profile as a reference, each ^{2}D separation (m_2) was warped to best match a reference comprised of the preceding ($m_2 - 1$) separation. This was performed as a moving pairwise warping from the second ^{2}D separation ($m_2 = 2$) to the last ^{2}D separation (M). The first separation ($m_2 = 1$) was not subjected to COW since there was no zeroth separation to align it to.

To prepare the raw data for downstream COW alignment it was first imported into Matlab as a nine-column array; eight columns of fluorescence emission intensity from the capillary array and a column with elapsed time. Each of the eight signal columns was baseline corrected using the inbuilt Matlab function msbackadj(), which estimates the baseline using windowed spline approximations and subtracts it from the original signal.

Each capillary produced a continuous data stream, comprised of concatenated separation windows, one for each injection made onto the ^{2}D separation. Figure 33 provides a visual representation of this effect when the ^{1}D was infused with tryptic serum peptides which were injected onto the ^{2}D array in sequence. Since injections were made sequentially, adjacent injections onto a single capillary were separated by the time required to perform injections on the other seven capillaries in the array. Thus, an eight-capillary array using a 12 s inter-capillary injection time resulted in 96 s between subsequent injection onto each of the capillaries. This 96 s intra-capillary injection time also set the maximum length of the ^{2}D separation windows.
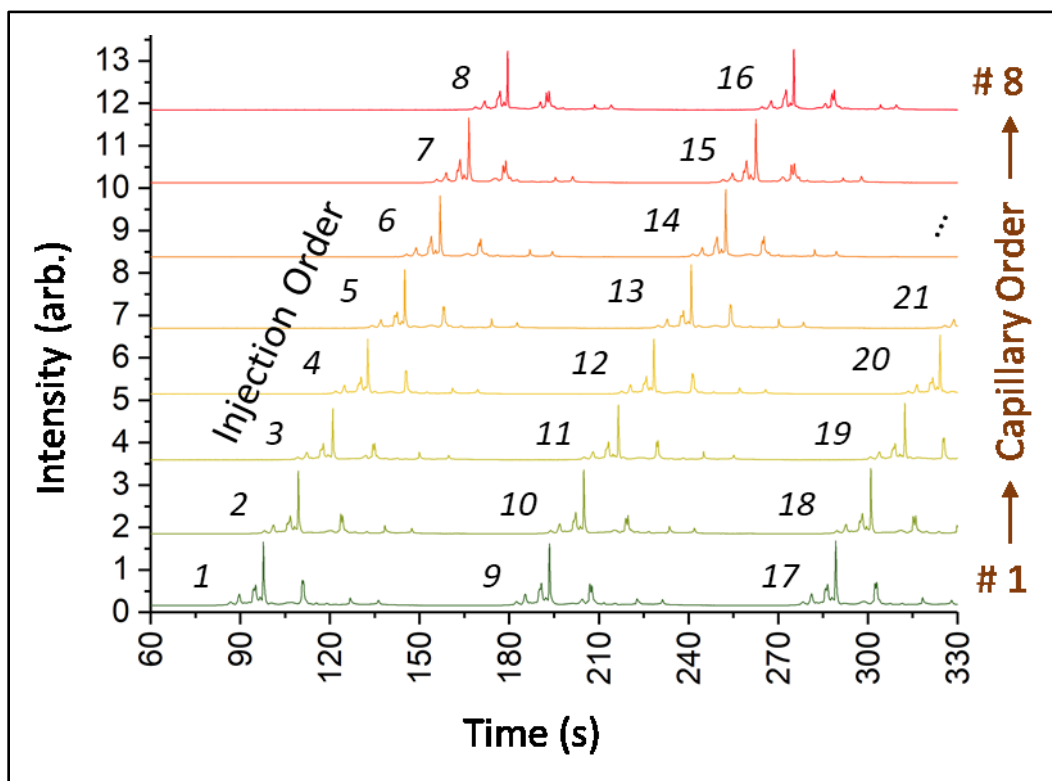
Figure 26 Raw data from continuous automated injections of tryptic serum peptides on a CE × CAE instrument. Signal traces are vertically offset for clarity. The ^{1}D was infused with serum peptides with a constant applied voltage to provide a constant stream of effluent. The MDS interface injected effluent into each ^{2}D capillary in order from capillary 1 (bottom trace) to capillary 8 (top trace). Once each ^{2}D capillary received one injection, the set of eight injections restarted. This sequence would repeat for the entire 2D separation time.

The dead time was removed from each capillary's data channel (Figure 34) to normalize the starting time across the array. This required the removal of the data points preceding the first injection onto each respective capillary and the time for the EOF to migrate to the detector following the first injections.
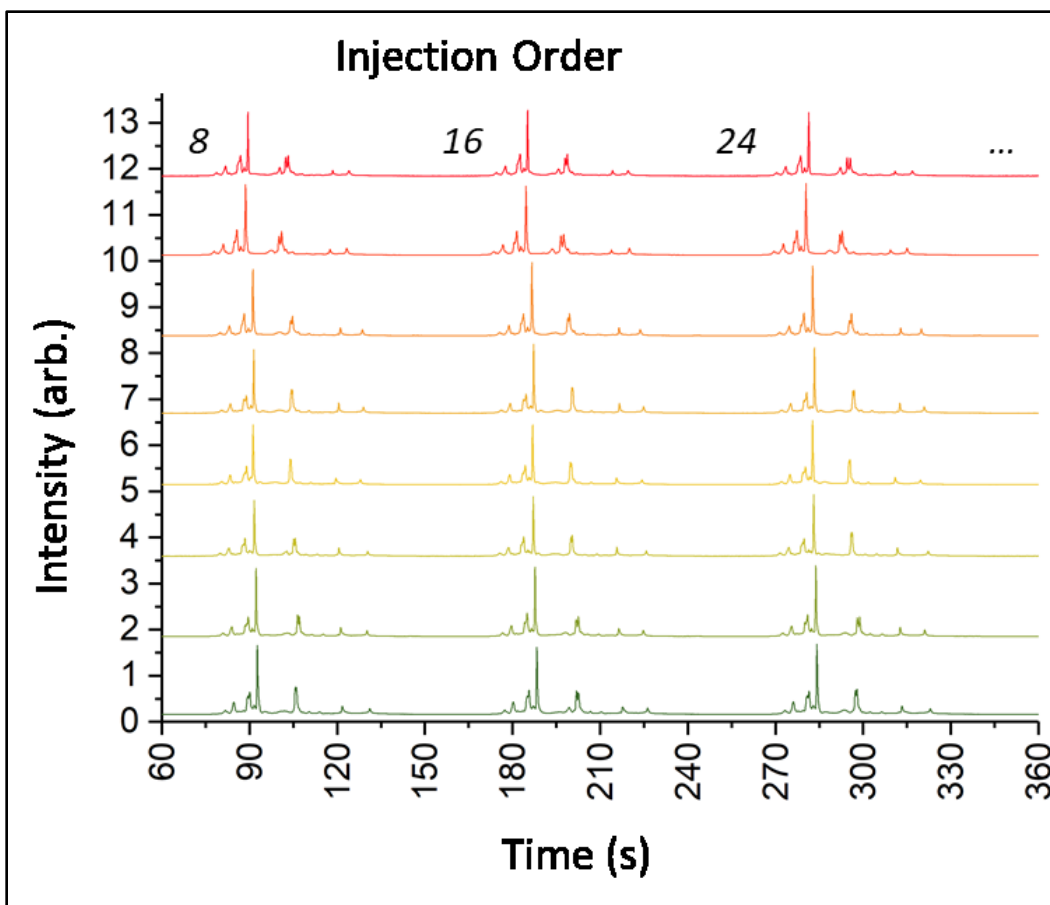
Figure 27 CE × CAE data of tryptic serum peptides, corrected to normalize the time of the first injection for each of the eight capillaries in the ^{2}D array. Signal traces are vertically offset for clarity.

The data was then restructured into a matrix of ^{1}D effluent sampling number across the columns and ^{2}D separation time across the rows, with the first 16 ^{2}D separations depicted in Figure 28 . Starting at the top of the raw data matrix a number of rows, equaling one separation window, was extracted and removed from each column. This set of eight separation windows was placed in a new matrix in columns 1 – 8. The following separation window segment was extracted from each raw data column to become columns 9 – 16 in the new matrix. This sequence of interleaving sets of separation windows was repeated until raw data array was exhausted to the nearest integer multiple of eight separation windows. Using the same 13 s injection cycle time, a 60-minute separation produced 276 injections on the eight-capillary array.
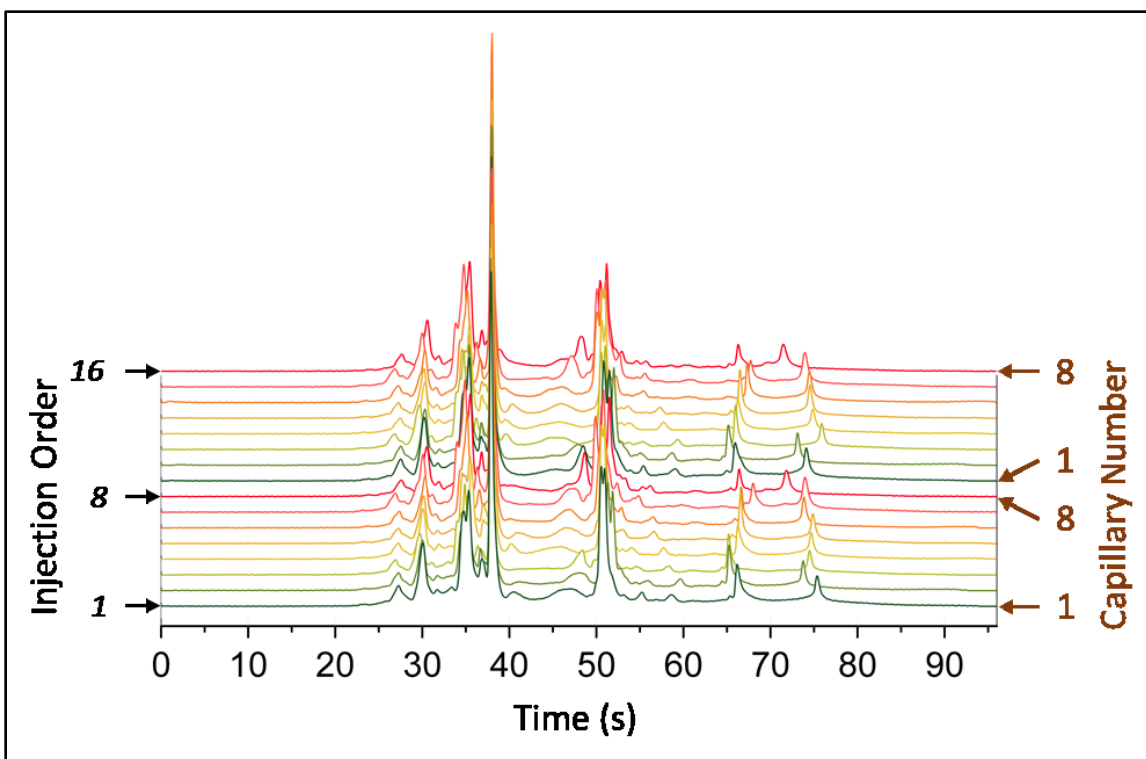
Figure 28 Electropherograms of the first 16 sequential injections of tryptic serum peptides made onto the ^{2}D capillary array after reshaping the separation windows to represent the injection order from the sampling of ^{1}D effluent. Signal traces are vertically offset for clarity.

Each column in the 2D separation matrix was padded with zeroes at the beginning and end of the separation window with the number of rows corresponding to the slack parameter. The slack parameter was estimated using a test separation where fluorescein was programmatically injected across the ^{2}D capillary array and determining the difference between the fastest and slowest migrating peak in the set. This was chosen as the minimum slack size used to stretch and compress separation profiles during COW. Slack sizes from 0.5% to 10% of the ^{2}D separation time ($\approx 5 - 100$ data points) were routinely used.

Before warping, the paired the sample (m_2) and reference (m_2 - 1) electropherograms were normalized using the nrm.m code, obtained from MATLAB File exchange (written by Christina de Bruyn Kops, 2015). This corrected capillary-to-capillary differences in signal intensities, which could be as large as 2-fold between the lowest and highest signal capillary.

The sample was then warped both stretching and compressing the sample separation window as in Figure 29 which shows the two extremes of the range as declared by the slack parameter. The sample electropherogram was warped stepwise from the lower to upper bounds slack parameter.

To accommodate the changing number of data points, the separation windows were interpolated during each iteration. Each iteration of separation window warpings was coupled with a set of time offsets and overlaid with the reference separation. The time offsets were stepped through the range of zero-padded rows in front of and behind the separation window, effectively sliding the sample window over the reference window. A correlation coefficient was calculated between the sample and reference electropherograms for each warping iteration and at each slide position. The sample separation warping and slide position with the highest correlation to the reference was then copied to its respective column in a new aligned 2D data matrix. This aligned column then acted as the reference separation window for the next sample separation column to undergo the same warping. Upon completion of pairwise alignment across the entire 2D separation space, the aligned data matrix was ready for visualization and analysis.
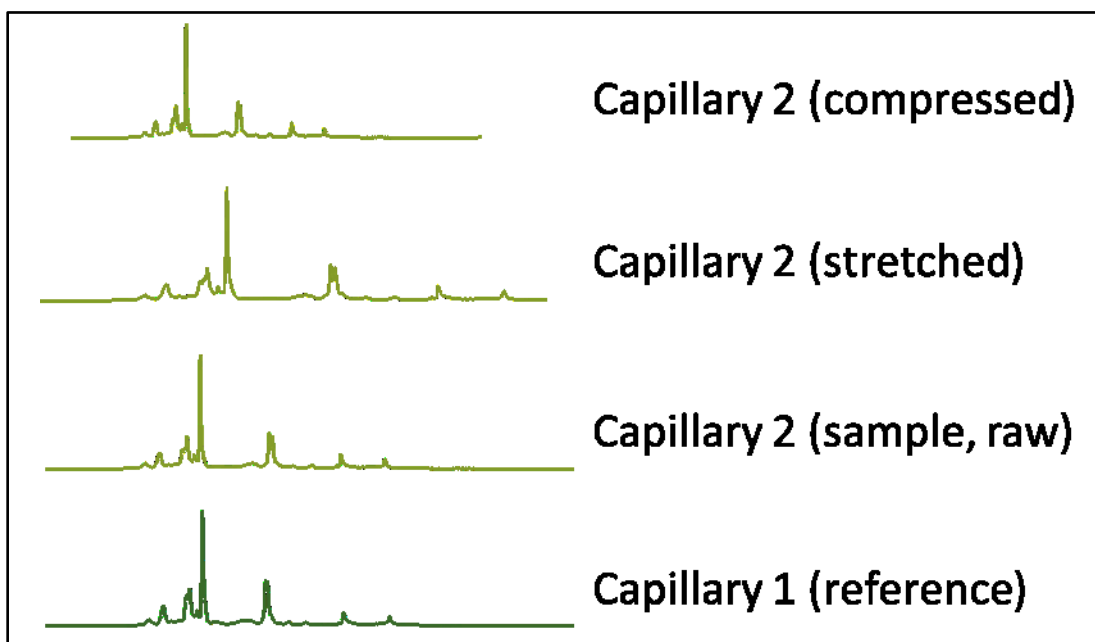
Figure 29 Depiction of a sample electropherogram warped by compressing and stretching it in the time dimension. Here, the injection performed on the first capillary was used as the reference and the injection performed on the second capillary was the sample. The sample electropherogram is shows at two extremes of the warping range such that it is at the extremes of compression and stretching. The sample electropherogram was warped iteratively so that it was compressed and stretched in small increments. Each warping iteration was compared to the reference electropherogram by calculating a correlation coefficient. The iteration with the highest correlation to the reference was saved to the final 2D electropherogram.

Although the above figures were demonstrated with identical tryptic digest sample injections onto all of the ^{2}D capillaries, the above described COW method was expected to work for 2D separations where the ^{1}D effluent was not constant but rather varied over the separation. The ^{1}D was operated slower than the ^{2}D, resulting in ^{1}D peaks that would be wider than the time between

injections onto the ^{2}D capillary array. Thus, any given ^{1}D peak would be split across two or more injections onto the ^{2}D. Although these peaks would be increasing or decreasing in height between adjacent separations, they would still act as landmarks for the COW algorithm to identify as correlated signal changes. For example, Figure 30 demonstrates an eight electropherogram subset of the total set of ^{2}D electropherograms from a 2D separation of serum peptides. Although there are no landmark peaks that span all eight injections, each electropherogram shares a peak with one or more adjacent electropherograms.
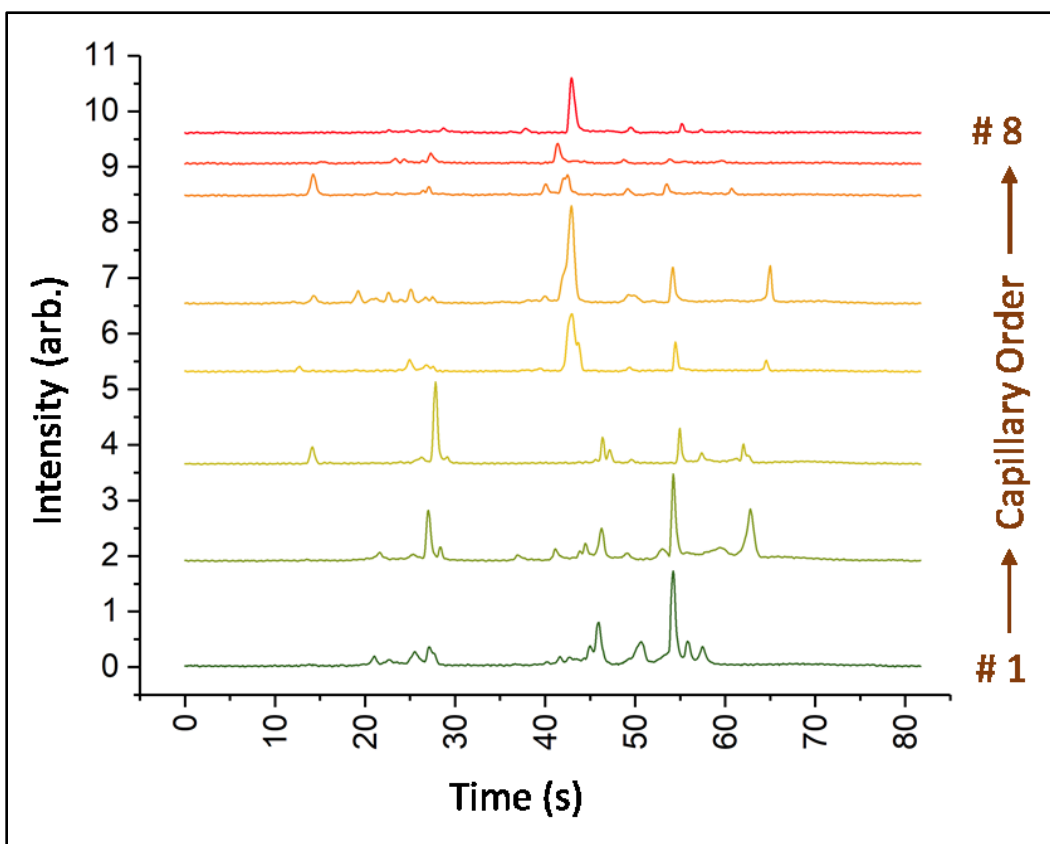
Figure 30 Raw data from a subset of electropherograms from a 2D separation of tryptic serum peptides showing the availability of landmark peaks for data alignment between ^{2}D separations. Eight separation profiles are shown from the sequential injection of effluent from the ^{1}D separation onto the ^{2}D capillary array. Signal traces are vertically offset for clarity.

Chapter 3   **Operation, Optimization and Characterization of the ^{2}D Capillary Array as Independent Parallel One-Dimensional Separations**

3.1 Capillary Array: Multidimensional Separations Interface Optimization

Prior to using the MDS interface to perform two-dimensional separations, a series of experiments were carried—out to evaluate the performance of the ^{2}D separations to ensure that the separation efficiency would be adequate for MDS. This chapter begins with a discussion of the important design and operational characteristics of the MDS interface. Then it provides an examination of experiments performed to evaluate the capillary array performance and relates them to typical figures of merit as found in the literature for well optimized instruments with a focus on its suitability for MDS.

3.1.1 Multiplexed Capillary Interfacing in a Laminar Flow Chip Device

The key function of the MDS interface, owing to its motorized position control in an X-Y plane (Figure 31), was to position the ^{2}D receiver capillaries in relation to the ^{1}D donor capillary such that they could be: (1) coaxial with (and below) the ^{1}D capillary during sample transfer or (2) out of coaxial alignment and away from the ^{1}D effluent stream. The constant downward laminar stream of BGE, that flowed through the MDS interface and surrounded the capillary tips, carried ^{1}D effluent downstream and coaxial with the capillary. This laminar stream directed the effluent to the opening of a ^{2}D receiver capillary during an injection. The same stream effectively removed excess sample from the ^{2}D capillary tip at the end of an injection and directed the ^{1}D effluent downstream to waste.
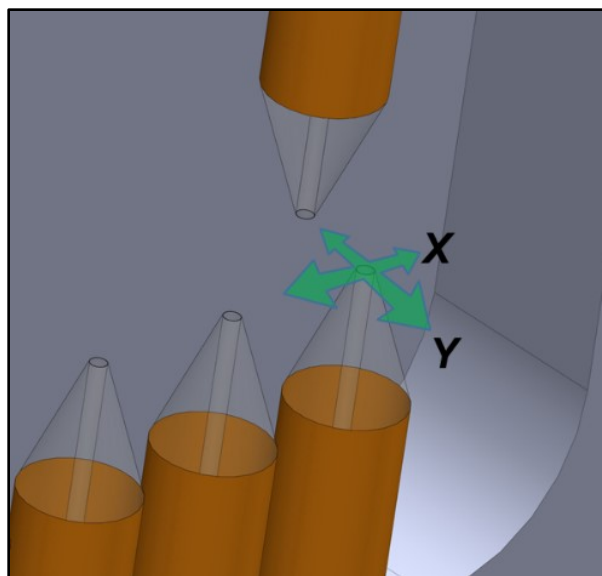
Figure 31 Depiction of the X-Y axes that was available for the ^{2}D MDS interface, as was provided by the attached motorized linear translation stages.

To facilitate efficient sample removal after injections, the ^{2}D capillary tips were positioned deep in the MDS interface chip, relative to its top face. This ensured they were surrounded by laminar flowing BGE. The calculated entrance length (see Section 2.2.1), where the laminar flow is fully developed, was estimated at 598 μm from the MDS chip entrance whereas the capillary tips were placed even deeper at 1300 μm. The calculations were performed with a BGE velocity of 3.3 mm/s flowing through entrance of the MDS interface chip; much higher than typical operating velocities. These overestimations were implemented as safety margins to ensure the flow regime in the region of interest was laminar and to provide the flexibility of operating at high flow rates in future experiments.

One consequence of placing the ^{2}D capillary tips deep in the MDS interface chip was that the ^{1}D capillary was extended ≈38 mm from the ferrule holding its PEEK sleeve in place. This long extension, and the narrowness of the channel (0.865 mm between the window and the back wall) meant that it was critical to control the angle of entry. Even a slight angle away from co-linearity with the ^{2}D capillaries would cause the ^{1}D capillary to bend as it contacted the edges of the chip entrance. The capillary angle relied on the PEEK tubing, that sleeved over the capillary, to be accurately straightened before mounting it in the suspension arm.

A disadvantage of the motion control system described herein, where each axis was controlled independently through the asynchronous USB bus, was inability to produce movements in the X-Y plane that were coordinated. Commands to move to a given position could result in steps along each axis being given pseudorandom priority over the other as a function of the complex path that software commands take as they are converted stepper motor movements. To relax the requirement for precision movement three notable procedural and design features were incorporated. First, all movements were broken down into separate X or Y movement commands to eliminate USB bus timing imprecision. This inspired the motion pattern (see Figure 23 above) used to perform round-robin injections across the entire capillary array. Second, the movement path was set so that the ^{2}D capillary array was always in front of the ^{1}D donor capillary so that there was no chance of an accidental contact with the front optical face of the chip. Later chip designs incorporated a 0.25 mm gap between the optical face and the edge of the capillary array to further minimize the likelihood of interference with the ^{1}D capillary during operation. Third, the ^{1}D capillary used was changed from a 365 μm o.d. to a 180 μm o.d. capillary, while keeping the 100 μm i.d. lumen. This allowed greater freedom of movement within the chip while also providing better ^{1}D cooling of the Joule heat due to the thinner silica wall which was important because the ^{1}D capillary was passively cooled by ambient air.

A notable convenience arising from the laminar flow design of this MDS interface is that the bulk sheathing buffer performs three functions. In addition to efficiently bounding injections when motorized transverse plane control is applied, it carries away waste, and provides a constant supply of fresh buffer to the MDS interface. This avoids problems of buffer depletion that is typical when buffer vials are used over long separation times. Also, the open-air design would otherwise be problematic as a 1-hour separation would lead to significant evaporation and concentration of the buffer if it was a static volume. The constant replenishment and meniscus control afford higher buffering capacity at the expense of greater buffer use.

3.1.2 Capillary Alignment in the X-Y Plane: Methodology

The computer control used in this work was conceptually simple with respect to the pattern of movement in the X-Y plane. However, determining the exact positions required to coaxially align the ^{2}D capillaries in the ^{1}D effluent stream was a non-trivial task. The CCD camera placed to view the front of the MDS interface provided an instructive view of the axial tip-to-tip (Z-axis) distance

between the donor and receiver capillary tips as well as their horizontal alignment (X-axis). However, the camera image provided no depth information (Y-axis), requiring a proxy indicator to determine depth alignment between capillaries. To perform successful automated injections, the optimal positions for sample transfer needed to be mapped and recorded for each ^{2}D capillary.

First, alignment was performed in the image plane (X- and Z-axes). Using the camera view, each of the eight ^{2}D capillary inlets was manually aligned to a uniform Z height (within 50 μm) within the laminar flow entrance length of the MDS interface. The tallest of the 2D capillaries set the "zero" of the Z-axis.

To set the height of the ^{1}D capillary tip, it was lowered (Z-axis) into the MDS interface, using the micrometer on its translation stage, until it contacted the tallest ^{2}D capillary at Z = 0. Contact was confirmed by moving the array along the X-axis until the ^{1}D capillary was visibly deflected a short distance. The ^{1}D capillary was then raised about 10 – 40 μm above the point where it was released, which is a similar distance to previously successful CE×CE couplings.[151,153,189] By performing this height setting procedure on the tallest ^{2}D capillary adequate clearance for all capillaries was insured.

Next, the capillaries were aligned horizontally by stepping the X-axis stage until the ^{1}D and selected ^{2}D capillary appeared to align in the camera image. The visual alignment was confirmed by observing dye as it was transferred between capillaries. This was performed with CBB under room light or fluorescein under illumination by fiber optic guided (see Figure 16) violet laser light (460 nm).

3.1.3 Capillary Alignment in the X-Y Plane: Characterization

To locate the optimal alignment along the Y-axis an injection search pattern was performed to "map out" the injection region and locate the position that maximized the amount of sample transferred from the ^{1}D to ^{2}D. Fluorescein was infused in the ^{1}D capillary with the ^{2}D capillary offset in front and to the right of it by ≈0.5 mm (see Figure 32). This distance was large enough to ensure that the bulk laminar flow carried the fluorescein to waste and would not enter the ^{2}D capillary. The MDS interface was then moved in a repeated square pattern such that the sides parallel to the X-axis were 1 mm in length and overlapped the ^{1}D effluent approximately at its center. The Y-axis length was set to 25.4 μm. The initial square path was placed where it was

known avoid any transfer of fluorescein onto the ^{2}D capillary. For each iteration, the path increased by 25.4 μm in the Y direction while maintaining the same origin and motion along the X-axis. After several iterations, the path extended far enough along the Y-axis such that injections were performed during the 1 mm transit along the X-axis. This produced a series of injections whose transfer efficiency varied with the capillary alignment along the Y-axis. This produced the series of peaks shown in Figure 33, where the optimal alignment produced the largest peaks indicating the greatest injection volume. Peak intensity decreased with increasing offset distance, indicating that less sample was being injected onto the capillary. It is noteworthy that the signal didn't decay to baseline above 200 μm (Figure 33 E). This was due to this data being collected on an earlier prototype of the MDS interface where there was insufficient space for the ^{1}D capillary clear the ^{2}D capillary array completely, which was improved in later designs.
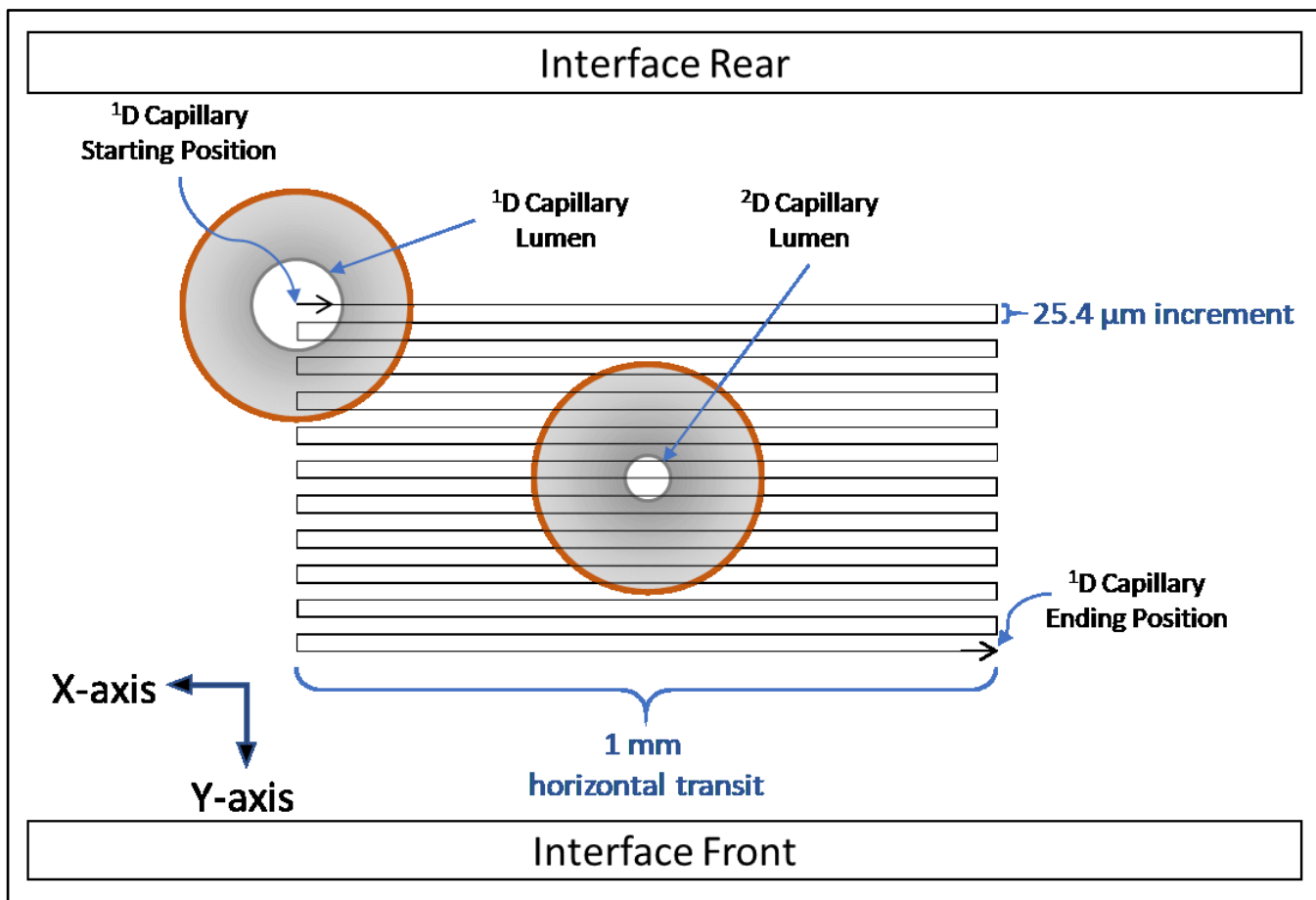
Figure 32 Depiction of a top-down view of the serpentine search pattern used to locate the coaxial alignment between the ^{1}D capillary outlet and a ^{2}D capillary inlet. Fluorescein was continuously emitted by the ^{1}D capillary. The two capillaries were initially positioned away from each other. The ^{1}D capillary transited horizontally in a straight line to the right, moved forward by a 25.4 μm increment, transited horizontally to the left and moved forward by a 25.4 μm increment. This pattern was repeated until the 20 increments were performed.
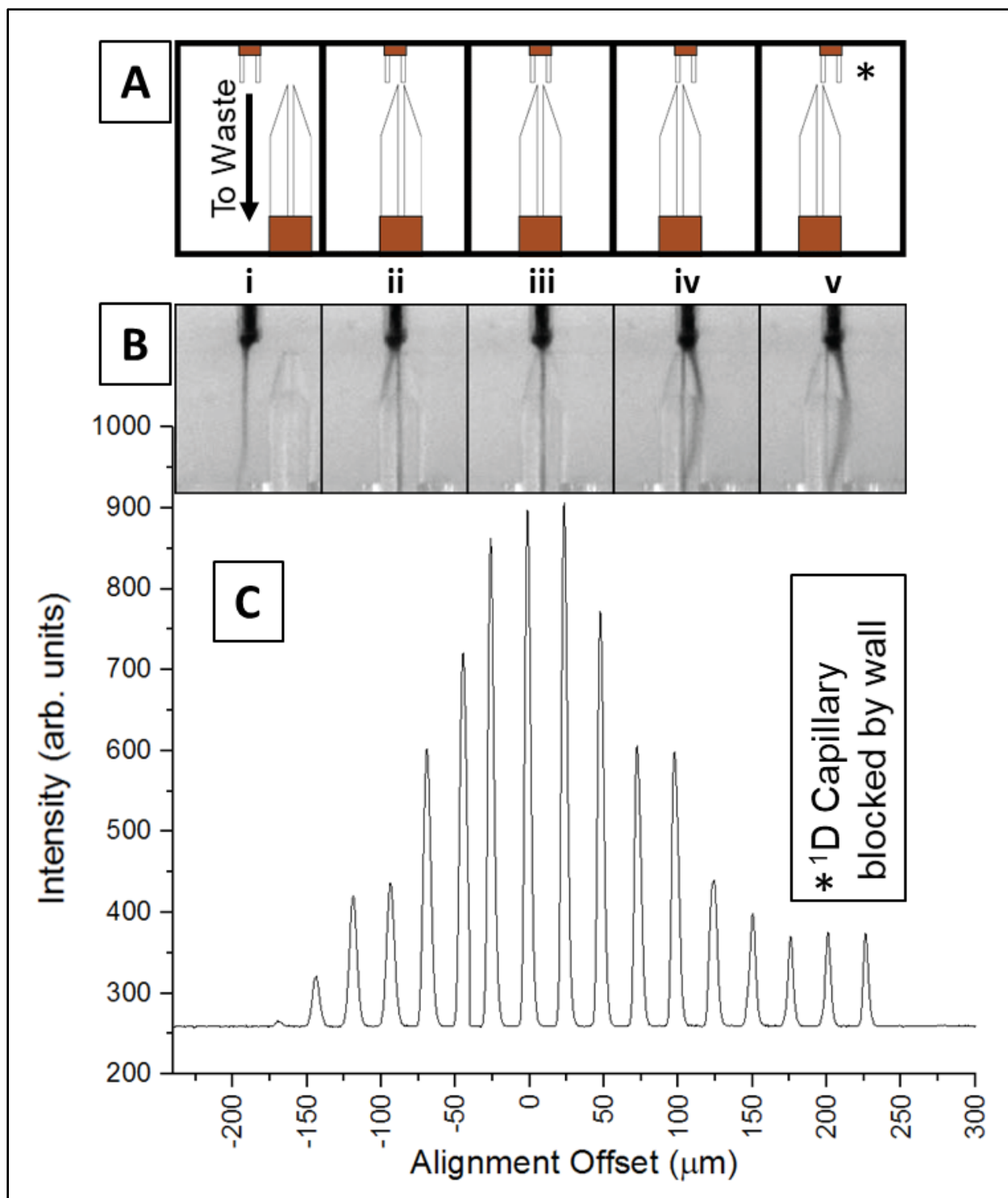
Figure 33 Effect of capillary alignment along the Y-axis. Top images (A) depict the receiver capillary placed in a series of positions along the Y-axis; during each it was transited past the donor capillary along the X-axis. Lower images (B) were captured with at the positions depicted in the above images, while aligned along the X-axis. Donor capillary effluent was Coomassie Brilliant Blue dye tracer solution. The plotted data (C) was produced from the fluorescein peaks generated as the receiver capillary was transited past the donor capillary effluent along the X-axis, while it was incremented through a series of positions along the Y-axis (25.4 µm apart). The donor capillary provided a steady effluent stream of fluorescein during the serpentine motion pattern.

The data showed that using a 100 μm i.d. donor capillary with a 50 μm i.d. receiver capillary could transfer an effectively equivalent sample at three positions along a single motor axis, spanning a 50.8 μm (nominal) range. The stepper motors used here were limited to a movement resolution of 25.4 μm/step, which is equivalent to operation in full stepping mode. Attempts to operate at fractional steps made positioning unreliable.

The fluorescein injection method described above provided quantitative information on the injection efficiency. However, given a horizontal transit time of 30 s in the serpentine search pattern at each 25.4 μm increment meant that generation of a full positioning profile would require about 10 min per capillary or nearly an hour and a half for a mere eight capillaries. This serpentine search method was required because the MDS interface geometry precluded effective fluorescence imaging of the injection. Thus, injection information could only be gathers by observing the eluted peaks at the sheath flow cuvette. Fortunately, using the non-fluorescent dye Coomassie Brilliant Blue G (CBB) allowed the same positional information to be obtained, as can be seen in the inset images in Figure 33 B. Using joystick control of the 2D translation stage, each receiver capillary could be incrementally moved until the CBB stream emerging from the ^{1}D donor capillary was captured by the receiver capillary.

The contrast provided by the opacity of the injected CBB dye allowed detection of translations as small as single-steps (25.4 μm, nominal). Initially, the capillaries were far apart with ^{1}D effluent entrained in the BGE and directed to waste (Figure 33 B-i). As the ^{2}D capillary was moved stepwise (to the left in the image) towards alignment with the ^{1}D capillary, the stream of CBB would first contact the side of the ^{2}D capillary. Upon closer co-axial alignment, some CBB would flow into the ^{2}D capillary (Figure 33 B-ii). As the two capillaries were brought into optimal alignment the entire lumen became filled (Figure 33 B-iii) with excess CBB flowing along the ^{2}D capillary outer wall. The behaviour of the tracer was mirrored as the ^{2}D capillary continued past the center of the effluent stream, with the CBB appearing as a stream that flowed along the right side of the lumen wall (Figure 33 B-iv). As was observed with fluorescein, one to two steps away from the optimal alignment typically caused a dramatic change in the observed opacity of the injected CBB. The midpoint between these "drop-off" positions was used as the optimum injection position for a given capillary. This method produced highly accurate positional information and

was used for the remainder of experiments and confirmed with repeat fluorescein injections onto the capillary array at the start of each day.

With some frustration, it was discovered that a considerable warm up time was required for accurate positioning and control. In the current design, the stepper motors were mounted to the translation stages and draw their maximum current when holding the stage at a fixed position. As such, they generated a steady supply of waste heat which caused thermal expansion of the 2D translation stage apparatus. Additionally, the way that the manifold was mounted to translation stage acted as a cantilever, which further magnified the heat expansion. This resulted in a visible shift in both the vertical and horizontal dimensions of about 1 mm as observed by the camera. Therefore, it was not possible to use the system until a steady state of heat flux was reached. The stepper motors were allowed at least 45 min to warm up before any use if in a cold state.

3.1.4 Axial Injection Distance

Since the laminar flow of BGE used in this MDS interface was oriented coaxial to the ^{1}D and ^{2}D capillary axes, compared to the perpendicular BGE flow in typical cross-flow interface designs, the effect of axial distance between the ^{1}D and ^{2}D capillary tips was investigated. As the vertical axis (Z-axis) was not motorized, the ^{1}D donor capillary was adjusted manually. The initial donor capillary axial distance was set as described (Section 3.1.2) and replicate injections of fluorescein solution were migrated to the detector and measured. This was repeated at distances starting from 20 μm and incremented by 50 μm intervals up to 220 μm. An inverse relationship between injection distance and resultant peak area is seen in Figure 34. The inset images show the different axial distances used for each set of injections, with 1 mM CBB infused in the ^{1}D capillary for visual clarity. Upon reaching a 220 μm gap between donor and receiver capillaries no discernable peaks could be observed.
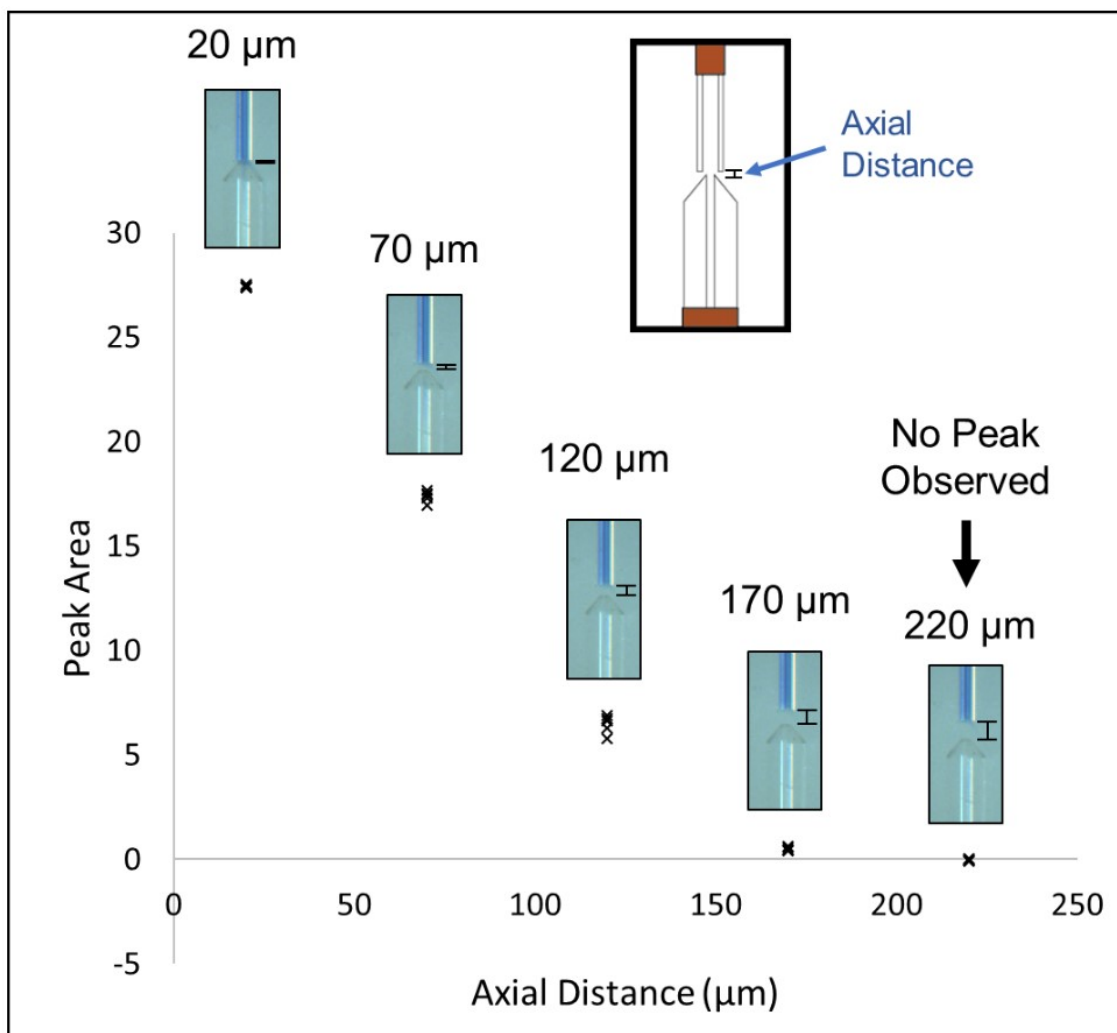
Figure 34 Effect of axial injection distance on quantity of [1]D effluent transferred to a [2]D capillary; varied from 20 μm to 220 μm. Plotted peak areas were of 300 ms injections (5 reps) of 100 nM fluorescein. Overlaid images show the [1]D donor capillary infused with CBB at the distances used to generate the replicate peak area measurements plotted in the figure.

The greatest injection efficiency occurred at the shortest axial distance, similar to previous designs that interfaced two electrophoresis capillaries[151,153,189]. The amount of sample transferred decreased rapidly with increasing axial distance, as evidenced by the recorded peak areas. The effective working range was therefore quite narrow, which meant that the capillaries had to be positioned very carefully to be in a straight line and be parallel to the plane of motion of the 2D translation stage. The introduction of any angle between them would cause the axial distance between the [1]D and each adjacent [2]D capillary to rise or fall in relation to the slop of the angle. Thus, to ensure effective injections it was critical to minimize the inter-capillary distance and ensure high precision in the height of each [2]D capillary in the array.

Considerable effort was required to align the ^{2}D capillaries with high precision. Thus, the prospect of relaxing the tolerances required, by using longer axial distances, was investigated. To further elucidate the behaviour occurring during successful and unsuccessful injections, video recordings were compared between injections were made at 20 μm and 220 μm injection distances. A series of images showing key time points across an 1800 ms window surrounding an injection sequence performed at 20 μm (Figure 35) and 220 μm (Figure 36) gap sizes. The ^{1}D donor capillary (uncoated) was infused with a 1 mM CBB solution prepared in BGE. During the injection sequence, the ^{2}D receiver capillary (uncoated, tapered) was moved (towards image right) to bring the two capillaries into alignment for a 300 ms injection and then returned to its original position to stop the injection.
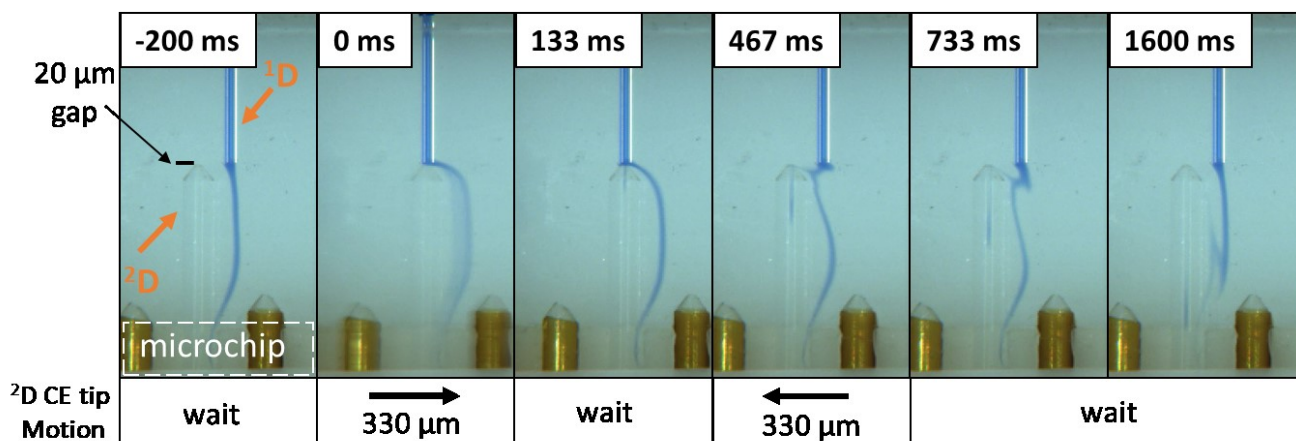
Figure 35 Injection sequence with axial distance of 20 μm for a 300 ms injection of CBB dye tracer.

Figure 35 shows the behaviour of a typical successful injection sequence, where the axial gap between ^{1}D and ^{2}D capillaries was set at 20 μm. The ^{2}D receiver capillary was initially (- 200 ms) located at the pre-injection position, 330 μm to the left of the donor capillary. CBB is shown infused within the donor capillary and entrained in a downward laminar flow to the right of the ^{2}D receiver capillary. The effluent path maintained a distance to the right of the ^{2}D capillary of approximately 200 – 300 μm until it was drawn into the interstitial space between the ^{2}D capillary and the square channel in the microchip (see Figure 17). At 0 ms, the receiver capillary moved towards the right until it was coaxial with the donor capillary. During the 300 ms injection time, the receiver capillary remained stationary as ^{1}D effluent flowed over it and entered its lumen (133 ms). To stop the injection, the ^{2}D capillary returned to the pre-injection position ending the injection sequence where the CBB was washed away from the lumen and down the tapered

113

capillary tip (467 ms – 733 ms). The original streamline of the effluent was re-established by fresh effluent travelling down the MDS interface in the post-injection position (1600 ms).

Figure 36 shows the same injection sequence as above but used a larger 200 μm gap between the donor and receiver capillaries. An interesting difference occurred in the behaviour of the effluent path during this injection sequence. As the MDS interface shifted to the right to bring the capillaries into alignment, the effluent stream that already exited the donor capillary followed suit to maintain its position within the bulk fluid volume as would be expected. What was surprising occurred when the MDS interface moved to the post-injection position. Despite the capillaries having been brought into coaxial alignment, the effluent that was expelled while they were aligned failed to maintain its position in the bulk flow field after the MDS interface moved to the post-injection position. Thus, it did not reach the entrance of the receiver capillary, instead being diverted towards the right while it maintained at least a 100 μm distance from the capillary throughout its travel. To the best of my knowledge this behaviour has not been described in the microfluidic separations literature.
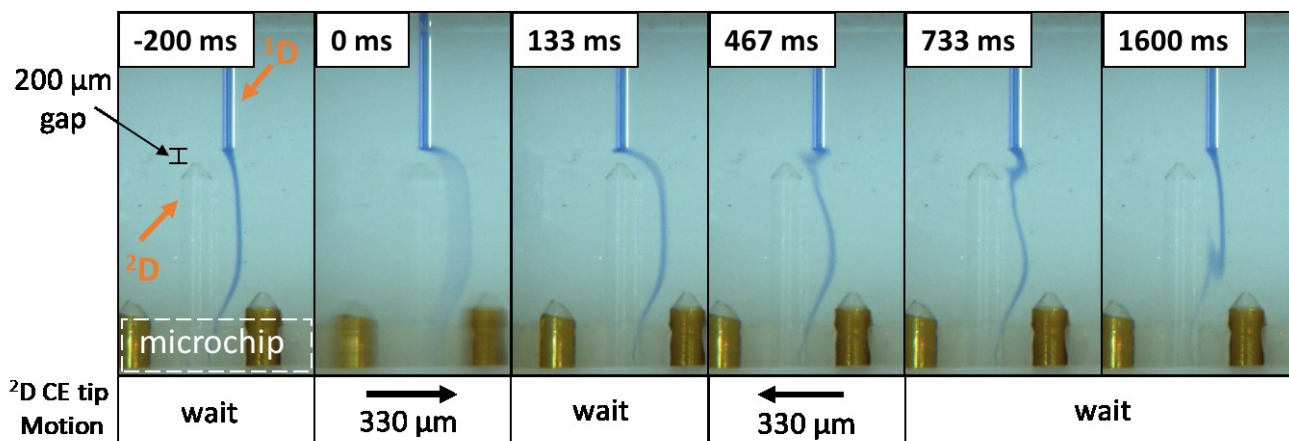
Figure 36 Injection sequence with axial distance of 200 μm for a 300 ms injection of CBB dye tracer.

This behaviour appeared to be the result of a combination of the no-slip condition (Section 1.14.1) and conservation of mass within the moving MDS interface. The no-slip condition resulted in a velocity gradient that extended outwards from the receiver capillary, normal to its surfaces. As a result, the BGE flow diverged away from the 2D capillary axis, starting at a (undetermined) point upstream of the capillary tip. As the MDS interface shifted the fluid system to the right, to bring the capillaries into coaxial alignment, the stationary donor capillary created a void which was then filled with nearby buffer. The donor capillary effluent stream appeared to simply move

horizontally with the outlet tip, as the wash flow filled the capillary displacement volume. During the complementary post-injection retraction, the lower velocity region surrounding the receiver capillary tip caused the secondary displacement of the donor capillary to have a greater effect. This was clearly demonstrated at 467 ms, where the effluent path was drawn upwards so that it appeared to be at the same height as the effluent exiting the ^{1}D. Since the effluent dispensed at the injection position had experienced a lower downward velocity than in the surrounding flow field, the displacement of the donor capillary was able to draw the effluent upwards to a position where the streamlines were oriented away from the receiver capillary. Thus, the effluent path adopted a trajectory that precluded an injection.

Early experiments demonstrated that injections could still be made using large axial distances. However, the injection position was not coaxial and had to be determined using dye tracers. More problematic was that the MDS interface assembly had to be held in the injection position for a much longer time for the effluent path be successfully directed to the receiver capillary. In CE, the theoretical plate number (plate height) is primarily determined by two factors: injection time and analyte diffusion. The optimum analytical performance (maximized peak area and minimized peak width) is generally encountered at the transition from diffusion controlled to injection time controlled peak widths. For small molecules, an instrument capable of short injections is desirable. Given the difficulty in finding the correct "spot" for long axial distance injections and the increased diffusion that would occur during long transit distances, further experiments used the shortest axial distance possible between capillaries during injections; typically, between 20 – 50 μm.

3.1.5 Injection Time

In order for a MDS interface to ameliorate the problem of undersampling in MDS, the ^{2}D separation efficiency must meaningfully contribute to the total peak capacity.[190] As, mentioned in the last section, injection efficiency is a major contributor to peak broadening in CE. Theoretical plate number, a key metric for evaluating separation performance in linear separations, can thus be determined as a function of injection time. Here, fluorescein was used as a small molecule probe to evaluate the impact of injection time on plate number and to determine the efficiencies achievable from each capillary in the 2D array.

The data shown in Figure 37, represents a series of injections from 50 ms to 800 ms. As expected, two types of response were observed: diffusion controlled and injection time controlled. The

theoretical plate number (100 000 – 115 000) at injection times less than 200 ms, compared favourably with the predicted diffusion limited plate number, of 114 000, for fluorescein. However, in this region poor reproducibility also suggests that the stepper motor driven linear actuators were not able to deliver reliable injections. At injections time in the 200 ms to 800 ms range an inverse proportional relationship between plate number and injection time was observed.
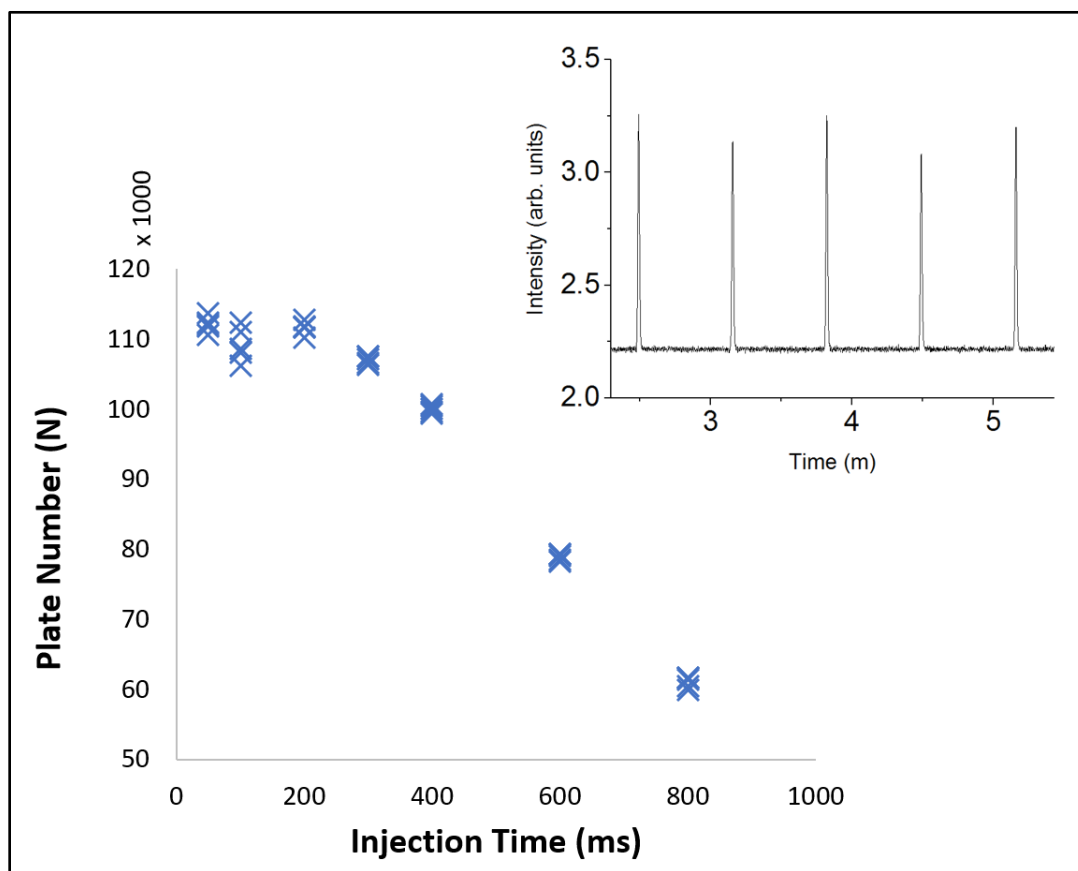
Figure 37 Effect of injection time on theoretical plate number for a series of 300 nM fluorescein injections (5 reps) onto a single [2]D capillary. BGE and sample solvent was prepared using 25 mM borate with 5 mM SDS, pH 9.2. Inset is a of typical peak profile from a set of five 300 ms injections.

These results clearly demonstrated that, by using precise motion control to bring the capillaries into coaxial alignment, injection plugs with sharp boundaries can be produced. The number of theoretical plates also compares well to optimized CE instruments[191–193], though it comes well below the most efficient separations.[194] The prototype presented in this thesis uses low cost stepper motors and drivers. Equipment exists with much higher speed and linear resolution, which would allow for further improvement in sample introduction control. The per capillary plate numbers spanned a range of 93 000 to 115 000 theoretical plates, which normalized to 604 000 to 747 000

plates per meter (Table 1) This result showed only a 24 % range which is encouraging as it suggested a variability between capillaries that was small enough for numerical correction if appropriate internal standards were introduced to the separation.[180] Capillaries 3 and 4 produced larger variability than the other capillaries due to a single peak in each set that with much higher plate number than the rest. The cause for these two apparent outliers could not be determined, however the remaining 4 data points were similarly closely spaced as compared to the other 6 capillaries.

Table 1 Optimal theoretical plate numbers for eight 15.4 cm capillaries in ^{2}D array for injections of 100 nM fluorescein dissolved in 25 mM borate, 5 mM SDS BGE. Injection time 200 ms, axial distance 20 – 50 μm. Equivalent theoretical plates/meter are also displayed.

Capillary Number	Average Plate Number (n=5)	Standard Deviation	%RSD	Plates / m
1	108 000	846	0.79	701 000
2	115 000	798	0.68	747 000
3	93 000	4493	4.9	604 000
4	119 000	11 082	9.3	773 000
5	100 000	723	0.73	649 000
6	106 000	743	0.70	688 000
7	106 000	666	0.63	688 000
8	112 000	927	0.83	727 000
Average Among All Capillaries	107 000			697 000
Standard Deviation	8400			
%RSD	7.9			

The 200 ms injection, at the inflection point, corresponded to a predicted 0.3 % capillary volume injection plug size with respect to the EOF, suggesting that up to a 600 ms injection could be used without significantly sacrificing peak width under matched ionic strength conditions. Since shorter injection times come at a cost to peak area, much of the later work used injections from 300 ms and upward to strike a balance between narrow peaks and signal intensity.

3.1.6 Laminar Flow Rate

An expected optimization parameter of the MDS interface used in this work was the velocity of the laminar wash flow. With the transverse flow interface from Jorgenson's group, the clearance of unused sample in the flow gate was decoupled from the injection, and thus only the slew time was affected by the wash flow rate.[127] The Dovichi group's design performed comprehensive injections, by transferring all of the ^{1}D effluent fraction within the gap between dimensions to the receiver capillary.[151] Our group's transverse design is the most similar, and found separation efficiency to have a small dependence on wash flow rate as long as it was sufficient to draw the ^{1}D effluent into two distinct and adjacent laminar flows down the waste channel.[156]

Before the flow rate could be evaluated for its effect on injection efficiency, it was important to determine the flow rate through the MDS interface chip. Since the MDS interface is assembled from a series of layered components, there were alternate circuitous paths for wash buffer to travel in addition to the milled channels in the MDS interface chip. Attempts to seal the alternate flow paths were not entirely successful. Therefore, using particle imaging velocimetry, the actual laminar flow velocity at the 2D capillary tips was measured.

The fiber optic used to illuminate the MDS interface was replaced with a 365 µm × 100 µm capillary with a tapered outlet and used to introduce the probe mixture instead of the ^{1}D separation capillary. This modification was done to avoid introduction of any downward momentum to the effluent exiting the capillary. An unfiltered 1 mM Nile Blue A solution prepared in sodium formate was delivered to the MDS interface at a distance 315 µm above the receiver capillary and 510 µm to the right. The unfiltered dye solution contained undissolved aggregates, allowing several 5 – 20 µm diameter particles to be used to track the fluid velocity by examining individual frames from the captured video (data not shown). Particles of undissolved Nile Blue A were monitored as they passed through a 460 µm vertical region with its midpoint at the height of the capillary inlet. A series of peristaltic pump speeds were used to adjust the MDS interface BGE velocity for use in producing the injection efficiency plot shown in Figure 38.
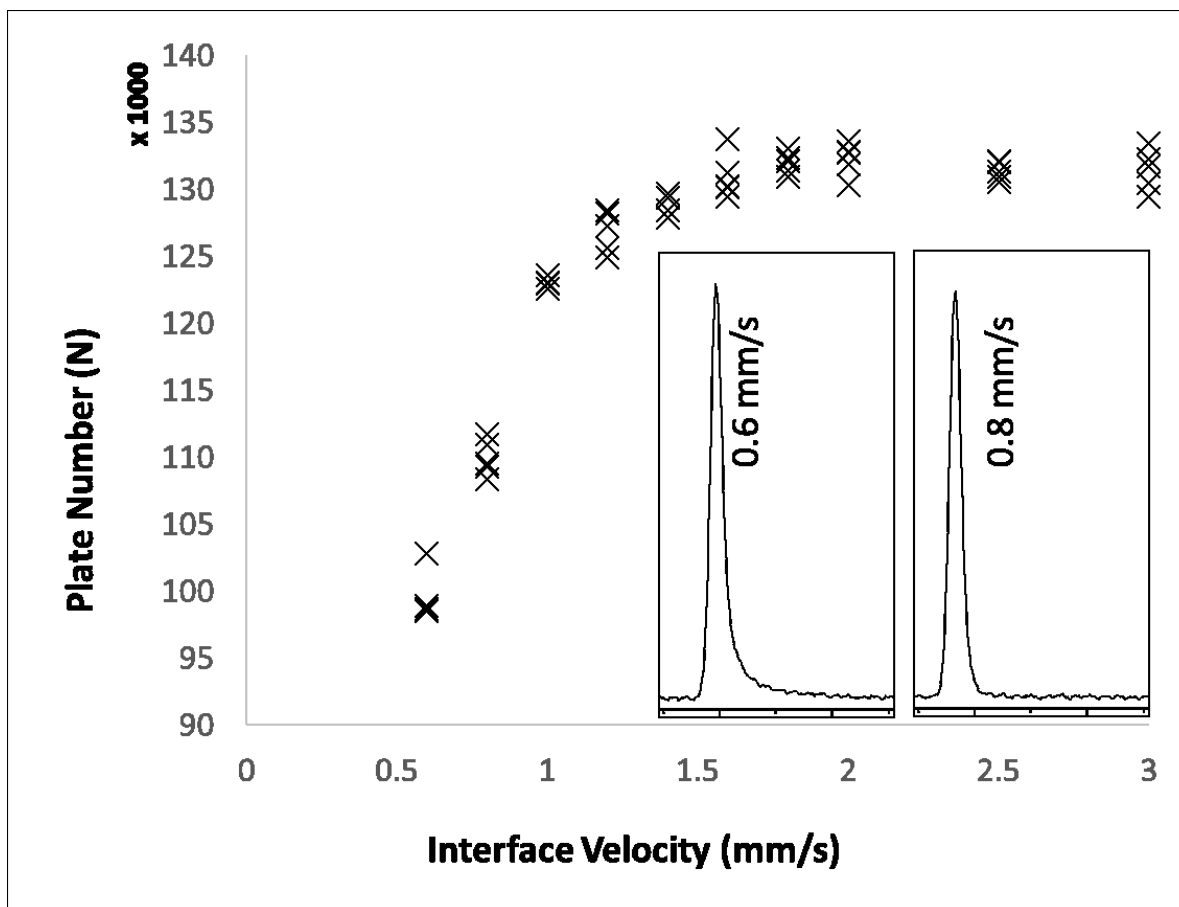
Figure 38 Effect of MDS interface BGE velocity on theoretical plate number for replicate 100 nM fluorescein injections on a single ^{2}D capillary. BGE velocity was varied from 0.6 mm/s – 3.0 mm/s. Inset peaks demonstrate tailing that was introduced blow 0.8 mm/s.

To evaluate the effect of MDS interface BGE velocity on injection efficiency, 300 ms injections were replicated on a single capillary while the MDS interface flow rate was varied from 0.6 – 3.0 mm/s. A 100 nM fluorescein solution dissolved in BGE was used as a fluorescent tracer. The data in Figure 38 show a rise in plate number corresponding to the injected peak width narrowing with increased flow rate of BGE through the MDS interface. The plate number rises with increasing BGE velocity from 0.6 mm/s to 2.0 mm/s, with the slope decreasing rapidly past 1.3 mm/s where further velocity increases up to 3 mm/s only raise the plate numbers by about 5 000 theoretical plates.

What is not represented in the plot is the sharp boundary where significant peak asymmetry is introduced. As can be seen in the inset images, the peak shape improves dramatically from 0.6 – 0.8 mm/s. Further experiments used a flow rate of 1.0 – 1.2 mm/s to maintain acceptable peak shape and strike a balance between injection efficiency and rate of buffer consumption.

3.1.7 ^{1}D Effluent Density Considerations

A cautionary note is introduced here, to cover an important event that shifted the focus of this dissertation. An original aim of this work was to design an instrument where the ^{1}D utilized a reversed-phase HPLC separation. Several months were dedicated to this avenue of research, with results best summarized as *chaotic*. The ^{2}D separation profiles were erratic, resulting in peaks that were shifted in time, peak heights that were unpredictable and peaks that were prone to disappear and reappear during a series of identical automated injections. The inconsistent results were observed between runs, days and weeks without any discernible pattern. Only upon fluorescent imaging of flows within the MDS interface, during a multidimensional separation using gradient elution in the first dimension, was the problem identified. A closer examination of the effects on the density challenges can be found in the appendices.

3.2 Capillary Array: Sheath Flow Cuvette Optimization

As with the MDS interface, the first order of business for the detector was to ensure proper alignment of the capillary array. Instead of having the luxury of individual positioning for each capillary inlet in the X-Y plane, the outlet tips must all be aligned along a linear path parallel to, and upstream of, the excitation laser. All parts of the assembly made use of the optical table mounting holes for positioning, which provided a coarse 90° orientation between the laser and camera paths with the cuvette at the intersection.

The cuvette was mounted to a two-dimensional translation stage, that allowed it to move in two directions that were both transverse to the laser beam. One direction was perpendicular to the optical table (Z-axis) and the other parallel to the table (Y-axis). The distance between the cuvette and laser (X-axis) was not used as an adjustment parameter, as the cuvette flow channel was centered upon waist of the beam and not modified. A sheet of polycarbonate plastic was screwed down onto the PDMS cuvette, fixing it to the translation stage. The polycarbonate sheet included a square hole that was centered about the emission window of the PDMS cuvette. This mounting setup provided enough freedom of movement to adjust the capillary array outlet tips to be just above the laser beam. However, fine adjustments to height, pitch and yaw—as commonly used to describe the axes of an aircraft—were accomplished using translation stage lead screws. Applying this coordinate system to the sheath flow cuvette, the laser excitation window (right side) is equivalent to the nose of an aircraft.
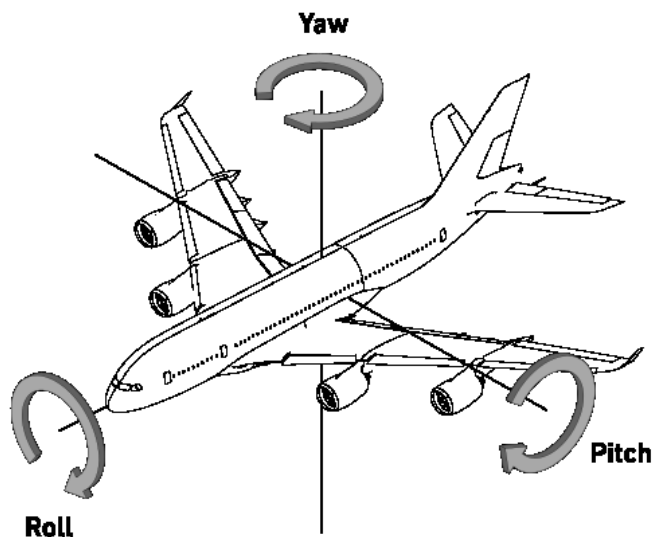
Figure 39 Orthographic projection demonstrating pitch, yaw and roll axes with respect to an aircraft. (Aashmango4793, 2019)[195]

Alignment procedures began during assembly (Figure 40), when the capillaries were inserted into the capillary channels of the PDMS flow cell until their tips were within a narrow range of heights. These channels sealed against each capillary to prevent BGE leakage. The capillaries were oriented with their outlets facing downwards, as guided by the PDMS channels, and held in a plane that was parallel to both the emission window and the camera image plane (Figure 40). The capillary tips were placed deep enough into the PDMS cell, so they were contained within the inner sheath flow channel. The path of the laser was made observable by the Raman scatter of the BGE, which broke through the long-pass optical filter placed between the sheath flow cuvette and the CCD camera. The laser entrance window was comprised of a PDMS outer layer, with an embedded inner glass window. The glass portion is visible in the camera image adjacent as a vertical shadow that is adjacent to the dummy capillaries. The laser was used to orient the rest of the apparatus, using an imaginary line created by the outlets of the array of separation capillaries.
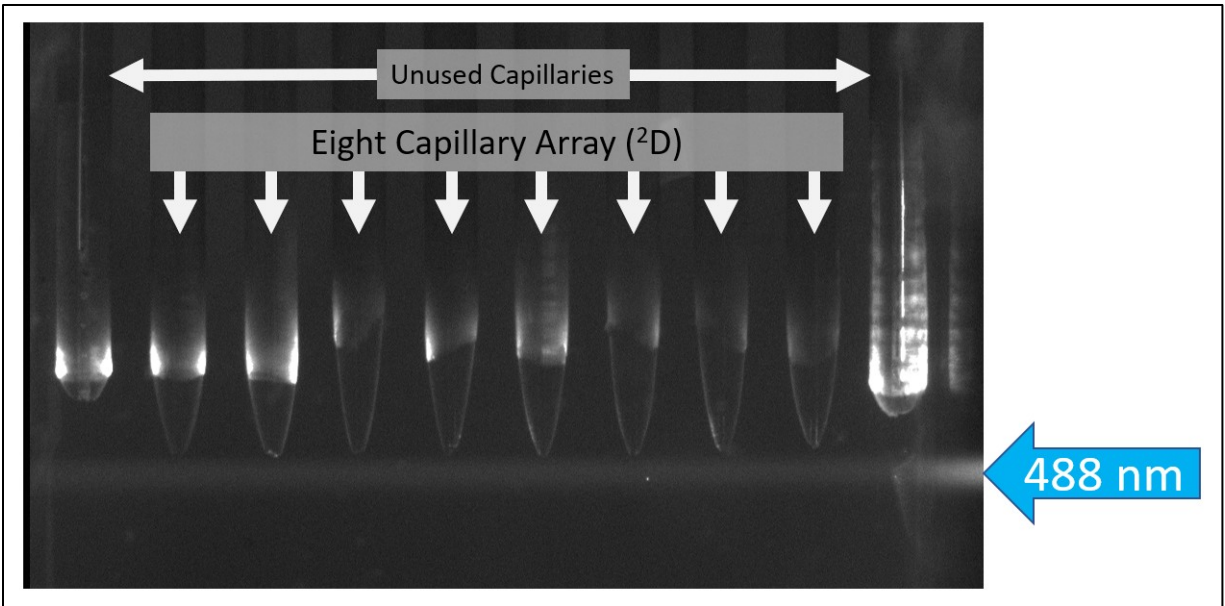
Figure 40 CCD detection system view of the sheath flow cuvette. The eight 365 μm o.d. separation capillaries (center) are shown with their outlet tips oriented downwards. Two unused capillaries were placed on the outermost capillary positions. The excitation beam was positioned directly under the capillary tips, entering from the right of the image.

To set the pitch rotation of the capillary tips, the cuvette was rotated within its holder, in the plane of the emission window, until the excitation window was oriented perpendicular to the laser path. This was confirmed by ensuring the faintly reflected laser beam was at the same height as the source.

Yaw rotation, in the plane of the table, was adjusted by rotating the L-bracket that held the sheath flow cuvette while its screws were loosened. This was particularly difficult since the 2D camera image was unable to provide any depth information. Additionally, the mounting slots of the L-bracket, which located the pivoting region, were placed ~50 mm behind the capillary array tips and restricted movement to wide arcing paths.

To orient the set of capillary tips to the laser, the outer dummy capillary nearest the laser was inserted deeply into the cuvette, until the polyimide coating was brightly illuminated by the laser. The micrometer and/or yaw adjustment screw were then manipulated until the laser was centered on the capillary. This outer capillary was retracted, and the same procedure was performed with the dummy capillary farthest from the laser (Figure 41).
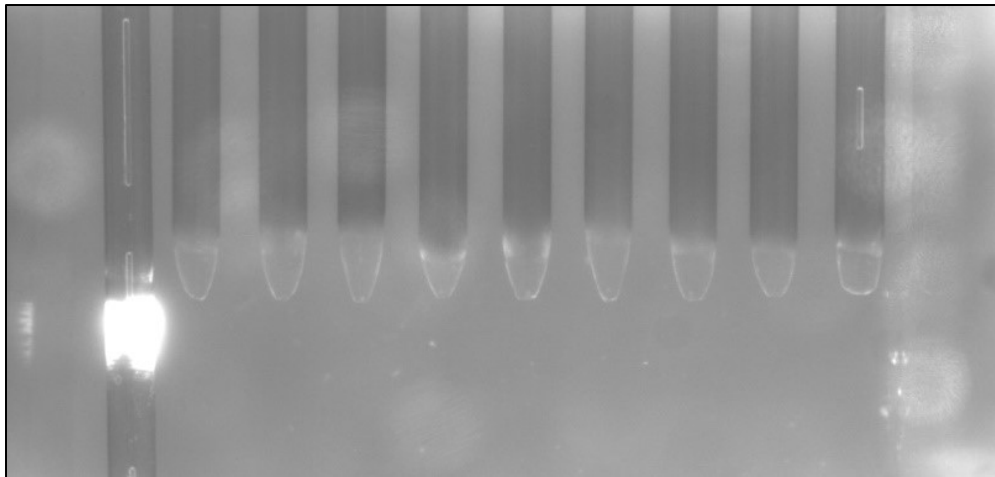
Figure 41 Procedure for aligning capillary array to the excitation laser. The sheath flow cuvette was manipulated while the left-hand dummy capillary was inserted deeply. The laser induced fluoresce of the polyimide coat guided the alignment of the capillary to the laser. A similar alignment performed on the right-hand dummy capillary ensured the laser path was linear with the capillary array.

This two-step sequence was repeated until both dummy capillaries were simultaneously aligned with the laser. Final confirmation of alignment with the laser was performed by infusing the working capillaries with a fluorophore and observing the fluorescing effluent stream as it exited the capillaries, see Figure 42.
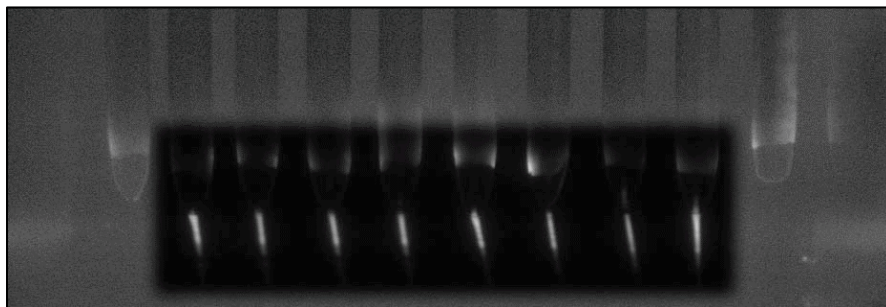
Figure 42 Composite image showing LIF of the effluent (50 nM fluorescein) exiting the capillary array simultaneously. Composite shows the image near the capillary tips as it was captured during a separation and the surrounding image was overexposed to display the other features within the detector cell. The fluorescence probe volume was visible for each capillary where the effluent stream and the laser beam (≈350 μm diameter) intersected.

Once the above steps were performed, the PDMS sheath flow cuvette was fixed in place and regular adjustment was only made to the depth of capillary insertion. This final adjustment was performed simply by increasing the laser output power and CCD camera gain until the laser path was easily visible. Each capillary was inserted so that their tips aligned to the uppermost point of the beam path, and then fixed in place by screwing the compression bracket in place. Fine

adjustment of the distance of the array to the laser beam was performed using the micrometer lead screws attached to the linear translation stages of the sheath flow cuvette assembly.

Development of the multi-capillary sheath flow cuvette detector proved to be challenging due to constraints caused by the design of the upstream MDS interface. These included: the [2]D capillary dimensions (14.5 mm long, 365 μm o.d.) and the range of movement required by the MDS interface to move through the range of capillary coupling positions. The [2]D capillary spacing required the translation stage to repeatedly travel an 8 mm distance along the Y-axis. To allow this, an S-curve (Figure 24 a) had to be introduced into the [2]D capillaries between the MDS interface and the detector. However, the short length of the 365 μm o.d. capillaries used resulted in them being stiff. This introduced a considerable axial spring force on the capillaries, which continuously varied as the MDS interface position changed. When left unchecked, this caused the capillaries to "creep" into the MDS interface and/or into the detector cell. Within the MDS interface, this pushed the capillaries out of the tight distance tolerances required for injections. Within the sheath flow cuvette, this pushed capillaries into the path of the laser beam resulting in scatter off the capillary tips or, if the movement was large (> 350 μm), intense fluorescence of the polyimide capillary coating. Thus, the capillaries required high clamping force to be applied by the screwed down polycarbonate support bar with PDMS padding. (Section 2.3.1)

Uniform laminar flow through the cross-section of the sheath flow cuvette channel, where capillary tips are contained, is a requirement for multiplexed CE detector cells. This prevents the effluent streams from being spuriously directed toward regions of lower velocity and away from the excitation laser. Early prototypes exhibited poor flow precision over time. One cause of this poor behavior, that was not obvious, was placement of the cathodic electrode in the BGE path of the sheath flow cuvette. Spontaneous bubble formation in the BGE was a frequent problem during long operations, starting several minutes into a run and increasing steadily over time. Nucleation of the bubbles primarily occurred inside the sheath flow cuvette but were also found along the tubing leading to the supply reservoir. Placement of the high-voltage electrode inside the cuvette at the PDMS cuvette BGE channel preceding the capillary array channel caused hydrogen gas formation as a by-product to electrolysis of the surrounding water. This would nucleate and grow on the electrode surface, as well as dissolve and appear at other locations within the BGE path.

These problems were largely overcome by placement of the cathodic electrode downstream of the cuvette.

The CCD camera used to photograph the sheath flow cuvette was also used to collect separations data. Fluorescence from the exiting effluent was captured by a rectangular portion of the viewable image, similar to the darkened area in Figure 42, as a series of time-spaced image frames. Within this frame, a smaller rectangular region-of-interest (ROI) was chosen for each capillary. This subset of ROIs was selected to bound the image regions where the each of the effluent probe volumes were visible. The pixel intensities within each ROI was summed to be used as the fluorescence signal for a given frame's sampling interval.

3.2.1 **Signal Variation Between Channels**

As described in Section 2.4, the effectiveness of chemometric treatment and analysis, when used with MDS separations, is dependent on the reproducibility between adjacent ^{2}D separations data. Shifts in migration time and signal intensity can bias the effect of the COW alignment algorithm used herein. Run-to-run reproducibility, on each capillary, was expected to be modest, due to the inherent precision limitations of CE methods which have relative standard deviations (%RSD) for peak area in the range of $5 - 6$ %[196]. This precision was expected to further worsen when compared across different capillaries, especially since there was no opportunity for washing/rejuvenation steps between injections/separations. Thus, an important first step in validation was to determine the signal reproducibility produced by the capillaries across the array.[156]

Fluorescein was used as a model fluorescent small molecule tracer. Each capillary in the ^{2}D received five replicate injections. Peak areas were used for comparison instead of peak heights, as is recommended for comparing precision in separations data.[196] The smallest and largest average peak areas were 27 and 43 which were collected from capillaries 5 and 7, respectively. The ratio of largest to smallest average peak area amounted to a 1.6-fold difference. %RSD ranged from $3.3 - 16.5$ % across all capillaries and did not appear to be correlated to the peak area. However, the observed standard deviations for raw peak areas were larger than the expected $5 - 6$ %.[196] There was no obvious correlation between the peak areas and the position of their originating capillary.

Table 2 Comparison of peak areas from replicate fluorescein injections for each capillary in the ^{2}D array by automated capture of the ^{1}D effluent using the MDS interface.

Capillary Number	Peak Area (time, s × intensity, arb)			$w_{1/2}$ (time, s)		
	Average (n = 5)	Standard Deviation	%RSD	Average (n = 5)	Standard Deviation	%RSD
1	33	1.1	3.3	0.87	0.0057	0.65
2	37	4.1	11	0.81	0.0053	0.66
3	40	3.5	8.7	0.75	0.0069	0.92
4	32	2.0	6.2	0.79	0.0038	0.48
5	43	7.1	17	0.91	0.0056	0.62
6	37	2.6	7.1	0.78	0.0033	0.42
7	27	3.1	11	0.80	0.0053	0.66
8	35	3.3	9.4	0.70	0.0050	0.72
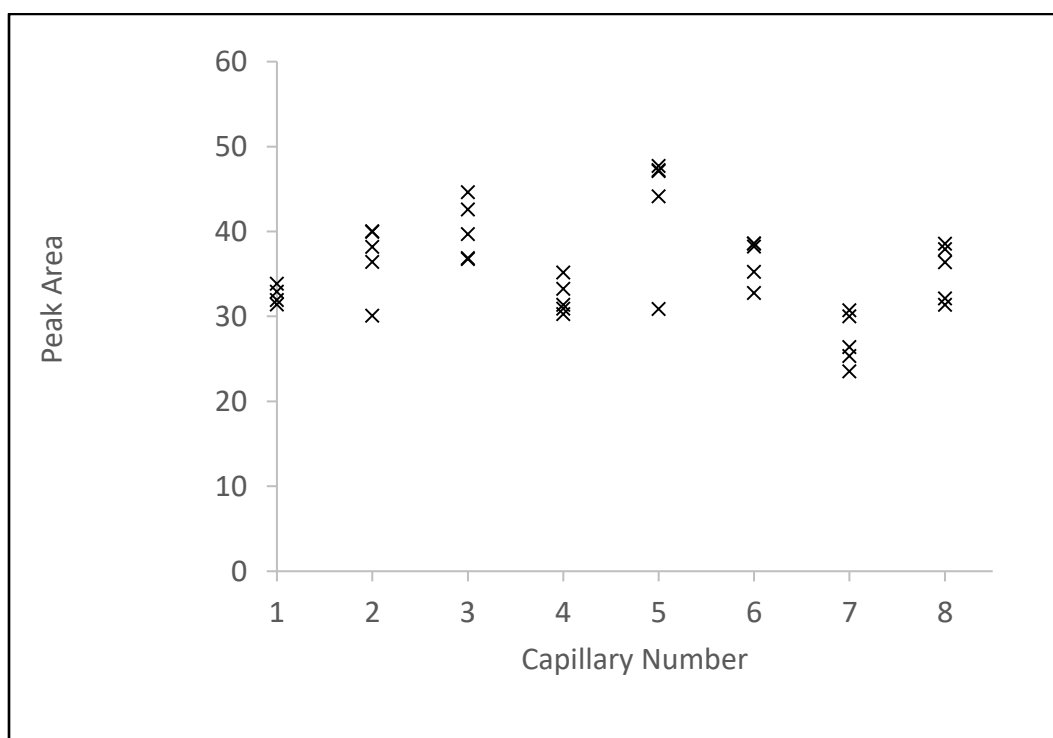
Figure 43 Measured peak areas from replicate fluorescein injections (5 reps) placed on each capillary in the ^{2}D array by automated capture of ^{1}D effluent using the MDS interface.

The demonstrated peak area variation was resultant from three main sources: injection precision, physical differences between each capillary and the effectiveness of how the sheath flow cuvette was designed and operated. The injection precision contribution to the variability, on a single

126

capillary, was expected to be mainly due to the precision of capillary positioning. This was assumed to be high due to the experiments performed in Section 3.1.3.

Early experiments (not shown) suggested that inlet tip shape impacted peak shape and injection efficiency thus between-capillary signal differences. A symmetric taper and small tip diameter have previously been shown to be important characteristics for efficient injections onto a capillary.[197] The jig used in this work, to set the taper angle, introduced some tip shape variability which likely increased injection variability between capillaries. Due to the laborious nature of the fabrication method used in this work, up to a ± 0.5 mm difference in length between ^{2}D capillaries was accepted. This would cause minor differences in peak width between capillaries due to slightly different field strengths within each capillary. Capillary wear was another source of inter-capillary differences. When samples such as serum or unfiltered protein digestates were subjected to MDS, analytes in the ^{1}D effluent varied in concentration by several orders of magnitude over the entire separation window. When high-concentration sample was introduced to a ^{2}D capillary protein analytes were more apt to adsorb to the capillary walls, altering the separation characteristics of the capillary. The non-uniform ^{1}D separation profile is split across the ^{2}D capillaries over time which ensured the degradation of each ^{2}D capillary was also non-uniform. Thus, a pH 9.2 ^{2}D BGE containing borate and submicellar amounts of SDS was selected to minimize capillary fouling during a 2D separation. To further ameliorate different rates in capillary aging processes, the capillary array was also flushed with solutions of sodium hydroxide and SDS to aide in reconditioning the capillary walls. However, complete avoidance of these aging processes was impossible. Quartz capillary manufacturing differences was expected to be a contributor as well but was not amenable to simple optimization.

A design mediated source of variability was due to the peristaltic pump that was used to establish hydrodynamic flow through the MDS interface. These pumps produced a pulsatile flow that generated a sinusoidal velocity through the MDS interface. Thus, the washing efficiency of the ^{2}D capillary tips was dependent upon the phase of the pump roller head. I conjecture that injections made during the low velocity phase resulted in more sample being injected than during the high velocity phase. This seems likely given that Section 3.1.6 demonstrated that low flow rates through the MDS interface resulted in longer residence times when effluent was introduced to a ^{2}D capillary inlet and unwanted sample entering the capillary. To minimize time-dependent variations

in the BGE velocity through the MDS interface, high rotational speeds were used to drive the pump roller head, but small perturbations in the BGE flow were unavoidable.

The largest design mediated source of variability was due to imprecise alignment of the ^{2}D capillary outlets with the excitation laser beam along the X-axis of the table. Despite being held by straight channels in the PDMS cuvette, the capillaries could stray from their intended parallel orientation. This was caused by inaccurate placement of the templating capillaries used during casting of the PDMS cuvette or uneven clamping force applied to the capillaries just above the cuvette entrance. Although each capillary was placed within a narrow range of heights above the laser path, each capillary's lumen could have been located at variable distances from the center of the Gaussian laser beam (see Figure 44).
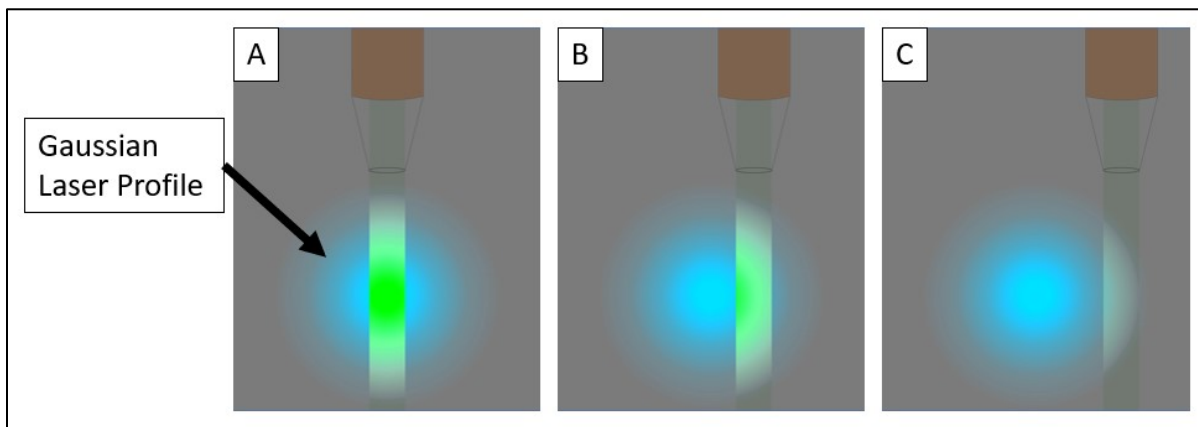
Figure 44 Depiction of a capillary outlet in the sheath flow cuvette as viewed from within the laminar flow channel and directed at the laser source. The series of images demonstrates the effect of capillary placement on the fluorescence signal produced by the exiting effluent. The probe volume is highest when the centers of the both the capillary and laser profile are aligned (A) and decreases the farther away that the capillary is placed from the center of the beam (B) (C).

The effluent stream from a ^{2}D capillary behaves much like a vertical cylinder of fluid containing fluorescent particles. The laser beam behaves like a cylinder of photons whose Gaussian profile results in the population of photons decreasing radially from the high intensity center. It is the intersection of these two cylinders that dictates the available detection volume of exiting effluent, with larger volumes allowing higher fluorescence intensities. The largest available detection volume occurs when the effluent stream and laser beam are centered upon each other (Figure 44 A). As the two intersecting cylinders move away from alignment, the effluent intersects a decreasing amount of area within the circular beam profile (Figure 44 B and C). The Gaussian beam profile also means that the farther away that the effluent is from central alignment to the

laser, the lower the irradiance will be for the same detection volume (Figure 44 A–C). Both factors led to a rapid decrease in signal intensity when capillaries were poorly aligned to the laser.

When initially constructed, the laser was focused to a beam waist of 50 – 100 μm—which was wide when compared to the 10 μm spot sizes found in ultra-sensitive sheath flow cuvettes[198]. Despite this, the detector produced unacceptably highly variability in signals across the capillary array. This behaviour was caused by the inability of the capillary tips to maintain straight line configuration. This resulted in some effluent streams that intersected laser beam at its periphery or be placed outside of it entirely. Identical injections typically led to sensitivity differences between capillaries that were greater than an order of magnitude—unacceptable for use as a family of separations data to be interleaved. Adjustment of the array above the beam via yaw rotation and translation along the X-axis was never able to produce intense illumination on more than half of the capillaries in the array. Thus, the alignment tolerance was relaxed by using a low power lens to focus the laser beam ca. 360 μm, at its narrowest point. The beam profile was confirmed by the observed light scatter from the laser in Figure 40 and the fluorescing effluent stream in Figure 42.

Although, this dramatically improved the detection sensitivity uniformity/precision across the capillary array, it was at the expense of increased background noise. Signal-to-noise ratio is inversely proportional to the probe volume (the intersection of the volume illuminated by the laser and the volume collected by the detector). This is due to multiple factors. When the ratio of probe volume to sample volume is large, as it is in single molecule detection using LIF, luminescence from impurities in the BGE is the largest contributor of background.[199] This is in addition to Raleigh and Raman scatter from the solvent. Specific to the collection filter used in this work (530 nm, long-pass), the Raman bands at 3400 cm^{-1} (585 nm) and 1640 cm^{-1} (530 nm) are expected to have some overlap with the emission of the fluorescein tracer and fluorogenic label used in this work, whose maxima are at 518 nm and 590 nm, respectively.

Given the reproducible narrow peak shape and high plate numbers demonstrated in Section 3.1.5, detector sensitivity appears to be the main contributor to differences in peak area and not the nature of the separation. Signal intensity can thus be amenable to numerical correction using internal standards without sacrificing separation quality.

3.2.2 **Capillary Spacing and Crosstalk**

One of the key benefits of the sheath flow cuvette is that it minimizes scatter and luminescence from the capillary wall and coating, which is commonly found with on-capillary detection. This arises from the small difference in refractive index between the effluent and the surrounding sheath buffer as compared to the large difference of a fused silica capillary. This benefit dramatically reduced a major source of stray light and invited the opportunity for the detector to exclude spatial filters (pinhole, iris *etc.*) in the optical detection path. However, an expected limitation was that while fluorescence was detected from a given capillary it would simultaneously result in spuriously detected stray light on neighbouring capillaries.

On an early prototype sheath flow cuvette, cross-talk was apparent on all unused capillaries when a single capillary produced a fluorescence signal (Figure 45). The cuvette had four ^{2}D capillaries placed adjacent to each other, with their centers 365 μm (nominal) apart. A single fluorescein injection made on the first capillary (bottom trace), displayed as a tall broad peak (A) when viewed at 1× scaling (Figure 45, left side). Scaled to 40× (Figure 45, right side) ghost peaks (A'), due to cross-talk from capillary one, were easily visible in the signal from capillaries two, three and four. Figure 46 shows the same experiment performed with a later sheath flow cuvette design as described in Section 2.3.2. In these later designs, the capillary centers were spaced 635 μm (nominal) apart. The peak on the first capillary did not produce detectable ghost peaks on any of the neighbouring capillary detection zones.
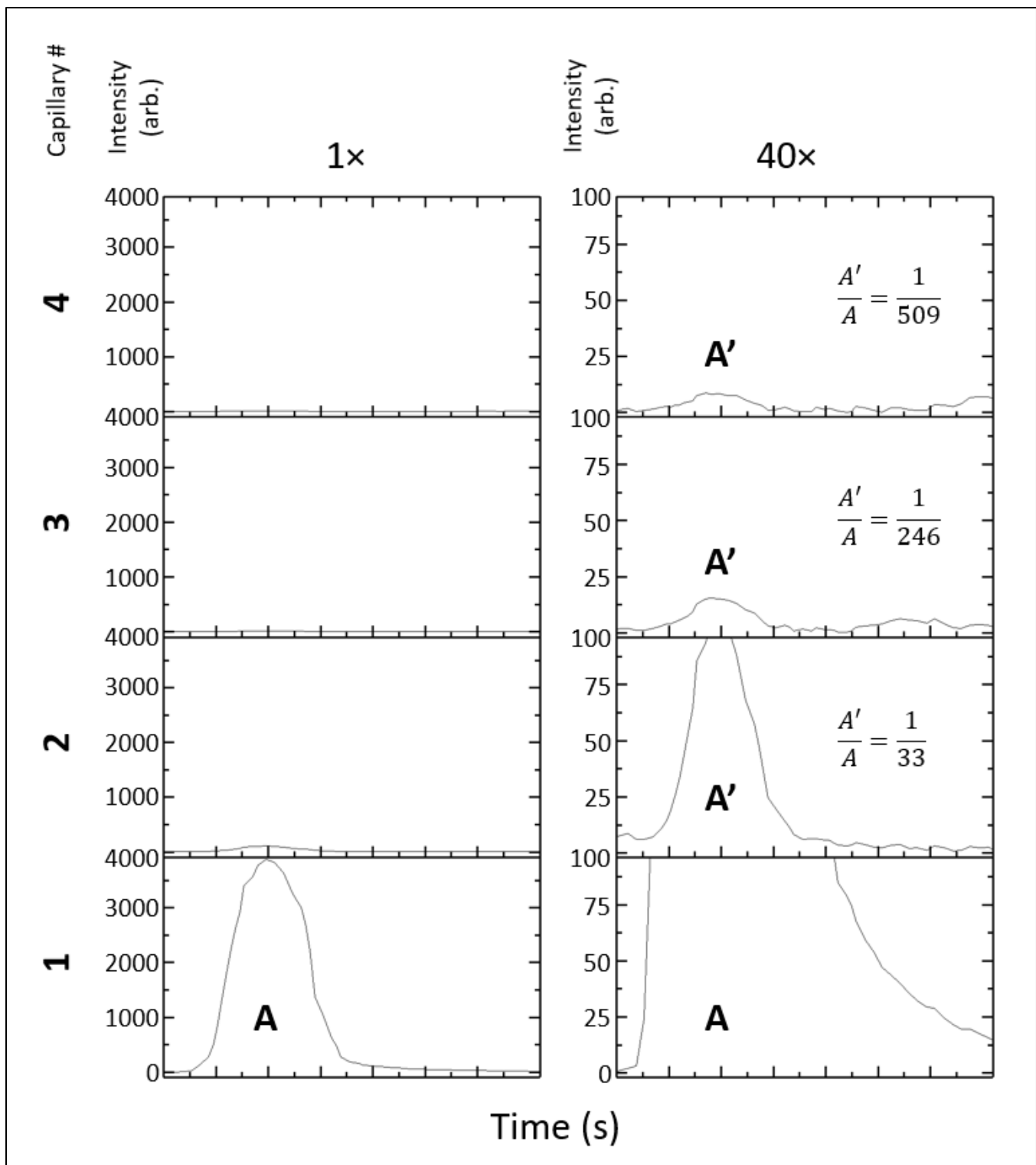
Figure 45 Signal crosstalk resulting from a fluorescein peak the capillary one on the three serially adjacent capillaries in an early prototype utilizing a four-capillary MDS interface and sheath flow cuvette. Both stacked plots show the same data, with the left plots scaled to the peak in capillary one. The righthand plots were scaled to 40×. Inset ratios are the height of the spurious cross-talk peak (A') versus the analytical peak in capillary one (A). Peaks were fitted to a modified gaussian function to determine peak heights.
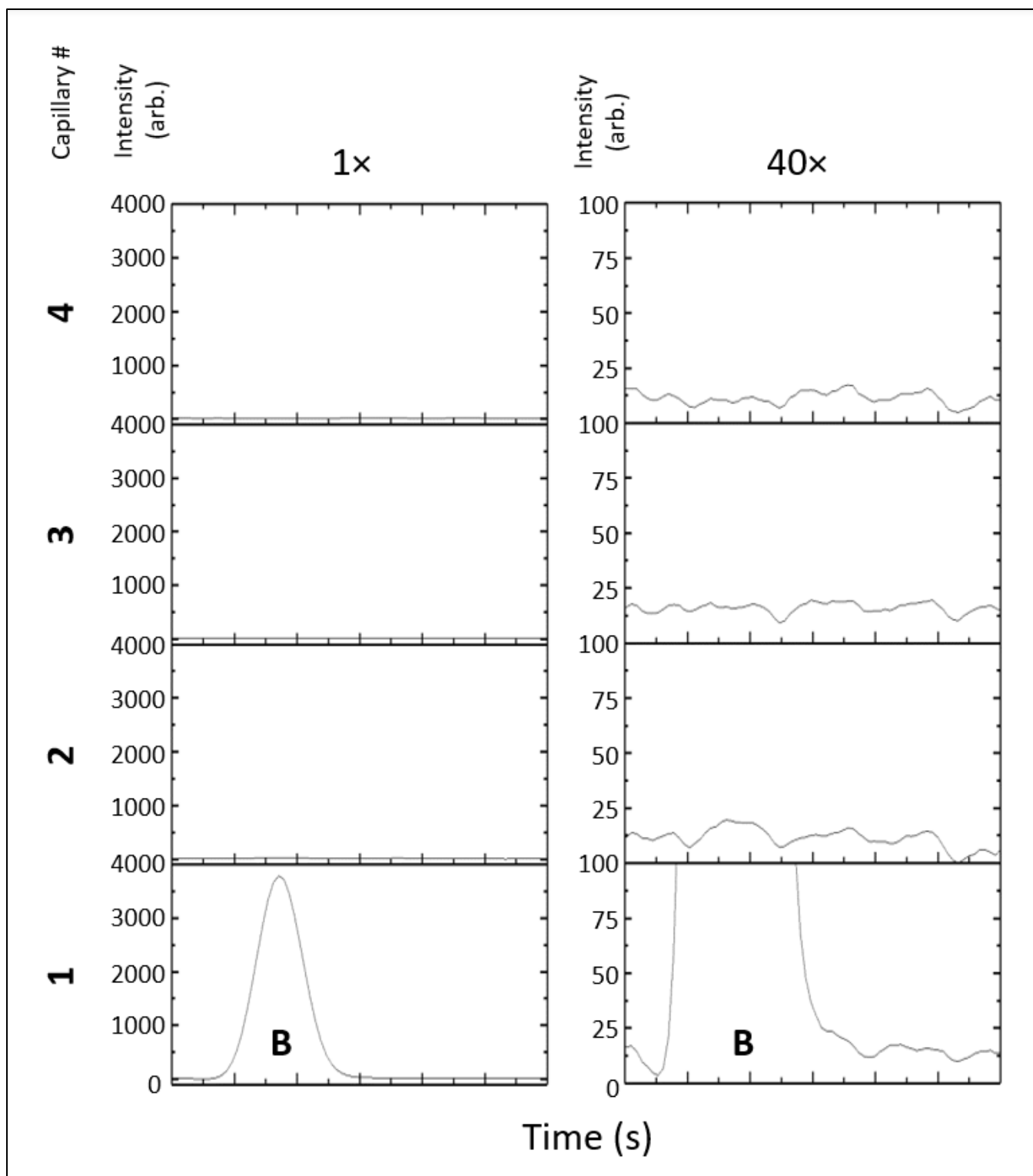
Figure 46 Signal crosstalk resulting from a fluorescein peak the capillary one on the three serially adjacent capillaries in an early prototype utilizing a four-capillary MDS interface and sheath flow cuvette. Both stacked plots show the same data, with the left plots scaled to the peak in capillary one. The righthand plots were scaled to 40×. There were no peaks observed in capillaries adjacent to the analytical peak.

The early prototypes developed for this thesis were inspired by capillary array sheath flow cuvette designs from Dovichi's group[168,200,201], which used quartz cuvettes that closely fitted around a bundle of adjacent capillaries. However, attempts to reproduce cuvettes using adjacent capillaries produced datasets that were frequently plagued with cross-talk between capillaries. This occurred due to the fluorescence being emitted from the effluent probe volume in all directions. Although the fluorescing effluent from a capillary would irradiate its respective ROI on the CCD camera sensor, off axis light rays reaching neighbouring ROIs caused spurious signals to be generated. This was prevalent when high concentration samples generated excessively high fluorescence intensities, which could be simply resolved by sample dilution.

However, cross-talk was also exacerbated by localized pressure and velocity gradient changes in the sheath flow channel after the capillaries were manipulated within the cuvette; such as capillary height adjustments or capillary replacements. These minor modifications to the capillary positions caused changes to restrictions in the hydrodynamic BGE path upstream of the detection zone, leading to laminar flow streamlines undergo commensurate changes. This led to streamlines that diverted a few degrees between adjustments. Cross-talk was sensitive to these changes because of the close capillary spacing. It meant that the ROI for each capillary was small relative to the size of the effluent stream. Small shifts in the effluent position within the captured ROI was large enough to be detected as stray light or even cross the border of an adjacent ROI and be detected as intense fluorescence signal.

The cross-talk between channels was prominent in an early design utilizing close packed capillaries as seen in Figure 45. The fluorescein peak, A, was readily seen as ghost peaks (A') as far as three capillaries away. Scaled to 40×, the ghost peaks (A') were easily visible with peak heights that decreased as the capillary distance increased. The height of these ghost peaks was observed to reach 1/33 of the originating peak's height.

Cross-talk between capillaries was reduced below the detection limits of the CCD camera acting as the signal transducer. This decreased cross-talk was achieved by two modifications, moving the capillaries farther apart and adding additional partitioning to the ROI designated to each capillary on the CCD camera sensor. First, the capillaries were moved apart. Rather than being placed adjacent to each other a ≈300 µm gap was introduced between each neighbouring capillary. Thus, neighbouring capillary centers were spaced 635 µm apart compared to the original 365 µm

spacing; a 74 % increase in distance. Second, only the central 20% of pixel columns were used for each capillary within its ROI on the CCD sensor. On either side of the central pixels of the detection zone, the large margins of unused pixels acted like a digital iris that excluded background signal that was produced outside of the effluent probe volume. In tandem, the larger physical spacing and digital region exclusion dramatically relaxed the tolerances required for the shape of the effluent stream. Even with a significant off-axis angle introduced into the effluent stream for any capillary, the signal remained confined and did not affect neighbouring capillary signals. However, large angle deviations would also reduce the detected probe volume of the affected capillary.

The current sheath flow cuvette design facilitates changes to physical characteristics (number of capillaries, capillary spacing, capillary diameter, depth of sheath flow channel) with only simple modifications required during the fabrication process. The number of capillaries and the spacing between them can be modified by using different set screws, which are available in a variety of lengths and thread pitches. The variety of capillary diameters used for CE can be accommodated by a similarly large variety of commercially available monofilament polymer fishing line diameters. The depth of the cuvette channel (distance from the capillaries to the detection window and opposing wall) can also be tuned by choosing different thicknesses of sacrificial film that is placed on the fishing line to mould the window against.

3.2.3 Flow Rate Optimization

Much like the MDS interface, flow rate in the sheath flow cuvette was an important parameter to optimize as it was found to affect signal quality because it affected the diameter of the ^{2}D effluent. The velocity of the sheath flow was varied while effluent was continuously introduced by a single ^{2}D capillary. Images were captured at each velocity to allow the effluent stream behaviour to be compared (Figure 47). The cuvette used gravity-fed siphon to generate the sheath flow past the capillaries. To vary the sheath flow velocity, the height of the supply and waste reservoirs were offset at varying heights. Increasing offset distance resulted in increasing the hydraulic head pressure as well as the sheath flow velocity. The supply height was varied from 0 mm – 106 mm. An image frame is shown at the top of the figure, where the sheath flow cuvette was under bright illumination, to provide a reference for the capillary configuration in the subsequent series of darkened images.
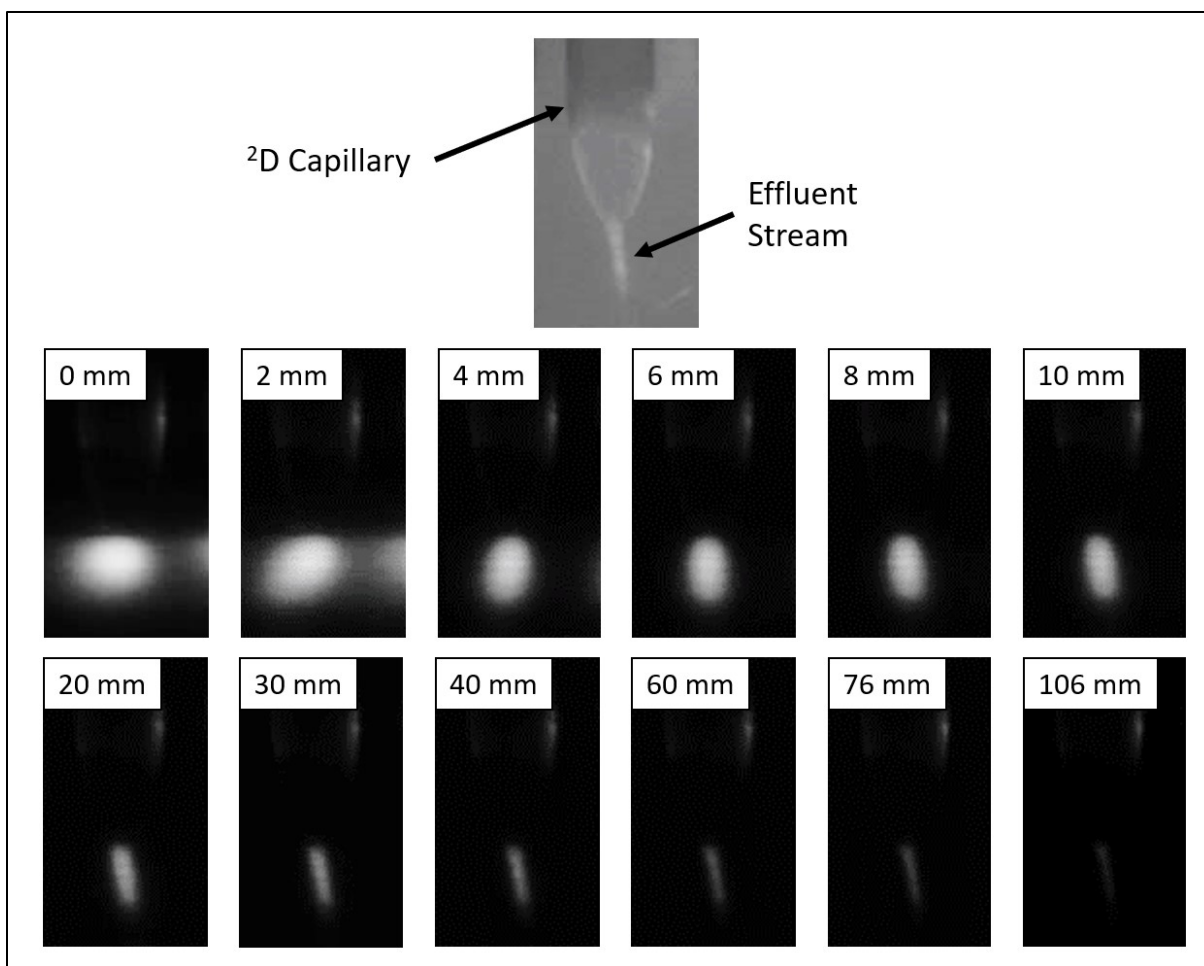
Figure 47 Effect of hydrodynamic head pressure on the shape of the effluent stream and probe volume. Performed via continuous injection of 50 nM fluorescein. Sheath flow cuvette supply and waste reservoirs were offset, by the heights overlaid in each frame, which generated the hydrodynamic head and established the velocity of the BGE sheathing fluid.

With no hydraulic head (0 mm offset) the BGE in the sheath flow cuvette was stationary, which caused the effluent to expand radially as it was emitted from the capillary tip. As the hydraulic head was increased to 10 mm, fluorescent effluent probe volume underwent a series of visible changes. The effluent probe volume changed from a semi-spherical spot to a one that narrowed horizontally, as it was entrained and hydrodynamically focussed by the surrounding laminar flow. As the head height was increased past 10 mm, the effluent stream continued to narrow. The decreasing effluent diameter caused the probe volume to decrease along with the fluorescence intensity. Once a 120 mm head height was reached the fluorescence intensity could not be detected by the CCD camera (not shown). The optimum offset was 30 mm, as it was the smallest offset (maximized signal) while still maintaining a sufficient BGE velocity to minimize the analyte stream diameter (minimize cross-talk).

An interesting observation was the change in analyte stream direction as a function of supply head height. At the lowest flows, 0 – 4 mm, the stream diverged to the left whereas it diverged towards the right above 6 mm. This indicated the presence of a pressure dependent restriction and imbalance in the flow across the width of the detection channel that was attributed to small protuberances of PDMS near the entrance of the multicapillary channel of the cuvette. These protuberances were caused by imperfections in the negative mold used to template the interior of the PDMS sheath flow cuvette. Any voids between two surfaces in the negative mold resulted in a thin sheet being formed and anchored to an inner wall as the PDMS cured. Some of the protuberances were inaccessible to cutting tools and remained in the finished cuvette. Their impact was only detectable in the transition from low flow to high flow and stabilized above 10 mm, which was far below the optimized head heights used (≈30 mm). This behaviour was minimized in later sheath flow cuvettes by filling voids in the negative templates using RTV silicon sealant prior to molding with PDMS.

In classically optimized sheath flow cuvettes, the laminar sheathing flow hydrodynamically focuses the effluent stream to diameters as narrow as 1 μm[198]. The intent of this action is to concentrate the sample into a small probe volume to be interrogated by the excitation laser and the detector in order to spatially minimize background for increased signal-to-noise. This setup requires detection optics that incorporate high-powered microscope lenses to concentrate the laser to a fine point as well as view the resulting small concentrated probe volume with a high numerical aperture. However, the excitation beam diameter and the probe volume sizes were relaxed in this sheath flow cuvette, as described at the start of Section 3.2. Along with the single CCD camera used, detection sensitivity was low as compared to leading designs in the literature.

Working head heights and flow rates were qualitatively chosen by balancing the sensitivity and risk of cross-talk as dictated by the diameter of the effluent stream and the resulting probe volume. Low flow rates resulted in larger probe volumes and higher sensitivity signals. However, when the diameter of the effluent streams increased larger portions of their respective ROI on the CCD sensor was used. This risked reintroduction of cross-talk that was eliminated in Section 3.2.2 by separation of the capillaries. High flow rates reduced cross talk, but at the expense of smaller probe volumes and lower signals. The sheath flow velocity, and thus the extent of hydrodynamic focusing, was adjusted such that the exiting effluent streams were narrow enough to avoid any

cross-talk with neighbouring capillaries, nanomolar detection limits were achievable, and that high mobility analytes would remain much slower than the sheath flow[202]. The head height selected for the remainder of experiments was 30 mm, since it provided easily observed hydrodynamic focusing and signal for an exiting solution containing 50 nM fluorescein.

Using a hydraulic head of 30 mm was also of practical importance in the latest prototype due to the gravity fed siphoning flow used. Since the reservoirs were also held at the high separation voltage, safe replenishment was impossible during long operation times. A low volumetric flow rate coupled with large surface area reservoirs were used to minimize the rate of meniscus change. However, this could still be significant at very long separation times.

3.2.4 Sensitivity and Laser Power

Further insight into the efficient operation of the sheath flow cuvette used as a post-column CE detector was gained by examining the signal, background and noise behaviour as a function of laser output power. Well optimized sheath flow cuvettes are typically shot noise limited, characterized by a background that scales with the square root of the signal intensity.[169] However, the large probe volume in the described setup precluded this. It remained instructive to examine the signal and noise behaviour as laser power was varied. An analysis of the sources and magnitudes of the system background was performed to determine whether the detection schema, first, was suitable for the low sample masses encountered in CE and, second, was amenable to future improvements through design modifications.

Figure 48 contains plots of signal characteristics observed while varying the excitation laser intensity. Replicate fluorescein injections (n = 5) were performed while the Ar-ion laser was set to four output powers within its operating range of 4 – 10 mW (nominal). The blank/background signal was collected as the average baseline signal preceding the separation window. Standard deviation was used as the root-mean-square (rms) noise. The signal-to-noise ratio (S/N) and signal-to-blank ratio were calculated using blank corrected peak heights as signal, rms noise and average baseline for the blank. A modest number of laser powers was tested as the main goal of this experiment was confirmatory and intended to support other figures of merit.
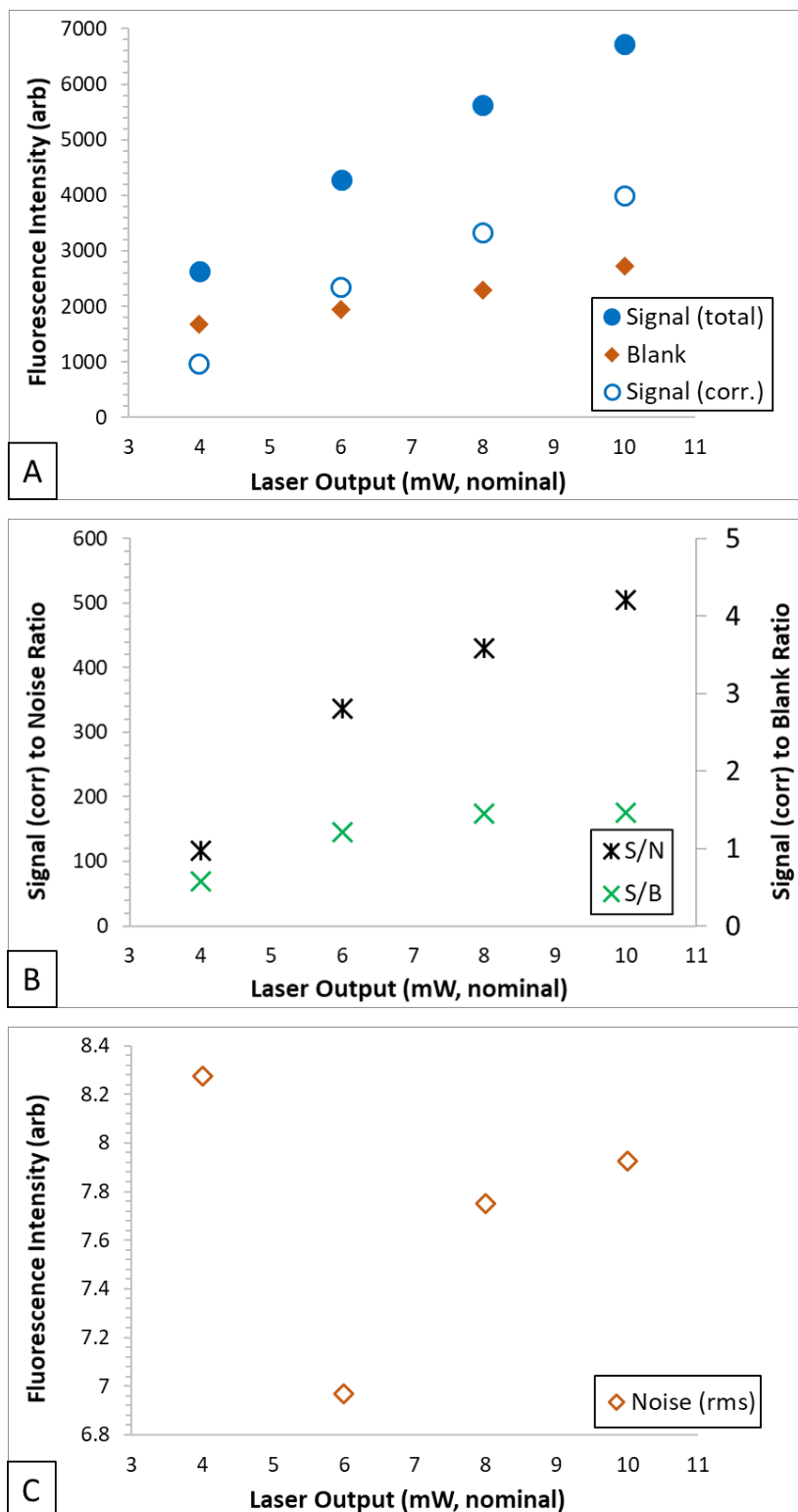
Figure 48 The effect of laser intensity on signal characteristics of the multicapillary sheath flow cuvette. Sets of five injections of 100 nM fluorescein (300 ms) were placed onto a single ^{2}D capillary while varying the laser intensity for each set from 4 mW to 10 mW. The data were treated to compare signal intensity for peak heights, baseline and noise. The three panels demonstrate average peak height, average blank signal and average blank corrected peak height (A), signal-to-rms noise ratio and signal-to-blank ratio (B) and rms noise (C) at each laser power.

The analytical signal showed a positive relationship with laser intensity across the range studied. The raw peak heights, background signal and blank corrected peak heights all exhibited linear correlation coefficients (R^2) above 0.97 (Figure 48 A). The signal-to-noise ratio and signal-to-blank ratio were less linear across the four laser powers (Figure 48 B), producing R^2 of 0.939 and 0.812, respectively. The rms noise did not follow a linear relationship with the increasing laser intensity (Figure 48 C). The minimum signal-to-noise ratio achieved by the system was S/N = 116, which allowed for a concentration LOD of 200 pM. These detection limits correlate to mass detection limits across the capillary array ranging from 3 – 17 attomoles using replicate fluorescein injections (not shown).

The results demonstrate that increasing the excitation laser intensity results in a proportional increase in the sensitivity of the detector system. The linear correlation of the raw and blank corrected peak heights to the laser power were not mirrored by the S/N. The invariance of the rms noise at all levels of excitation power resulted in a disproportionally lower S/N at 4 mW than the remainder of points. This contributed to the non-linearity of the S/N curve within the range studied. The S/N curve is expected to linearize at higher irradiance intensities.

To evaluate the efficiency of using laser intensity to improve S/N, a comparison was made between the change in S/N that resulted from a doubling of laser power from 4 mW to 8 mW. The doubling in laser power caused the S/N to increase by a factor of 3.71 (Figure 48 B), whereas the calculated increase in S/N was by a factor of 2.61 (not shown). As a ratio of increase in S/N vs laser intensity, the S/N rose an additional 85.5 % (measured) or 30.5 % (calculated) compared to the level of increase in irradiance. Further investigation is warranted, using a different laser is with higher output intensity, to determine the limits that this parameter has on sensitivity improvements.

Background luminance is the largest source of background signal even in highly optimized systems.[199] The magnitude of the blank signal was larger than the blank corrected peak height at 4 mW, with a crossover point around 5.5 mW at which point the analytical signal becomes dominant. This is further seen by the increasing S/B ratios which ranged from $0.57_3 – 1.4_6$. I would conjecture to say that the high ratio of blank to analytical signal was masking other sources of noise in the system. The high background was an unavoidable result of the large beam diameter chosen in Section 3.2.1, which subsequently led to a large probe volume and increased scatter measured by the CCD camera. 10 mW produced the highest S/N, but it didn't increase linearly

with laser power. This suggests that increasing laser power caused a disproportionate increase in the noise.

The primary focus of this work was to demonstrate multidimensional separations and not to explore detector sensitivity limits. 4 mW was found to be sufficient for quantitative detection of low nanomolar quantities of analyte, without undue wear on the gas laser. Thus, 4 mW was used for the majority of the presented work. 6 mW was used in a few noted exceptions where sample mass was expected to be limited.

3.3 Performing Automated Injections Using the MDS Interface for Parallel 1D Separations of a Model Small Protein Digestate

The focus of this chapter was to characterize the components of the ^{2}D separation instrument independent of the ^{1}D; which served simply as a sample delivery device. Fluorescein was a useful small-molecule tracer to quantify figures of merit for separation performance and identify areas for future researchers to investigate or optimize. The next logical step was to investigate the ^{2}D capillary array performance on 1D separations with moderately higher sample complexity.

Thus, this chapter concludes with a qualitative examination of separation profiles generated by injections of a β-casein trypsin digestate that were replicated across the capillary array. Sample was delivered to the MDS interface by applying a constant voltage across the ^{1}D capillary infused with the tryptic peptides. Once the ^{1}D effluent stream was stabilized, the MDS interface was programmed to perform automated injections onto the ^{2}D capillary array in sequence. A five second delay was introduced between each injection. During the entire sequence, voltage was applied to all of the ^{2}D capillaries from the common power supply, ensuring all of the ^{2}D separations were operated concurrently. For visual clarity, each of the electropherograms in Figure 49 were normalized to their respective injection times by time-shifting them to "the left" as well as vertically offsetting them for clarity. They are otherwise unmodified from the raw data so that inter-capillary differences could be identified from these, otherwise, identical separations.
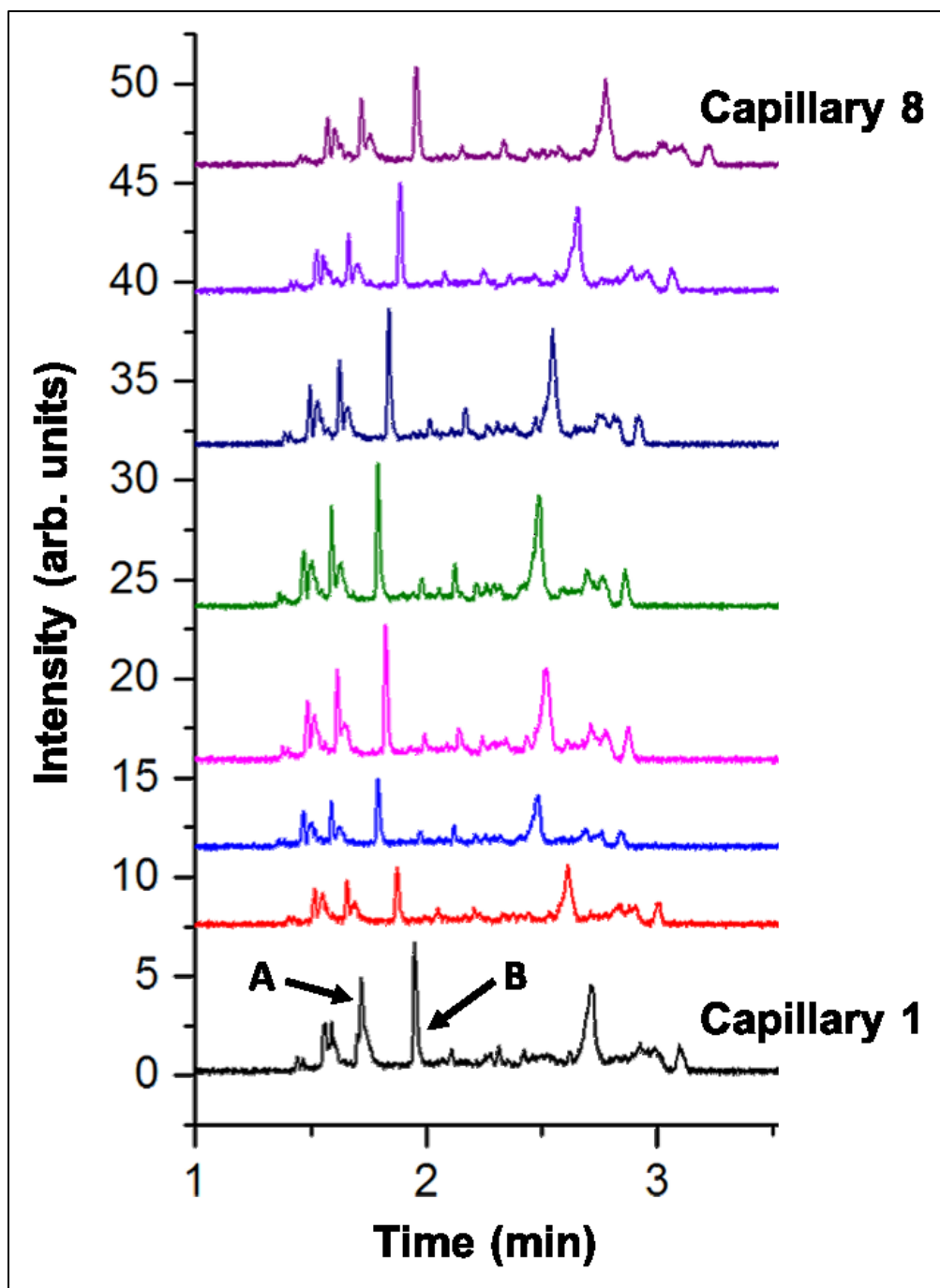
Figure 49 Replicate 1D separations of FQ-labelled β-casein tryptic digest (0.7 mg/mL) across the capillary array. BGE: pH 9.2, borate 25 mM, SDS 5 mM. A voltage was applied across the [1]D capillary, infused with tryptic peptides in BGE, to produce a continuously flowing stream of effluent. MDS interface automated sequential sample injections onto the [2]D capillaries by momentarily placing each [2]D in the stream of [1]D effluent for 300 ms, with a 5 s delay between injections. Electropherograms for capillaries 2 – 8 were time offset to normalize their injection times relative to capillary 1, and they have been offset vertically for visual clarity.

The timing program for sequential injections is shown in Figure 50, which was used by the motion control software of the MDS interface. At the start of an injection cycle, the ^{1}D and ^{2}D capillaries are positioned 220 μm apart from each other. A series of four commands are issued repeatedly, with each capillary simply using a different set of coordinates. First, the MDS interface brings the capillaries into alignment/injection position (Step 1), followed by a wait (Step 2) period for the injection to occur, then capillaries are moved out of alignment (Step 3) and finally the MDS interface moves to the pre-injection position for the following capillary in the set (Step 4). Steps 1 and 3 require a constant time (74 ms) for the motors to move. The only parameters that the user needed be set were: the wait time (a.k.a. injection time; Step 2) and the total cycle time, which is the sampling time for the ^{1}D effluent. The software simply subtracted the allotted time for the first 3 steps from the total time to set the time required for Step 4. Positions of all eight capillaries were stored in an array within the software and used with this injection cycle to repeatedly perform injections across the eight capillaries in order.
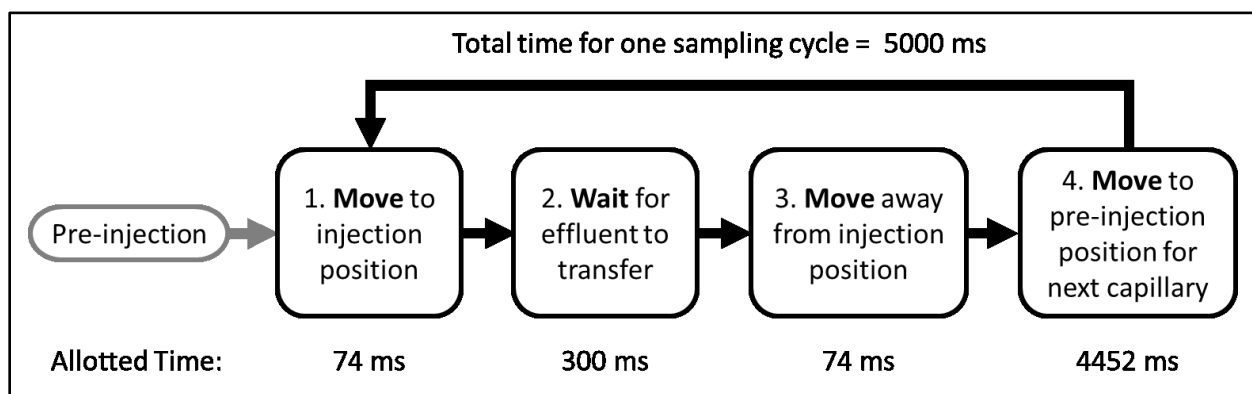
Figure 50 Flow chart of the automated injection sequence used by the MDS interface. The flow chart is described for a single capillary but was iterated for each of the eight capillary coordinates entered into the motion control software. The MDS interface aligned the capillaries (step 1) and allowed an injection to be performed by waiting for a preset time (step 2), followed by moving the capillaries out of alignment (step 3) and then moving the next capillary into its pre-injection position (step 4).

The separation profiles in Figure 49 demonstrate similar separation behaviour between capillaries with respect to the order of peaks and relative peak heights. As expected from the analysis performed in Section 3.2.1, the raw signal intensities result in peak height differences between capillaries that were less than 2-fold. This caused low intensity peaks to be obscured and difficult to distinguish from the baseline noise when capillaries with low sensitivity signals were scaled to match their higher sensitivity neighbours. However, the major peaks are easily identifiable with their counterparts in all the other capillaries. The poorly resolved peak pair, A in Figure 49, has

markedly worse resolution in Capillary 1 (at 1.72 min) where it appears as a single, broad, non-Gaussian peak whereas the other capillaries show a taller peak preceding and overlapping a shorter one. There was a small, but obvious, shift in the separation windows towards earlier migration times from the outer capillaries towards the center of the array. This data set was collected using an earlier version of the MDS interface, where 1/8" end mill cut horizontal slots were omitted as described in Section 2.2.1. Due to a hydrodynamic bias, that remains not fully understood, the MDS interface flow rate dramatically increased towards the outermost capillaries in the array (Capillaries 1 and 8) at their inlets. The higher velocity flow appeared to have resulted in lowering the hydrodynamic pressure at these inlets, relative to the center of the array, and introducing backflow which caused these separation windows to migrate more slowly to the detector. It was also a likely contributor to the poor peak pair resolution in capillary 1 mentioned above, as any introduction of laminar flow within the capillary is known to reduce separation efficiency and the resolution of the underlying electrophoretic separation.

An important metric for determining the expected ease of data alignment for interleaving multiplexed data is the degree of variation present in the raw data; when there are both shifts in time and signal intensity. For example, consider the well-resolved Peak B, at 1.95 min in capillary 1 (Figure 49), which was common to all electropherograms. The between-capillary precision in migration time was 3.5 %RSD and was 28.8 %RSD in peak area. When comparing against replicate fluorescein injections (n = 5) within a single capillary, precision in migration time was observed to be 3.1 %RSD and 2.1 %RSD in peak area. The large variation in peak area between capillaries, for the same analyte, was attributed to the nearly 1.6-fold difference in signal sensitivity between channels. Whereas within a single capillary, for replicate fluorescein peaks, was within the typical reproducibility range for optimized CE instruments.

The investigations comprised in this chapter serve as demonstration that a milestone has been reached in the use of a motion controlled MDS interface for coupling the effluent of a ^{1}D separation capillary with an eight-capillary CE array. Thus far with the ^{1}D acting as a simple sample delivery tool, repeatable high-quality injections have been validated within and between capillaries. Although sub-optimal instrumental factors/design elements remain, and there is certainly room for improvement, it should be possible to demonstrate the key aim of this project—high peak capacity

MDS within the 1 – 3 hour timeframe—chiefly facilitated by the increased sampling rate owing to the advent of a highly-multiplexed ^{2}D.

Chapter 4 The Path to Multidimensional CE × CAE Separations

Chapter 3 detailed extensive characterization of the ^{2}D capillary electrophoresis array and its detector system. This was primarily performed with the ^{2}D acting as a multiplexed set of 1D separation instruments, where the ^{1}D capillary solely acted as a sample delivery device. This chapter will now demonstrate how the capillary array was integrated into a 2D instrument, where it could further separate the effluent of ^{1}D separation. First, fluorescein was used as a model small molecule to demonstrate 2D operation, which generated data for comparison against a commercial CE instrument. Then a serum digest was used as a model biological sample to demonstrate the benefits gained from moving from 1D separations to a 2D separation.

4.1 Toward 2D Separations

4.1.1 Rapid and Continuous Heart-Cutting of a Single ^{1}D Peak

To be effective, the MDS interface must be able to maintain the original peak shape generated on the ^{1}D after it is separated by the ^{2}D. Ideally, the ^{2}D separations should not be sensitive to the changing concentration of the ^{1}D peak or differences between ^{2}D capillaries. To determine if a single ^{1}D peak could be split across the capillary array while preserving the peak shape, fluorescein was injected onto the ^{1}D capillary and separated on the MDS instrument in 2D mode. Continuous 1.2 s injection were used with 4 s sampling intervals, allowing for 32 s cycle times between adjacent injections on any given capillary (Sections 2.4, 3.3). Figure 51 shows two views of the raw data collected from the ^{2}D sheath flow cuvette. Figure 51A shows a view of all eight capillaries combined on a single graph. The traces are vertically offset in Figure 51B to more clearly see the behaviour of each capillary, with the same data treatment applied as was described for Figure 26 in Section 2.4. Other than baseline correction, neither were scaled or otherwise modified. The ^{1}D peak is first observed in the ^{2}D (Figure 51B) at injection 546 and ends at injection 577.
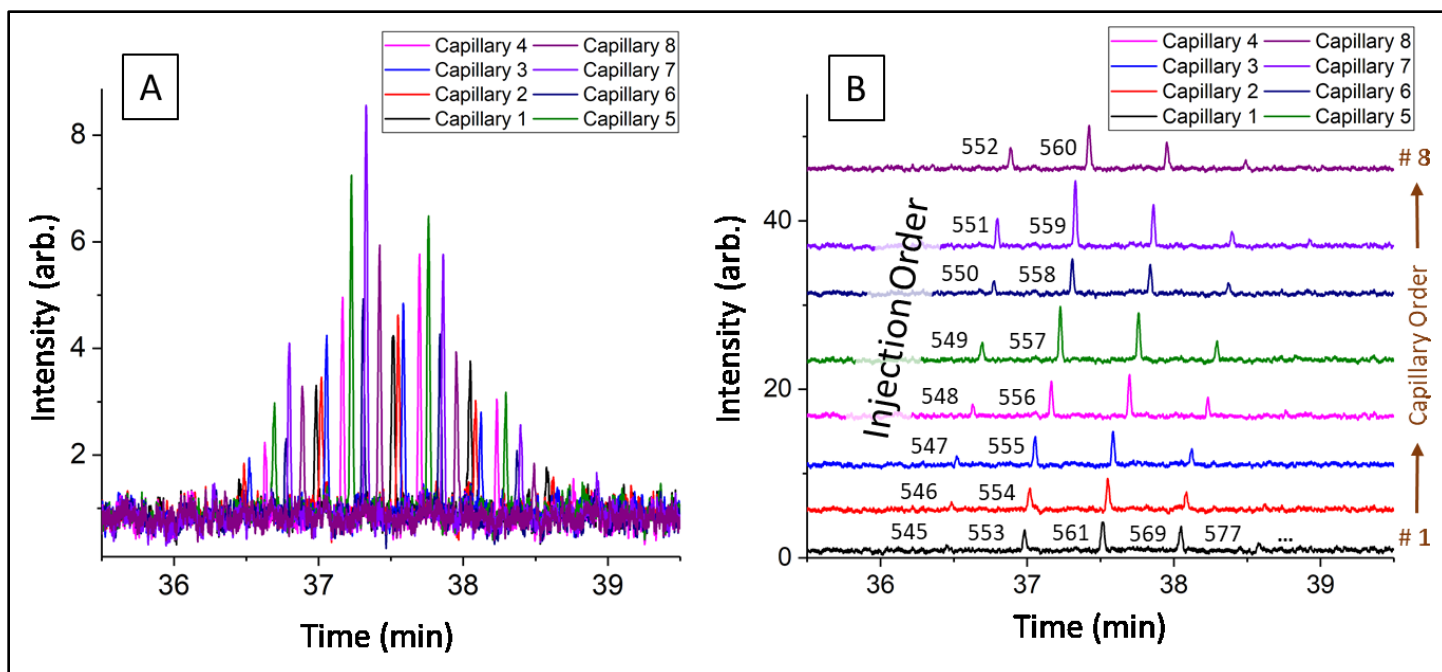
Figure 51 Rapid continuous sampling of a ^{1}D fluorescein peak by the ^{2}D capillary array. A 0.4 % capillary volume injection of 1 μM fluorescein was injected onto the ^{1}D capillary and electrophoresed in a BGE of pH 5.8 acetate buffer 10 mM at an electric field strength of 158 V/cm. The ^{2}D BGE was 25 mM borate, pH 9.2, with 5 mM SDS and operated at 333 V/cm. The ^{1}D effluent was sampled by the ^{2}D every 4 s with a 1.2 s injection time. The raw data is shown identically in both plots, with the plots overlaid (A) and stacked (B).

By operating the ^{2}D at a high sampling rate, it effectively captured and reproduced a ^{1}D peak with minor distortions. The sampling rate is readily seen Figure 51A with narrow spacing between ^{2}D peaks, whereas Figure 51B better visualizes the sequential capture of the ^{1}D peak by the capillary array. Looking at the signal precision between capillaries, capillaries 5 (green) and 7 (purple) produced higher signal intensities than the remainder which reduced the fidelity of the originating ^{1}D Gaussian peak. However, the signal variation between capillaries did not deviate by more than a factor of two suggesting that numerical normalization across the capillary array should be possible since their signal sensitivities were comparable.

The original ^{1}D peak was sampled 30 times across its 2.55 min baseline width; a rate of 11.8 samples per minute. At 30 samples over a peak, 99.9_8 % of the ^{1}D peak capacity (^1n_c) is predicted to be retained (Section 1.9). Fluorescein was chosen as the tracer molecule, which is a dianionic species with a high charge-to-size ratio. This caused it to migrate slowly under the separation conditions used, which produced an excessively wide peak as it exited the ^{1}D capillary. Even if a more realistic 30 s peak width was considered, this sampling rate would have allowed 5.9 samples per peak and result in 99.6_9 % of the ^1n_c to be retained.

146

Using eight capillaries, and four second sampling times, means that each capillary has 32 seconds between subsequent injections, and thus a 32 second separation window. This would provide, up to, 32 s of space in the electropherogram for the separation of the analytes without concern of peaks overlapping between the separation windows of adjacent injections. By comparison, this marked a significant improvement over the two capillary array previously developed in this lab which required 30 s between injections to permit a 60 s separation window for each capillary.[156] For 2D instruments utilizing a single capillary in the ^{2}D, the sampling time must match the length of the separation window.[149–151,153]

There was concern that after making a full set of injections, the return transit from capillary 8 to 1 would have disturbed the ^{2}D separations if operated at higher transit velocities. Shorter cycle times would have been possible by utilizing a different injection pattern that avoided a single long transit across the entire capillary array. Ultimately, a combination of a more efficient injection pattern and addition of more 2D capillaries will allow for continuous sampling using even shorter sampling times and a closer approach to a comprehensive separation. This will permit much longer ^{2}D separation windows while continuing to avoid any separation window overlap.

4.2 2D Peak Capacity Estimation Using 1D Separations of Fluorescein on the Capillary Array and a Commercial Instrument

Experiments using fluorescein were performed to determine if two 1D separation methods could be transferred to the CE×CAE instrument without degrading performance, operated both in offline (1D) and online (2D) modes. Although the ^{2}D demonstrated good performance in isolation, a concern was that peak capacity could be degraded upon method transfer to online 2D operation. An in-house built instrument may also underperform versus an optimized commercial instrument so comparison was important.

The peak capacity was evaluated using fluorescein injections using two separation conditions: low pH (25 mM acetate, pH 5.8) and/or high pH (25 mM borate, 5 mM SDS, pH 9.2) BGE. To establish the benchmark peak capacity 1D separations, under both BGE conditions, were carried-out on a commercial Beckman P/ACE MDQ (MDQ) CE instrument. Then the same separations were carried-out on each dimension of the CE×CAE instrument in both 1D and 2D modes (^{1}D = low pH, ^{2}D = high pH). The collected data allowed comparison of 1D peak capacities (n_c) on the MDQ,

[1]D (HP 3D-CE) and [2]D (CAE), as well as compare hypothetical 2D peak capacities ($n_{c,2D}$) from the 1D separations with the theoretical $n_{c,2D}$ of the on-line CE×CAE instrument. This set of experiments also allowed identification of degradation in separation performance that would be expected when combining a low pH acetate BGE with a high pH borate, SDS BGE and when transferring from 1D to 2D separations.

Table 3 List of combinations of 1D and 2D separations for used to evaluate suitability of pairing low and high pH buffers for use as paired buffer systems for on-line 2D separations of biological samples.

Instrument	Dimensions	BGE System
HP 3D CE	1D	Acetate
Array Capillary	1D	Borate, SDS
MDQ #1	1D	Acetate
MDQ #2	1D	Borate, SDS
CE×CAE	2D	[1]D Acetate × [2]D Borate

To operate the HP 3D-CE instrument in 1D mode, the autosampler was used to inject peptides onto the capillary and the separation was eluted into the MDS interface that was disabled except for maintaining a constant wash flow. The [1]D capillary tip was positioned away from any [2]D capillary tips. Fiber optic guided laser light (Section 2.1.3.2) was used to excite the effluent. Analyte fluorescence was captured by a CCD camera. To operate one CAE capillary as a 1D separation, the MDS interface was operated as normal (i.e. making periodic injections onto the CAE) while the [1]D (HP 3D-CE) infused the serum peptide solution continuously. Although direct comparison of the electropherograms was not possible as the MDQ uses UV-Vis absorbance detector whereas the CE×CAE instrument uses fluorescence detection, it still provided a comparison to a known well-behaved CE instrument.

The capillaries used on the MDQ instrument (15 kV applied voltage) were: 60 cm (50 cm to window) × 100 μm × 365 μm for low pH and 30 cm (20 cm to window) × 50 μm × 100 μm for high pH. The HP 3D-CE capillary (14 kV and low pH only) was 67 cm × 100 μm × 180 μm. The capillary array (5 kV and high pH only) was 14.5 cm × 50 μm × 365 μm. The 2D MDS separation experiment used the HP 3D-CE capillary as the [1]D and the capillary array as the [2]D with the above conditions.

1D peak capacities were determined by first calculating the separation window and baseline width of fluorescein peaks generated by a separation on each combination of instrument, capillary and BGE. Then the number of peak widths that could fit within their respective separation window was calculated to estimate the value of the 1D peak capacity. An ideal/hypothetical 2D peak capacity calculation was then performed for each of the MDQ instrument separations, and the HP 3D-CE and array capillary separations as a pair, by calculating the product of their respective 1D peak capacities from their respective low pH and high pH separations. The observed 2D peak capacity was determined using triplicate fluorescein peaks separated by online 2D CE×CAE and fitting them to a 2D Gaussian to calculate the baseline widths in each dimension. The peak capacity for each dimension was then calculated as the number of baseline peak widths that could fit into the separation window for that dimension. The product of the peak capacities in each dimension then provided the 2D peak capacity of the online CE×CAE system.

Due to the lack of suitable early and late migrating fluorescent markers, mobility measurements on the MDQ instrument were used to estimate separation window lengths for the CE×CAE instrument. A low pH separation of proteins and longer peptides is expected to generate cations, anions and neutral species with a moderate net charge for both ions. Thus, the start of the separation window, t_A, was conservatively estimated using the mobility of a fluorescein ion but applying an imaginary +1 charge to it (i.e. mirroring the measured mobility about the t_{eof}). The end of the separation window, t_Z, was set as the measured t_m of an injected fluorescein peak with a -1 charge. This is a slightly conservative estimation as it assumes that there will be no species with higher mobilities than these +1 and -1 small molecules. Under the high pH borate buffer, the vast majority of biomolecules were expected to be neutral or carry a negative net charge. Thus, the t_A was estimated to equal the EOF using mobility calculations, while the t_Z was set as the t_m of the later migrating peak of fluorescein-5-(and-6)-sulfonic acid (FL-SO$_3^{-3}$) which carries a -2 charge which is fairly common for biomolecules at high pH.

First, considering the 1D peak capacities on the MDQ, the low pH separation generated a predicted $^1n_c = 16._9$ in a 431 s separation window, and the high pH separation generated a predicted $^1n_c = 45._1$ in an 83 s separation window. Using these two 1D peak capacities from the MDQ, a hypothetical 2D peak capacity, $n_{c,2D} = {}^1n_c \times {}^2n_c$, was calculated to be 760. Second, the 1D peak capacities using the CE×CAE instrument are considered. The peak capacity produced on the HP 3D-CE at low pH

was $^1n_c = 16._5$ in a 330 s separation window, and on the array capillary at high pH was $^1n_c = 48._3$ in an 80 s separation window. Using the two 1D peak capacities from the HP 3D-CE and the array capillary, the hypothetical $n_{c,2D}$ was calculated to be 794.

Table 4 Peak capacity estimation using fluorescein dye tracer, calculated as the quotient of the separation window and the baseline peak width. Low pH and high pH separations were used as ^{1}D and ^{2}D conditions, respectively. Separations performed in 1D on a commercial instrument as well as the MDS system with each dimension operating independently. 2D separations were performed on the MDS system.

	^{1}D Separation Conditions (pH 5.8)		^{2}D Separation Conditions (pH 9.2)		$n_{c,2D}$
Commercial Instrument (P/ACE MDQ)	n_c peak capacity (N = 2)	$16._9$	n_c Peak capacity (N = 3)	$45._1$	760 (simulated)
MDS System (HP 3D CE)	n_c Peak capacity (N = 2)	$16._5$			794 (simulated)
MDS System (array capillary)			n_c Peak capacity (N = 3)	$48._3$	
MDS System (2D mode)	^1n_c Peak capacity (N = 3)	$10._5$	^2n_c Peak capacity (N = 3)	$40._4$	423

Table 4 shows that the performance for each combination of 1D separations were comparable. The peak capacities of the CE×CAE instrument was not observed to be degraded compared to the commercial MDQ instrument. The low pH separation on the MDQ generated a 2.4 % higher peak capacity than the on the HP 3D-CE ($16._9$ vs $16._5$). The high pH separation on the array capillary generated a 6.6% higher peak capacity than on the MDQ ($48._3$ vs $45._1$). The theoretical 2D peak capacity was 4.5 % higher for the HP 3D-CE and array capillary than the MDQ instrument used under two conditions (794 vs 760). This demonstrated that the two instruments demonstrated very similar peak capacities when both were operated as 1D separations, pointing to little practical difference between their separation performances.

Figure 52 shows examples of the triplicate 2D fluorescein peaks separated on the CE×CAE instrument. The 2D separation was performed with the same borate BGE in both dimensions as data was not available with an acetate ^{1}D separation. The peaks were modeled using non-linear fitting for 2D Gaussians in Origin Pro to determine peak parameters (migration time, peak width).

The ^{1}D and ^{2}D peak capacities were $^1n_c = 10._5$ and $^2n_c = 40._4$, respectively. The ^{1}D and ^{2}D separation windows were predicted to be 569 s and 77.7 s, respectively. This resulted in an ideal 2D peak capacity of 423.
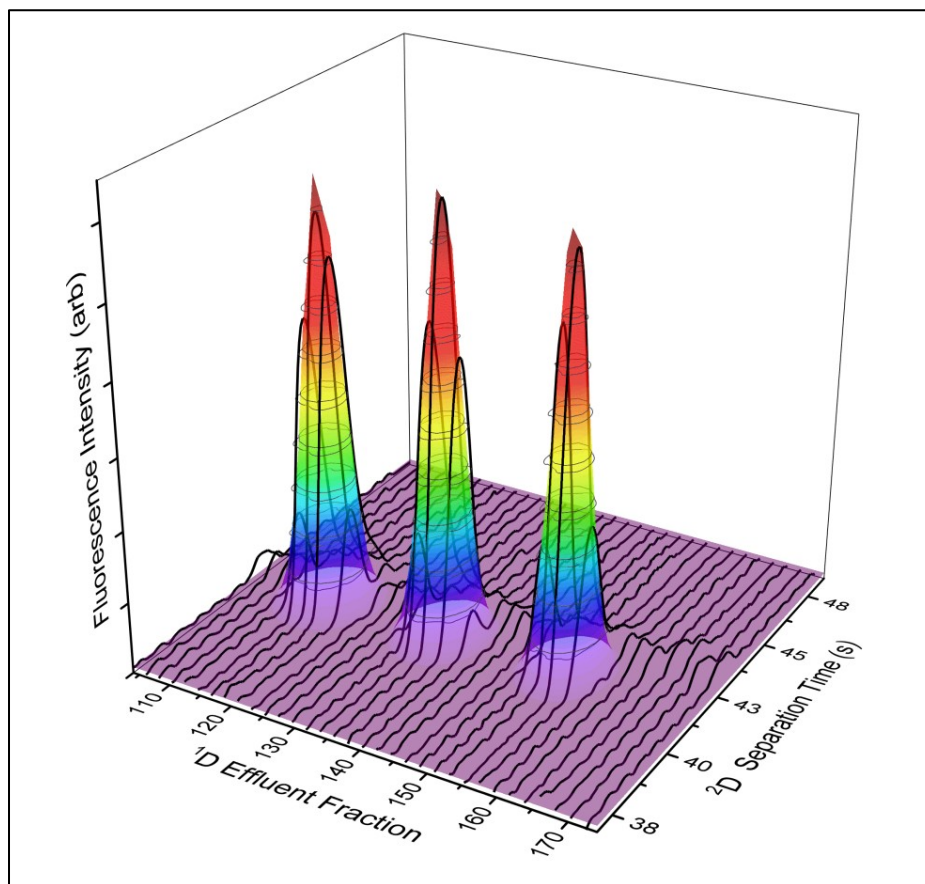
Figure 52 Triplicate fluorescein injections separated by 2D CE×CAE. The ^{1}D and ^{2}D used the same BGE: 25 mM borate, 5 mM SDS, pH 9.2. Fluorescein peaks from the ^{1}D were injected onto array capillaries using a sampling interval of 6 s between each capillary.

The 2D CE×CAE peak capacity represented a 44.$_3$ % decrease from the hypothetical 2D peak capacities from the 1D MDQ separations and a 46.$_7$ % decrease from the 1D separations using the HP 3D-CE and array capillaries. A small system peak was observed in each ^{2}D electropherogram overlapping the migration time of the fluorescein peaks at ca. 43.5 s. This was caused by the degradation product of a late migrating internal standard used in each ^{2}D injection (not shown). Though the separation conditions were kept the same for every pair of separations, the 2D separations observed a significant decline in peak capacity. This was expected due to the partial undersampling of the ^{1}D effluent, only 62.$_1$ – 63.$_6$% retained, caused by the effluent being washed away in the BGE as the MDS interface transited between capillaries (Section 1.10). As the 2D

peaks each had three data points taken across them by the ^{2}D sheath flow cuvette, they were predicted to retain 85.$_4$ % of the original ^{2}D peak capacity (Section 1.9). However, it was more promising that the ^{2}D peak capacity remained within 83.$_3$ – 89.$_6$ % of the equivalent 1D separations.

The 2D peak capacities demonstrated here are lower than those typically found in the literature for biological samples, particularly in the ^{1}D. The weakly acidic acetate BGE generated a modest EOF, resulting in a long ^{1}D migration time for fluorescein compared to the high pH borate BGE. This increased peak width due to longer diffusion times and the slow migration past the detector since fluorescein is a negatively charged small molecule.

4.3 1D and 2D Separation of a Complex Human Serum Digest

4.3.1 1D Separations of Serum Digest Using Low and High pH BGE

To demonstrate the challenge that complex samples present, each dimension of the CE×CAE was operated in 1D mode (as above in Section 2D Peak Capacity Estimation Using 1D Separations of Fluorescein on the Capillary Array and a Commercial Instrument4.2) to separate the 3 kDa to 10 kDa fraction of an FQ-labelled tryptic digest of human serum.

These configurations allowed the ^{1}D (HP 3D-CE) separation to operate with BGE that differed by 3.5 pH units to produce two 1D separation profiles. These separations were not compared to the commercial MDQ instrument because its UV-Vis absorbance detector produced separation profiles that differed too greatly, precluding their direct comparison (not shown).

Figure 53 demonstrates that the 1D separations for both low pH and high pH buffer systems inadequately resolved this complex peptide sample. The low pH separation was underpowered as can be seen by the many unresolved, overlapping peaks in the analytical signal from 13 min – 24 min (Figure 53A). The high pH separation showed a dramatic reduction in peak coverage (Figure 53B). However, it does show a separation profile that is unlike the low pH separation. By using a pH shift between buffer systems, the mobilities of the sample components could be modified to provide very different selectivities and resulting separation profile. Such a tactic could be used to provide orthogonality between dimensions in a 2D CE separation.[151] Peak capacity calculations of the 1D separations were not investigated since the ^{1}D separations did not have adequately resolved peaks to reliably determine the peak width or efficiency.
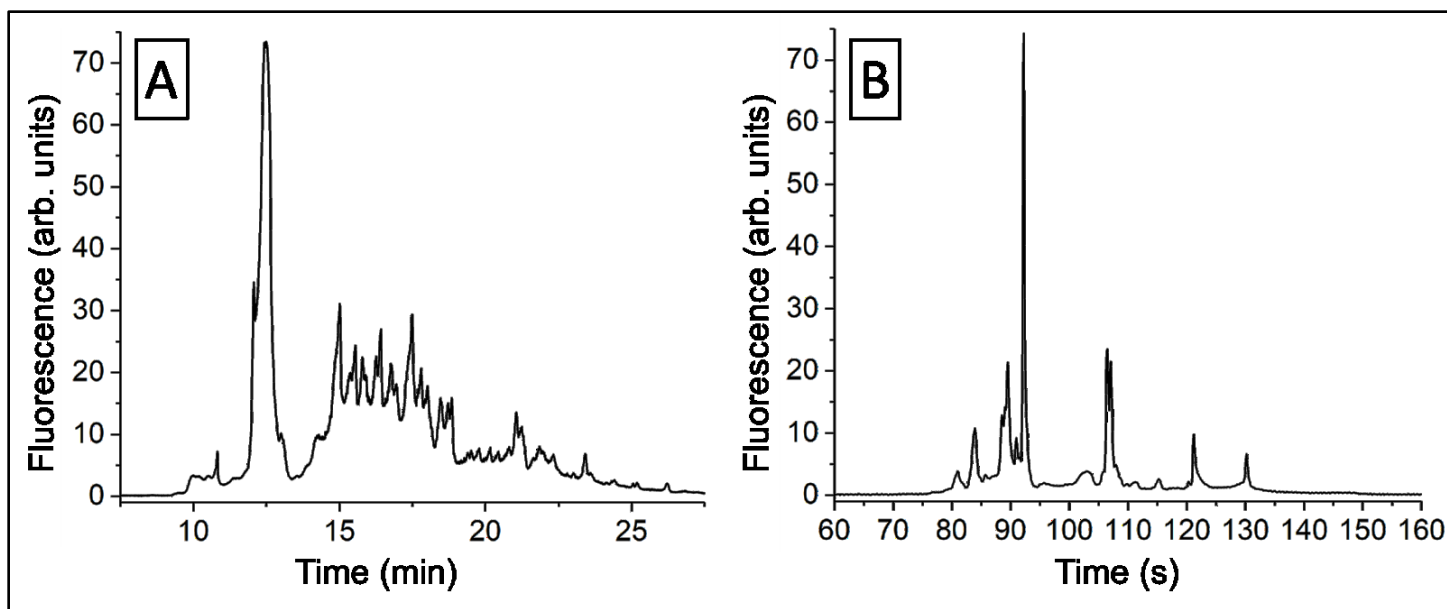
Figure 53 Two 1D separations using the same sample comprised of a 3 kDa to 10 kDa fraction of FQ-labelled trypsin digested serum. HP 3D-CE separation (A) was injected hydrodynamically using 150 mbar · s. CAE capillary separation (B) was injected using the MDS interface by aligning ^{1}D sample capillary and one ^{2}D separation capillary for 2 s. BGE: (A) 25 mM acetate buffer pH 5.8 (B) 25 mM borate buffer pH 9.2 with 5 mM SDS.

4.3.2 Determination of ^{2}D Injection Sequence

The 1D separations performed in Section 4.3.1 also served as preparatory runs for determining the operating parameters for 2D separation on the MDS system. Importantly, the high pH separation window was calculated from the difference between the earliest (t_A) and latest (t_Z) migrating components, $t_Z - t_A$ as 96 s.

This time was used as the target time between adjacent injections on any one ^{2}D capillary in the array. Recall that with an 8 capillary array there will be seven sequential injections on the remaining capillaries before returning to the original capillary 96 s later for a subsequent injection. Thus, the sampling time was calculated as: *96 s (t$_{cycle}$) ÷ 8 (# of capillaries) = 12 s (^{1}D sampling time)*.

4.3.3 On-line 2D CE×CAE Separation of Serum Digest

To generate a selectivity change between the ^{1}D and ^{2}D, the tactic of shifting pH has been successfully used to exploit the highly varied isoelectric points within proteomic samples in CE×CE[151], LC×LC[123] and CE×uFFE[159] separations. Any peaks exiting the ^{1}D and entering the ^{2}D capillary undergo rapid exposure to the new buffer system, where analytes adopt new ionic

mobilities and migrate within the new separation space. Thus, a multidimensional separation of the FQ-labelled serum digest used in Section 4.3.1 was used to demonstrate the improved separation power achieved when performing a 2D CE×CAE separation. The 2D separation utilized the same two buffer conditions as the 1D separations in Section 4.3.1, while operating the CE×CAE instrument in an online 2D separation mode. The sample was separated on the ^{1}D capillary, with effluent sampled by the ^{2}D every 12 s, providing each ^{2}D capillary with a 96 s separation window as described in Section 4.3.2.

4.3.3.1 Injection cycle modifications

To minimize the amount of ^{1}D effluent lost to waste, two modifications were made to the sequence used between each ^{2}D injection. First, the injection time was set to 2 s instead of the plate number optimized 0.3 s injections times (Section 3.1.5). These long injection times were used to increase the amount of sample transferred from the ^{1}D to improve detection of low abundance analytes. This also partially compensated for the low-power of the excitation laser and an older CCD camera with reduced sensitivity. This increased injection time was, in principle, at the expense of efficiency (Section 3.1.5 found 200 ms injection times to be optimal) but the loss may not be as dire given the larger MW of the biological analytes. Second, a high-voltage (HV) relay was used to interrupt the ^{1}D voltage potential for 7 s in each 12 s sampling interval, as depicted in Figure 54. Within the 5 s window where ^{1}D voltage was applied, sampling was initiated after 2.5 s had elapsed. This was done to ensure the effluent flow had stabilized before an injection was performed.
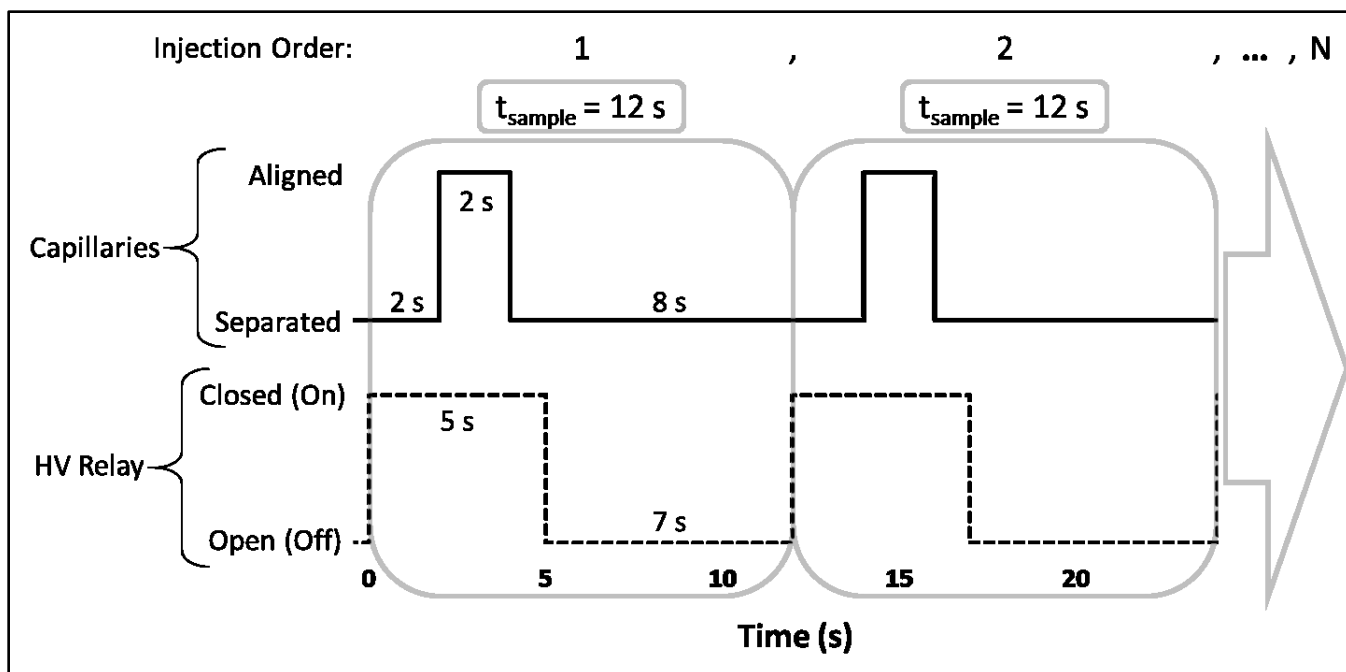
Figure 54 Timing program used each sampling interval used to inject ^{1}D effluent onto a ^{2}D capillary. A 12 s sampling interval was used where the ^{1}D separation was operated in a stop-and-go fashion by using a HV relay while MDS interface concurrently performed motion controlled injections onto the ^{2}D capillaries. During the 12 s sampling interval, the ^{1}D HV circuit followed the pattern: 0 – 5 s closed (on), 7 – 12 s open (off). During the same interval, the MDS interface positioned a ^{2}D capillary in relation to the ^{1}D effluent with the pattern: 0 – 2 s separated, 2 – 4 s aligned, 4 – 12 s separated; during the 4 – 12 s segment the next ^{2}D capillary in the injection sequence moved to its pre-injection position. Two sampling intervals are shown, which would result in injections onto two capillaries. A full injection cycle would require 96 s = *12 s sampling interval × 8 capillaries*.

4.3.3.2 2D CE×CAE Separation Profile for Serum Digest

Figure 55A shows the 2D CE×CAE separation of a tryptic digest of serum, including a heat map of the full 2D separation time as well as a selection of 96 s long electropherograms (Figure 55B, aka fractions) recorded from individual ^{2}D capillaries. The ^{1}D axis is displayed as the number of effluent fractions captured, each of which is equivalent to the 12 s sampling intervals used. The ^{2}D axis is displayed in the time required for the ^{2}D separation window to elapse, 96 s, which was set by the sampling interval and the number of capillaries in the array. Rescaled versions of the 1D separations in acetate and borate separations (Figure 53), respectively, were placed at the top and right edges of heat map in Figure 55A. In principle, the MDS interface should have begun transferring fractions of ^{1}D effluent to the ^{2}D capillary array at the time the serum sample was injected onto the ^{1}D. However, this resulted in a large dead time before any sample component (from the ^{1}D) could reach the MDS interface. To shorten this dead time, the ^{1}D HV relay was set to the closed (on) position for the first 8 minutes, after which it was operated using the stop-and-go HV sequence (Section 4.3.3.1).

156
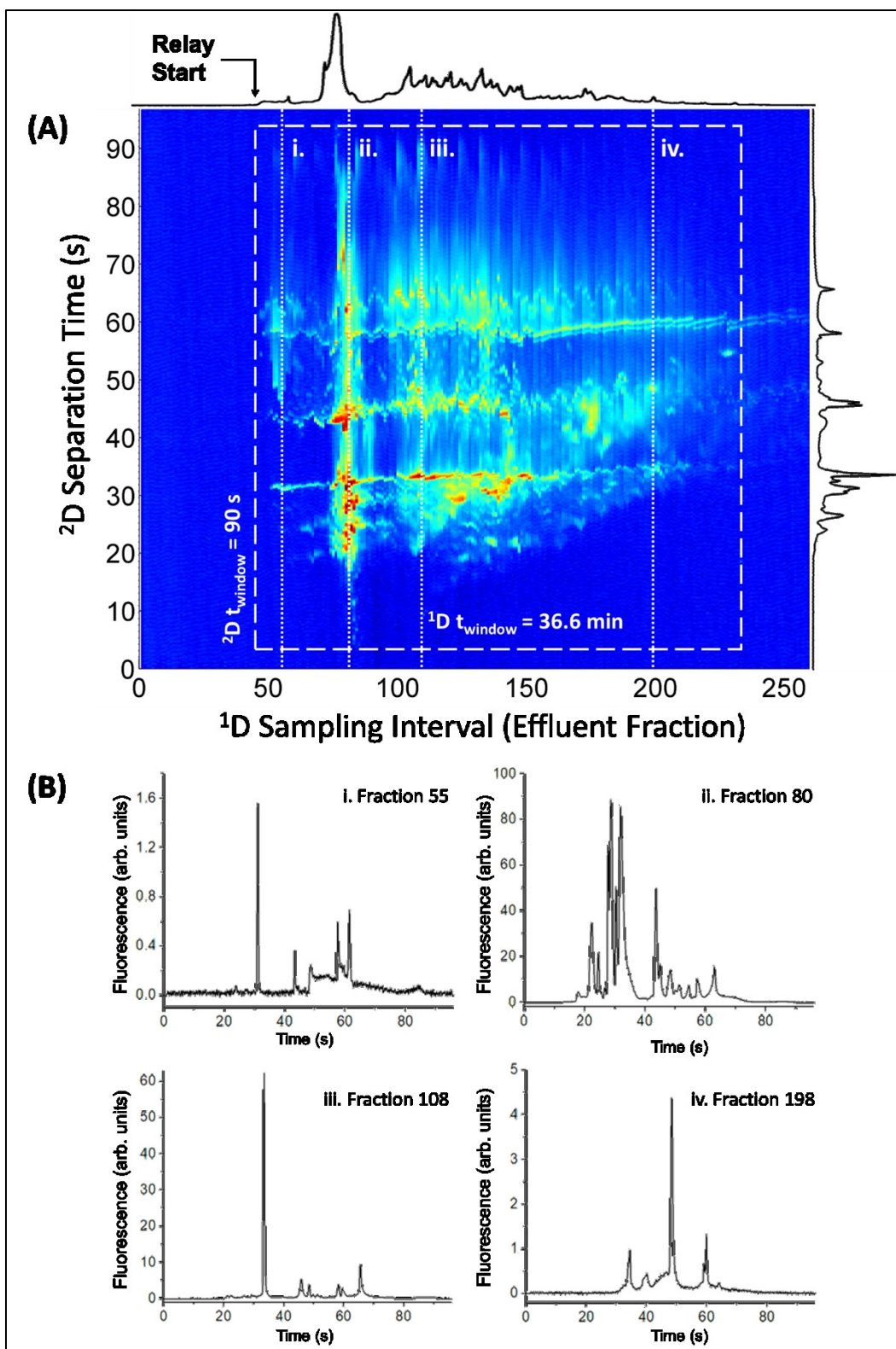
Figure 55 Two-dimensional separation of FQ-labelled serum digest. Rescaled 1D separations from Figure 53 are inset along the top and right axes. ^{1}D: 25 mM acetate buffer, pH = 5.7. ^{2}D: 25 mM borate, 5 mM SDS, pH = 9.2. The displayed log scaled 2D heat map (A) of interleaved ^{2}D CE-LIF electropherograms. Separation window used for peak capacity calculations enclosed by dashed line region. Individual linearly scaled ^{2}D electropherograms (B) from select ^{1}D fractions whose positions are marked by the vertical dotted lines.

By operating the system in a stop-and-go regime the ^{1}D was stopped/interrupted for 7 s of each 12 s sampling interval (Section 4.3.3.1). This effectively slowed down the ^{1}D separation to extend the total separation time to: *(1D separation time) × (sampling interval ÷ time voltage was applied)* *= 19 min 10 s × 12 s ÷ 5 s = 46.0 min.*

Using a stop-and-go ^{1}D separation, as mentioned above, two principle advantages were gained: a higher fraction of the 1D separation was sampled since the effluent during the 7 s would have been lost to waste and; the period between adjacent injections on the same capillary was matched to the separation window (96s). Operating with 96 s of separation time ensured each ^{2}D separation window was non-overlapping. This is shown in the 2D heat map (Figure 55A) where baseline is clearly visible at the beginning and end of each ^{2}D separation.

In Figure 54A, the ^{1}D was sampled 352 times (70.4 min), but the effective separation time was chosen to end at fraction 230 (46 minutes) to encompass the last clearly resolved ^{1}D peak (fraction 228, 54 s). The 46.0 min ^{1}D separation time was longer than the previously shown 1D separation (Figure 53, at 30 min) due to the stop-and-go operation. Had a single ^{2}D capillary been used in a serial fashion under the same separation conditions, the total separation time required would have been the product of the number of effluent fractions sampled and the ^{2}D separation time: *230 (fractions) × 96 s = 22 080 s = 368 min.*

There was considerable similarity between the two 1D separations and the resulting 2D separation. Despite being time aligned via COW, there was a drift toward longer ^{2}D separation times as the overall separation time increased. This can be observed in the behaviour of the two ridges from effluent fractions 150 to 210 whose ^{2}D migration times extend from 56 to 62 s. The peaks in the 2D heat map do not all accurately coincide with peaks in the 1D separation profiles displayed along top and right borders, indicating peak shifts had occurred. Both of these peak shifting effects were likely due to the gradual increase in the room temperature due to heat generated by all of the equipment required to operate the MDS system and potentially capillary surface changes. It was presumed to have and had a significant effect on the ^{2}D array which is simply air-cooled using a nearby low noise fan placed inside of the continually warming room.

The combination of low pH and high pH separations resulted a dramatic expansion of coverage over the 2D separation space as compared to either of the underlying 1D separations. Much of the

2D separation window, marked by the dashed rectangle, had detectable signal from sample components. This suggests that the instrument could perform orthogonal separations that are able to access most of the separation space. However, there were also non-random features within the heat map that represented poorly resolved components in the electropherogram. The three distinct examples at 30 s, 43 s and 60 s in the ^{2}D, which appeared as three low signal intensity ridges that were not observed during blank runs. These ridges spanned most of the ^{1}D separation window and continued to tail past the end of the separation. These peaks were suspected to be peptides strongly interacted with the ^{1}D capillary wall under the moderately acidic acetate BGE used. The trailing peak signal was indicative of their slow dissociation from the wall over the course of the separation.

Select individual fractions from the set of 230 interleaved ^{2}D electropherograms are shown in Figure 53B, which demonstrate that narrow peak widths were achieved within the ^{2}D separations of ^{1}D fractions that were sampled during an on-line 2D separation. It was also representative of the capillary array's robustness to the concentration dynamic range and number of analytes found in the effluent within the ^{1}D separation window. The 2D separation window, enclosed in the dashed-line rectangle, was selected to enclose distinguishable peaks in the separation space but cut off the tailing signal that continues past fraction 230. This resulted in ^{1}D and ^{2}D separation windows of 36.6 minutes and 91 s, respectively.

Five well resolved peaks distributed across the separation space were selected and modeled as 2D Gaussians using non-linear peak fitting. The ^{1}D time required for the stop-and-go sequence and was unmodified. The average baseline peak width in the ^{1}D was 33.5 s, resulting in a ^{1}D peak capacity, ^1n_c, of 65. Similarly, the ^{2}D peak capacity, ^2n_c, was 74 arising from 1.16 s average baseline peak widths. However, this peak width was conspicuously narrower than the injection time. This likely resulted from two factors. Firstly, the selected peaks were chosen to have baseline separation to ensure better fit during modeling and this constraint meant the entire separation space was well represented, likely causing overestimation in the ^2n_c. Secondly, there was likely a small amount of electrokinetic sample focussing due to the lower total BGE conductivity in the ^{1}D compared to the ^{2}D.

The theoretical 2D peak capacity, $n_{c,2D}$, was 4874 in a 36.6 min separation window, resulting in a peak generation rate of 133 peaks/min. The 12 s sampling time between ^{2}D capillaries implied that

^{1}D peaks were sampled 2.79 times on average. Thus, the calculated ^1n_c retained by the ^{2}D was 83.7 %, with the remainder lost due to the ^{1}D effluent being sampled at less than 3 samples/peak, known as ^{1}D peak broadening from undersampling (Section 1.9, 1.10).

Increasing the sampling rate of the ^{1}D effluent could be achieved by modifying the ^{1}D HV relay sequence and the MDS interface injection sequence (Figure 54). During each sampling interval, a shorter duration of applied voltage across the ^{1}D could be used while in close synchrony with the MDS injection.

The demonstrated 2D separation used an injection sequence where each 12 s sampling interval had voltage applied across the ^{1}D for 5 s and the MDS interface positioned ^{2}D capillaries to receive an injection for 2 s. Thus, 3 s of sample was directed to waste for each sampling interval. The time that voltage was applied to the ^{1}D was successfully reduced to 3 s in a 12 s sampling interval without reduction of injection efficiency (data not shown). This modified injection sequence would, of course, be at the expense of increasing the total separation time along with diffusion mediated peak broadening within the ^{1}D capillary.

Due to the constant replenishment and large volume of the laminar flowing BGE at the ^{2}D inlets, this MDS interface design benefits from being highly flexible in the combinations of separation conditions that can be paired. Since the ^{1}D effluent volume was small relative to the surrounding BGE, the ^{2}D BGE in the MDS interface rapidly surrounded and mixed with the ^{1}D effluent as it was transferred to the ^{2}D capillaries. The surrounding laminar flow also served to effectively segregate the ^{1}D effluent within the bounds of the path it was entrained within, preventing it from poisoning surfaces within the MDS interface (such as the plastic walls). This is a challenge with flow-gated interface designs where the ^{1}D effluent fills the cavity between the ^{1}D and ^{2}D capillaries.

4.3.3.3 Comparison to Other Multidimensional Separations

CE×CAE that utilized a motorized capillary array in the ^{2}D demonstrated a unique approach to performing 2D separations with high sampling rates, sample transfer efficiency and peak capacity. Although a high-voltage relay was used to periodically pause the ^{1}D separation between ^{2}D injections, no other separation conditions required modification. The result was that low-resolution 1D acetate and borate separations were combined into a 2D separation with a high

level of coverage across the 2D separation space. This separation served as a proof of principle that the present instrument can be subjected to a challenging sample with promising results. It is beneficial to place this work in the context of other 2D systems found in the literature.

Table 5 summarizes recent milestones for continuously operated on-line 2D liquid-phase separations of complex biological samples aimed at high peak capacity and high-throughput. These systems each have specific benefits when looking at their figures of merit (peak capacity, peak generation rate) as well as their practical operation and potential for improvement (ease of use, complexity, per sample analysis time). An analysis of each system in the table will clarify their strengths and weaknesses. Both the CE×CE[153] and LC×CE[203] separations utilized a single ^{2}D capillary. This required the sampling interval for the ^{1}D effluent to be shorter than the ^{2}D separation windows, causing each separation window to overlap with adjacent separation windows. Thus, analyte peaks from one ^{2}D injection frequently overlapped with those from the subsequent injection, leading to a loss of peak capacity and generation of overly complicated data sets. The CE×CE separation also required long analysis times (355 min), precluding its use in a high-throughput setting, although it didn't have inter-capillary variability. When considering the microscale/microchip device-based instruments—such as µChip CE×CE, nLC×µFFE, CE×µFFE—impressive total peak capacities and peak generation rates were achieved. Chip based devices require expert construction and require remanufacture of the device when fouling occurs on the interior surfaces. Specific to the µFFE based systems, they demonstrate a unique continuous separation whose sampling time is dependent on the capture rate of the CCD detector at the end of the chip. While this practically eliminates the negative effects of undersampling the ^{1}D effluent, the inherently lower resolution of µFFE separations[204] limit the available peak capacity that it can contribute to the overall separation. In both generations of µFFE systems (nLC×µFFE[158], CE×µFFE[159]), the µFFE dimension demonstrated identical ^{2}D peak capacity of 24. Indication was not given as to whether there was room for improvement for ^{2}D separation efficiency. Detectors for µFFE mainly rely on LIF, with limitations to using other detection methods such as mass spectrometry. Specific to the microchip CE×CE device[205] and LC×CE instrument[203], separation windows of 0.7 s – 2.0 s were used in the ^{2}D, which is at the limit that these separations can be operated. The LC×array LC instrument[206] used 12 parallel capillary LC columns in the ^{2}D, which incorporated three mechanical valves and two gradient pumps, along with their concomitant timing program complexity. Despite the dramatic increase in the number

of parallel ^{2}D separations, both sampling times and overall separation time remained long due to the column regeneration steps required between injections onto the ^{2}D.

Table 5 Separation characteristics of reference high-throughput 2D separation techniques for complex biological samples. (*reported as number of differentiated peaks)

Hyphenation	$n_{c,2D}$ (ideal)	^2n_c	$t_{window, 2D}$ (min)	$^2t_{sep}$	n_{rate} (peaks/min)	$t_{sampling}$	Reference
CE×CE	550	18	355	4 min	1.4	158 s	[153]
LC×CE	650	43	2.8	0.7–2.5 s	232	0.35–2.5 s	[203]
nLC×µFFE	2352	24	10	15 s	235	0.5 s	[158]
CE×µFFE	2592	24	7.6	10–20 s	342	0.25 s	[159]
µChip CE×CE (speed mode)	1950	21	4.4	0.9 s	443	0.9 s	[205]
µChip CE×CE (peak capacity mode)	4100	21	25	1.5 s	195	1.5 s	[205]
LC×array LC (×12)	900*	—	252	21 min	3	15 min	[207]
CE×array CE (×8)	4874	74	36.6	96 s	133	12 s	Current Work

In comparison, the multiplexed ^{2}D of the CE×CAE system presented herein allowed sampling rates to increase without risking overlapped separation windows or heavily taxing the ^{2}D separation conditions. Although the sampling rate is lower than the leading MDSs, this system benefits from a scalable design which can be leveraged to improve separation efficiency. The laminar flow regime in the MDS interface entrains the ^{1}D effluent in the injection zone, preventing it from contacting and fouling these surfaces, including the optical window of the interface.

Obvious and simple modifications to improvements the MDS system include: adding additional capillaries, using shorter capillaries, higher electric fields and providing improved capillary thermostatting. The independent nature of the fused silica capillaries used means that a single fouled capillary can be replaced with an "off-the-shelf" replacement capillary that is inexpensive and simple to prepare. Although, laborious, replacement capillaries can be removed and inserted through MDS interface and sheath flow cuvette after assembly. The CE×CAE system has the advantage of being well suited to achieving higher ^2n_c that can contribute greatly to the overall

peak capacity. The CE×CAE system also benefits from a mature ecosystem of CE detector mechanisms, which can be amenable to miniaturization and/or modularization. User operation of the CE×CAE system is simple, with injection time and sampling time being the only two interface parameters to adjust between runs. Complex mechanical valve connections and timing programs are avoided. The ^{1}D separation is limiting in the demonstrated serum digest separation. Improvement to the overall peak capacity is expected with investigation and optimization of other combinations of separation modes such as micellar electrokinetic chromatography, capillary electrochromatography, capillary isoelectric focusing and capillary gel electrophoresis. Interfacing the capillary array to other liquid-phase separation instruments, such as HPLC, will provide further improvement to peak capacity from a wider array of orthogonal separation mechanisms.

Chapter 5 Dual Injections for Ameliorating Alignment Challenges

Chapter 4demonstrated that a capillary array can be used to accept sequential samplings of a ^{1}D separation containing either a single peak or a complex biological sample. A shortcoming of the data presented on the 2D separation of a serum digest in Section 4.3.3, was errors of time shifting in the ^{2}D. Two major contributors were inter-capillary differences across the ^{2}D array and a slow drift towards longer ^{2}D migration times as the 2D separation progressed, possibly caused by temperature drift from Joule heating in sub-optimally cooled capillaries. These forms of imprecision are common in MDS and are very problematic because changing peak positions complicates comparison between samples. This has garnered considerable attention in the literature with two general strategies. One is the discovery of suitable internal standards that can behave as time markers and used to time normalize the analyte peaks.[180,208–211] The other is designing data processing software to correct the data automatically using time alignment/optimization algorithms.[188, 212–216]

A challenge with using internal standards for migration time in CE separations is that a laborious search is required for each set of separation conditions. Ideally, a pair of small molecule fluorophores (when LIF is used) should be used, one cationic and one anionic, and each multiply charged. This provides the best likelihood that the markers will have migration times at the edges of, or even outside, of the separation window, one before and one after. However, this is not assured as biomolecules having many charge sites may have a charge-to-volume ratio that matches even the smallest charged fluorophore and result in unavoidable comigration between sample and internal time standard. Also, these same molecules can interact with the wall and/or the analyte species, altering their migration.

In this chapter a modification of the CE×CAE instrument will be presented that enables injections onto the ^{2}D capillary array using two ^{1}D sources. This allows for independent injection of the sample and a migration time (t_m) marker. Independent injection makes the separation data robust to time shifts in the ^{2}D, simplifying data processing to greatly improve the precision of the aligned data.

The 1/16" PEEK sleeve that held the ^{1}D capillary outlet at the MDS interface was replaced with a fluoroelastopolymer (FEP) dual lumen sleeve (Upchurch, Part F-235) with two 400 μm lumens whose centers were nominally spaced 698.5 μm apart (see Figure 56). The primary ^{1}D separation

capillary (180 μm o.d.) was inserted into a short length of 250 μm i.d./365 μm o.d. capillary in the left-hand lumen, while a new ^{1}D capillary was similarly inserted into the right-hand lumen. The second ^{1}D capillary was attached to a syringe pump to deliver the t_m marker, 100 nM fluorescein-5-(and-6)-sulfonic acid (FL-SO$_3^{-3}$) solution, at a linear velocity of 0.35 mm/s. The motorized injection sequence was modified to perform a t_m marker injection after completing the sample injection, as explained below. Alignment of both ^{1}D capillaries was similar to what was described in Section 3.1.2.
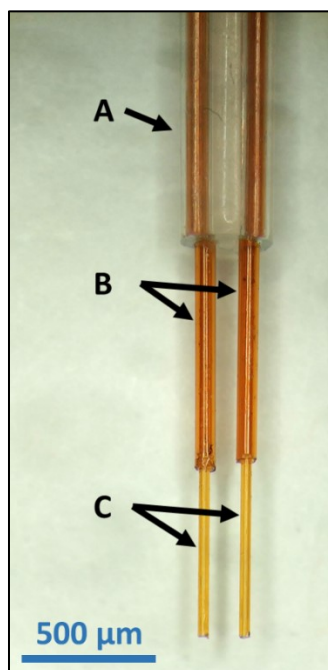
Figure 56 Dual-lumen FEP sleeve with nested capillaries installed. (A) FEP sleeve: o.d. 1/16", i.d. 400 μm. (B) Interstitial sleeve capillaries: o.d. 365 μm, i.d. 250 μm. (C) Separation and t_m marker capillaries: o.d. 180 μm, i.d. 100 μm.

The sulfonic acid functional group imparts an additional -1 charge to the dianionic parent fluorescein under basic conditions. At a MW = 478.31 g/mol and having a -3 charge, the mobility of FL-SO$_3^{-3}$ will strongly oppose the EOF and therefore migrate with a slow velocity towards the cathodic (detector) end of the capillary, making it a good candidate for a small molecule standard that will successfully migrate outside of the separation window. Before a demonstration of its use, a quick analysis of the behaviour of the FL-SO$_3^{-3}$ was made. Here, the ^{1}D was infused with FL-SO$_3^{-3}$ to perform replicate automated injections onto the capillary array with 5 s sampling times (40 s array cycle time); data for one ^{2}D capillary is shown. The FL-SO$_3^{-3}$ injection produces a small system peak, x, at 92.3 s. This was believed to be from trace amounts of degraded FL-SO$_3^{-3}$ with the sulfonic acid detached. The next two migrating peaks, α_1 at 121.6 s and α_2 at 125.5 s, were the

two isomers of FL-SO$_3^{-3}$ which were partially separated using this buffer system. No attempt was made to differentiate the two isomers. Two replicate sets of peaks followed, resultant from two subsequent replicate injections. These reproduced the same three peak profiles well. The degradation peak was expected to overlap the separation window but was acceptable due to its small size and would not likely be present in freshly purchased/prepared solutions. The two-peak pattern produced by the FL-SO$_3^{-3}$ made it easily identifiable by eye in an electropherogram, and well suited to use with a biological sample in the next section.
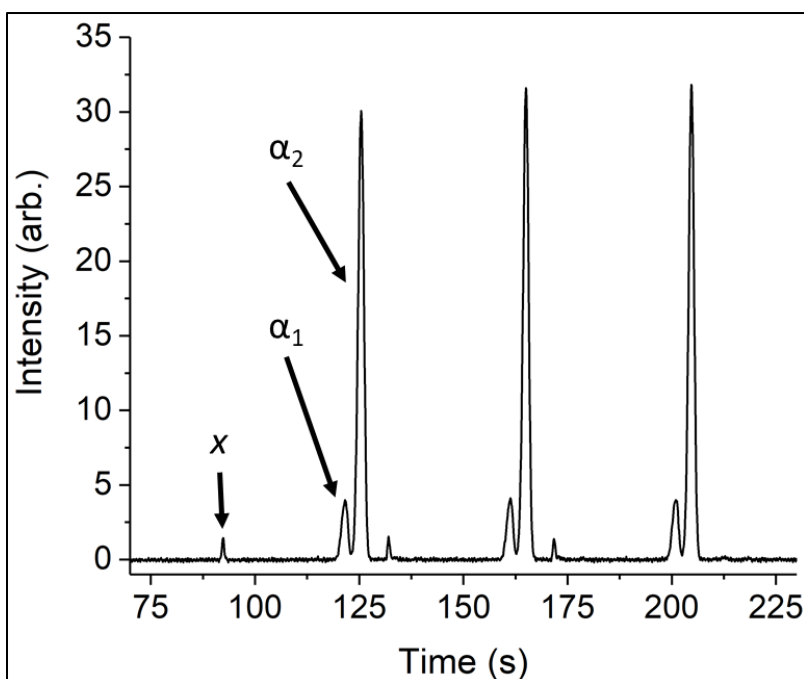
Figure 57 Triplicate injections ($t_{sampling}$ = 5 s, t_{cycle} = 40 s) of t$_m$ internal standard (fluorescein-5-(and-6)-sulfonic acid, mixed isomers) on one capillary in the ^{2}D CAE. The separation resolves the two isomers; seen as peaks (α_1) and (α_2). A degradation product of the internal standard appears as an early migrating system peak (x).

5.1 Controlling the t$_m$ Marker Injection Delay

The addition of a secondary ^{1}D capillary enabled arbitrary injection/placement of the FL-SO$_3^{-3}$ relative to the sample separation window in the completed electropherogram. To demonstrate this, a series of separations were performed on the ^{2}D, while operated in 1D mode. FL-SO$_3^{-3}$ was introduced as a migration time (t$_m$) marker alongside a sample of FQ-labelled β-casein digest. Using the modified motor injection program, the FL-SO$_3^{-3}$ injection was performed after the sample injection using three different delay times: 1.5 s, 5.5 s, and 7.5 s. To compare against a t$_m$ marker injection with no time delay, FL-SO$_3^{-3}$ was added to the sample matrix.
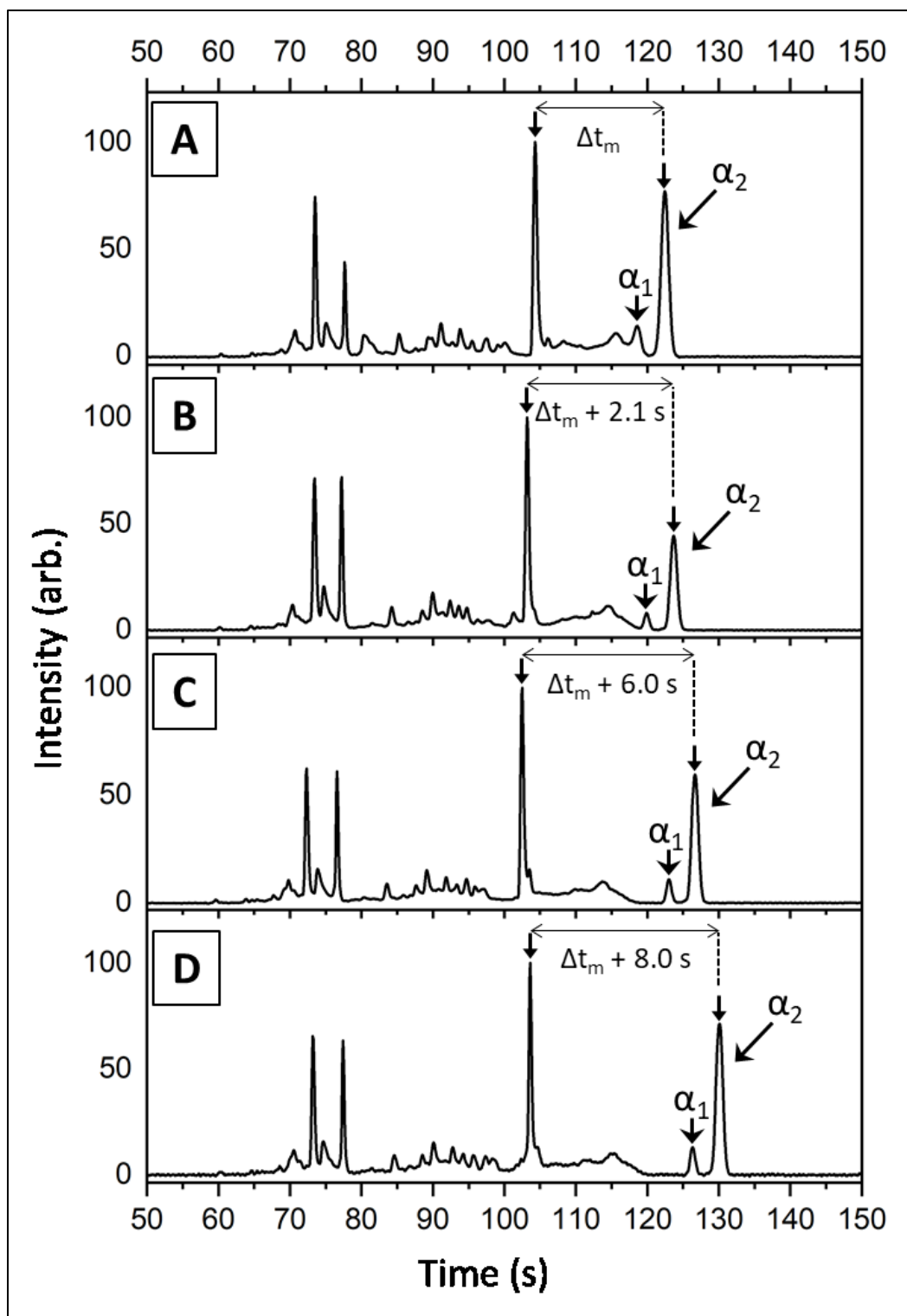
Figure 58 Dual-capillary injections of FQ labelled β-casein sample and time delayed t_m marker (fluorescein-5-(and-6)-sulfonic acid, mixed isomers). The t_m marker is included in the sample matrix (A) or after the sample with a delay of 1.5 s (B), 5.5 s (C) or 7.5 s (D). The t_m of the second marker peak, α2, increases with delay times, as indicted relative to the largest sample peak. The less intense marker peak, α1, overlaps the sample separation window in (A), and progressively migrates later than the sample peaks until it is baseline resolved (B to D). All traces were scaled to the tallest peak in each separation.

The stacked plots in Figure 58 show the results of the delayed injections of FL-SO_3^{-3}. The two prominent FL-SO_3^{-3} peaks were indicated as α_1 and α_2 for the early and late migrating isomers, respectively. In Figure 58A, with no time delay, the α_1 peak completely overlapped with the end of the sample separation window. With the first delay of 1.5 s (Figure 58B), α_1 still overlapped the separation window minimally, but baseline resolution was achieved at longer delay times (Figure 58C, D). The α_2 peak was near the tail of the last broad peak in the sample window when FL-SO_3^{-3} was included in the sample matrix. It was placed well behind the separation window in all other iterations. When used as an internal standard, the t_m marker overlapped the separation window. Whereas it can be effectively placed at an arbitrary non-overlapping position by using a secondary ^{1}D injector to inject the t_m marker. This was done without changing the sample separation window and with a predictable gap between the separation window and the t_m marker. For the time delays chosen, there was a linear increase in the time between the intense sample peak at 104 s and the t_m marker peak α_2. The ca. 0.5 s increase in the Δt_m over the injection time delay was due to the difference in the electrophoretic mobility between the two peaks being compared.

5.2 Correcting t_m Errors in a 2D β-casein Separation

To demonstrate how an externally injected t_m marker can simplify and improve data processing when performing ^{2}D time alignment, a 2D separation was generated and the data processed with and without use of the t_m marker. The FQ-labelled β-casein sample used in Section 5.1 was subjected to a 2D separation using the same conditions as the 2D serum separation in Section 4.3.3 with the following modification. Each sample injection was followed by a 7.5 s wait and then a 300 ms t_m marker injection. The raw data was processed in two ways to demonstrate alignment with and without the benefit of the t_m marker. First, COW was applied directly to the raw data in the 2D separation space in the usual, rolling pairwise, fashion. (Figure 59A) Second, COW was applied to the t_m marker portion of the raw data twice using the following sequence (Figure 59B). The first separation on each ^{2}D capillary was extracted for COW alignment, creating an eight column data array. The first separation for each capillary contained only ^{1}D effluent and the t_m marker from the secondary injection. This allowed the eight separations to be aligned to the t_m marker. For each capillary, the difference between the raw data and the COW modified data was used to generate per-capillary t_m offsets. The calculated offset for each capillary was then subtracted from each of their subsequent separations. This resulted in a coarse migration time

correction for the entire 2D separation space. Then a COW treatment was applied to the entire 2D separation space, but only allowed to warp shift the ^{2}D separation profiles in the region between 78 – 96 s.
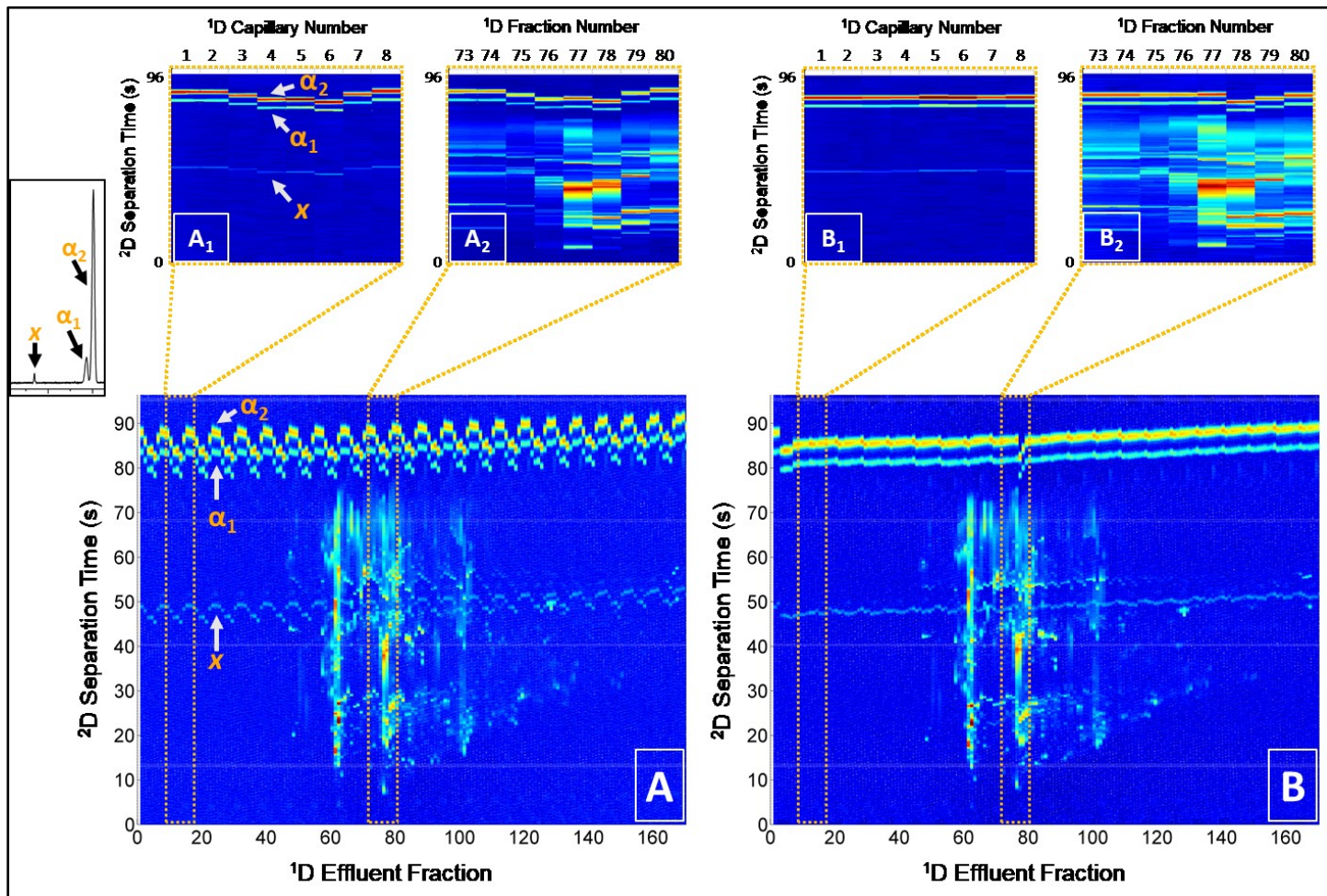
Figure 59 The effect of correlation optimized warping when directly applied to raw 2D separation data. ^{1}D BGE: 25 mM acetate pH 5.7. ^{2}D BGE: 25 mM borate pH 9.2, 5 mM SDS. The full log scaled 2D electropherograms of a FQ-labelled β-casein digest and FL-SO$_3^{-3}$ t$_m$ marker are shown for the raw fluorescence data (A) and COW treated data (B) using a slack size of 15. Example peaks arising from the t$_m$ marker have been indicated in the boxes A, A$_1$ and the inset from Figure 58. Expanded views of fractions 9 – 16 are shown for the raw (A1) and COW treated (B1) data with the capillary number indicated. Expanded views of fractions 73 – 80 are also shown for the raw (A2) and COW treated (B2) data.

Figure 59 shows the raw 2D separation data after interleaving each ^{2}D separation window (Figure 59A) and the same data after direct pairwise treatment of COW to the raw data (Figure 59B). The top of the figure shows two expanded views of identical regions of interest for each of the raw and COW treated separations. The early migrating region (A$_1$, B$_1$) includes ^{1}D fractions 9–16 (1.6 min– 3.2 min), corresponding to one injection onto each ^{2}D capillary. The late migrating region (A$_2$, B$_2$)

169

includes ^{1}D fractions 73–80 (14.4 min–16 min) and has the same capillary ordering for each column of heat mapped data.

Direct application of the COW time alignment without using the t_m marker did not provide satisfactory correction of the time shift artifacts in the ^{2}D. In Figure 59A, there was a clear periodicity in the migration time that was mirrored by all three t_m marker peaks, x, α_1 and α_2. This formed a range that the FL-SO$_3^{-3}$ peaks were positioned across the capillary array, spanning 78 s–92 s, which had a periodicity caused by inter-capillary differences across the ^{2}D array. This periodic set of eight time shifts was reproducible and easily seen when comparing the two FL-SO$_3^{-3}$ peaks from each capillary at the start of the separation (Figure 59A$_1$) and late in the separation (Figure 59A$_2$). Figure 59B depicts the best time alignment achieved among COW slack sizes equivalent to 0.5 %–5 % of the ^{2}D separation time.

While much of the periodicity was eliminated using COW and the t_m marker, it was not entirely removed by the alignment procedure. Instead, each period was transformed into blocks of eight adjacent separations that were closely aligned but included a noticeable drift towards longer migration with increasing effluent fraction number. Two blocks of eight ^{2}D separations were drastically misaligned; at ^{1}D effluent fractions 1 – 8 and 73 – 80. In the expanded view of the start of the separation (Figure 59B$_1$) the COW had brought all three t_m marker peaks into much closer alignment, with α_2 being the most centered. The degradation peak, x, retained some misalignment due to its different electrophoretic mobility with the α_2 peak that the COW algorithm was biasing toward. In Figure 59B$_2$, fractions 73–77, the α_2 peaks were aligned correctly, but the injections on the last 3 capillaries were incorrectly aligned. Here, a pattern was retained where, in fractions 6–8, the migration time of the α_2 peak increased with capillary number.

The three heat maps, in Figure 60, show a progression of data alignment using the two-step alignment procedure that incorporated the t_m marker injection. When the raw 2D separation (Figure 60A) was subjected to a simple per-capillary offset correction, only the longer drift component remained in the data (Figure 60B).
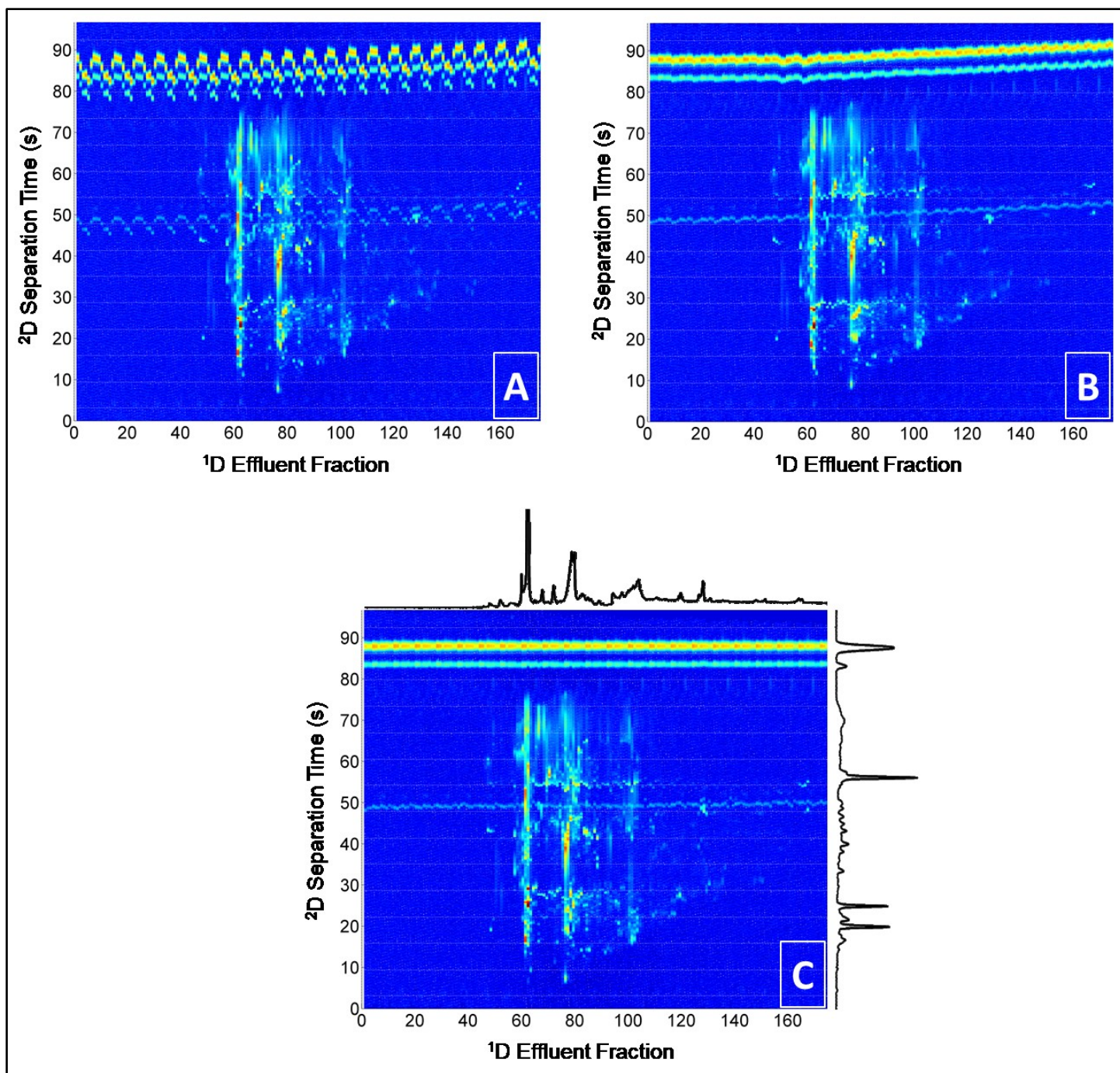
Figure 60 Piecewise time alignment of interleaved raw ^{2}D fluorescence data (A) of a FQ labeled β-casein digest as shown in Figure 59A. Initial alignment (B) was performed by COW of the first eight ^{1}D fractions and applying these shifts as offsets for every capillary array cycle. Secondary alignment (C) was achieved by applying COW to the 80 s-96 s segment of each ^{2}D separation and applying the resulting warping parameters to the whole respective electropherogram.

A final COW treatment across every ^{2}D electropherogram, but constrained within the region of the FL-SO$_3^{-3}$ peaks removed the drift and brought all t$_m$ marker peaks into good alignment (Figure

60C), which then aligned the overall separation space. The 2D separation had good agreement with the overlaid 1D separations that were performed on the CE×CAE instrument.

The ability to introduce a t_m marker at an arbitrary point in the ^{2}D separation, instead of being co-injected with the sample in the ^{1}D, enabled a unique approach for data processing. To my knowledge, this is the first reporting of such a capability in a 2D separation system. By simply setting an appropriate delay time between sample and t_m marker injection, any possibility of overlap between the sample separation window and the t_m marker was avoided. Increasing the delay, so there were several seconds of baseline between the end of the separation window and the FL-SO$_3$$^{-3}$ peaks, allowed software discrimination of these peaks versus the rest of the electropherogram. While a two-stage COW alignment was used here, the reliable placement of t_m markers outside of the sample separation window was useful with other alignment techniques.[180] In the case where FL-SO$_3$$^{-3}$ was used as an internal standard infused in the ^{1}D effluent, any intense sample peaks near the end of a ^{2}D separation window would be at risk of coeluting with FL-SO$_3$$^{-3}$ peaks.

Since the spacing between separation window and t_m marker can be varied instrumentally, there was opportunity to use t_m markers that would normally migrate sooner than the FL-SO$_3$$^{-3}$ example shown here. However, there was expected to be a limit to the difference in the mobility of the t_m marker and the latest migrating component of the separation window. The per-capillary offsets seen across the capillary array were primarily due to EOF differences that produced a largely constant velocity shift to all analytes within a ^{2}D separation window. Early migrating components spent less time being affected by this velocity offset than late migrating components. Thus, a t_m marker with the same mobility as the x peak (Figure 57), it would have a smaller t_m shift than late migrating components such as the α_2 peak. Although this earlier migrating t_m marker could be placed after the separation window, it would cause the initial t_m offset calculation to be biased to that of an early migrating marker. The sample components at the end of the separation window would have experienced a greater time shift than the t_m marker. This could introduce error in the offsets calculated using the t_m marker. Converting to mobilities from migration time may help, but the use of a secondary "early t_m" marker would be more robust and effective.[180]

A second t_m marker that migrates ahead of each ^{2}D separation window will need a third ^{1}D capillary to be introduced into the apparatus and the motor program modified. Each modified ^{2}D injection

would follow the pattern: (1) inject early t_m marker, (2) inject ^{1}D effluent, (3) inject late t_m marker. Though this was not attempted in the current work, the physical dimensions of the current MDS interface allows for the addition of another capillary with only structural modification being the replacement of the dual lumen sleeve capillary holder with a three lumen one.

Since the ^{1}D separation capillary is not used to inject the t_m marker, the marker cannot be relied upon to correct for variations arising from sample transfer efficiencies from the ^{1}D separation capillary (Sections 3.1.2 – 3.1.4, 3.1.6). However, it can correct for variability in detector sensitivity between capillaries (Section 3.2.1) that can occur outside of injection processes. Thus, the t_m marker can still be exploited to act as internal standards for inter-capillary signal correction. Commercially available t_m markers may not be available with the exact electrophoretic mobilities, excitation and emission properties and solubilities required for a specific application, but this can be ameliorated by the custom preparation of suitable markers that will not interfere with analyte peaks.[180]

Chapter 6 **Conclusions and Future Directions**

6.1 Conclusions

An instrument was designed and built with a novel CE×CAE MDS interface that performed automated coupling of two CE separations by placing their ends proximal to each other while axially aligned in a laminar flowing stream. The MDS interface performed efficient sample transfers from a 1D CE separation to an array of independent 2D separations which generated high peak capacity 2D separations in highly reduced analysis times. The CE×CAE system generated an ideal 2D peak capacity of 4874 in a 36.6 minute separation for FQ labelled serum peptides, resulting in a peak generation rate of 133 peaks/min. This was two-thirds of the highest peak production rate achieved by online microchip CE×CE.[205] The design enables geometric increases to the sampling rate of the ^{1}D effluent with each additional ^{2}D capillary, which allowed the ^{2}D capillaries to use 32 s separation times while sampling the ^{1}D every 4 s. The MDS interface is easily scalable, and with more capillaries it can flexibly reduce sampling times further, or permit even longer ^{2}D separation times, at the same sampling rate.

The laminar flow based MDS interface enabled different modes of CE separations to be used between dimensions. This was demonstrated by pairing a low pH with a high pH separation of a tryptic digest of human serum (Chapter 4). A shift of 3.4 pH units provided sufficient orthogonality between dimensions that the 2D separation had dramatically higher peak capacity than either of the constituent 1D separations. Since pH differences have been used extensively in the literature to introduce orthogonality between dimensions, there is a wealth of knowledge that can be leveraged for future use of this instrument; including any modifications to incorporate an LC as the ^{1}D separation.

When ^{1}D and ^{2}D separation conditions were used to perform independent 1D separations, the simple product of their separation profiles was comparable to subsequent 2D separations using analogous conditions as shown in Chapter 4. Since the 1D separations profiles can be expected to maintain fidelity when transferring them to 2D separation mode, the individual separation conditions can be optimized as 1D separations. This was beneficial for more efficient use of the 2D instrument since an independent 1D CE instrument could be run in parallel to perform optimization runs.

The MDS interface and the multi-capillary sheath flow cuvette for detection were both constructed using low technology fabrication methods that can be implemented in nonspecialized lab environments (Chapter 2). The materials were chosen to be low cost, off the shelf products. The tooling requirements primarily included a milling machine for subtractive manufacturing steps and a low temperature oven for polymer casting. Although the prototype parts were machined by the department machine shop staff using specialized equipment, the machining steps could easily be transferred to low cost hobbyist grade CNC milling machines. Thus, these parts could be made within a typical analytical laboratory without prior microfluidic expertise and with minimal capital costs.

Migration time shifts across the 2D capillary array remains a challenge as seen in the raw data from the demonstrated 2D separations. This was partially addressed using software alignment algorithms, as was shown with COW (Chapter 4). However, additional measures are necessary for higher reproducibility, as shown with the secondary injection apparatus. The on-line addition of internal standard to each ^{2}D separation acted as reference markers at the end of each separation window for improved time alignment (Chapter 5).

6.2 Future Directions

6.2.1 Beyond Eight Capillaries

The highest impact advancement to this MDS instrument will be to scale up the number of ^{2}D capillaries to remove restrictions currently imposed by a limited capillary array size. Chiefly, the ^{1}D effluent sampling rate is limited by the separation window and the number of ^{2}D capillaries. The 12 s sampling interval used with the eight-capillary instrument required the ^{1}D to be operated in a stop-and-go fashion and for ⅔ of the effluent to be sent to waste ^{2}D. As the sampling interval is $^2t_{window}$ / *no. ^{2}D capillaries*, the 3 s sampling time enabled by a 32 capillary instrument would enable multiple benefits. The ^{1}D could be operated continuously, speeding up the total separation time by the amount of time spent in the "stopped" phase. The higher sampling rate would ensure that ^{1}D effluent was only sent to waste during the transit between ^{2}D capillaries. This would allow the generation of data that is qualitatively comprehensive, if not strictly so (i.e. 100% of sample is ultimately passed to the ^{2}D). Alternatively, additional ^{2}D separation channels would permit the ^{2}D separations to be operated more slowly if a lower EOF, or a different CE mode, was desirable. The

[1]D separation would also gain flexibility in the variety of separation mechanisms used since faster separations would be possible when the [2]D sampling rate limit was lifted.

6.2.2 Alternate MDS Mechanism Pairings

Although a high theoretical peak capacity was achieved by using a simple pH shift between the [1]D and [2]D separations, both dimensions relied on the same separation mechanism. This reduces the potential for orthogonality and limits the efficient use of the 2D separation space and the attainable peak capacity.

A highly promising tactic would be to use alternate liquid-phase separations in the [1]D, that are fundamentally different mechanistically, and coupling them to the [2]D capillary array. The prime candidate would be HPLC, which is prevalent in proteomic separations and exists in the capillary format which provides better flow rate matching to CE. Particularly interesting modes of HPLC to try include hydrophilic interaction chromatography (HILIC) and RPLC; HILIC being based on hydrophilicity and molecular polarity, RPLC based on hydrophobicity. Capillary HILIC has recently been demonstrated to be effective at achieving a 200 peak capacity in a 25 min elution window.[217] RPLC is a mainstay of proteomic separations since adequate resolution can be achieved with minimal expertise[37] and high resolution is available to the determined researcher[93]. Narrow open-tubular liquid chromatography (nOTLC) has made significant advances in the field of RPLC, reaching peak capacities of 810 in a 54 min separation window.[75] If this were to be coupled to my [2]D capillary array, a theoretical peak capacity of 59 940 is possible! While this peak capacity is tantalizing, coupling HILIC and RPLC with the [2]D CAE will only be possible once the challenge of controlling density difference induced flow in the MDS interface (Section 3.1.7).

Plans to address this density issue include the testing of an already designed and built MDS interface that uses inverted [2]D capillary inlets. In this configuration, the floatation of the low density organic solvents in the aqueous BGE is expected to facilitate entrance of sample into the [2]D capillaries, solving the problems demonstrated in Section 3.1.7.

6.2.3 Other Design Enhancements for Improved Separation Quality

The injection variability identified in Chapter 3 was primarily due to challenges with mounting the [2]D capillaries precisely in a single plane. The obvious solution is to include a third motor-controlled axis of motion in the Z (vertical) direction. Full programmatic X-, Y-, and Z-axis

control would greatly improve the injection efficiency since the heights of the ^{2}D capillary inlets could be simply mapped, like the X and Y coordinates demonstrated herein.

The next prototype will make a significant change where the ^{1}D capillary will be mobile, while the ^{2}D capillary array will be fixed in space. The current design moves the MDS interface, which has a high mass such that the motors are subject to high load when moving to align capillaries during injections. By, instead, moving the lightweight ^{1}D capillary motor wear will decrease significantly leading to an increase in robustness of the MDS interface. This will also reduce perturbations in the bulk BGE from momentum generated during each movement. Furthermore, high resolution stepper motors (5 μm/step vs 25.4 μm/step) have been acquired for the new design, which will enable higher accuracy and higher precision coupling of the capillaries when transferring sample from the ^{1}D to the ^{2}D.

6.2.4 Capillary Array Thermostatting

With a stationary MDS interface, the path of the capillary array could be redesigned with a thermostatted path to the sheath flow cuvette. This would reduce Joule heating related problems that are prevalent when CE capillaries are air-cooled, such as band broadening, peak distortions and drift. Implementation of a thermostatted capillary array will require the design of a channel surrounding the capillaries as they bridged the distance between the MDS interface and sheath flow cuvette. The channel would allow a liquid heat transfer medium to surround and flow over the capillaries to provide a stable defined temperature to the separation medium during operation.

6.2.5 Streamlined Operation

Currently, maintenance and operation of the capillary array apparatus is inaccessible to non-expert users. Two of the most complicated procedures is the replacement of ^{2}D capillaries and mapping out the injection positions for each of the ^{2}D capillaries. Specifically, the capillaries require delicate insertion into tight-fitting, sub-millimetre channels molded within PDMS which then requires precisely positioning the capillary inlet and outlets manually; both in the MDS interface and in the sheath flow cuvette. A unified MDS interface/detector design could incorporate larger openings for each capillary to be inserted which narrow to replaceable seals. Internally, the MDS interface and cuvette could include self-guiding elements to non-linear capillary paths that would improve the exit angle precision of each capillary as well as provide tension to keep them stationary. In

combination with the additional axis of motion for the injection apparatus, only the capillary outlets in the cuvette would require precise alignment with the laser.

6.2.6 **Improved Alignment Procedure**

Currently, aligning the ^{2}D capillaries with the ^{1}D and mapping their positions is a laboriously manual and time-consuming process, with the user making judgements on the alignment quality that are ill-defined. The procedure uses tracer dyes that are necessarily injected onto the ^{2}D to determine their positions, mandating that additional washing and conditioning steps be performed before any subsequent separations. Thus, an improved capillary alignment procedure is needed.

Two alignment configurations are under consideration. First, the MDS interface apparatus can incorporate two optical fibers, one alongside the ^{1}D capillary and one alongside the first capillary in the ^{2}D array. The distal end of each fiber could be coupled to either a laser or a diode detector. When used as a laser guide, light exiting the fiber would illuminate the separation capillaries of the opposing dimension. The light would scatter off the sharpened capillary tip(s) as a function of the tip shape and be imaged by the CCD camera. This will allow faster determination of the relative capillary positions as it does not require ^{1}D effluent to be injected to the ^{2}D, which avoids the need to perform electrophoresis and reduces waste. This would enable the ^{1}D fiber optic to generate a map of the relative positions of the ^{2}D capillaries, while the ^{2}D fiber optic would determine the position of the ^{1}D capillary. To complete the registration between the capillaries in both dimensions, one of the two fibers would be connected to a detector. In this mode, the illuminated fiber would be aligned to the detector fiber by searching for the position with maximal transmission of laser light. By combining these sets of positioning data, the motor positions required to align the ^{1}D capillary to each of the ^{2}D capillaries can be numerically determined.

Second, alignment can be achieved by attaching the ^{1}D capillary to a force sensor. By moving around the MDS interface and contacting the structures within, the force information can be used to determine the locations of the ^{2}D capillaries. A common sensor for detecting this type of deflection includes load cells fitted with a strain gauge. Load cells are available as small metal structures that are designed to flex minimally, with the deformations detected by the attached strain gauge circuit as a change in voltage. Load cells are inexpensive and sensitive, able to detect forces in the milligram (micronewton) range. If the ^{1}D capillary is too flexible, a secondary rigid capillary, can be placed alongside it for feature detection. Though both methods should allow the ^{2}D

capillaries in the MDS interface to be mapped, optical alignment is the elegant and preferred method. The load cell method is expected to have lower precision due to the distance between the sensor and the ^{2}D capillary tips.

6.2.7 **Detector Improvements**

Another avenue of investigation would be to adapt the sheath flow cuvette to allow multiwavelength detection. Migration time markers could then be selected with different emission wavelengths than the analytical sample. In this way, markers could be allowed to comigrate with the sample peaks, while remaining distinguishable from each other. Having internal standards within the separation window would provide more granular information of shifts in the EOF that may occur locally within the separation window. The Cy-Dye fluorophores used in 2D-DIGE are available in three wavelengths and use lysine chemistries to attach to peptides and proteins while allowing the residue to maintain the same charge and thus separation profile.

While fluorescence detection provides exquisite sensitivity at low operating costs, it is limited to proteomic analytes that fluoresce. To ensure all sample components are detectable, they were labelled with a fluorophore. However, there are only handful of protein residues for which reliable fluorophore attachment chemistries exist. Additionally, signal intensity can be disproportionate to the number of analyte molecules since residues aren't equally distributed among the sequences of peptides, or on the available surfaces of proteins with higher order structures. Attaching fluorophores is also time consuming and can introduce interferences.

These problems could be solved by using alternate detectors for the capillary array, such as absorbance and electrochemical detection (ECD). These detection methods offer universal detection and avoid additional sample preparation steps, though provide lower sensitivity. Suitable ECD detectors include amperometric detection and capacitively coupled contactless conductivity detection, which afford near universal detection limits in the range of 0.5 – 4.3 nM and low μM, respectively.[218,219] Direct and indirect absorbance detection can achieve detection limits in the low μM range.[106] However, designing a long pathlength absorbance detector has the potential of increasing sensitivity by several factors, as has been shown using a long pathlength sheath flow cuvette for fiber optic guided CE-LIF.[220] If these small form factor sheath flow cuvettes were modified to use UV absorbance detection, they could be built into a compact array arrangement and allow each capillary its own independent detector cell.

6.2.8 **Improving Data Reproducibility**

To address the data preprocessing issues identified in the conclusions would be to implement routine use of migration time markers. These landmark peaks dramatically improve migration time correction during data preprocessing. The secondary injection system can be further improved by including another reference peak to each ^{2}D run—one that that migrated ahead of the separation window. This way the separation window could be bounded on each side by a marker so that the time correction would be interpolated rather than extrapolated by a single peak. This would also allow the electrophoretic mobility of each marker to better suit the region of the separation window it migrated with. This could be simply achieved by the adding a fluorescent tracer with high electrophoretic mobility to the secondary injection supply reservoir. Additionally, other software algorithms for time correction have been demonstrated in the literature and could be implemented to further optimize the software-based time alignment.

6.2.9 **^{2}D Effluent Capture**

While MDS data are suitable for generating proteomic fingerprints that can be used in predictive and prognostic models of health states, a clear weakness of the MDS instrument is that the fluorescence detection does not provide any structural information of the detected peaks. MS is the favoured detection mode for electrophoretic separation of proteomic samples. However, the multiplexed nature of the ^{2}D would require each capillary in the array to be coupled to an independent MS. Thus, CAE detection by MS is untenable due to size and cost constraints. Another option is manual manipulation of fraction collected samples, which would be resource intensive and invite possibilities for contamination and manipulation errors.

With demonstrated instrumentation for automated and efficient transfers of sample between serially oriented capillaries, a pseudo-third dimension can be considered. A second moving MDS interface could be placed downstream of the ^{2}D capillary array. In conjunction with the ^{2}D fluorescence detection, this ^{3}D capillary would capture peaks of interest from the ^{2}D effluent in real-time for further processing. An obvious implementation would incorporate an immobilized enzyme reactor as the ^{3}D capillary, enabling on-line proteolytic digestion which would then be interfaced directly to an MS for bottom-up proteomic analysis. Immobilized enzyme reactors demonstrate much faster processing times than digestions performed in bulk solutions. This

property would maintain the high level of automation and throughput of the system compared to fraction collection and bench chemistry processing.

6.2.10 Better (Faster) Prototyping Through 3D Printing

Although the MDS interface and sheath flow cuvette do not require exotic fabrication methods, the various subtractive manufacturing and polymer casting steps are time consuming; each component of the instrument requiring several days to produce. To simplify the process of making these custom parts, 3D printers were previously considered since they build a three-dimensional object from a computer-aided design model in a single manufacturing step. However, when the instrument was being built existing 3D printing was deemed cost prohibitive or was limited to printing at lower resolutions (250 μm and up) unsuitable for CE. However, 3D printers have evolved dramatically and are now able to print at feature sizes comparable to capillary external dimensions (~20 μm) as well as use a wider variety of materials with different chemical compatibilities. On demand 3D printing services have also proliferated, making the manufacture of single prototypes inexpensive.

A 3D printed unified MDS interface and sheath flow cuvette could integrate many of the improvements laid out in this section. One of the benefits of 3D printing is that it lifts restrictions that are imposed by subtractive manufacturing. Chief among them is that 3D printing allows the flexibility to design channels with arbitrary paths inside a structure that would be onerous to do through subtractive manufacturing and parts assembly.

A 3D printed MDS interface could scale the number of capillaries by simply copying and pasting the voids for the capillary channels within the CAD file. Self-guiding capillary replacement features to guide the capillary during insertion would involve simple CAD instructions instead of trying to mill micron sized conical structures at each of the capillary channel openings. The ^{2}D thermostating apparatus could be simply printed as a bridge between the MDS interface and detector. The process of constructing new detector designs would be streamlined considerably. 3D printed capillary and fiber optic channels are geometrically aligned during CAD model design and can be faithfully reproduced during printing, unlike preparing polymeric microfluidic detectors where templating structures must first be built. Some of these design features are under active investigation in our lab.

6.2.11 **Applications**

In the near term, this MDS instrument has immediate applicability to previous work performed in this lab. In Boisvert's work, CE separation profiles of amniotic fluid (AMF) samples were used to predict health outcomes for the mother and the foetus. Similar treatment performed on in vitro fertilization (IVF) media samples were predictive of the likelihood of successful implantation. Boisvert's work showed that highly overlapped segments of 1D CE separations of these samples could be used to build a predictive chemometric model with high sensitivity and specificity.

The models leveraged the transformation of raw data into wavelets, short independent time intervals within the separation space. The predictive wavelets were found at reliable migration times, despite being buried within a mound of overlapping peaks of varying species of human serum albumin (HSA). Using the signal intensity change of the underlying proteomic species, a pair of networked wavelets were discovered to act as reliable predictors of health outcomes. Since they were undifferentiated peak signals, their intensity change was postulated to be due to conformational changes/chemical modifications that caused the migration of the predictive species into, or out of, their respective wavelet bands. Since the wavelets were not isolated from their parent peak, the responsible species could not be identified.

With the increased separation power of an MDS system, the analytes contained within these wavelets would have a much greater likelihood of being resolved from the previously overlapped peaks. MDS may identify expression patterns among the different HSA species that predict health outcomes with even greater sensitivity or specificity.

An alternate promising target of this MDS instrument is its application to metagenomic samples, where genomic analysis is applied to all constituents of a biological ecosystem—such as the human microbiome or from ecological niches in the environment. The taxonomic compositions and functional relationships within microbial communities are largely unknown because the vast majority of microbes cannot be cultured. This key microbial isolation and amplification step confounds conventional metagenomic studies.

Next generation sequencing technologies (NGS) can analyze sparing amounts of DNA, obviating the culturing step. However, all DNA in a sample is fragmented (sheared) randomly which produces an array of gene fragments. Sequencing these complex DNA fragment samples suffers

from the same complexity and concentration dynamic range problems that plague proteomic samples. The diversity of gene sequences that are read in a sample biases towards high abundance microbes and to host DNA, leading low abundance microbes to be missed. Interferences from coexisting species with similar genomes complicate sequence assembly.

Pre-fractionation of microbiome samples prior to sequencing would minimize these challenges and enable them to be probed more deeply for constituent genomes contained within. The CE format has been used for the 1D separation of cells from wastewater microbiome samples but required culturing and had overlapping species in each peak.[221] An MDS system would be ideal for providing greater resolution of individual microbial species and to minimize interferences.

The MDS system could be extended so each ^{2}D separation continues onto a capillary reactor to lyse the separated cells. The capillary reactors would be followed by an aspirator module for sample deposition of each fraction of lysed cells onto multi-well plates to complete DNA extraction and removal of interferents (proteins, RNA, etc.). This product would be suitable for automated aspiration onto NGS cartridges for downstream sequencing which, today, is already a highly multiplexed process.

The technology developed in this body of work has just entered its infancy and requires adjustments before it can act as a turn-key instrument for production settings. However, it has demonstrated a novel means to couple one-to-many separations, utilizing a facile ^{2}D multiplexing schema to increase throughput and resolving power when analyzing highly complex samples. I have mentioned just a few possible applications for the instrument and methods developed in this body of work, but they could be applied to challenging matrices found in medical, biological, pharmaceutical, forensic and environmental samples. Each of these fields have untapped biomarker potential that could lead to new avenues of research with diagnostic, prognostic and treatment direction at the small and large scale; from enabling personalized medicine to deciphering aquatic ecosystems.

References

1. Berger, D. A brief history of medical diagnosis and the birth of the clinical laboratory. Part 4: Fraud and abuse, managed-care, and lab consolidation. *Med. Lab. Obs.* **12**, 38–42 (1999).

2. Mackiewicz, P. *et al.* How many protein-coding genes are there in the Saccharomyces cerevisiae genome? *Yeast* **19**, 619–629 (2002).

3. Goffeau, A. *et al.* Life with 6000 genes. *Science (80).* **274**, 546–567 (1996).

4. Ramirez-Gaona, M. *et al.* YMDB 2.0: A significantly expanded version of the yeast metabolome database. *Nucleic Acids Res.* **45**, D440–D445 (2017).

5. Atkinson, A. J. *et al.* Biomarkers and surrogate endpoints: Preferred definitions and conceptual framework. *Clin. Pharmacol. Ther.* **69**, 89–95 (2001).

6. Omenn, G. S. *et al.* Progress on identifying and characterizing the human proteome: 2018 metrics from the hupo human proteome project. *J. Proteome Res.* **17**, 4031–4041 (2018).

7. Wishart, D. S. *et al.* HMDB 4.0: The human metabolome database for 2018. *Nucleic Acids Res.* **46**, D608–D617 (2018).

8. Anderson, L. Six decades searching for meaning in the proteome. *J. Proteomics* **107**, 24–30 (2014).

9. Klose, J. Protein mapping by combined isoelectric focusing and electrophoresis of mouse tissues - A novel approach to testing for induced point mutations in mammals. *Hum. Genet.* **26**, 231–243 (1975).

10. Westermeier, R. 2D gel-based proteomics: There's life in the old dog yet. *Archives of Physiology and Biochemistry* vol. 122 236–237 (2016).

11. Köhler, G. *et al.* Continuous cultures of fused cells secreting antibody of predefined specificity. *Nature* **256**, 495–497 (1975).

12. Geyer, P. E. *et al.* Revisiting biomarker discovery by plasma proteomics. *Mol. Syst. Biol.* **13**, 942 (2017).

13. Domon, B. *et al.* Mass spectrometry and protein analysis. *Science (80).* **312**, 212–217 (2006).

14. Fenn, J. B. *et al.* Electrospray ionization for mass spectrometry of large biomolecules. *Science* vol. 246 64–71 (1989).

15. Vandermarliere, E. *et al.* Getting intimate with trypsin, the leading protease in proteomics. *Mass Spectrom. Rev.* **32**, 453–465 (2013).

16. Gillet, L. C. *et al.* Mass spectrometry applied to bottom-up proteomics: Entering the high-throughput era for hypothesis testing. *Annu. Rev. Anal. Chem.* **9**, 449–472 (2016).

17. Schmit, P. O. *et al.* Towards a routine application of top-down approaches for label-free discovery workflows. *J. Proteomics* **175**, 12–26 (2018).

18. Zhang, Y. *et al.* Protein analysis by shotgun/bottom-up proteomics. *Chemical Reviews* vol. 113 2343–2394 (2013).

19. Karpievitch, Y. V. *et al.* Liquid chromatography mass spectrometry-based proteomics: Biological and technological aspects. *Ann. Appl. Stat.* **4**, 1797–1823 (2010).

20. Nesvizhskii, A. I. Protein identification by tandem mass spectrometry and sequence database searching. in *Methods in molecular biology (Clifton, N.J.)* vol. 367 87–119 (Humana Press, 2007).

21. Picotti, P. *et al.* Selected reaction monitoring-based proteomics: Workflows, potential, pitfalls and future directions. *Nat. Methods* **9**, 555–566 (2012).

22. Addona, T. A. *et al.* Multi-site assessment of the precision and reproducibility of multiple reaction monitoring-based measurements of proteins in plasma. *Nat. Biotechnol.* **27**, 633–641 (2009).

23. Chapman, J. D. *et al.* Multiplexed and data-independent tandem mass spectrometry for global proteome profiling. *Mass Spectrom. Rev.* **33**, 452–470 (2014).

24. Surinova, S. *et al.* Non-invasive prognostic protein biomarker signatures associated with colorectal cancer. *EMBO Mol. Med.* **7**, 1153–1165 (2015).

25. Surinova, S. *et al.* Prediction of colorectal cancer diagnosis based on circulating plasma proteins. *EMBO Mol. Med.* **7**, 1166–1178 (2015).

26. Davis, M. T. *et al.* Towards defining the urinary proteome using liquid chromatography-tandem mass spectrometry II. Limitations of complex mixture analyses. *Proteomics* **1**, 108–117 (2001).

27. Ludwig, C. *et al.* Data-independent acquisition-based SWATH - MS for quantitative proteomics: A tutorial. *Mol. Syst. Biol.* **14**, e8126 (2018).

28. Gillet, L. C. *et al.* Targeted data extraction of the MS/MS spectra generated by data-independent acquisition: A new concept for consistent and accurate proteome analysis. *Mol. Cell. Proteomics* **11**, O111.016717 (2012).

29. Liu, Y. *et al.* Quantitative measurements of N-linked glycoproteins in human plasma by SWATH-MS. *Proteomics* **13**, 1247–1256 (2013).

30. Schmidlin, T. *et al.* Assessment of SRM, MRM3, and DIA for the targeted analysis of phosphorylation dynamics in non-small cell lung cancer. *Proteomics* **16**, 2193–2205 (2016).

31. Amodei, D. *et al.* Improving precursor selectivity in data-independent acquisition using overlapping windows. *J. Am. Soc. Mass Spectrom.* **30**, 669–684 (2019).

32. Hu, A. *et al.* Joint precursor elution profile inference via regression for peptide detection in data-independent acquisition mass spectra. *J. Proteome Res.* **18**, 86–94 (2019).

33. Smith, L. M. *et al.* Proteoform: A single term describing protein complexity. *Nature Methods* vol. 10 186–187 (2013).

34. Ponomarenko, E. A. *et al.* The size of the human proteome: The width and depth. *Int. J. Anal. Chem.* **2016**, 1–6 (2016).

35. Williams, B. Drug discovery in renin-angiotensin system intervention: Past and future. *Ther. Adv. Cardiovasc. Dis.* **10**, 118–125 (2016).

36. Black, C. A. A brief history of the discovery of the immunoglobulins and the origin of the modern immunoglobulin nomenclature. *Immunol. Cell Biol.* **75**, 65–68 (1997).

37. Astefanei, A. *et al.* Different stationary phase selectivities and morphologies for intact protein separations. *Chromatographia* vol. 80 665–687 (2017).

38. Han, J. *et al.* Towards high peak capacity separations in normal pressure nanoflow liquid chromatography using meter long packed capillary columns. *Anal. Chim. Acta* **852**, 267–273 (2014).

39. Paul, P. H. *et al.* Imaging of pressure- and electrokinetically driven flows through open capillaries. *Anal. Chem.* **70**, 2459–2467 (1998).

40. Sun, L. *et al.* Capillary zone electrophoresis for bottom-up analysis of complex proteomes. *Proteomics* vol. 16 188–196 (2016).

41. Štěpánová, S. *et al.* Recent developments and applications of capillary and microchip electrophoresis in proteomics and peptidomics (2015–mid 2018). *Journal of Separation Science* vol. 42 398–414 (2019).

42. Ramautar, R. *et al.* CE-MS for metabolomics: Developments and applications in the period 2016–2018. *Electrophoresis* **40**, 165–179 (2019).

43. van Mever, M. *et al.* CE–MS for anionic metabolic profiling: An overview of methodological developments. *Electrophoresis* **40**, 2349–2359 (2019).

44. Britz-Mckibbin, P. Chapter 12: Multisegment injection-capillary electrophoresis-mass spectrometry: a robust platform for high throughput metabolite profiling with quality assurance. in *New Developments in NMR* 255–282 (Royal Society of Chemistry, 2018).

45. FDA-NIH Biomarker Working Group. BEST (Biomarkers, EndpointS, and other Tools) Resource. *Food and Drug Administration (US). Co-published by National Institutes of Health (US), Bethesda (MD).* https://www.ncbi.nlm.nih.gov/books/NBK326791/ (2016)

46. Fleming, T. R. *et al.* Surrogate end points in clinical trials: Are we being misled? *Ann. Intern. Med.* **125**, 605–613 (1996).

47. Hayes, D. F. Biomarker validation and testing. *Mol. Oncol.* **9**, 960–966 (2015).

48. Baker, S. G. *et al.* A perfect correlate does not a surrogate make. *BMC Med. Res. Methodol.*

3, 1–5 (2003).

49.   Fleming, T. R. *et al.* Biomarkers and surrogate endpoints in clinical trials. *Stat. Med.* **31**, 2973–2984 (2012).

50.   Weintraub, W. S. *et al.* The perils of surrogate endpoints. *Eur. Heart J.* **36**, 2212-2218a (2015).

51.   Gordon, T. *et al.* High density lipoprotein as a protective factor against coronary heart disease. The Framingham study. *Am. J. Med.* **62**, 707–714 (1977).

52.   Wilson, P. W. F. *et al.* High density lipoprotein cholesterol and mortality. The Framingham heart study. *Arteriosclerosis* **8**, 737–741 (1988).

53.   Ali, K. M. *et al.* Cardiovascular disease risk reduction by raising HDL cholesterol - Current therapies and future opportunities. *Br. J. Pharmacol.* **167**, 1177–1194 (2012).

54.   Toth, P. P. Niacin in patients with low hdl cholesterol levels receiving intensive statin therapy. *Yearb. Med.* **2012**, 426–430 (2012).

55.   Barter, P. J. *et al.* Effects of torcetrapib in patients at high risk for coronary events. *N. Engl. J. Med.* **357**, 2109–2122 (2007).

56.   Landray, M. J. *et al.* Effects of extended-release niacin with laropiprant in high-risk patients. *N. Engl. J. Med.* **371**, 203–212 (2014).

57.   Tardif, J. C. *et al.* Pharmacogenomic determinants of the cardiovascular effects of dalcetrapib. *Circ. Cardiovasc. Genet.* **8**, 372–382 (2015).

58.   Tardif, J. C. *et al.* Genotype-dependent effects of dalcetrapib on cholesterol efflux and inflammation: Concordance with clinical outcomes. *Circ. Cardiovasc. Genet.* **9**, 340–348 (2016).

59.   Chen, H. *et al.* Pathway mapping and development of disease-specific biomarkers: Protein-based network biomarkers. *J. Cell. Mol. Med.* **19**, 297–314 (2015).

60.   Anderson, N. L. The clinical plasma proteome: A survey of clinical assays for proteins in

plasma and serum. *Clin. Chem.* **56**, 177–185 (2010).

61. Anderson, N. L. *et al.* The riddle of protein diagnostics: Future bleak or bright? *Clin. Chem.* **59**, 194–197 (2013).

62. Micheel, C. M. *et al. Evaluation of biomarkers and surrogate endpoints in chronic disease*. (National Academies Press, Washington, D.C., 2010).

63. Rifai, N. *et al.* Protein biomarker discovery and validation: The long and uncertain path to clinical utility. *Nat. Biotechnol.* **24**, 971–983 (2006).

64. Mazzara, S. *et al.* CombiROC: An interactive web tool for selecting accurate marker combinations of omics data. *Sci. Rep.* **7**, 45477 (2017).

65. He, Z. Biomarker discovery. *Data Min. Bioinforma. Appl.* 69–78 (2015)

66. Ioannidis, J. P. A. *et al.* Waste, leaks, and failures in the biomarker pipeline. *Clin. Chem.* **63**, 963–972 (2017).

67. Kyzas, P. A. *et al.* Almost all articles on cancer prognostic markers report statistically significant results. *Eur. J. Cancer* **43**, 2559–2579 (2007).

68. Kuligowski, J. *et al.* Application of discriminant analysis and cross-validation on proteomics data. in *Methods in Molecular Biology* vol. 1362 175–184 (Humana Press, New York, NY, 2016).

69. Varoquaux, G. Cross-validation failure: Small sample sizes lead to large error bars. *Neuroimage* **180**, 68–77 (2018).

70. Hernández, B. *et al.* Why have so few proteomic biomarkers 'survived' validation? (Sample size and independent validation considerations). *Proteomics* **14**, 1587–1592 (2014).

71. Hayes, D. F. *et al.* Breaking a vicious cycle. *Sci. Transl. Med.* **5**, 196cm6 (2013).

72. Anderson, N. L. *et al.* The human plasma proteome: history, character, and diagnostic prospects. *Mol. Cell. Proteomics* **1**, 845–867 (2002).

73. Surinova, S. *et al.* On the development of plasma protein biomarkers. *J. Proteome Res.* **10**,

5–16 (2011).

74.   Ahlf, D. R. *et al.* Developing top down proteomics to maximize proteome and sequence coverage from cells and tissues. *Curr. Opin. Chem. Biol.* **17**, 787–794 (2013).

75.   Yang, Y. *et al.* Narrow, open, tubular column for ultrahigh-efficiency liquid-chromatographic separation under elution pressure of less than 50 bar. *Anal. Chem.* **90**, 10676–10680 (2018).

76.   Bellei, E. *et al.* High-abundance proteins depletion for serum proteomic analysis: Concomitant removal of non-targeted proteins. *Amino Acids* **40**, 145–156 (2011).

77.   Tu, C. *et al.* Depletion of abundant plasma proteins and limitations of plasma proteomics. *J. Proteome Res.* **9**, 4982–4991 (2010).

78.   Gianazza, E. *et al.* With or without you - Proteomics with or without major plasma/serum proteins. *Journal of Proteomics* vol. 140 62–80 (2016).

79.   Button, K. S. *et al.* Power failure: Why small sample size undermines the reliability of neuroscience. *Nat. Rev. Neurosci.* **14**, 365–376 (2013).

80.   Krzywinski, M. *et al.* Points of significance: Power and sample size. *Nat. Methods* **10**, 1139–1140 (2013).

81.   Dua, S. *et al. Data Mining for Bioinformatics* (CRC Press, Boca Raton, FL., 2012)

82.   Hastie, T. *et al.* Model assessment and selection. in: The elements of statistical learning. Springer series in statistics. 219–259 (Springer, New York, NY., 2009).

83.   Krzywinski, M. *et al.* Points of significance: Error bars. *Nat. Methods* **10**, 921–922 (2013).

84.   Forshed, J. Experimental design in clinical 'omics biomarker discovery. *J. Proteome Res.* **16**, 3954–3960 (2017).

85.   Wright, P. C. *et al.* A review of current proteomics technologies with a survey on their widespread use in reproductive biology investigations. *Theriogenology* **77**, 738–765 (2012).

86.   Klose, J. *et al.* Two-dimensional electrophoresis of proteins: An updated protocol and

implications for a functional analysis of the genome. *Electrophoresis* **16**, 1034–1059 (1995).

87.   Bjellqvist, B. *et al.* Isoelectric focusing in immobilized pH gradients: Principle, methodology and some applications. *J. Biochem. Biophys. Methods* **6**, 317–339 (1982).

88.   Strohkamp, S. *et al.* Possibilities and limitations of 2DE-based analyses for identifying low-abundant tumor markers in human serum and plasma. *Proteomics* **16**, 2519–2532 (2016).

89.   Westermeier, R. Looking at proteins from two dimensions: A review on five decades of 2D electrophoresis. *Arch. Physiol. Biochem.* **120**, 168–172 (2014).

90.   Issaq, H. J. *et al.* Two-dimensional polyacrylamide gel electrophoresis (2D-PAGE): Advances and perspectives. *Biotechniques* **44**, 697–700 (2008).

91.   Zhou, H. Advancements in top-down proteomics. *Anal. Chem.* **84**, 720–734 (2012).

92.   Unger, K. K. *et al.* Liquid chromatography-its development and key role in life science applications. *Angew. Chemie - Int. Ed.* **49**, 2300–2312 (2010).

93.   Horváth, K. *et al.* Generation and limitations of peak capacity in online two-dimensional liquid chromatography. *Anal. Chem.* **81**, 3879–3888 (2009).

94.   Jandera, P. Programmed elution in comprehensive two-dimensional liquid chromatography. *J. Chromatogr. A* **1255**, 112–129 (2012).

95.   Eeltink, S. *et al.* Advances in organic polymer-based monolithic column technology for high-resolution liquid chromatography-mass spectrometry profiling of antibodies, intact proteins, oligonucleotides, and peptides. *J. Chromatogr. A* **1498**, 8–21 (2017).

96.   Wolters, D. A. *et al.* An automated multidimensional protein identification technology for shotgun proteomics. *Anal. Chem.* **73**, 5683–5690 (2001).

97.   Gao, M. *et al.* Development of multidimensional liquid chromatography and application in proteomic analysis. *Expert Rev. Proteomics* **7**, 665–678 (2010).

98.   Mauri, P. *et al.* Multidimensional protein identification technology for clinical proteomic

analysis. *Clin. Chem. Lab. Med.* **47**, 636–645 (2009).

99. Wu, C. C. *et al.* A method for the comprehensive proteomic analysis of membrane proteins. *Nat. Biotechnol.* **21**, 532–538 (2003).

100. Rinas, A. *et al.* Fast photochemical oxidation of proteins coupled to multidimensional protein identification technology (MudPIT): Expanding footprinting strategies to complex systems. *J. Am. Soc. Mass Spectrom.* **26**, 540–546 (2015).

101. Gilar, M. *et al.* Two-dimensional separation of peptides using RP-RP-HPLC system with different pH in first and second separation dimensions. *Journal of Separation Science* vol. 28 1694–1703 (2005).

102. Kwiatkowski, M. *et al.* Application of displacement chromatography to online two-dimensional liquid chromatography coupled to tandem mass spectrometry improves peptide separation efficiency and detectability for the analysis of complex proteomes. *Anal. Chem.* **90**, 9951–9958 (2018).

103. Hennrich, M. L. *et al.* Improving depth in phosphoproteomics by using a strong cation exchange-weak anion exchange-reversed phase multidimensional separation approach. *Anal. Chem.* **83**, 7137–7143 (2011).

104. Gauci, S. *et al.* Lys-N and trypsin cover complementary parts of the phosphoproteome in a refined SCX-based approach. *Anal. Chem.* **81**, 4493–4501 (2009).

105. Zhang, N. *et al.* Parallel channels-multidimensional protein identification technology. *J. Am. Soc. Mass Spectrom.* **31**, 1440–1447 (2020).

106. Landers, J. P. Introduction to capillary electrophoresis. in *Handbook of capillary and microchip electrophoresis and associated microtechniques, Third Edition* (ed. Landers, J. P.) 1–73 (CRC Press, 2007).

107. Krylov, S. N. *et al.* Capillary electrophoresis for the analysis of biopolymers. *Anal. Chem.* **72**, 111R-128R (2000).

108. Gritti, F. *et al.* Optimization of the peak capacity per unit time. *J. Chromatogr. A* **1263**,

125–140 (2012).

109. Štěpánová, S. *et al.* Recent applications of capillary electromigration methods to separation and analysis of proteins. *Anal. Chim. Acta* **933**, 23–42 (2016).

110. Malá, Z. *et al.* Contemporary sample stacking in analytical electrophoresis. *Electrophoresis* **36**, 15–35 (2015).

111. Breadmore, M. C. Electrokinetic and hydrodynamic injection: Making the right choice for capillary electrophoresis. *Bioanalysis* **1**, 889–894 (2009).

112. Foley, J. P. *et al.* Peak capacity and peak capacity per unit time in capillary and microchip zone electrophoresis. *J. Chromatogr. A* **1523**, 80–89 (2017).

113. Wahab, M. F. *et al.* Total peak shape analysis: detection and quantitation of concurrent fronting, tailing, and their effect on asymmetry measurements. *J. Chromatogr. A* **1509**, 163–170 (2017).

114. Imai, K. *et al.* Towards clinical proteomics analysis. *Biomed. Chromatogr.* **25**, 59–64 (2011).

115. Webb, K. J. *et al.* Modified MuDPIT separation identified 4488 proteins in a system-wide analysis of quiescence in yeast. *J. Proteome Res.* **12**, 2177–2184 (2013).

116. Adahchour, M. *et al.* Recent developments in comprehensive two-dimensional gas chromatography (GC × GC). I. Introduction and instrumental set-up. *TrAC - Trends Anal. Chem.* **25**, 438–454 (2006).

117. Giddings, J. C. Two-dimensional separations: concept and promise. *Anal. Chem.* **56**, 1258A-1270A (1984).

118. Murphy, R. E. *et al.* Effect of sampling rate on resolution in comprehensive two-dimensional liquid chromatography. *Anal. Chem.* **70**, 1585–1594 (1998).

119. Davis, J. M. *et al.* Effect of first-dimension undersampling on effective peak capacity in comprehensive two-dimensional separations. *Anal. Chem.* **80**, 461–473 (2008).

120. Thekkudan, D. F. *et al.* A study of the precision and accuracy of peak quantification in comprehensive two-dimensional liquid chromatography in time. *J. Chromatogr. A* **1217**, 4313–4327 (2010).

121. Stoll, D. R. *et al.* Comparison of the practical resolving power of one- and two-dimensional high-performance liquid chromatography analysis of metabolomic samples. *Anal. Chem.* **80**, 268–278 (2008).

122. Liu, Z. *et al.* Geometric approach to factor analysis for the estimation of orthogonality and practical peak capacity in comprehensive two-dimensional separations. *Anal. Chem.* **67**, 3840–3845 (1995).

123. Gilar, M. *et al.* Orthogonality of separation in two-dimensional liquid chromatography. *Anal. Chem.* **77**, 6426–6434 (2005).

124. Rutan, S. C. *et al.* Fractional coverage metrics based on ecological home range for calculation of the effective peak capacity in comprehensive two-dimensional separations. *J. Chromatogr. A* **1255**, 267–276 (2012).

125. Schure, M. R. *et al.* Orthogonal separations: Comparison of orthogonality metrics by statistical analysis. *J. Chromatogr. A* **1414**, 60–76 (2015).

126. Erni, F. *et al.* Two-dimensional column liquid chromatographic technique for resolution of complex mixtures. *J. Chromatogr. A* **149**, 561–569 (1978).

127. Bushey, M. M. *et al.* Automated instrumentation for comprehensive two-dimensional high-performance liquid chromatography of proteins. *Anal. Chem.* **62**, 161–167 (1990).

128. Blahová, E. *et al.* Two-dimensional and serial column reversed-phase separation of phenolic antioxidants on octadecyl-, polyethyleneglycol-, and pentafluorophenylpropyl-silica columns. *J. Sep. Sci.* **29**, 555–566 (2006).

129. Stoll, D. R. *et al.* Fast, comprehensive online two-dimensional high performance liquid chromatography through the use of high temperature ultra-fast gradient elution reversed-phase liquid chromatography. *J. Chromatogr. A* **1122**, 123–137 (2006).

130. Potts, L. W. *et al.* The impact of sampling time on peak capacity and analysis speed in on-line comprehensive two-dimensional liquid chromatography. *J. Chromatogr. A* **1217**, 5700–5709 (2010).

131. Bedani, F. *et al.* Theories to support method development in comprehensive two-dimensional liquid chromatography - A review. *J. Sep. Sci.* **35**, 1697–1711 (2012).

132. Sarrut, M. *et al.* Optimization of conditions in on-line comprehensive two-dimensional reversed phase liquid chromatography: Experimental comparison with one-dimensional reversed phase liquid chromatography for the separation of peptides. *J. Chromatogr. A* **1421**, 48–59 (2015).

133. Alexander, A. J. *et al.* Comprehensive two-dimensional liquid chromatography separations of pharmaceutical samples using dual fused-core columns in the second dimension. *J. Chromatogr. A* **1216**, 1338–1345 (2009).

134. Opiteck, G. J. *et al.* Comprehensive two-dimensional high-performance liquid chromatography for the isolation of overexpressed proteins and proteome mapping. *Anal. Biochem.* **258**, 349–361 (1998).

135. Unger, K. K. *et al.* Is multidimensional high performance liquid chromatography (HPLC) an alternative in protein analysis to 2D gel electrophoresis? *HRC J. High Resolut. Chromatogr.* **23**, 259–265 (2000).

136. Wagner, K. *et al.* An automated on-line multidimensional HPLC system for protein and peptide mapping with integrated sample preparation. *Anal. Chem.* **74**, 809–820 (2002).

137. Matějíček, D. Multi heart-cutting two-dimensional liquid chromatography-atmospheric pressure photoionization-tandem mass spectrometry method for the determination of endocrine disrupting compounds in water. *J. Chromatogr. A* **1231**, 52–58 (2012).

138. Zhang, K. *et al.* Analysis of pharmaceutical impurities using multi-heartcutting 2D LC coupled with UV-charged aerosol MS detection. *J. Sep. Sci.* **36**, 2986–2992 (2013).

139. Pursch, M. *et al.* Loop-based multiple heart-cutting two-dimensional liquid chromatography for target analysis in complex matrices. *Anal. Chem.* **87**, 5310–5317 (2015).

140. Groskreutz, S. R. *et al.* Selective comprehensive multi-dimensional separation for resolution enhancement in high performance liquid chromatography. Part I: Principles and instrumentation. *J. Chromatogr. A* **1228**, 31–40 (2012).

141. Pirok, B. W. J. *et al.* Optimizing separations in online comprehensive two-dimensional liquid chromatography. *J. Sep. Sci.* **41**, 68–98 (2018).

142. Schure, M. R. Limit of detection, dilution factors, and technique compatibility in multidimensional separations utilizing chromatography, capillary electrophoresis, and field-flow fractionation. *Anal. Chem.* **71**, 1645–1657 (1999).

143. Horváth, K. *et al.* Detection issues in two-dimensional on-line chromatography. *J. Chromatogr. A* **1216**, 7785–7792 (2009).

144. Zhang, M. *et al.* Two-dimensional microcolumn separation platform for proteomics consisting of on-line coupled capillary isoelectric focusing and capillary electrochromatography. 1. Evaluation of the capillary-based two-dimensional platform with proteins, peptides, and human serum. *J. Proteome Res.* **5**, 2001–2008 (2006).

145. Bushey, M. M. *et al.* Automated instrumentation for comprehensive two-dimensional high-performance liquid chromatography/capillary zone electrophoresis. *Anal. Chem.* **62**, 978–984 (1990).

146. Yang, C. *et al.* On-line hyphenation of capillary isoelectric focusing and capillary gel electrophoresis by a dialysis interface. *Anal. Chem.* **75**, 215–218 (2003).

147. Zhang, J. *et al.* Comprehensive two-dimensional chromatography and capillary electrophoresis coupled with tandem time-of-flight mass spectrometry for high-speed proteome analysis. *Electrophoresis* **25**, 2374–2383 (2004).

148. Kohl, F. J. *et al.* Capillary electrophoresis in two-dimensional separation systems: Techniques and applications. *Electrophoresis* **36**, 144–158 (2015).

149. Lemmo, A. V. *et al.* Transverse flow gating interface for the coupling of microcolumn LC with CZE in a comprehensive two-dimensional system. *Anal. Chem.* **65**, 1576–1581 (1993).

150. Hooker, T. F. *et al.* A transparent flow gating interface for the coupling of microcolumn LC with CZE in a comprehensive two-dimensional system. *Anal. Chem.* **69**, 4134–4142 (1997).

151. Michels, D. A. *et al.* Fully automated two-dimensional capillary electrophoresis for high sensitivity protein analysis. *Mol. Cell. Proteomics* **1**, 69–74 (2002).

152. Jorgenson, J. W. Comprehensive liquid chromatography-capillary electrophoresis for separation of complex mixtures. *Am. Chem. Soc.* (1997).

153. Michels, D. A. *et al.* Capillary sieving electrophoresis-micellar electrokinetic chromatography fully automated two-dimensional capillary electrophoresis analysis of Deinococcus radiodurans protein homogenate. *Electrophoresis* **25**, 3098–3105 (2004).

154. Flaherty, R. J. *et al.* Nicked-sleeve interface for two-dimensional capillary electrophoresis. *Analyst* **138**, 3621–3625 (2013).

155. Sanchez-Vega, B. Capillary electrophoresis of DNA biomedical applications. *Mol. Biomethods Handb. Second Ed.* **Chapter 2**, 65–87 (2008).

156. Skinner, C. D. A liquid chromatography to capillary array electrophoresis interface for two-dimensional separations. *Analyst* **135**, 358–367 (2010).

157. Skinner, C. D. A PDMS sheath flow cuvette for high-sensitivity LIF measurements in CE. *Electrophoresis* **30**, 372–378 (2009).

158. Geiger, M. *et al.* Comprehensive multidimensional separations of peptides using nano-liquid chromatography coupled with micro free flow electrophoresis. *Anal. Chem.* **86**, 5136–5142 (2014).

159. Johnson, A. C. *et al.* High-speed, comprehensive, two dimensional separations of peptides and small molecule biological amines using capillary electrophoresis coupled with micro free flow electrophoresis. *Anal. Chem.* **89**, 1665–1673 (2017).

160. Johnson, A. C. *et al.* Micro free flow electrophoresis. *Lab Chip* **18**, 27–40 (2018).

161. Pritchard, P. *et al. Fox and McDonald's introduction to fluid mechanics*. (John Wiley & Sons, Inc., Hoboken, NJ. 2016).

162.   White, F. M. *Fluid mechanics*. (McGraw-Hill, New York, NY, 2011).

163.   Galievsky, V. A. *et al.* "Getting the best sensitivity from on-capillary fluorescence detection in capillary electrophoresis" – A tutorial. *Anal. Chim. Acta* **935**, 58–81 (2016).

164.   Weiss, S. Fluorescence spectroscopy of single biomolecules. *Science (80).* **283**, 1676–1683 (1999).

165.   Cheng, Y. F. *et al.* Subattomole amino acid analysis by capillary zone electrophoresis and laser-induced fluorescence. *Science (80).* **242**, 562–564 (1988).

166.   Yong Chen, D. *et al.* Yoctomole detection limit by laser-induced fluorescence in capillary electrophoresis. *J. Chromatogr. B Biomed. Sci. Appl.* **657**, 265–269 (1994).

167.   Chen, D. Y. *et al.* Single-molecule detection in capillary electrophoresis: molecular shot noise as a fundamental limit to chemical analysis. *Anal. Chem.* **68**, 690–696 (1996).

168.   John Crabtree, H. *et al.* Construction and evaluation of a capillary array DNA sequencer based on a micromachined sheathflow cuvette. *Electrophoresis* **21**, 1329–1335 (2000).

169.   Johnson, M. E. *et al.* Fundamentals and practice for ultrasensitive laser-induced fluorescence detection in microanalytical systems. *Electrophoresis* **25**, 3513–3527 (2004).

170.   Mikšík, I. *et al.* Separation of proteins and peptides by capillary electrophoresis in acid buffers containing high concentrations of surfactants. *J. Chromatogr. A* **852**, 325–336 (1999).

171.   Strege, M. A. *et al.* Micellar electrokinetic chromatography of proteins. *J. Chromatogr. A* **780**, 285–296 (1997).

172.   Giansanti, P. *et al.* Six alternative proteases for mass spectrometry-based proteomics beyond trypsin. *Nat. Protoc.* **11**, 993–1006 (2016).

173.   Ramsay, L. M. *et al.* Femtomolar concentration detection limit and zeptomole mass detection limit for protein separation by capillary isoelectric focusing and laser-induced fluorescence detection. *Anal. Chem.* **81**, 1741–1746 (2009).

174. Ghasemi, F. *et al.* Improvements to direct quantitative analysis of multiple microRNAs facilitating faster analysis. *Anal. Chem.* **85**, 10062–10066 (2013).

175. Panchuk-Voloshina, N. *et al.* Alexa dyes, a series of new fluorescent dyes that yield exceptionally bright, photostable conjugates. *J. Histochem. Cytochem.* **47**, 1179–1188 (1999).

176. Watanabe, Y. *et al.* Pre-column labelling for high-performance liquid chromatography of amino acids with 7-fluoro-4-nitrobenzo-2-oxa-1,3-diazole and its application to protein hydrolysates. *J. Chromatogr. A* **239**, 723–732 (1982).

177. Heilemann, M. *et al.* Super-resolution imaging with small organic fluorophores. *Angew. Chemie - Int. Ed.* **48**, 6903–6908 (2009).

178. Pinto, D. M. *et al.* Picomolar assay of native proteins by capillary electrophoresis precolumn labeling, submicellar separation, and laser-induced fluorescence detection. *Anal. Chem.* **69**, 3015–3021 (1997).

179. Craig, D. B. Multiple labelling of proteins. *Anal. Chem. 70* (1998).

180. Pugsley, H. R. *et al.* Fluorescein thiocarbamyl amino acids as internal standards for migration time correction in capillary sieving electrophoresis. *J. Chromatogr. A* **1216**, 3418–3420 (2009).

181. Oliveri, P. *et al.* The impact of signal pre-processing on the final interpretation of analytical outcomes – A tutorial. *Analytica Chimica Acta* vol. 1058 9–17 (2019).

182. Gerretzen, J. *et al.* Simple and effective way for data preprocessing selection based on design of experiments. *Anal. Chem.* **87**, 12096–12103 (2015).

183. Vu, T. N. *et al.* Getting your peaks in line: A review of alignment methods for NMR spectral data. *Metabolites* vol. 3 259–276 (2013).

184. Jiang, X. *et al.* Comprehensive two-dimensional liquid chromatography for the characterization of functional acrylate polymers. *J. Chromatogr. A* **1076**, 51–61 (2005).

185. Peters, S. *et al.* Development of a resolution metric for comprehensive two-dimensional

chromatography. *J. Chromatogr. A* **1146**, 232–241 (2007).

186.   Nielsen, N. P. V. *et al.* Aligning of single and multiple wavelength chromatographic profiles for chemometric data analysis using correlation optimised warping. *J. Chromatogr. A* **805**, 17–35 (1998).

187.   Piruska, A. *et al.* The autofluorescence of plastic materials and chips measured under laser irradiation. *Lab Chip* **5**, 1348–1354 (2005).

188.   Tomasi, G. *et al.* Correlation optimized warping and dynamic time warping as preprocessing methods for chromatographic data. *J. Chemom.* **18**, 231–241 (2004).

189.   Kraly, J. R. Reproducible two-dimensional capillary electrophoresis analysis of Barrett's esophagus tissues. *Anal. Chem. p* **78**, 5977–5986 (2006).

190.   Guiochon, G. *et al.* Implementations of two-dimensional liquid chromatography. *J. Chromatogr. A* **1189**, 109–168 (2008).

191.   Harstad, R. K. *et al.* Capillary electrophoresis. *Anal. Chem.* **88**, 299–319 (2016).

192.   Changqun, N. *et al. High performance capillary electrophoresis analysis for cyclosporins*. *Chinese Journal of Antibiotics* vol. 23 (Agilent Technologies, 1998).

193.   Gilliland, W. M. *et al.* Coupling microchip electrospray ionization devices with high pressure mass spectrometry. *Anal. Chem.* **89**, 13320–13325 (2017).

194.   Batz, N. G. *et al.* Chemical vapor deposition of aminopropyl silanes in microfluidic channels for highly efficient microchip capillary electrophoresis-electrospray ionization-mass spectrometry. *Anal. Chem.* **86**, 3493–3500 (2014).

195.   Aashmango4793. File:Flight dynamics with text ortho.svg. *Wikimedia Commons* https://commons.wikimedia.org/w/index.php?curid=81688701 (2019).

196.   Dose, E. V. *et al.* Internal standardization technique for capillary zone electrophoresis. *Anal. Chem.* **63**, 1154–1158 (1991).

197.   Cheng, Y. Q. *et al.* A simple fabrication method for tapered capillary tip and its applications

in high-speed CE and ESI-MS. *Electrophoresis* **35**, 1484–1488 (2014).

198. Zarrin, F. *et al.* Sub-picoliter detection with the sheath flow cuvette. *Anal. Chem.* **57**, 2690–2692 (1985).

199. Affleck, R. L. *et al.* Reduction of luminescent background in ultrasensitive fluorescence detection by photobleaching. *Anal. Chem.* **68**, 2270–2276 (1996).

200. Dada, O. O. *et al.* Capillary array isoelectric focusing with laser-induced fluorescence detection: Milli-pH unit resolution and yoctomole mass detection limits in a 32-channel system. *Anal. Bioanal. Chem.* **397**, 3305–3310 (2010).

201. Zhang, J. *et al.* A multiple-capillary electrophoresis system for small-scale DNA sequencing and analysis. *Nucleic Acids Res.* **27**, e36 (1999).

202. Nirode, W. F. *et al.* Evaluation of a sheath flow cuvette for postcolumn fluorescence derivatization of DNA fragments separated by capillary electrophoresis. *Anal. Chem.* **70**, 182–186 (1998).

203. Moore, A. W. *et al.* Rapid comprehensive two-dimensional separations of peptides via RPLC-optically gated capillary zone electrophoresis. *Anal. Chem.* **67**, 3448–3455 (1995).

204. Saar, K. L. *et al.* Enhancing the resolution of micro free flow electrophoresis through spatially controlled sample injection. *Anal. Chem.* **90**, 8998–9005 (2018).

205. Henley, W. H. *et al.* High electric field strength two-dimensional peptide separations using a microfluidic device. *Electrophoresis* **33**, 2718–2724 (2012).

206. Zhu, Z. *et al.* Two-dimensional chromatographic analysis using three second-dimension columns for continuous comprehensive analysis of intact proteins. *Talanta* **179**, 588–593 (2018).

207. Ren, J. *et al.* Two-dimensional liquid chromatography consisting of twelve second-dimension columns for comprehensive analysis of intact proteins. *Talanta* **182**, 225–229 (2018).

208. Xue, G. *et al.* Multiplexed capillary zone electrophoresis and micellar electrokinetic

chromatography with internal standardization. *Anal. Chem.* **71**, 2642–2649 (1999).

209. Hyötyläinen, T. *et al.* Determination of morphine analogues, caffeine and amphetamine in biological fluids by capillary electrophoresis with the marker technique. *J. Chromatogr. A* **735**, 439–447 (1996).

210. Jumppanen, J. H. *et al.* Marker techniques for high-accuracy identification in CZE. *Anal. Chem.* **67**, 1060–1066 (1995).

211. Li, X. F. *et al.* Migration time correction for the analysis of derivatized amino acids and oligosaccharides by micellar capillary electrochromatography. *J. Chromatogr. A* **869**, 375–384 (2000).

212. Allen, R. C. *et al.* Semi-automated alignment and quantification of peaks using parallel factor analysis for comprehensive two-dimensional liquid chromatography-diode array detector data sets. *Anal. Chim. Acta* **723**, 7–17 (2012).

213. Pierce, K. M. *et al.* Review of chemometric analysis techniques for comprehensive two dimensional separations data. *J. Chromatogr. A* **1255**, 3–11 (2012).

214. Furbo, S. *et al.* Pixel-based analysis of comprehensive two-dimensional gas chromatograms (color plots) of petroleum: A tutorial. *Anal. Chem.* **86**, 7160–7170 (2014).

215. Parastar, H. *et al.* Comprehensive two-dimensional gas chromatography (GC×GC) retention time shift correction and modeling using bilinear peak alignment, correlation optimized shifting and multivariate curve resolution. *Chemom. Intell. Lab. Syst.* **117**, 80–91 (2012).

216. Zhang, D. *et al.* Two-dimensional correlation optimized warping algorithm for aligning GCxGC-MS data. *Anal. Chem.* **80**, 2664–2671 (2008).

217. Gargano, A. F. G. *et al.* Capillary HILIC-MS: A new tool for sensitive top-down proteomics. *Anal. Chem.* **90**, 6601–6609 (2018).

218. White, B. Capillary electrophoresis with electrochemical detection. in *Capillary Electrophoresis and Microchip Capillary Electrophoresis: Principles, Applications, and Limitations* 161–176 (John Wiley & Sons, Inc., Hoboken, NJ, 2013).

219. Da Silva, J. F. *et al.* Capacitively coupled contactless conductivity detection (C4D) applied to capillary electrophoresis (CE) and microchip electrophoresis (mCE). in *Capillary Electrophoresis and Microchip Capillary Electrophoresis: Principles, Applications, and Limitations* 145–160 (John Wiley & Sons, Inc., Hoboken, NJ, 2013).

220. Skinner, C. D. Fiber optic illumination of a poly(dimethylsiloxane) sheath flow cuvette for diode laser induced fluorescence detection in capillary electrophoresis. *Electrophoresis* **36**, 502–508 (2015).

221. Huge, B. J. *et al.* Capillary zone electrophoresis with fraction collection for separation, culturing, and identification of bacteria from an environmental microbiome. *Anal. Chem.* **91**, 4649–4655 (2019).

222. Zhang, Q. *et al.* Prototyping of poly(dimethylsiloxane) interfaces for flow gating, reagent mixing, and tubing connection in capillary electrophoresis. *J. Chromatogr. A* **1324**, 231–237 (2014).

223. Chenvidyakarn, T. *Buoyancy effects on natural ventilation*. (Cambridge University Press, New York, NY, 2012).

224. Morton, B. R. *et al.* Turbulent gravitational convection from maintained and instantaneous sources. *Proc. R. Soc. London. Ser. A. Math. Phys. Sci.* **234**, 1–23 (1956).

Appendix I Preparation of the Negative Mold for the Sheath Flow Cuvette

Fabrication of the sheath flow cuvette required multiple curing and assembly steps. Capillary alignment is ensured by use of a standard 1" × 3" microscope slide template. A 4-40 set screw was epoxy cemented near, and centered upon, each of the two 1" edges of the microscope slide. (Figure 25 a). Each set screw was angled so the threads were perpendicular to the same edges. Fishing line (12 lb, diam. 0.034 mm nominal) was wound around the microscope slide and through the troughs of the set screw threads, providing equal spacing of ≈0.635 mm in a plane 2.45 mm from the front of the microscope slide (Figure 25 b, c, d, e). Each end of the fishing line was secured to the rear side using a piece of office-use adhesive tape (Figure 25 b). Nylon fishing line has been used previously for moulding channels into PDMS flow gating interfaces.[222] It has a convenient size similarity to capillaries used in CE and does not suffer from similar fragility, making it ideal as a negative template when casting in PDMS moulds.

The moulding templates for the front fluorescence emission window and the rear walls were prepared from two sections of 0.25 mm plastic film (Figure 25 h-1:matte plastic shrink film, Gary M Burlin & Co., Cleveland, USA; h-2: Hytrel) that were cut to the same width as the bundle of parallel fishing lines (≈4.479 mm for 8 capillaries). The sheets were arranged to closely follow the fishing line. One sheet was inserted to lie under and one atop the fishing lines, centered between the set screws (Figure 25 d). The top sheet was curled upwards at the ends nearest the set screws by creasing the last 1.5 mm of the sheet. The bottom sheets were cut ≈1.5 mm shorter than the top sheets so the length contacting the fishing line was equal. The total plastic length equalled ≈35 mm. To adhere plastic sheets to the fishing line, aluminum sheets were first placed between the fishing line and glass slide to apply minimal tension to the fishing line. The rear plastic sheet was inserted between the fishing line and aluminum risers. A drop of uncured PDMS was placed on the fishing line and allowed to flow across the plastic sheet surface and rise above the top of the fishing line. The front sheet was placed on top of the fishing line. Both sheets were aligned to the fishing line under a microscope. An aluminum block was placed on the front sheet while the PDMS cured. Upon curing, the block and aluminum risers were removed from the assembly.

Four glass walls were placed with their largest face along the open edges of the plastic sheets that sandwiched the fishing line to become fluorescence excitation windows. These glass walls were prepared by cutting the ends of microscope slides, measuring ≈6 mm × ≈15 − 20 mm (Figure

25 e). By using the ends of the glass slides, an in-built square edge ensured the wall was placed perpendicular to the glass base during attachment with a small amount of PDMS following by curing at room temperature.

A wall was placed transverse to the axis of the fishing line and at the midpoint along their lengths and between the two sets of plastic sheets (Figure 25 g, d). The wall was prepared from a 25 mm × 6 mm × 1 mm aluminum sheet. A slot was made starting from the center of one 6 mm edge using a 1/16" end mill and extending 20 mm into the sheet. This cut-out allowed the aluminum sheet to slide over the fishing line and span the width of the microscope glass base.

Two 25.4 mm lengths of 1/16" or 1/8" PTFE tubing were cut to cast buffer inlet and outlet holes. A lengthwise cut was made at the center of the tubes to make a 6.5 mm slit. Two transverse cuts were made from the exterior to the ends of the slit, but each on opposite sides of the tube. This produced two mirrored tubes with a 6.5 mm section with half of the tube removed (Figure 61). The remaining lumens were filled with PVA glue (LePage, Carpenter's glue) and allowed to harden. Each of the inner faces of the 6.5 mm sections was placed against the section of plastic sheet that was bent away from the fishing line and held in place using red silicone sealant (Figure 25 h-2). This approximated an intact tube, with the row of fishing line passing through a centrally located axial slot, whose length spanned the 1" width of the underlying glass slide.

Figure 61 Image of fabricated 1/8" PTFE tubes after being cut and filled with PVA glue. The right-hand section with half of the tube removed was placed against the fishing line to act as a template for the conduits that joined the laminar flow channel to the BGE supply and waste tubing.

The above assembly was placed into a rectangular aluminum mould to enclose the template and PDMS while it cured. The mould was prepared from an aluminum block (8 mm × 95.3 mm × 38.1 mm), which was milled through it's largest face to produce an aluminum

tube along the 8 mm edge. Two versions were prepared. One version was separated into two parts with one 95.3 mm wall was removable (Figure 25 f). The other version was retained as a single piece, with tapped holes at the far ends of one of the 95.3 mm walls (Figure 25 g). The interior of each mould was prepared with filleted corners, which overlapped the corners of a 1" × 3" microscope slide (Figure 25 f, †). The filleted corners were machined on one 95.3 mm × 38.1 mm face to create four shelves at a depth of 1.5 mm, which could accommodate the thickness of the microscope side rear face (Figure 25 g). A 25.4 mm × 8 mm section of microscope glass slide was epoxy cemented onto each of the interior 95.3 mm walls of the tube (Figure 25 f, ‡). These acted as templates for indented excitation windows which were on the upper right-hand and lower left-hand sides of the sheath flow cuvette (Figure 25 k, *) on either sides of the bisecting aluminum wall. The microscope slide assembly was placed in the mould with the front corners resting on the shelves in the filleted aluminum tube corners and fixed in place by placing a drop of PDMS onto each corner and allowing it to cure. Sheets of ¼" plate glass were placed on the front and rear faces of the aluminum tube to ensure the PDMS cured against a smooth template surface. The two sheets of glass were held tightly against the aluminum tube using mechanical spring clamps. PDMS was injected through the respective openings in the 95.3 mm wall of the aluminum tube, taking care to not introduce bubbles or voids, until it was slightly overfilled. The tube was enclosed by replacing the wall (Figure 25 f) or inserting parafilm wrapped screws (Figure 25 g). The final assembly was placed in a 37 °C oven to cure for 24 – 48 hours until fully cured.

Appendix II Density Issues with ^{1}D Organic Mobile Phases

The fluorescence images in Figure 62 show a time lapsed view of a motor injection sequence, where the ^{1}D capillary was constantly emitting effluent comprised of a fluorescein solution dissolved in BGE with 20 % ACN. Illumination was provided by a fiber optic that whose entrance was coupled to a laser. The fiber optic exit was positioned in the interface above the upper left corner of the image. Auto-fluorescence from the polyetherimide optical window obscures the view, but the dashed lines approximate the most intense portion of the cone of light in the first frame. An image mask has been applied to highlight the ^{1}D capillary, the five ^{2}D capillaries and the upper edge of the interface chip that held the ^{2}D capillaries in place. An empty capillary channel was placed between each ^{2}D capillary to permit higher BGE flow rates through the interface. Wash buffer flowed downward at the maximum velocity allowed by the gravity mediated flow rate this early generation prototype. The velocity was about 10 mm/s in the region of the capillary tips.
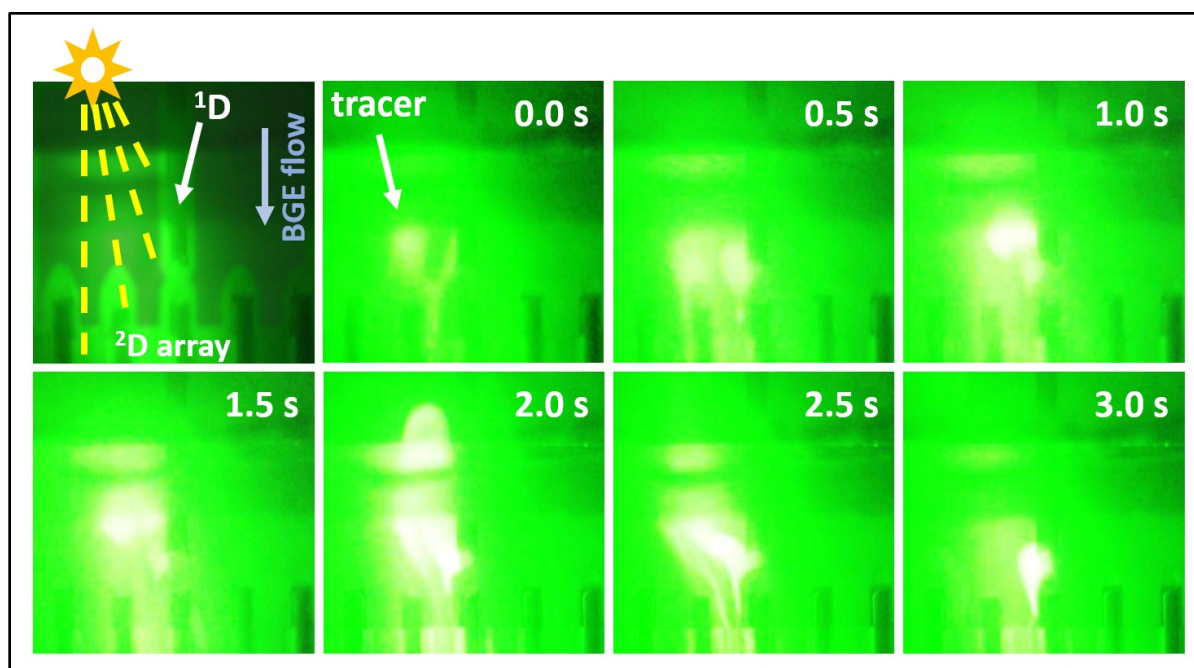

Figure 62 Unpredictable path of low organic solvent HPLC effluent when introduced to high velocity BGE flow directed downward in the interface. BGE flow was directed downwards at ~10 mm/s. HPLC effluent was kept constant at 2 μL/min as it exited from a 180 μm i.d. capillary. HPLC mobile phase: 20 μM borate, 20 % ACN, 10 μM fluorescein. Interface BGE: 20 mM borate pH 9.2. The first image was overlaid and masked to outline features that were obscured in the time series. The rays outline the fiber optic guided laser light, which was positioned out of view, in the upper-left and directed towards the ^{1}D capillary outlet. The partial grey mask outlines the positions of the capillaries for the ^{1}D outlet and five ^{2}D inlets.

At 0.0 s, the donor and receiver capillaries have just been moved into coaxial alignment for injection. This perturbation caused the ^{1}D effluent to form a plume that rose upward (despite being surrounded by a $\approx$ 10 mm/s downward flow) to the top of the interface BGE pool. By 2.0 s and 2.5 s the plume was fully developed and, more importantly, none of the effluent was being injected onto the ^{2}D capillary. It is noteworthy that the ^{1}D effluent was prepared with 20 % ACN, a common starting concentration for many RPLC elution gradients used in protein separations. Since a gradient separation would introduce even higher concentrations of organic solvent, RPLC ^{1}D separations were precluded from use in the presented design.

In retrospect, this density difference effect was somewhat obvious. However, given that the ^{1}D effluent was ensheathed in a high-velocity BGE flow it was assumed that the effluent would be swept past the ^{2}D capillary tip. It is worth noting that the buoyant force caused by density differences in mixed fluids is a well-studied field, important in areas such as oceanic and atmospheric convection processes as well as in architectural airflow design. The following simplified analytical solution describes the flow behaviour observed above.[223,224]

$$\beta = g\frac{\rho_0 - \rho}{\rho_0} \tag{15}$$

Here, β is the buoyant force, g is the gravitational force (9.8 m/s^2), ρ_0 is the reference fluid density and ρ is the density of the fluid under inspection. Thus, β can be readily obtained by calculating the ratio of the density difference between the two fluids over the bulk reference fluid and relating this ratio to the force of gravity. Since gravity is large relative to the velocity scales used in the MDS interface, this causes a large change in the velocity of the ^{1}D effluent as it enters the aqueous flow in the interface. Above 20 % ACN, having an approximate density of 0.93 g/mL, the buoyant force is predicted to produce a 684 mm/s^2 upward acceleration when introduced into a pure water bulk solution.

By considering an average axial injection distance of 35 μm and using a fast ^{2}D EOF velocity of 2 mm/s, 17.5 ms would be required to traverse the gap between donor and receiver capillaries. Using this interval as the expected time for effluent to transfer from the ^{1}D to the ^{2}D,

To demonstrate the magnitude of the buoyant force, the velocity change that would occur during this short 17.5 ms effluent transfer interval was plotted as a function of ACN concentration in Figure 62 using published density information of ACN-water solutions. The buoyant force of a solution containing just 18 % ACN would result in a 12 mm/s upward velocity change during the transit. At 100 % ACN, a typical mobile phase at the end of a gradient separation, the velocity change would reach 38 mm/s. These results demonstrated that a new, inverted, interface design would be necessary for successful integration of a chromatographic [1]D utilizing organic mobile phases. Thus, the work presented in this dissertation was focused using aqueous-only media and electrophoretic separations.
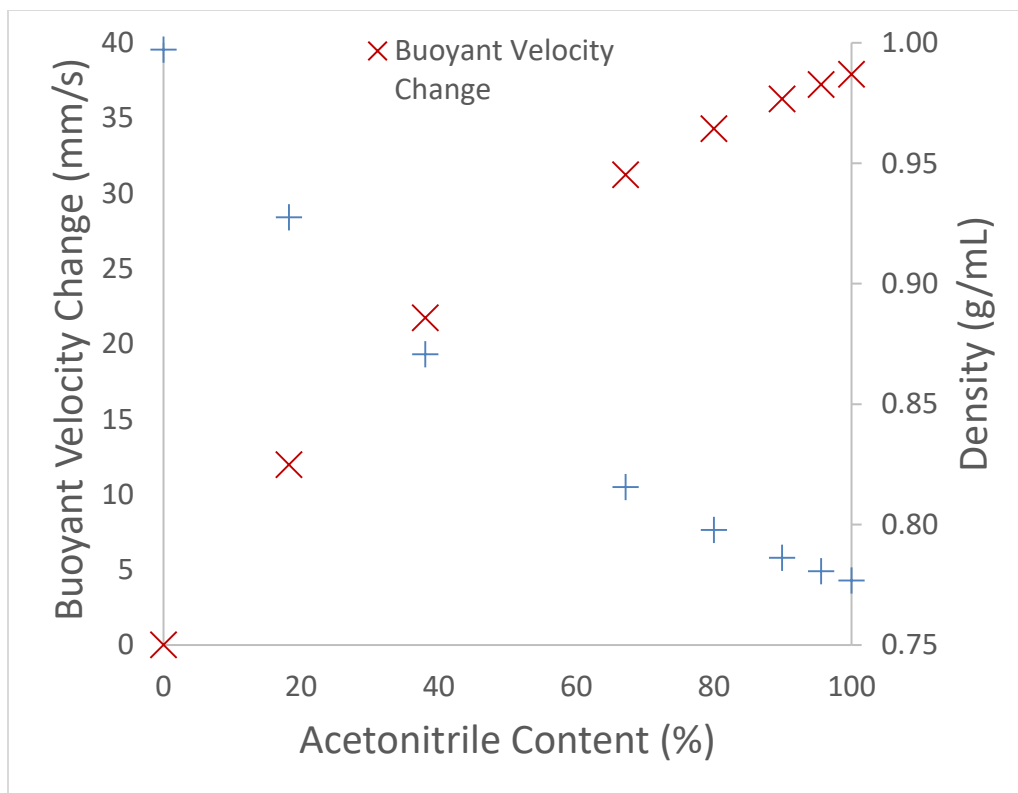

Figure 63 The effect of buoyant acceleration of a low-density fluid after introduction into a high density fluid. Plot shows the calculated velocity of various concentrations of ACN solutions 17.5 ms after introduction below the surface of a body of water. Density information was obtained from Cunningham et al. 1967.